Powder Characterisation, Microstructure, and Mechanical Property Evolution of IN625 and IN718 During Selective Laser Melting and Heat Treatment

Submitted to Swansea University in fulfilment of the requirements for the Degree of Doctor of Philosophy

Swansea University

2021

Christopher David Pleass

Abstract

Additive layer manufacturing is a blanket term for a wide range of processes operating on the same underlying principle. 3D geometry is created by depositing material, layer by layer to create a final 3D geometry. Selective laser melting (SLM) is a branch of additive layer manufacturing, using a laser to fuse a powder bed of metal into each layer. This thesis investigates the SLM process and its application to nickel based superalloy materials, IN625 and IN718.

IN625 and IN718 are similar nickel-based superalloys developed for use in aerospace gas turbine engines. In their conventionally manufactured form, these materials have excellent high temperature mechanical properties which make them idea for use in the hot section of gas turbine engines. The aim of this thesis was to investigate how these materials interact with the SLM process and how the material produced can be optimised to improve the range of applications it can be used for.

A gap in knowledge regarding a detailed understanding of how the powders morphological and rheological properties influence its ability to be processed by SLM was identified and investigated. A wide range of characterisation methods were implemented with certain important properties being identified to assess a powders processability, namely the particle size distribution and how a significant content of fine particles below 10 µm in size can be detrimental to processability. There is also a lack of a standard powder characterisation methodology specifically for SLM applications. This is addressed with certain methods and measurements being suggested as most promising for wider SLM application. Avalanche flow testing is found to be most applicable to the critical recoating process in SLM and most able to differentiate suitable and unsuitable SLM powders.

Following characterisation of the raw material feedstock powder, this thesis also investigates the influence of processing parameters on the microstructure of the material produced by the SLM process. Significant microstructural changes were observed as a result of process parameter changes. This was identified to potentially enable for in-situ modification of material microstructure to suit a manufactured material to its end application. Of the process parameters investigated, laser scan speed was most interesting, suggesting that a faster laser scan speed was able to create a similar microstructure to a much slower one. This was attributed to the reheating effect of the laser beam returning quickly to the adjacent scan line. The validity of this explanation was investigated using a simple, computational thermal model. The result is a new understanding of laser scan speed SLM and its nonlinear relationship with material temperature and microstructure evolution.

Finally, post process heat treatments of SLM manufactured IN718 material were investigated. This investigation was in response to a gap in current knowledge regarding heat treatments designed specifically for SLM material. SLM IN718 has been found to have reduced high temperature mechanical properties, specifically stress rupture, which limits its application in demanding environments. In this thesis a range of post process homogenisation heat treatments were investigated, with treatments between 1030 °C and 1060 °C being found to produce material with characteristics consistent with material with excellent stress rupture properties. This novel heat treatment route could provide a method for SLM IM718, and the increased design and geometric freedoms, to be applied in more demanding applications.

An evolution of the grain structure in the material was also observed and measured during high temperature homogenisation treatments. This was investigated in the final chapter, and a novel mechanism is suggested for the process of grain coarsening observed. Previously published literature explains similar evolutions as recrystallisation however this did not fit the observations during this thesis. The evolution of grain structure was observed using a process of quasi in-situ electron back scatter diffraction, and a mechanism of grain boundary length reduction, followed by grain growth, is suggested to better fit the observations. It was determined that grains are preferentially selected for growth based on their proximity to a 'path of least resistance' of lower angle grain boundaries.

The results of this work should benefit industrial users of SLM in the fabrication of Nickel-Based Superalloy material for aerospace applications. The conclusions on powder characterisation offer an insight into available methods to better control and characterise powder feedstock materials for consistent production. Aerospace users especially may find the work regarding post process heat treatments designed specifically for SLM material, to recover lost stress rupture performance, useful in enabling the use of SLM materials, and the design freedom that brings with it, in mor demanding environments than are currently possible.

Declarations and Statements

1. I declare that this work has not previously been accepted in substance for any degree and is not being concurrently submitted in candidature for any degree.

2. I declare than this thesis is the result of my own investigations, except where otherwise stated and other sources are acknowledged by footnotes giving explicit references and that a bibliography is appended.

3. I give consent for this thesis to be made available online in the University's Open Access Repository and for inter-library loan, and for the title and summary to be made available to outside organisations.

4. I declare than the University's ethical procedures have been followed and, where appropriate, that ethical approval has been granted.

Signed:

19-10-21

Christopher Pleass

Contents

Acknowledgements

I would like to thank my supervisors throughout this project, Dr D.G. Leo Prakash and Dr Sathiskumar Jothi.

I would also like to thank my industrial supervisors with whom I have had the pleasure of working for the provision of materials, time, expertise and so much more. Dr Krishnam Manickavasagam and the rest of the team at A*STAR ARTC, Singapore for their help warm welcome and support during my time in Singapore. Dr Alphons Antonysamy and the rest of the AM team at GKN Aerospace, Filton for being so accommodating during my visits to their site.

I am also indebted to the Peter Davis, James Russel, Gareth Davies and Dagmar Butkovicova for their long running and seemingly endless help with set up, maintenance and repair of heat treatment furnaces, coupon preparation equipment and microscopes. Also, for their patience with my numerous queries and questions throughout the project.

This work would not have been possible without the full financial support provided to me by EPSRC covering research, conference expenditure, stipend and tuition fees throughout my project.

Without any of the people or organisations mentioned above this project would not have been possible.

Publications from this thesis

The Effects of powdered feedstock characteristics and process parameters on the properties of IN625 produced my laser powder bed fusion – Presented at 2017 Student Conference in Metallic Materials, Sheffield

Influence of powder characteristics and additive manufacturing process parameters on the microstructure and mechanical behaviour of Inconel 625 fabricated by Selective laser Melting – Journal Article – Additive Manufacturing

Figures

Tables

Equations

1 Introduction

In 2018 aviation was responsible for 895m tonnes of CO_2 emissions ("Air Transport Action Group," 2006), making up roughly 12% of CO_2 emissions from transportation and 2% of global CO_2 emissions ("Air Transport Action Group," 2006; Climate Central, 2012). This is a significant proportion and gives the aviation industry a significant responsibility in achieving global environmental goals. The largest climate change agreement of all, the Paris agreement sets out a target to limit any average global temperature increase to 1.5°C in order to reduce the risks of climate change.

On top of the moral obligation to reduce the impact of aviation on global climate change improving the efficiency of aircraft brings an undeniable economic benefit to airlines. Aviation fuel is the most significant cost for airlines, and the most volatile. Prices of fuel rose by 167% in the years between 2000 and 2018 (Airlines For America (A4A), 2010). Ultimately, reductions in emissions will come from reduced fuel consumption, which will bring with it a reduction in costs and volatility for airlines.

Setting targets for reduced emissions is one thing however achieving them requires innovation and the development of new technology. There are several approaches to this problem; reducing the weight of aircraft, developing cleaner burning or bio fuels (MIT Technology Review, n.d.) and improving efficiency of the engines themselves, this latter point being of particular interest.

In general, the efficiency of a gas turbine engine is improved by increasing the fan pressure ratio and the turbine inlet temperature. As the operating temperature within the hot section of gas turbine engines increases, so too do the demands on the components working in those environments. To address these demands, high performance materials are required, of which, nickel-based superalloys Inconel 625 and Inconel 718 are the focus in this work. To enable innovative and more efficient designs, new manufacturing techniques are also required, specifically additive manufacturing. It is essential to develop a better understanding of how nickel-based superalloys respond to additive manufacturing processes and how they can be improved. This knowledge will enable designers and engineers to apply these materials and techniques in suitable applications while understanding the limitations.

1.1 Nickel-Based Super Alloys – IN625 and IN718

Nickel-based superalloys are a family of highly complex alloys with many constituent elements which use nickel as the base solvent metal. Developed for use in demanding, high temperature aggressive environments these materials are essential in the production of aerospace gas

turbine engines, specifically components in the hot section of the engine, downstream of the combustion chamber.

Initially developed for aerospace applications IN625 and IN718 are common materials used in the production of low-pressure turbine blades and disks, thrust reversers and high temperature bolts for gas turbine engines. This makes them an essential research topic in the push towards more efficient aviation. As engine temperatures increase, many of these components will most directly feel these changes, requiring altered designs.

Outside of aviation these superalloy materials see use in many other demanding applications where the same high temperature stability is essential. Applications such as pressurised water reactors and heat exchangers in nuclear power plants (Office of Nuclear Energy, 2016; Physical Sciences Inc., 2009), high performance automotive turbine wheels and exhausts (Alfa Romeo Sauber, n.d.; McLaren, 2015; Newman John, 2011; Taylor Edward, 2016), high current electric car battery connectors and liquid fuel rocket thrust chambers and manifolds.

1.2 Additive Manufacturing

Additive layer manufacturing is a blanket term for a wide range of processes operating on the same underlying principle. 3D geometry is created by depositing material, layer by layer to create a final 3D geometry. First developed in the early 1980's, AM was initially intended as a quick and relatively cheap path from digital design to prototype (rapid prototyping) without the need for creating tooling or fixtures (Wong & Hernandez, 2012).

An additive, rather than conventionally subtractive, approach to manufacturing brings with it a range of advantages. The ability to create complex internal geometries unrestricted by the need for tooling access and the lack of need for specific tooling or jigs are the principal advantages. They make the manufacturing process very agile, able to produce any desired component at any time with fast iterations to designs. These advantages and increased geometric freedoms enable designers and engineers to produce more efficient designs of components while also producing less waste and potentially using less energy. Component designs can not only be made more efficient but also component count can be reduced with assemblies being reduced to single components, reducing failure points.

In this work, Selective Laser Melting (SLM) is the additive manufacturing process being investigated. The SLM process used a laser beam to fuse a powder bed of material to create the final geometry of the part. SLM is an additive manufacturing technique aimed at the manufacture of smaller, higher accuracy new parts. The small laser beam spot lends itself to

higher resolution parts while the need for an enclosed machine with a controlled, inert atmosphere makes the cost of increasing the build volume of a machine high.

1.3 Nickel-Based Super Alloys Produced by SLM

The geometric freedom and potential for optimised, efficient designs is greatly beneficial to nickel-based superalloys. As has already been highlighted, there is a drive for improved efficiency in aerospace gas turbine engines, necessitating increased temperatures and expanded use of superalloy materials. Through the application of SLM, the improved properties of nickel-based superalloy material can be applied in combination with improved designs to further improve efficiency.

A secondary benefit of SLM in the production of components from nickel-based superalloys is that it avoids common issues that come from working with high strength material. IN718 for example poses some difficulties when forming and machining as it work hardens significantly leading to high tool temperatures, chatter and premature tool wear (Dudzinski et al., 2004). By manufacturing the material additively this is avoided, instead leveraging its excellent weldability to create the final geometry directly, the need to subtract material is removed or limited to much smaller, critical features.

1.4 Powder Feedstock Material for SLM

The raw material for the SLM process is a powdered metal. This is typically manufactured using a process of gas atomisation to create acceptably spherical particles (Mostafaei et al., 2018; Slotwinski & Garboczi, 2015). This powdered feedstock material introduces an additional layer of complexity to the manufacturing process.

Whenever it is moved, a powder is required to flow. In the SLM process the most critical powder movement is when a new layer is deposited onto the build pate. The quality of this layer directly affects the quality of the finished part.

In all manufacturing it is important that the process is controlled, reliable and repeatable however, in aerospace manufacturing these requirements are heightened by the consequences of any part defects. It is therefore essential, for any wider adoption of SLM as a manufacturing method, that the flow properties, or rheology, of the powder are understood and controlled.

This requires the careful study of powder flowability to establish the critical powder properties which must be controlled and monitored by any user. To achieve this is also necessary to assess the available methods for characterising these properties and understand which of them provide the best analogue for the SLM process.

1.5 Stress Rupture Limitation of Nickel-Based Superalloys Produced by SLM

One limitation of nickel-based superalloys produced by SLM is their high temperature performance, specifically stress rupture. In IN718 is has been found that while other room temperature mechanical properties are of an acceptable level or superior to conventionally manufactured material, the stress rupture properties, both life and elongation, were significantly below what is acceptable. Results, following standard heat treatments (AMS 5662 and AMS 5664), from a comparison with conventionally manufactured material are provided in Figure 1 form IN718 material. Failure of the sample, even after the application of heat treatments, occurred much sooner than desired and/or at a significantly reduced elongation. This highlights both the shortcomings of superalloys produced by SLM as well as the need for the development of specific heat treatment routes tailored for the unique material they produce. A modified heat treatment route specifically designed for SLM material might be able to recover some or all of these lost properties. This would open new potential applications for superalloys produced by SLM into higher temperature, higher sustained load applications.

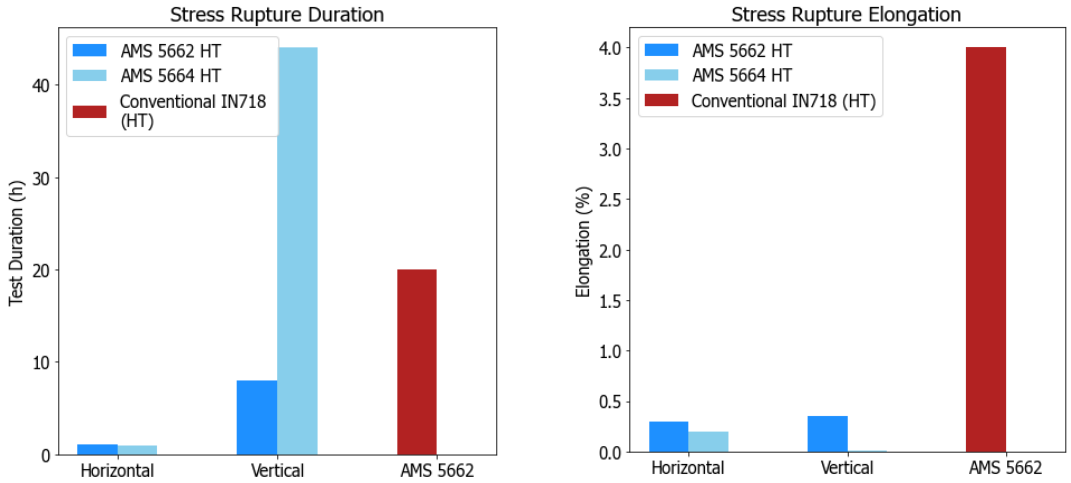

Figure 1 – Plots showing the stress rupture properties, rupture duration and elongation of SLM IN718 material compared to conventionally manufactured material. Plots supplied by GKN Aerospace.

1.6 Unique Thermal History of SLM Nickel-Based Superalloys

The root cause of the difference in high temperature properties and response to heat treatments of SLM material compared to conventionally manufactured is in their thermal history. Scanning and melting by a small laser spot during SLM results in steep thermal gradients and rapid cooling of the material. This creates a very different microstructure with differently sizes and oriented grains as well as dramatic differences in the distribution and segregation of the alloying elements.

Further to this, since the microstructural properties of the material are so significantly altered by the way the material is manufactured, this presents an opportunity for in situ control. The

heat input and cooling of the material is controlled by the laser spot as it traverses the material, the laser spot is in turn controlled by the processing parameters selected. It may therefore be possible to control the microstructure created in the material through modification of these processing parameters, enabling specific microstructures to be created in the material directly in the as fabricated state, removing the need for heat treatments and increasing productivity for certain applications.

1.7 Aims of the Project

The aim of this work was to expand the current understanding of the manufacturing of IN625 and IN718 by SLM. This was approach from three primary angles:

1. Improve the understanding of the powder feedstock material and its characterisation. This work should enable users to better control the raw material for the SLM process, improving consistency, reliability and repeatability. There are a number of methods available for characterising powders rheology and a range of published literature on the behaviours of powder however, its application specifically to superalloys for SLM is limited. Investigating this and understanding how this literature applies to a new process and materials will be valuable to the wider adoption of SLM (and potentially other additive manufacturing) techniques.
2. Understand how the SLM process and the processing parameters selected affect the microstructure of the material produced. The differences in microstructure between conventional and additively manufactured materials are well documented. The aim of this work was to further this knowledge by examining the specific microstructural changes which are caused by changes to individual processing parameters. The motivation behind this investigation was the improved understanding of processing parameters to better inform the selection of parameters with the possibility of modifying the materials microstructure in situ. This might allow for the tailoring of microstructures to specific applications without the need for heat treatments.
3. Developing an SLM specific heat treatment route for the improvement of mechanical properties. The microstructural differences between conventional and additively manufactured material have been demonstrated to significantly alter the materials response to heat treatments. This leads to a loss of important mechanical properties such as stress rupture life and elongation following a standard heat treatment. The aim of this work was to develop a new heat treatment route, designed specifically to work with the microstructure created by SLM, which might improve or restore the lost mechanical properties. The heat treatment route is developed for a general

improvement in properties however some focus is put on predicting its effect on stress rupture life.

1.8 Thesis Structure and Chapter Summaries

From this point forwards this thesis is divided into 7 further chapters. These chapters are briefly summarised below:

2. Literature review: A review of existing publications and data surrounding the topic of manufacturing nickel-based superalloys via SLM. The literature review briefly covers the history of both material and manufacturing methods before characterising the current state of the art and identifying three gaps in current knowledge which will be the focus of this work.
3. Experimental Methodology: This chapter contains an explanation of the experimental methods carried during this work. The intention of this chapter is to give the reader and understanding of what work has been completed and provide a guide which could be followed to reproduce the results obtained. Where appropriate the justification behind the selection of certain experiments is also given. In the interest of succinctness certain standard procedures, such as sample polishing or SEM settings are omitted.
4. Results and Discussion: In this chapter the key results from the investigation carried out as part of this work are presented and explanations for the findings are given. In the case of multiple tests giving similar results, only one set of results or images may be presented as the inclusion of more would not provide any additional information.
5. Conclusions: This chapter provides a brief summary of the key findings from the investigations carried out. The key findings selected relate to the initial aims of the project with any additional novel findings also included.
6. Appendix: This chapter contains some additional experimental results which are not critical to the findings of the thesis however provide additional context and information where relevant.
7. Abbreviations: This chapter provides a list of abbreviations used for the readers understanding. Care has been taken to clarify abbreviations in the text where they are used, but this list provides an easy to browse list.
8. Bibliography: A list of all references cited in the text

2 Literature Review

2.1 Introduction to Nickel-Based Superalloys – IN625 and IN718

Nickel-based superalloys are a family of materials developed to have suitable properties for demanding applications in aggressive environments. Nickel-based superalloys are characterised by excellent mechanical properties over a wide range of service temperatures and a good resistance to corrosive environments.

Superalloys are complex alloy systems which can contain upwards of 10 alloying elements. Nickel-based superalloys use nickel as the solvent metal into which the other elements are dissolved. The two alloys of interest in this work are Inconel 625 and Inconel 718, referred to as IN625 or IN718.

2.1.1 Development of IN625 and IN718

IN625 was developed in the 1950's by the International Nickel Corporation. The aim was to create a new material for use in steam lines for super critical steam power plants to replace the 316L stainless steel being used at the time. During this development, it was discovered that different combinations of Nb and Mo with a Ni base produced a material with the ability to age harden significantly. This discovery led to a separate material being developed which would become IN718, delaying the development of IN625. When the development of IN625 resumed, the needs of super critical steam plants had been met by other alloys. It was decided that, to compete with these new alloys, superior room temperature properties were required. The elements added to achieve this, Cr and Mo, also significantly improved the corrosion resistance of the material, which resulted in a material with desirable properties for a wider range of applications.

IN625 and IN718 were granted patents on the 24th January 1962 and the 13th November 1962, patent numbers US3160500A and US3046108A respectively (*Age-Hardenable Nickel Alloy*, 1958; Eiselstein & Tillack, 1991; C.-M. Kuo et al., 2009; Louis & John, 1962; X. S. Xie et al., 2007)

2.1.2 Comparison of IN625 and IN718

Compositionally IN625 and IN718 are similar, the main components of both being chromium, iron, niobium and molybdenum, which are added to increase the strength of the material and improve the corrosion resistance. The difference between the two alloys is in the composition of each element. IN718 has significantly more Fe content whereas IN625 has more Mo and Cr, balancing the rest of the difference with Ni. The compositional difference of a few main elements is given in Table 1. Maximum Ni and Fe content for IN625 and IN718 are specified as a

balance of the rest of the elements, the value of the maximum content was calculated assuming the minimum content of all other elements.

Table 1 – Table giving the maximum allowable content of each element in IN625 and IN718. Maximum Ni and Fe content are calculated assuming the minimum content of all other elements in the alloy.

	% wt.		Δ
	625 (Max)	**718 (Max)**	
Ni	68.85	55	-13.9
Cr	23	21	-2
Fe	5	24.6	19.6
Nb	4.15	5.5	1.35
Mo	10	3.3	-6.7
Ti	0.4	1.15	0.75

These compositional differences dictate the difference between the two alloys. Although both have good corrosion resistance and high temperature strength, IN625 is more corrosion resistant while IN718 is higher strength (tensile properties listed in Table 2). As a result, IN625 is used in applications such as exhausting and ducting in gas turbine engines as well as wet scrubbers in furnaces and acidic processing equipment (*Inconel 625 (Tm) Super Alloys [Altemp 625 (Tm),Chronin 625 (Tm),Custom Age 625 Plus Alloy (Tm),HAYNES 625 Alloy,Nickelvac 625 (Tm),Nicrofer 6020 HMo (Tm),Pyromet Alloy 625 (Tm),Udimet 625 (Tm),VLX625 (Tm)] Material Property Data Sheet*, n.d.; Special Metals Corporation, 2013). IN718 on the other hand is used for disks and turbine blades in jet engines, liquid rocket engine components, high temperature bolts and airframe parts (Aircraft Materials, n.d.; Clavel & Pineau, 1978; Jinhui et al., 2017a; C.-M. Kuo et al., 2009; Special Metals Corporation, 2004).

Table 2 – Room temperature tensile properties of IN625 and IN718 (Special Metals Corporation, 2007, 2013)

	YS (Mpa)	**UTS (MPa)**
IN625	415 - 750	830 - 1100
IN718	1035	1240 - 1275

Despite the compositional differences, as the main alloying elements in both alloys are the same, the precipitate phases which can form in either alloy are the same, so they will be discussed together in later sections.

2.1.2.1 IN718

The chemical composition of IN718 is given in Table 3. Although nickel is the primary element of the alloy, due to its significant iron content, IN718 is correctly termed a nickel-iron based superalloy.

Table 3 – Table listing the textbook chemical composition of the alloy IN718 (Special Metals Corporation, 2007)

	Ni	Cr	Fe	Nb	Mo	Ti	Al	Co	C	Mn	Si	P	Si	B	Cu
Min	50.0	17.0	Bal	4.75	2.80	0.65	0.20		-	-	-	-	-	-	-
Max	55.0	21.0		5.50	3.30	1.15	0.80	1.0	0.08	0.35	0.35	0.015	0.015	0.006	0.30

IN718 has many properties which make it ideal for a wide range of applications. Its chemical composition encourages most of its age hardening to come from the slower precipitating γ'' phase, this makes IN718 weldable and resistant to strain age cracking (Çam & Koçak, 1998), it has excellent high temperature properties and good microstructural stability. It is also ductile and has good stress rupture and fatigue properties, remaining serviceable up to 650 °C (Clavel & Pineau, 1978; Du et al., 2007; Ghosh et al., 2008; Kobayashi & Yamaguchi, 2005; Lingenfelter, 1989; Ping et al., 2007). The properties and high strength of IN718 poses some difficulties when forming and machining as it can work harden, leading to high tool temperatures, chatter and premature tool wear (Dudzinski et al., 2004). Despite this, IN718 has become the most widely used superalloy in the world (X. S. Xie et al., 2007; Yeh et al., 2011).

2.1.2.2 IN625

The chemical composition of IN625 is given in Table 4.

Table 4 – Table giving the textbook chemical composition of the alloy IN625 (Special Metals Corporation, 2013)

	Ni	Cr	Fe	Nb	Mo	Ti	Al	Co	C	Mn	Si	P	Si
Min	58.0	20.0	-	3.15	8.0	-	-	-	-	-	-	-	-
Max	Bal	23.0	5.0	4.15	10.0	0.40	0.40	0.10	0.10	0.50	0.50	0.015	0.015

IN625 is a solid solution strengthened alloy although it is also possible for to be age hardened due to its Nb content (Dinda et al., 2009; Special Metals Corporation, 2013). It has excellent resistance to oxidation and corrosive environments as well as good creep, fatigue and yield strength (Dinda et al., 2009; Xiang Xu et al., 2017). With similar Al and Nb content to IN718 the primary strengthening phase in IN625 is γ'', making it readily weldable (Çam & Koçak, 1998) and resistant to strain age cracking.

2.1.3 Microstructural Phases of IN625 and IN718

Both being alloys of the same elements, although in different weights, the microstructural phases capable of precipitating in both IN625 and IN718 are the same. For this reason, they will be discussed together.

2.1.3.1 γ Phase

The γ phase of both IN625 and IN718 is a continuous austenitic, FCC, matrix phase in which all other phases reside. Elements such as nickel, iron, chromium and molybdenum, all with similar atomic radii, partition to the γ phase matrix. These elements act to stabilise the γ phase.

The FCC structure of the γ phase is the lowest energy arrangement of the atoms and is therefore stable. The stability of the γ phase is essential in conveying the excellent high temperature properties of IN625 and IN718 (Reed, 2006b) .

2.1.3.2 γ'' and γ' Phase

γ' is a face centre cubic $L1_2$ ordered phase of Ni_3(Al, Ti). When forming within the material γ' precipitates will typically have a round morphology. The γ' phase has a cubic lattice and similar lattice parameter to the continuous γ matrix, this allows it to form coherently within the γ matrix.

The γ'' phase is a metastable body centre tetragonal phase of Ni_3Nb. The γ'' phase also precipitates coherently within the γ matrix (Reed, 2006a; Sundararaman et al., 1992). The γ'' phase is typically observed with an elongated disk-shaped morphology having an aspect ratio of 3-6 depending on the thermal history of the material. The γ'' precipitates usually form at dislocations within the material. The γ'' phase coarsens as the material is held in the precipitation range longer (Chaturvedi & Han, 1983; Devaux et al., 2008; Radavich, 2004; Reed, 2006a; Slama et al., 1997).

The main reported factor for determining whether a nickel-based superalloy will form γ' or γ'' as its primary strengthening element is the Nb: (AL, Ti) ratio (Jinhui et al., 2017a; Quist et al., 1971; Radavich, 2004; Slama et al., 1997). Where the ratio is higher the alloys for γ'' as is the case for both IN625 and IN718. This means that the bulk of the strengthening in these material is obtained through precipitation of the γ'' phase with only a marginal effect from γ' (Deng et al., 2017; Devaux et al., 2008; Reed, 2006a), this is unlike many other superalloys. In IN718 the volume fraction of γ'' and γ' is roughly 16% and 4% respectively in the aged condition (Chamanfar et al., 2013; Ram et al., 2005; Slama et al., 1997). This characteristic makes IN625 and IN718 more weldable because the γ'' phase precipitates more slowly than γ', due to high coherency strains, making the material less susceptible to strain age cracking in the heat affected zone (Çam & Koçak, 1998; Reed, 2006a).

With Nb being a major component of the γ'' phase the result is that precipitation has been reported to require a high concentration of Nb (Anderson et al., 2017; Niang et al., 2010; Slama

et al., 1997). Consequently, the distribution of the γ'', and therefore the mechanical properties of the material, is dictated by the degree and location of Nb segregation in the material.

The mechanical properties of materials like IN625 and IN718 are correlated directly with the morphology and distribution of the γ'' precipitates within the γ matrix (Devaux et al., 2008; Rao et al., 2003; Y. Zhang et al., 2017). It has been reported that the presence of γ'' precipitates within the material results in improved tensile properties, both yield and ultimate strength, hardness and high temperature properties (Reed, 2006a; Shankar et al., 2001; Slama et al., 1997; K. H. Song & Nakata, 2010) although these properties come at the expense of ductility (D. Zhang et al., 2015).

Both γ' and γ'' are formed during aging heat treatments. The γ'' phase can precipitate between 500 °C and 900 °C however at temperatures below 700 °C the γ' phase will form preferentially. Aging treatments aimed at precipitating the γ'' phase therefore are in the 700 °C to 900 °C range, where the γ'' forms and coarsens most rapidly (Slama et al., 1997). The standard aging treatment in IN718 is a duplex process with two aging temperatures applied, the first at 720 °C with the material held for 8 hours, followed by furnace cooling to 620 °C where the material is help for a further 8 hours before a final air cool to room temperature.

As γ'' is a metastable state for the elements it is susceptible to transformation to its equilibrium state, δ phase at higher temperatures. This transformation is detrimental to the material strength as is conveys no strength to the matrix. The transformation happens more rapidly at higher temperatures, being reported from 800 °C and up (Shankar et al., 2001), this is the reason for the selection of 720 °C as the aging temperature to precipitate γ'' phase.

2.1.3.2.1 Mechanism of strengthening

The process responsible for the increase in strength obtained through γ'' precipitation is coherency strain hardening. The γ'' precipitates coherently with the γ matrix, this introduces a small area or field of strain into the lattice. The effect of these strain fields is that they provide resistance to the movement of dislocations through the lattice and act to increase the hardness of the material.

The amount of hardening which is achieved depends on the size and spacing of the precipitates, something which is determined by the thermal history of the material. This is the purpose of aging heat treatments; hardness is increased by coarsening the γ'' precipitates and increasing the size of strain fields in the matrix. Initially aging will increase the strength and hardness of the material as γ'' precipitates form and coarsen in the material. After a time, a peak hardness will be achieved, aging beyond this leads to further coarsening of the γ'' precipitates resulting in the

strain fields being too widely spaced, allowing dislocations to glide between them relatively unimpeded. This phenomenon is known as overaging and starts to decrease the strength of the material (Chaturvedi & Han, 1983; MATTER & Andrew Green, 2001; Radavich, 2004; Slama et al., 1997). The effects of overaging are presented in Figure 2 where the hardness of the material following aging for 4 hours at various temperatures is plotted. At the highest temperatures, the material shows a dramatic reduction in hardiness due to overaging.

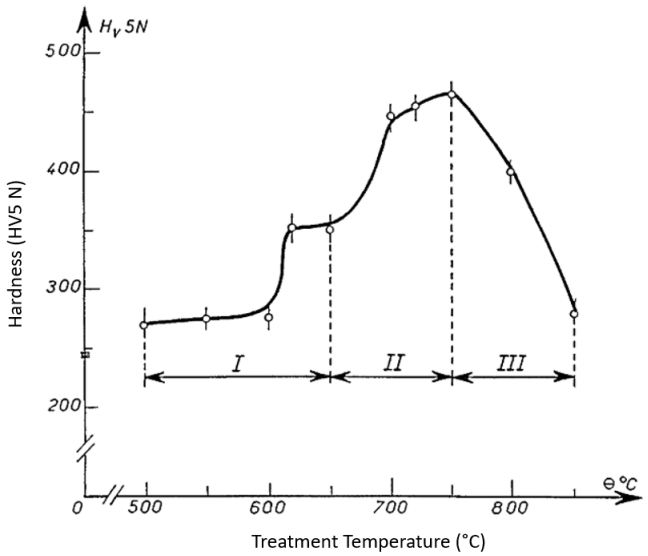

Figure 2 – Graph showing the hardness of IN718 following isochronal aging for 4 hours at various temperatures. The effects of overaging are clear as the temperature exceeds 750 °C. The γ'' phase starts coarsen or transform to δ, reducing the hardness of the material (Slama et al., 1997)

2.1.3.3 δ Phase

The δ phase in nickel-based superalloys like IN625 and IN718 is a stable orthorhombic Ni_3Nb phase which precipitates between ~700 °C and ~1000 °C (Saied Azadian et al., 2004; Brooks & Bridges, 1988; Niang et al., 2010; Reed, 2006a). It is incoherent with the γ matrix and does not provide any strengthening of the material (Saied Azadian et al., 2004; Reed, 2006a). δ phase typically precipitates with a needle shaped morphology (Deng, 2018; Ferrer et al., 1991; Y.-L. Kuo et al., 2017; D. Zhang et al., 2015). Precipitation of δ is slow and requires a high local Nb concentration, 6-8 % meaning that although it is the more thermodynamically stable phase, at lower temperatures, <900 °C, its precipitation is usually preceded by γ'' and long hold times are required for δ to precipitate. For temperatures between 900 °C and solvus, ~1000°C, δ will be the preferred phase (Anderson et al., 2017; Saied Azadian et al., 2004; Radavich, 2004; Reed, 2006a).

Precipitation of δ phase occurs at the grain boundaries with the precipitates coarsening and growing in plates along the {100} plane adjacent to the grains over time (Anderson et al., 2017; Saied Azadian et al., 2004; Brooks & Bridges, 1988). Where temperatures are lower, <900 °C, long hold times make it possible for possible for δ to form at stacking faults or twin boundaries within γ'' precipitates within grains (Saied Azadian et al., 2004; Slama et al., 1997).

The δ phase has a variety of effects on the mechanical properties of the material. The morphology and distribution of the precipitates are as important as the content. The most commonly reported detrimental effect of δ is that it depletes the local area of the Nb required to precipitate γ''. Areas lacking γ'' are often observed around δ precipitates. The lack of strengthening precipitates in these areas means they exhibit micro plasticity where they are much more ductile than the bulk material. Although these Nb depleted areas are still capable of precipitating γ' phase this is not enough to compensate for the lack of γ'' (Radavich, 2004). These areas allow deformation and relaxation of stress, typically at the grain boundaries, until weak precipitates or boundaries nucleate cracks leading to failure (S. Li et al., 1994). This can be detrimental to both room and elevated temperature yield strength although not ultimate tensile strength (Saied Azadian et al., 2004; Brooks & Bridges, 1988; Jinhui et al., 2017a; S. Li et al., 1994).

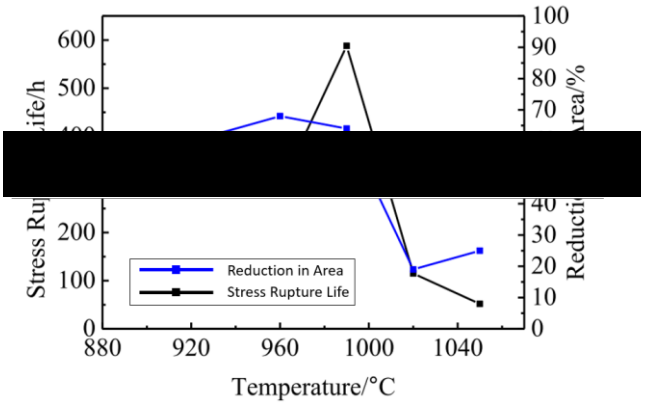

Figure 3 – Graph illustrating the improvement in stress rupture life as correct heat treatments are applied to control the δ content of the material to the correct level (Jinhui et al., 2017b)

Another reported benefit of δ precipitates within the material highlights the importance of the distribution of δ phase. Where δ is present at grain boundaries it provides Zener pinning of the boundaries, this helps to control and restrict grain growth during solution treatment, allowing for fine microstructure to be achieved (Saied Azadian et al., 2004; Geng et al., 1997; Reed, 2006a). Grain boundary δ also controls the grain boundary morphology, causing them to become serrated, which can have a significant effect on mechanical properties such as stress

rupture and creep significantly (Hong et al., 2009; Slama et al., 1997; Yeh et al., 2011). The effect of serrated grain boundaries on the creep life of IN718 is shown in Figure 4 for wrought material. The serrated grain boundary material (SE) demonstrates a significantly longer creep life due to improvements in its tertiary creep behaviour (Yeh et al., 2011). These beneficial effects are however strongly dependent on the content and distribution of δ phase, other literature reports that δ phase can allow micro voids to nucleate and coalesce, reducing fatigue and creep strength.

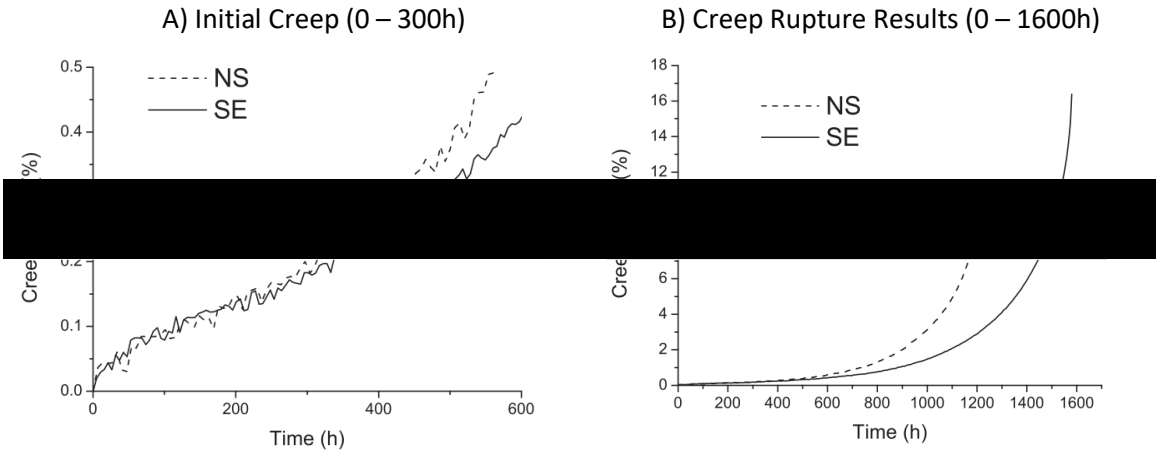

Figure 4 – Improvement of creep life of wrought IN718 material due to serration of grain boundaries. A) shows the primary and secondary creep phase of both materials during the first 300 h of testing, showing little difference in behaviour. B) Shows the entire creep test, showing the longer creep life of serrated grain boundary coupons. Serrated grain boundaries – SE, No Serrated grain boundaries – NS (Yeh et al., 2011).

Considering the δ phase, it is important to find a balance between its positive and negative effects on the material's mechanical properties. A compromise between having enough δ phase to pin grain boundaries and relax crack tip stress without having too much so as to introduce weak interfaces into the material with large Nb deplete zones and a lack of strengthening γ'' precipitating during aging.

2.1.3.4 Laves

Laves are a brittle intermetallic, solidification phase with an HCP structure and a composition of $(Ni, Fe, Cr)_2(Nb, Mo, Ti)$ (Guo et al., 2017; Ma et al., 2015; Ch. Radhakrishna et al., 1995; Schirra et al., 1991). During solidification of the material, Nb, Mo and Ti tend to accumulate at the solidification front (Radavich, 2004; CH Radhakrishna & Prasad Rao, 1997; Sui et al., 2017). This leads to the enrichment of these elements in the interdendritic regions (Dinda et al., 2012; Sohrabi et al., 2018). Precipitation of Laves requires a local concentration of Nb (10 – 12%) (Biswas et al., 2004), thus occurs most often in the interdendritic regions (Antonsson &

Fredriksson, 2005; Biswas et al., 2004; Knorovsky et al., 1989; Manikandan et al., 2014; CH Radhakrishna & Prasad Rao, 1997; Sohrabi et al., 2018; Y. Zhang et al., 2017). Laves are an inevitable part of the solidification (Janaki Ram et al., 2004) although it has been reported that increased cooling rates (Antonsson & Fredriksson, 2005; Manikandan et al., 2014; Shi et al., 2018; Y. C. Zhang et al., 2013) and increased Ni and reduced Fe (Lingenfelter, 1989) can reduce their occurrence and continuity. Homogenisation heat treatments can be implemented to further reduce or eliminate the laves phase.

Laves have a detrimental effect on mechanical properties. Similar to δ phase their formation depleted the material of the elements, specifically Nb, necessary to precipitate the strengthening γ'' phase at lower temperatures, this limits the ability of the material to strengthen through precipitation (Chen, Zhang, et al., 2016; W. C. Liu et al., 1999; Y. Zhang et al., 2020; Y. C. Zhang et al., 2013). The weak interface between laves and the γ matrix introduces a weak point in the material which is a preferential site for crack initiation and propagation (Mills, 1984; CH Radhakrishna & Prasad Rao, 1997; Schirra et al., 1991). Laves have also been reported to deteriorate tensile, high temperature properties, impact toughness and low cycle fatigue (Shi et al., 2018; Sui et al., 2017). Laves can also be detrimental for the weldability of the material, causing initiation and propagation of liquation cracking (Chen, Zhang, et al., 2016), which is detrimental to fabrication or repair of components.

2.1.3.5 Carbides and Nitrides

Both IN625 and IN718 contains relatively large proportions of Nb, an element which tends to react with C, for this reason there is a prominent carbide phase which forms upon solidification, NbC. Different precipitates are seen to form in IN718 and IN625. IN718 is most susceptible to the formation of Nb rich MC carbides whereas IN625 is more commonly seen to precipitate $M_{23}C_6$ and M_6C carbides (Sundararaman & Mukhopadhyay, 1993).

This NbC behaves in a similar manner to the laves phase previously discussed and is equally detrimental to material properties. There are two types of NbC which can form, referred to as primary and secondary. Primary NbC forms on solidification of the material and is unavoidable, these primary carbides are usually distributed uniformly throughout the material as fine precipitates. As with laves it has been reported that increased solidification rates can inhibit its precipitation (Shi et al., 2018).

The presence of NbC carbides is deleterious to the materials properties. In IN718 carbides have been reported to create Nb depleted zones where strengthening phases, γ'', cannot precipitate during aging (Sundararaman & Mukhopadhyay, 1993), reducing the mechanical properties of

the material. There are two causes for this phenomena, firstly, NbC causes solute depletion of Nb, a key component of Ni_3Nb γ'' and secondly the lattice misfit between NbC and the γ matrix leads to a depletion of nucleation sites as vacancies migrate towards the carbides to relieve the internal stress (Sundararaman & Mukhopadhyay, 1993). No such effect is noted around carbides in IN625 (Sundararaman & Mukhopadhyay, 1993). Presence of NbC also makes the material susceptible to liquation cracking as a result of insipient melting (Thompson et al., 1989), making the material more difficult to weld.

NbC carbides have also been reported to alter the failure mechanics of the material. When present in a continuous or near continuous path along a grain boundary the failure of the material becomes predominantly intergranular, rather than the transgranular nature of carbide free material (Sundararaman & Mukhopadhyay, 1993)

There is also a nitride phase, TiN, which can form in where nitrogen is present in high enough quantities. The limit for N solubility in liquid IN718 has been reported to be 44 ppm, if the levels of N in exceed this there will always be some level of nitrides present, even in the liquid state, these nitrides have been reported to act as stable nucleation sites for NbC, with TiN regularly being found in the centre of NbC precipitates.

2.1.4 Heat Treatment of IN625 and IN718

2.1.4.1 Homogenisation or Solution Heat Treatment

A homogenisation heat treatment can be used for a number of reasons, usually to eliminate elemental segregation, dissolve phases which have precipitated, relieve stress resulting from manufacturing and modify the grain size or structure of the material (D. Zhang et al., 2015; Y. Zhang et al., 2017). In materials like IN625 and IN718 the main segregated element of interest is Nb. As previously discussed, the excessive segregation of Nb during solidification leads to the formation of the detrimental laves phase (Antonsson & Fredriksson, 2005; Biswas et al., 2004; Knorovsky et al., 1989; Manikandan et al., 2014; CH Radhakrishna & Prasad Rao, 1997; Sohrabi et al., 2018; Y. Zhang et al., 2017, 2020).

Homogenisation heat treatments involve holding the material at a high temperature, around the dissolution temperature of the phases of interest. This temperature is maintained for long enough that back diffusion can take place, which allows the precipitated phases to dissolve and the segregated elements to redistribute back into the γ matrix. This redistribution of segregated elements improves the ability of the material to precipitate desirable phases, such as the strengthening γ'' phase, during subsequent aging treatments (Sohrabi et al., 2018). A perfect homogenisation treatment results in a material with uniform distribution of all elements and no

precipitate phases (CH Radhakrishna & Prasad Rao, 1997). This is unlikely to be practically possible however it is possible to get close to this situation and restore much of the materials ability to age harden.

The dissolution temperature of the laves phase present in the material has been reported to change depending on the thermal history of the material and the morphology of the laves present. Generally it is 1170 °C +, with the temperature increasing as the laves become larger and form a continuous network in the material (CH Radhakrishna & Prasad Rao, 1997). The dissolution temperature of the δ phase is around 1000 °C. Homogenisation temperature required depends on the specific phases being targeted and the initial condition of the material. In some cases higher temperatures will be implemented to remove the laves phases however in some cases this may lead to a coarsening of the grain structure and a loss of other material characteristics which might be desired. (Miao et al., 2010; Sohrabi et al., 2018; Y. Yang et al., 1994; Y. Zhang et al., 2017).

When heating a material with a significant presence of laves to the dissolution temperature or above there is a danger of insipient melting taking place. Laves have a lower melting point than they bulk γ matrix. When the Laves are heated too quickly they can melt rather than back diffuse their atoms into the γ matrix, this can lead to cracking of the material as the liquid expands, the is the same problem as can occur during welding (CH Radhakrishna & Prasad Rao, 1997). It is important to note that these temperatures are below the solvus temperature of common carbide precipitates and so homogenisation has little to no effect on their distribution.

Regarding homogenisation time, it has been reported that the amount of laves remaining in the material decreases with an exponential relationship as the hold time increases. As the temperature approaches the dissolution temperature the rate at which laves dissolve and the time required to eliminate all laves decreases. Previous studies into IN718 have found the time to total laves dissolution for 1140 °C (Y. Yang et al., 1994), 1150 °C (Sohrabi et al., 2018), and 1160 °C (Miao et al., 2010) to be 35 h, 28 h and 13h respectively.

Equations have been presented to model this relationship:

Equation 1 allows B, the segregation degree of the material to be calculated from the time to total laves dissolution τ (hours), and the homogenisation temperature (°C).

$$B = \frac{\tau}{e^{-0.036T}}$$

Equation 1 – Equation used to estimate the segregation degree of material based on the time to total Laves dissolution. B – Segregation degree of material, τ – *time to total laves dissolution, T – time of treatment.*

Equation 2 allows the volume fraction of laves, C_{laves} after homogenisation at a certain temperature for time t (hours) to be calculated. Coefficient K_T is determined by the homogenisation temperature and by rearranging and combining Equation 1 and Equation 2 it is possible, with some experimental data, to determine the value of the coefficients and C for different times and temperatures (Miao et al., 2010).

$$C_{laves} = Ae^{-K_T t}$$

Equation 2 – Equation for the calculation of the volume fraction of Laves phase remaining in the material after homogenisation. C_{laves} – Volume fraction of Laves phase in material, K_T coefficient determined from homogenisation temperature and Equation 1*, t – time of heat treatment.*

The optimal time and temperature for homogenisation treatment will vary depending on the material's thermal history and the desired properties of the material. Other factors such as the refinement of the grain morphology also need to be considered, treatment at excessively high temperatures can lead to coarsening of the grains which can be detrimental to material properties such as tensile properties through Hall-Petch softening. Correctly selected homogenisation treatments are required to strike a balance between dissolving unwanted phases and maintaining the grain structure.

Homogenisation is not suitable, and is never applied, as a standalone heat treatment. The dissolution of strengthening phases and the increase in grain size generally will result, in many cases, in worse mechanical properties compared to the as fabricated material. The homogenisation treatment is applied to bring the material to a condition in which it will respond best to subsequent heat treatments, aging. Homogenised and aged material will yield improved mechanical properties compared to directly aged, no homogenisation applied, material.

2.1.4.1.1 Stress Relief and Recovery

One of the aims of a solution or homogenisation heat treatment is the relief of residual stresses within the material. This is achieved through a process referred to as recovery.

The residual stresses are found within the material matrix as a distribution of low angle misorientations where small amounts of deformation and dislocations are stored within the material. The dislocations form sub grain structures where the crystal lattice of the material has slight misalignment. These areas of misalignment store energy within the material.

The process of recovery involves the movement of these sub grain structures of misalignment. The misalignments, driven by their stored energy, can rearrange themselves by short range dislocation interactions. This rearrangement occurs via a process of short-range dislocation interactions and allows the dislocations to be reconfigured to minimise the stored energy. This

reduction in stored energy occurs through annihilation of dislocation di-poles or more efficient arrangement into lower energy configurations (Guy, 1976; Kestens & Pirgazi, 2016).

The recovery process is thermally activated, occurring more quickly as temperature is increased and greater thermal energy is available to drive diffusion and dislocation movement (Callister & Rethwisch, 2014; Guy, 1976; Mercier et al., 2002; D. Zhang et al., 2015). In wrought IN718 the recovery process has been observed to occur from temperatures of 950 °C and up for times of 10 minutes (H. Y. Zhang et al., 2017).

2.1.4.2 Aging

Aging heat treatments are the primary mechanism to increase the strength of the material. Aging is responsible for precipitating the strengthening phases γ' and γ'' in the γ matrix, causing precipitation strengthening of the material. Aging is most commonly achieved via a duplex process, or two stage, with two different treatment temperatures and times, each of which targets γ'' and γ' precipitation separately.

As previously discussed, the primary strengthening phase in IN718 is γ'', Ni_3Nb, so for the aging treatments to be effective and for the material to achieve optimal hardening, there needs to be a homogenous distribution of Nb available throughout the γ matrix which is not already consumed in laves phase or the more stable Ni_3Nb δ phase.

It is also possible to overage the material. Overaging occurs when the material is held within aging temperature for too long, this allows two processes to occur, both reducing the hardness and strength of the material. The first process is a further coarsening of the γ'' precipitates, growing to sizes larger than optimal. When this occurs the coherency strain fields surrounding the precipitates become too widely spaced, allowing dislocations to glide between them unimpeded (MATTER & Andrew Green, 2001). The second process which can take place is the transformation of the metastable γ'' precipitates to their stable arrangement, δ phase. As discussed in 2.1.3.3 the δ phase conveys no strength to the γ matrix, so the hardness of the material will decrease as beneficial γ'' precipitates undergo this transformation. This process of transformation occurs more quickly as temperatures are increased.

Figure 5 shows in illustration of the aging and overaging process. The initial material in Figure 5 A) is free from precipitates. Aging leads to the precipitation of γ'' phase in Figure 5 B) as well as a small amount of δ along the grain boundaries. As the aging process continues the γ'' precipitates coarsen and the δ along the grain boundaries begin to form needle shaped precipitates Figure 5 C). The δ along the grain boundary can begin to create serration of the grain boundary as shown in Figure 5 D) and reported by Yeh et al (Yeh et al., 2011). The final frame in

Figure 5 E) shows the overaging process where γ'' become too large to provide coherency strain hardening and some begin to transform to the stable δ phase.

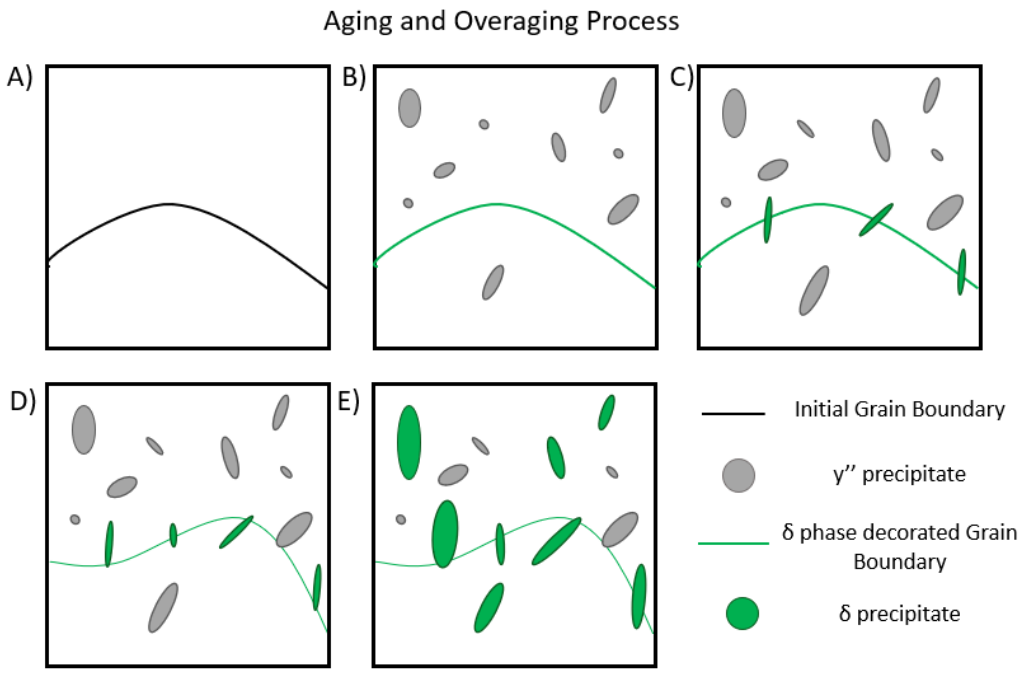

Figure 5 – Illustration of phase precipitation and transformation during the aging process. This shows how the material ages and can become overaged as γ'' precipitates become too large or transform to δ phase.

2.1.4.2.1 Aging Procedure for IN718

A standard aging treatment for IN718 would be a first heating to 720 °C for 8 hours followed by a furnace cool to 620 °C until the total aging time reaches 18 hours before air cooling to room temperature (ASM International, 1996), times are typically 720 °C 8h, FC 620 ° 8h, AC (Deng et al., 2017). The first temperature, 720 °C is in the lower region of the more rapid γ'' precipitation temperature range, this this temperature allows γ'' to precipitate while minimising the changes of the precipitates transforming to the more stable δ, a process which happens more commonly and rapidly as temperature increases (Slama et al., 1997), reducing hardness (Dinda et al., 2012). The second temperature, 620 °C, is used to both coarsen the γ'' precipitates present as well as precipitate the γ' phase with any Ti or Al available in the γ matrix. Other standard aging treatments are listed in Table 5 however the temperatures involved are typically in the same region. Many studies have implemented and investigated similar aging treatments, with the duplex process being the most widely used (Deng et al., 2017; Du et al., 2007; Jinhui et al., 2017b; C.-M. Kuo et al., 2009; Miller et al., 1999; Ch. Radhakrishna & Rao, 1994; Ram et al., 2005; Slama et al., 1997; Tanner, 2009; Yeh et al., 2011).

Table 5 - Alternative AMS standard aging treatments for IN718 material (ASM International, 1996)

Temperature 1 (°C)	Time 1 (hours)	Cooling 1	Temperature 2 (°C)	Time 2 (hours)	Cooling 2
720	8	FC	-	-	-
620	8	AC	-	-	-
760	10	FC	620	20	AC

2.2 Introduction to Additive Layer Manufacturing

Additive layer manufacturing (ALM) is a blanket term for a wide range of processes. All these processes operate on the same underlying principles. A 3D geometry is formed by depositing or fusing material as opposed to removing it, which is usually the case in conventional, subtractive manufacturing (milling, drilling, turning etc).

2.2.1 History

The first commercial ALM process was patented in 1984 by Charles W. Hull (Hull, 1984) and was able to create 3D plastic parts. The process was stereolithography and used a moving UV beam to cure the surface of a resin in the desired cross section. This process was repeated layer by layer to build up a three-dimensional plastic part directly from a computer-generated design. This was an improvement on previous techniques which used multiple, intersecting beams to selectively cure specific locations within a large volume of UV curable resin, Hull's 1984 patent was the first to approach the problem in a true layer-wise fashion, the approach still in use in nearly every ALM process today. The stereolithography process described in the patent is still widely available in one form or another in many different modern commercially available machines today.

2.2.2 Additive Manufacturing of Metallic Materials

Since its invention, ALM has been developed with new methods and materials becoming possible. One big step for the process was the ability to additively manufacture metallic materials. Many methods exist for this purpose, however the process of interest for this work is selective laser melting (SLM), first patented in 1986 (Deckard, 1987) and 1993 (Larson, 1994), respectively. Examples of other methods for ALM of metallic materials are:

- Binder Jetting: A binding agent is printed, much like an inkjet printer, layer by layer onto a bed of powdered metal. The finished bed is then cured at high temperature to achieve the finished object. This technique gave rise to the popular name 3D printing, used to describe many ALM processes.

- Directed Energy Deposition: Operating much like a traditional welding process, raw material in the form of either wire or powder is fed into a heat source, usually a focused laser beam, where it melts and deposits onto a substrate material. Usually implemented on a robotic arm material is deposited in the desired shape and machined back to final dimensions.
- Electron Beam Melting: First patented in 1993 (Larson, 1994) electron beam melting is a similar process to selective laser melting. The laser beam energy source is replaced with a directable electron beam which is used to fuse a bed of metallic powder into the desired cross section.

2.2.3 Selective Laser Melting Process

A typical SLM machine contains 3 chambers. The first, labelled (1) in Figure 6, contains the powder feedstock which will be used to build the component, this chamber is often referred to as the powder hopper. The second chamber, labelled (2), is the build chamber, this contains the build plate onto which the component will be built. The volume of this chamber determines the build volume of the machine and the maximum size of components that can be manufactured. The final chamber, (3) is the overflow, where any excess powder will be collected after each layer is deposited.

Compared to other ALM processes, such as directed energy deposition, SLM is capable of good surface finish and relatively tight dimensional accuracy. This allows manufactured parts to be very close to net shape, sometimes requiring no post build machining on non-critical surfaces. It also enables more detailed internal structures to be produced which are serviceable in their as fabricated condition.

The SLM process can be divided into two stages, layer deposition and layer fusion, each of which is explained below:

2.2.3.1 Layer Deposition Process

Layer deposition is the process of creating a layer of powder on the build plate. For an SLM build to be successful and produce fully dense material it is essential that the layer deposition is properly configured and controlled and produces layers with uniform thickness and distribution of powder particles.

Layer deposition is achieved by lowering the build plate (2) by the height of one layer, typically 20 – 50 µm, and raising the powder hopper (1). The recoating arm or blade (4) is then used to push powder across from the hopper over the build plate. The powder accumulates in front of the blade and is deposited by flowing into the gap between the blade and the lowered build

plate. Any excess powder not required to cover the build plate will be pushed into the overflow (3), the blade then returns to its home position behind the powder hopper.

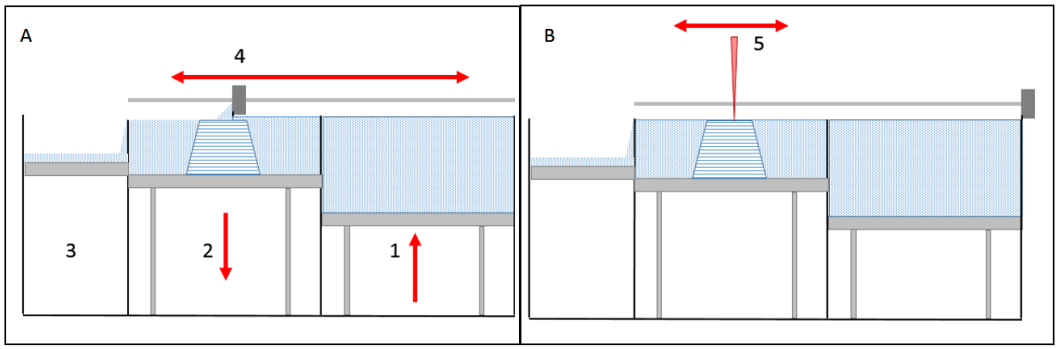

Figure 6 - Basic schematic illustration of the SLM process showing both the layer deposition and layer fusion process.

2.2.3.2 Layer Fusion Process

The fusion process is responsible for consolidating the powder into the shape which is being manufactured. The powder is melted and therefore fused by the laser beam which is focussed onto the layer surface and moved to fill the cross section for that layer. The focus diameter or spot size of the laser ranges between ~30 – 100 µm (EOS, n.d.; Trumpf, n.d.), depending on the machine, however there is an additional heat affected zone (HAZ) around the spot where powder reaches a high enough temperature to melt.

Since the build material is heated to high temperatures and melted during fusion it is susceptible to reactions with the atmosphere, for this reason the entire process is performed inside a controlled atmosphere usually argon or nitrogen. In the case of the nickel-based superalloys, which are the subject of this study, an argon atmosphere is preferred.

2.2.3.3 Powder Bed Fusion Process Parameters

In SLM there are many different processing parameters which can be manipulated to alter the process. These parameters can be used to tailor the process to different materials with different melting points as well as tune the process to remove porosity or reduce build times. A selection of the most important parameters are discussed below.

2.2.3.3.1 Rastering

Rastering describes the pattern of parallel lines which are traced out by the laser beam spot on the powder bed surface which act to fill the desired area and consolidate the loose powder material. There are several variables which can be selected for rastering patterns, each of which has a significant effect on the quality of the final material produced.

2.2.3.3.1.1 Rastering Hatching Distance

Hatching distance is the distance, centre to centre, between two consecutive rastering lines. Some amount of overlap between lines is desirable, as this ensures full fusion of the material, however too much overlap reduced productivity. A properly selected hatching distance is a balance between these two factors. The correct hatching distance will vary depending on the melt pool geometry created by the beam focus diameter other process parameters, such as beam power and speed as well as the thermal conductivity of the powder bed.

2.2.3.3.1.2 Rastering Patterns/ Strategy

There are several common patterns which the laser spot can trace out to fill the desired shape. The shape of the rastering has a big impact on the distribution of heat and the thermal gradients and cooling rates in the material. The thermal history of different parts of the material can alter the microstructure, residual stresses and the formation of defects that form.

A few common approaches are illustrated in Figure 7. The most basic approach is shown in Figure 7 A), the entire surface filled with parallel lines running the full width of the shape. Figure 7 B) is referred to as a chess board strategy, the surface is divided into a grid of uniformly sized squares which, as with the stripes, are individually filled with parallel scans and completed one by one. Figure 7 C) shows a striped strategy. The surface is divided into several fixed width stripes which are then individually filled with parallel laser scans, one stipe being filled entirely before the next is started. Generally, patterns such as A) are not preferred because they lead to uneven heating of the powder bed and rapid cooling. Chess board B) or Striped C) strategies aim to avoid this uneven cooling by making the lasers scan width, or scan vector length, much shorter. This means that the beam returns to scan adjacent tracks much faster, giving a more gradual and even cooling of all the material within the stripe or square.

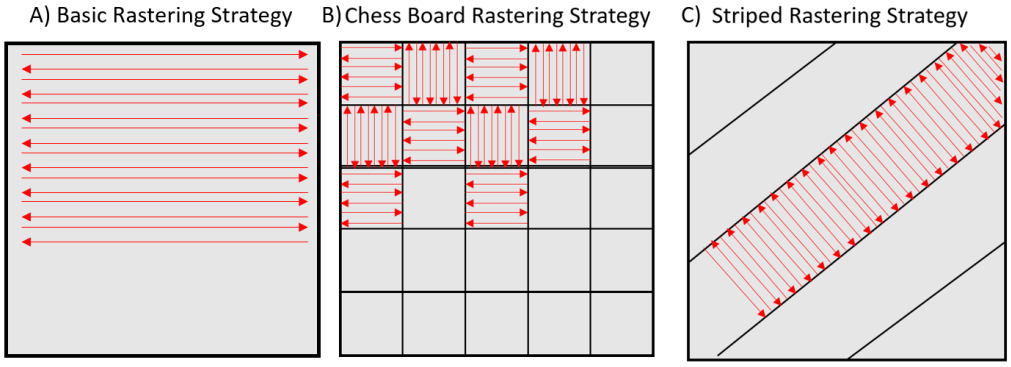

Figure 7 – Schematic illustrations showing three possible rastering strategies used during SLM manufacturing

There are a few additional techniques which can be applied to rastering pattern to further improve the distribution of heat over the layer. For the chess board strategy, the direction of

scanning for adjacent squares can be changed, avoiding areas which might have more or less beam spot dwell time as a result of the beam changing directions at the end of a scan vector, in Figure 7 B) a difference in angle of 90 ° between squares is illustrated. Another technique is to scan the squares in a random or non-consecutive order. This is known as random island scanning and avoids any overall thermal gradient from once side of the shape to the other.

2.2.3.3.1.3 Rastering Pattern Rotation

If the rastering pattern is unchanged throughout the build, then the slight differences in thermal experience across the part will occur on top of each other over the height of the build. This can lead to material more susceptible to defects or unfavourable microstructure. To avoid this happening, the rastering pattern will often be rotated or translated between layers (Carter et al., 2014; Y. Lu et al., 2015). An example how repeating rastering patters can be visible in the microstructure of the manufactured material is shown by Carter et al, who report that, when using a 5 mm chess board strategy with translation between layers, found a repeating structure of 1mm squares defined by fine grans around their perimeter (Carter et al., 2014). This bimodal structure demonstrates how the scan strategy can influence the grain structure formed. Rotating the rastering pattern can distribute that structure more evenly throughout the material.

2.2.3.3.2 Laser Power

The power of the laser beam, measured in watts, is an essential processing parameter. This determines the amount of energy being imparted by the laser into the powder bed.

With a Yt-Fibre laser, commonly found in SLM machines, laser power is typically between 100W and 200W although slightly higher powers can be used (Sadowski et al., 2016). The work of Sadowski reports that when producing IN718 by SLM, powers between 100 W and 150 W produce the best melt tracks, with higher powers such as 200 W – 300 W producing greater levels of porosity.

Controlling the temperature of the melt pool via laser power is essential to create suitably dense material. Incorrect temperatures in the melt pool can lead to unwanted effects such as keyhole ejection, balling and vaporisation which will greatly reduce the quality of the manufactured material and lead to complete build failures (Choi et al., 2017; Gu & Shen, 2009; J. P. Kruth et al., 2004a; Kusuma, 2016; R. Li et al., 2012)

2.2.3.3.3 Scanning Speed

Scanning speed is the linear speed at which the laser spot traverses the rastering pattern. This is an essential process parameter as it dictates how long the laser spot dwells on each point of the material and therefore the amount of energy received at each point.

Scan speed influences both melt pool temperature and geometry (Kusuma, 2016) with melt pools becoming narrower and longer in the scanning direction as speed is increased (Lynch, 2013). The melt pool geometry is an essential factor in the SLM process. It determines the remelting of previous layers as well as the overlap of adjacent laser scan tracks, both essential in producing fully dense material. The melt pool geometry also contributes to residual stress creation, with larger melt pools resulting in faster cooling and subsequently greater thermal stresses (Y. Lu et al., 2015). The volume of molten material available during solidification will also affect the solidification dynamics of the material and the size of grains which can form, larger melt pools resulting in coarser grain structures.

2.2.3.3.4 Layer Thickness

The powder layer thickness used during the SLM process has several effects on the process. At a basic level it determines productivity and resolution of the process. Thicker layers will reduce how many layers are required to produce a part, increasing productivity. This comes at the expense of resolution and ability to produce curved geometry (in the build direction). As the part is comprised of several layers stacked on top of each other, any curves in the build direction will, on a micro scale, be stepped. This Is referred to as the stair case or discretisation effect (Vrancken, 2016). This is illustrated in Figure 8 where the trade-off between geometric resolution and number of layers required is shown for a doubling of the layer thickness.

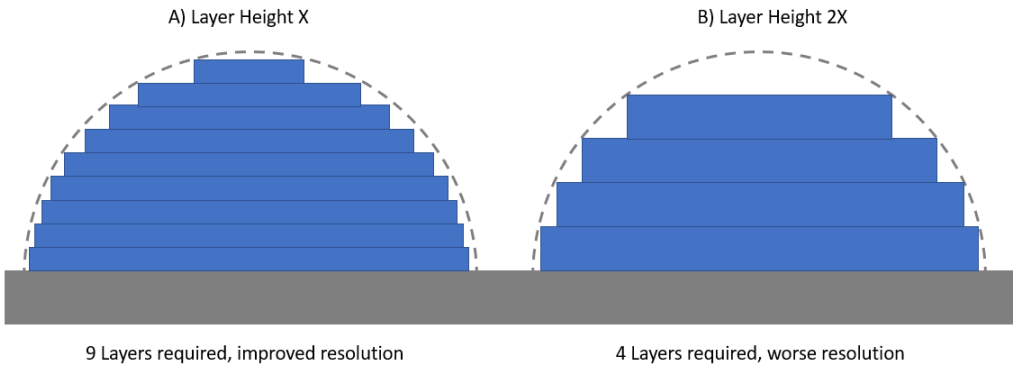

Figure 8 – Illustration showing the practical trade-off between geometric resolution and the number of layers required when doubling the layer thickness during SLM.

The layer thickness also has implications on the properties of the melt pool and the process parameters required. Thicker layers require a greater volume and depth of powder to be melted at one time, this leads to larger melt pools and higher temperatures. The potential issues with this are instability of the melt pool, leading to balling (Choi et al., 2017; Gu & Shen, 2009; J. P. Kruth et al., 2004a; Kusuma, 2016; R. Li et al., 2012), and the increased cooling rate of a larger melt pool (Y. Lu et al., 2015).

2.2.3.3.5 Energy Density

While all the process parameters of the SLM process are described and altered individually, their effect on the build process is inseparable. For this reason the parameters are often combined to calculate their energy density, first proposed by Nelson et al, (Nelson et al., 1993). Energy density is a measure of the amount of energy input into each unit length or unit volume of the powder bed. Calculation of linear, area and volumetric specific energy density are given in Equation 3, Equation 4 and Equation 5with the units Jmm^{-1}, Jmm^{-2}, Jmm^{-3} respectively.

Equation 3 – Calculation of linear specific energy density. E_{dl} – Linear Specific energy density, P – Beam power (W), t – Layer thickness (mm), V_s – Scan speed (mms^{-1}), H_d – Rastering hatching distance (mm)

$$E_{dl} = \frac{P}{V_s}$$

Equation 4 - Calculation of area specific energy density. E_{da} – area Specific energy density, P – Beam power (W), t – Layer thickness (mm), V_s – Scan speed (mms^{-1}), H_d – Rastering hatching distance (mm)

$$E_{da} = \frac{P}{V_s \times H_d}$$

Equation 5 - Calculation of volumetric specific energy density. E_{dv} – Volumetric Specific energy density, P – Beam power (W), t – Layer thickness (mm), V_s – Scan speed (mms^{-1}), H_d – Rastering hatching distance (mm)

$$E_{dv} = \frac{P \times t}{V_s \times H_d}$$

Assuming that the selected parameters are reasonable (certain laser powers for example will never yield powder bed fusion regardless of how slow the scanning speed is), energy density calculation offers a quick way to determine the suitability of a set of processing parameters.

2.2.3.3.5.1 The Effect of Energy Density on Melt Pool Geometry and Thermals

The energy density has a major influence on the geometry and behavior of the molten pool during sintering. The general relationship is that the pool gets wider with higher powers and longer with higher speeds. The depth of the pool, an important factor in remelting previous layers and properly fusing layers together, increases with energy density. Proper fusion between layers is important and contributes heavily to the mechanical properties of the material

produced, the likelihood of build failures (delamination) and the anisotropy of the components produced. Lack of fusion defects in the material will always lie in the XY plane (parallel to the build plate), this directionality of the defects means that the material is disproportionately weakened in different directions. This is visible in Figure 9 where two similar lack of fusion defects are present. Where the defect is perpendicular to the loading axis it reduces the effective area of the sample as well as introducing sharp corners and stress raisers and concentrations. This results in premature failure (Vilaro et al., 2011). Proper laser power and scan speed combinations can significantly reduce these defects and therefore the degree of anisotropy. There are many papers which look more in depth at the relationship between scan speed and laser power and try to accurately model the thermal behavior and geometry of the pool using finite element analysis (Hussein, Hao, Yan, & Everson, 2013; R. Li et al., 2009; Lynch, 2013).

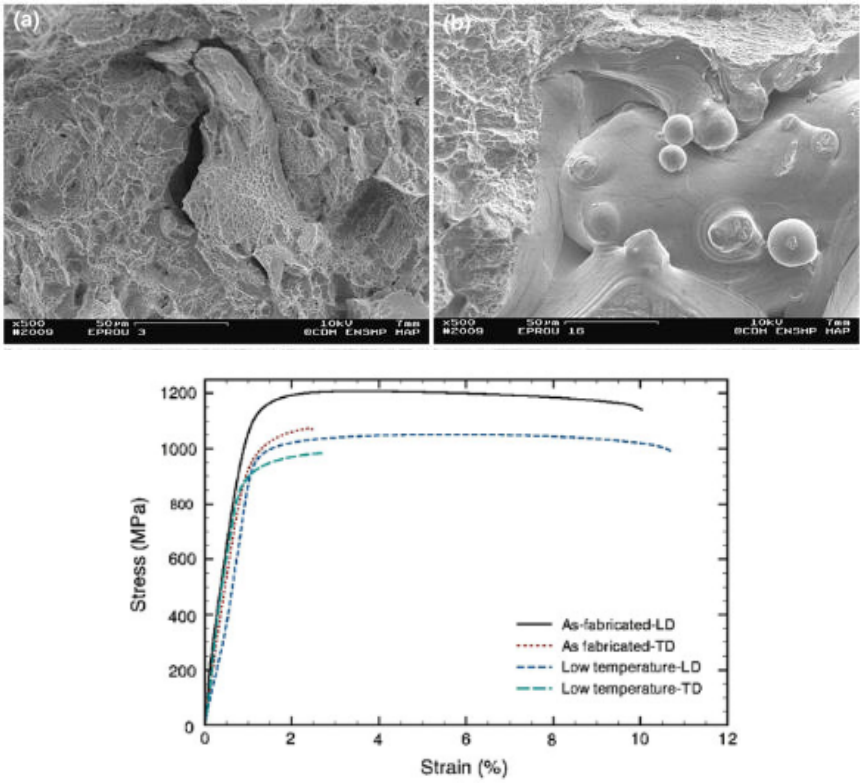

Figure 9 - SEM images of fracture surfaces showing the anisotropy created by lack of fusion defects due to incorrect process parameters (Vilaro et al., 2011)*. The illustrate the difference in cross sectional area of the defect when the stress axis is changed. Stress and strain curve for these samples showing the premature failure of transverse direction (TD) samples compared to the longitudinal direction (LD), due to this alignment of the defects.*

2.2.3.4 The Use of Process Parameters to Control As Fabricated Microstructure

The influence of individual or combined process parameters on the process thermals and material quality is well established and researched however this opens the possibility for additional investigations.

The process parameters directly control the thermals experienced by the material, which in turn dictates the microstructure of the material produced through cooling rates, melt pool size and thermal gradient direction. While the general microstructure produced is well established and reported, elongated columnar grains in the build direction, there is a lack of investigation of smaller changes which can be made to this.

It is possible that, once the process parameters are in a suitable window to produce fully dense material, there is further scope for material modification. Slight changes to the process thermals might facilitate the microstructure of the material to be changed, even if only slightly. Such a change might be able to tailor a material slightly better towards an application or subsequent heat treatment. It might also be possible to improve the productivity of the SLM process by selecting process parameters which complete layers faster, while still being able to produce material with the desired microstructure. Analysis of the microstructure could facilitate an improved process of parameters selection based on more advanced principles.

This is a subject in which currently published literature is lacking and will be the focus of investigation in this work.

2.3 Manufacturing Nickel-Based Superalloys with SLM

2.3.1 Applications

ALM is still an invaluable tool for prototyping with many modern industries implementing it in the design process, however some industries, mainly in high value or demanding applications, can take advantage of more than just the quick design to manufacture route of ALM.

Forming a three-dimensional object one layer at a time gives ALM the unique ability to create complex internal geometries within solid parts which would be difficult or impossible to manufacture with conventional processes. Applications of this ability include creating optimal cooling channels within injection moulding dies, oil/fuel galleries or honeycomb structure within components or simply reducing the number of separate parts, joins and hardware required for a component. The addition of complexity to parts produced by ALM is unique from conventional manufacturing processes because it comes with little to no additional cost (Hague, 2006).

The significant benefits of ALM are not without limitation or drawbacks. Firstly, ALM is a slow process, depending on the volume of a component builds can take from hours to days to complete, so while it is quicker to produce small production runs of components via ALM, once the tooling is in place a conventional manufacturing process, assuming it is capable of creating the same geometry, will likely be faster. Secondly the material needs of ALM generally lead to

higher costs, the supply chain for the atomised metal powders necessary for SLM or EBM is not as well established as that of bars or billets. Although this will improve as the demand for metal powder increases into the future, creation of powder is always likely to involve additional steps when compared to using billet material (Dawes & Bowerman, 2015; Wohlers Associates, 13 C.E.). Finally there are some geometric constraints to the capabilities of ALM, overhanging structures, where there is a downward facing plane of material, require a support structure to be build under them, requiring removal post manufacturing (Hussein, Hao, Yan, Everson, et al., 2013; J.-P. Kruth et al., n.d.; Ö. Poyraz, E. Yasa, G. Akbulut, A.Orhangül, n.d.), the surface finish of as manufactured ALM material might not be sufficient for certain applications and may require post processing (Chan et al., n.d.; J. L. Song et al., 2007) and, as methods such as SLM or EBM require an inert or vacuum environment, they are restricted in their build volumes by the size of machines commercially available.

The drawbacks of ALM, specifically the time and cost, currently restrict its use in production predominantly to demanding applications where even small improvements in designs or efficiency have a high value such as aerospace (Bandyopadhyay & Bose, 2015; Boen, 2015; CFM, n.d.; General Electric, n.d.; SpaceX, n.d.), nuclear energy (Office of Nuclear Energy, 2016; Physical Sciences Inc., 2009) and automotive industries (Alfa Romeo Sauber, n.d.; McLaren, 2015; Newman John, 2011; Taylor Edward, 2016).

Primary applications for SLM nickel-based superalloys will be in the replacement of existing uses, as discussed in 2.1, such as aerospace gas turbine engine components, specifically in the hot section such as turbine blades, discs or thrust reversers.

2.3.2 Mechanical Properties of Nickel-Based Superalloys Produced by SLM

2.3.2.1 Low Temperature

2.3.2.1.1 Tensile Strength

Tensile properties of SLM nickel-based superalloys are reported to be highly anisotropic with yield stress, ultimate tensile stress and elongation all varying depending on the build direction/stress axis. Ni et al present the graph given in Figure 10 B) (Ni et al., 2017). The transverse coupons, build direction parallel with stress axis Figure 10 A), achieve an improved yield and ultimate tensile strength. This is attributed to the strong {100} fibre texture observed in the build direction aligning the {111}<110> slip systems favourably, roughly 55 °, to the stress axis (Ni et al., 2017). The anisotropy of elongation is attributed to the defects within the material providing, generally aligned along build layers and therefor parallel with the stress axis in transverse coupons (Trosch et al., 2016).

A) Coupon build directions

B) Tensile results

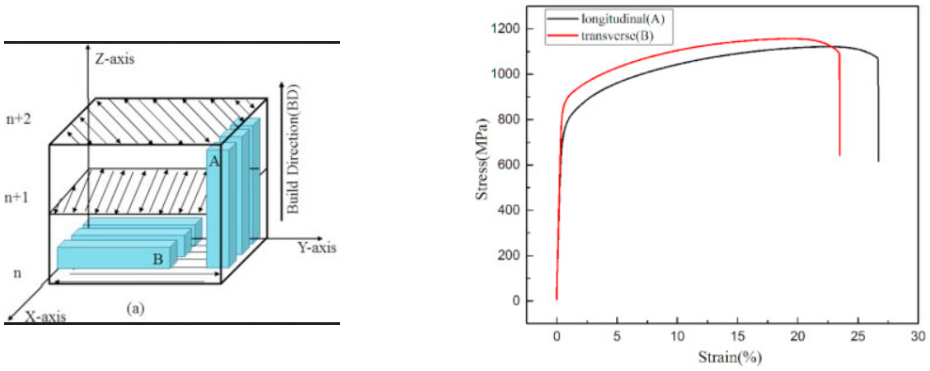

Figure 10 – The reported difference in tensile properties between coupons manufactured with different build orientations. IN718 coupons fabricated by SLM (Ni et al., 2017)*. Build orientation of the coupons are illustrated in A) and tensile stress strain curves are plotted in B)*

Comparisons of SLM material to conventionally manufactured material, such as forged or cast, are difficult. Due to the anisotropy previously discussed as well as the strong influence of defects the properties of SLM coupons manufactured from the same material can vary (Marchese et al., 2018). The generally reported properties of both IN625 and IN718 material produced by SLM are superior to cast material and comparable to wrought or forged material, (Marchese et al., 2018; Nguejio et al., 2019; Ni et al., 2017; Z. Wang et al., 2012) however this can vary depending on the coupon.

For the discussion of the tensile properties of IN625 or IN718 produced by SLM it may be more suitable to address the potential sources of superior or inferior mechanical properties:

- Grain structure – SLM is reported to produce material with a very fine grain structure. The grains have been reported to be smaller than forging and casting by a factor of 10 and 100 respectively (Trosch et al., 2016). This leads to a process of Hall-Petch hardening where increased grain boundary length provides greater barrier to dislocation movement through the material. This increases the room temperature strength of the material (Marchese et al., 2018).
- Dislocation density – Due to the rapid solidification and cooling undergone by the material during SLM there is a tendency for a greater density of dislocations to be found within the material. These dislocations slow the movement of further dislocations through the material and improve the room temperature mechanical properties of the material (Marchese et al., 2018).
- Micro-Segregation – A secondary effect of the rapid solidification on the manufactured material is the formation of micro-segregation of the Nb (Cieslak et al., 1989; Deng,

2018; Dinda et al., 2012; Gao et al., 2019; Marchese et al., 2018; Popovich et al., 2017b). This segregation leads to the inability of the SLM material to age and precipitate γ'' strengthening phases. This reduced the potential mechanical properties of the as fabricated material, requiring homogenisation heat treatments to rectify (Gao et al., 2019).

2.3.2.1.2 Fatigue

Fatigue is a critical property of nickel-based superalloys such as IN625 and IN718. The service life of components is typically dictates by their low cycle fatigue (LCF) life (J. Xu et al., 2017). With IN625 and IN718 being commonly used to produce components for the hot section of gas turbine engines, such as discs and blades, they are subjected to constant cyclical loading.

In IN718 material the fatigue performance of forged material has been reported to vary depending on the microstructure, specifically the precipitates present following heat treatment. Xu et al report a difference in fatigue performance between material with δ precipitation or only γ'' precipitation. They find that δ precipitates prevent dislocation slip which can relax the stress built up in the material. Whereas γ' and γ'' precipitates were observed to facilitate dislocation glide by shearing, providing a softening effect in the material (Mahobia et al., 2014; Xiao et al., 2005; J. Xu et al., 2017).

The fatigue life of material produced by SLM is found to be roughly comparable with cast material (Chastand et al., 2018), shorter than that of wrought. This is due to several common issues found with SLM material. The first issue is the presence of defects within the material such as pores, cracks or rough a surface finish (Choi et al., 2017; Gong et al., 2014; Strano et al., 2013; Sui et al., 2019). The defects of a rough surface have been observed to provide sites for crack initiation, shortening fatigue life (Ellyson et al., 2017; Koutiri et al., 2018; Periane et al., 2019). Even when post fabrication surface machining is applied to improve surface finish this has been reported to reveal new sub surface pores or defects which present the same problem (Brandl et al., 2012; Edwards & Ramulu, 2014). Post processing such as hot isostatic pressing (HIP) have been successfully applied to SLM material to close porosity and reduce the size of defects within the material (Chang et al., 2014; Chastand et al., 2018). This has been reported to successfully recover some, but not all, of the lost fatigue life of the SLM material (Chastand et al., 2018; Hirata et al., 2020; Tillmann et al., 2017; Wu et al., 2017). It is the nature of additively manufactured material however, to have some level of defects present which will but it at a disadvantage relative to conventionally manufactured material.

Another issue unique to SLM manufactured material is that the properties of the material are anisotropic. The influence of build orientation on the fatigue life of coupons has been investigated and it is reported that fatigue life is shorter in coupons manufactured horizontally (stress axis perpendicular to build direction) (Damon et al., 2019; Sarkar et al., 2019). This happens as a result of the alignment of build defects and grain/layer boundaries and the loading axis and due to the anisotropic columnar grain structure characteristic of SLM material (Sabelkin et al., 2019). The greater number of grain and layer boundaries present when loaded in this direction facilitate diffusion creep and provide an easier path for dislocation movement with fewer boundaries.

2.3.2.2 High Temperature Properties

A materials strength is simply a measure of the ease with which dislocations can move through the material lattice. The easier it is for dislocations to travel through the material, the less force and stress is required for a crack to propagate and lead to failure.

At elevated temperatures the strength is determined in the same way, however with the higher temperature comes an increase in the amount of energy available to the atoms within the material. This increase in energy makes it easier for the atoms to move and therefore processes like diffusion and dislocation movement happen more rapidly with lower applied stresses. This is the reason that the mechanical properties of metals are seen to degrade as their temperature is increased.

Nickel based superalloys, although still susceptible to this inevitable process of temperature induced softening, use a combination of solid solution strengthening and precipitation strengthening to delay the deleterious effects of increased temperatures. Atoms of solution strengthening elements (Nb in the case of IN625 and IN718) or precipitates (γ'' for IN625 and IN718) sit within the material lattice and provide physical barriers to dislocations. This improves mechanical properties both at room temperature and, most importantly, elevated temperatures. These atoms and precipitates are stable up to the operating temperature of the material, remaining within the material lattice and providing a barrier to dislocations. This gives superalloys their characteristic high temperature mechanical properties.

2.3.2.2.1 High Temperature Tensile Strength

Trosch et al report the elevated temperature tensile properties of SLM IN718 material, testing at both 450 °C and 650 °C, (Trosch et al., 2016). The results are presented below in Figure 11. All the material underwent a standard duplex aging treatment, 718 8h, FC, 620 8H, AC to precipitate strengthening γ'' precipitates 2.1.4.2.

The room temperature properties of the SLM material are similar to those of the forged material, with some anisotropy depending on the build direction, as previously discussed, section 2.3.2.1.1. The cast material achieves significantly lower ultimate and yield strength due to the large grain size and porosity detected within it (Trosch et al., 2016)

All the materials demonstrate a reduction in their strength and elongation as the temperature is increased, Figure 11. The most notable change in the SLM material is the loss of ductility, Figure 11 C). This is attributed to the presence of intragranular δ phase precipitates due to micro-segregation of Nb (Trosch et al., 2016). This δ inhibits the precipitation of γ'', responsible for imparting high temperature strength. In contrast δ precipitates are only observed at grain boundaries in conventionally processed material resulting in greater levels of γ'' precipitation throughout the grains and the retention of mechanical properties at 450 °C and 650 °C.

The build orientation of the coupons is also reported to be a source of mechanical property anisotropy at elevated temperatures, as was noted at room temperature. The elongation when tested at 650 °C was measured to be 14.2 % and 3.6 % in vertical and horizontal coupons respectively, Figure 11 C). The issues of defect alignment with the stress axis, discussed in section 2.3.2.1.1, compound with the unfavourable δ precipitation to further reduce mechanical properties.

As well as elongation, the SLM coupons also demonstrate a more rapid decrease in yield strength compared to forged material as the temperature is increased, Figure 11 B). This is attributed to the loss of the Hall-Petch hardening effect obtained from the fine grain structure of the SLM material (Trosch et al., 2016).

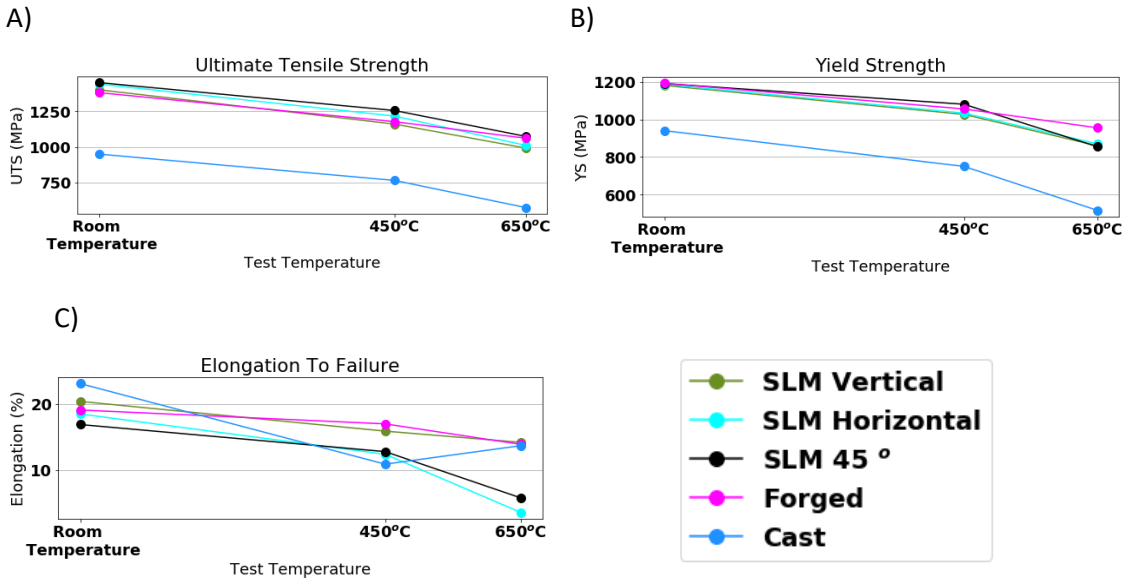

Figure 11 – Tensile testing results at room temperature, 450 °C and 650 °C. The results compare the performance of SLM IN718 built in different orientations (vertical, horizontal and 45 °) and conventionally manufactured material, forged and cast (Trosch et al., 2016).*A) gives the ultimate tensile strength reported from the tests. B) gives the yield strength reported in the tests, C) gives the elongation to failure reposted from the tests.*

2.3.2.2.2 Creep and Stress Rupture

Creep is a high temperature, time dependant material property. Measured in hours, it is the time taken for the material to fail when subjected to sustained tensile loading below its yield stress at elevated temperatures. This type of loading results in slow deformation of the material. Stress rupture is very similar to creep however the loading used during testing is higher and the tests are done to failure of the material, allowing for the calculation of a stress rupture lifetime of the material.

For materials such as IN718 and other nickel-based superalloys stress rupture is a critical material property. Superalloys are commonly used in the hot section of gas turbine engines and other temperatures where they are subjected to precisely this type of high temperature constant loading.

A material can fail at high temperatures in two ways, the first is by excessive deformation. This would result in the material or component elongating to such an extent that it is no longer able to perform its intended task, this is a less common mode of failure. As the temperature is increased it is most likely that the failure will occur by rupture, with the degree of strain decreasing with increased temperatures.

2.3.2.2.2.1 Characteristics of Creep

When creep is measured in a material it can be divided into three distinct stages. The first stage occurs as soon as the loading is applied to the material. This is essentially the same response as

the material would display during uniaxial tensile testing. The second stage of creep is a steady state portion, the constant stress being applied to the material leads to a linear increase in the strain where the strain vs time graph will display a constant gradient. The third and final stage of creep sees an increase in the gradient of the graph as strain increases more rapidly. This is a result of the decreasing cross-sectional area of the specimen as necking occurs prior to rupture.

2.3.2.2.2.2 Mechanisms of Creep

There are several different mechanisms which can take place within a material which facilitate creep deformation in polycrystalline materials.

The first possible mechanism is grain boundary sliding, also known as Coble creep. Grain boundary sliding requires the diffusion of atoms along grain boundaries which leads to the elongation of the grains in the direction of the stress axis. The rate at which this type of creep and the elongation of the grains can take place is dependent on the grain boundary area per unit volume of the material and the ability of the atoms to diffuse. It is therefore a thermally activated process with the rate of diffusion, and therefore Coble creep, increasing with increasing temperatures. It is also inversely proportional to the grain size of the material.

Another diffusion-based method of creep is called Nabarro-Herring creep. The tensile stress applied to the material, during service or testing, results in atoms aligned normally to the stress axis being pulled apart from each other and those aligned parallel to the stress to be pushed closer together, via Poisson contraction. The atoms being pulled apart by the stress see an increase in their separation while the opposite is true for those being forced together by Poisson contraction. This leads to a diffusion of atoms through the lattice from those boundaries parallel to the stress towards those normal to it, resulting in an elongation of the material in the stress axis. This is the cause of plastic deformation and specimen elongation during the creep and stress rupture tests.

Nabarro-Herring creep is more thermally dependent than Coble creep, since atoms must diffuse through the lattice rather than along grain boundaries, where vacancies are more common. As temperature is increased the ratio between Nabarro-Herring and Coble creep will increase.

The final mechanism of creep is dislocation motion or slip. A dislocation is any defect in the crystal structure of the material. When a stress is applied to the material it is possible for these dislocations to shift by a lattice point. The plane in which this movement of lattice points takes place is known as the slip plane. This movement of dislocations, when repeated many times is responsible for deformation during slip creep.

The slip and movement of dislocations is determined by the number of obstacles in the dislocations path and the ease with which a dislocation can overcome them. An example of an obstacle to dislocation movement would be a strengthening phase precipitate in the crystal lattice. When a dislocation encounters an obstacle in its slip plane it requires move energy to pass through, if the stress applied to the material is not great enough for the dislocation to pass through the obstacle, then the dislocation cannot move further in that direction. In order to avoid the obstacle, the dislocation must therefore move out of its slip plane, a process known as climb. The climb process requires a diffusion process to take place to move the dislocation perpendicular to its current slip plane to reach a different parallel plane. As it is a diffusion dependent process creep by dislocation climb is temperature dependent, increasing as temperature increases.

2.3.2.2.2.3 Factors Controlling Creep life in Nickel Superalloy

2.3.2.2.2.3.1 δ phase

The role of δ phase precipitation in the creep life of nickel-based superalloys is complicated. The δ precipitates are incoherent with the γ matrix and do not directly provide any strengthening to the material, they also consume Nb, an essential element required to precipitate the strengthening γ'' phase. The δ phase has also been reported to provide cavities which allow creep cracks to form and propagate more easily (Kong et al., 2013). Despite all of this however it has been found that it can be beneficial to have some amount of δ phase present within the material, providing several improvements to the creep and stress rupture life (Jinhui et al., 2017b; M. Wang et al., 2015).

The first of the benefits which δ precipitation brings stems from one if its negative impacts, its consumption of elements required to precipitate strengthening γ''. During cooling at a sufficiently slow rate or a heat treatment in the δ precipitation range ~1000 °C , the δ phase will form at a higher temperature, and therefore prior to the γ'' phase (which begins to form from ~900 °C and below) (Saied Azadian et al., 2004). Upon formation, the δ (Ni_3Nb) precipitation consumes the Nb around it creating a Nb depleted zone (Rahimi et al., 2017). This Nb depleted zone is not capable of precipitating the strengthening γ'' precipitates during subsequent aging treatments, meaning it does not undergo precipitation hardening (in the microscopic region surrounding the precipitate) (Kong et al., 2013). The result of this limited hardening is the creation of a small area with greater plasticity than the bulk material around the δ precipitate (Jinhui et al., 2017b), this is known as microplasticity. When a crack is present in this region, for example during the propagation of a creep crack, the stress concentration which builds up at the crack tip causes the softer material to deform, relieving some amount of the stress. This

slows the propagation of the crack and extends the stress rupture life of the material (Jinhui et al., 2017b).

The benefits of δ induced microplasticity for relaxing stresses at the crack tip also extend to improving the notch sensitivity of the material. The notch behaves much like a crack tip, generating a stress concentration within the material which can lead to earlier onset of failure in the material. The ability of the material around δ precipitates to relax this stress reduce the sensitivity of the material to the notch (M. Wang et al., 2015).

The δ phase also influences the mechanism of the material deformation taking place during stress rupture. Forming primarily at the grain boundaries, the δ precipitates have a pinning effect on the grain boundaries (Kong et al., 2013; C.-M. Kuo et al., 2009; Yeh et al., 2011). They provide resistance to grain boundary slip motion, either through their physical presence or through their effect on the grain boundary morphology itself, An-Chou Yeh et al, found that δ precipitation lead to the formation grain boundaries with a jagged appearance, referred to as serrated grain boundaries, within the material (Yeh et al., 2011). Du Jinhui et al, show how, following stress rupture testing, material with little to no δ content displays undeformed grains where deformation has taken place entirely via grain boundary sliding and twinning whereas when δ content is increased to 5%, dislocation slip becomes the predominant deformation mechanism. The grains are observed to be significantly deformed with dislocations around the boundaries, images shown in Figure 12 (Jinhui et al., 2017b). Similar findings are reported with relation to the serrated grain boundaries caused by δ precipitation with a significant increase in creep life resulting (Yeh et al., 2011).

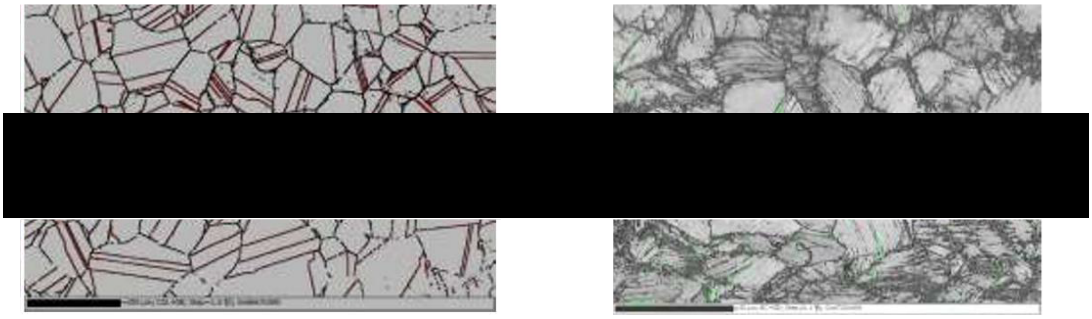

Figure 12 – Left – EBSD images of material post stress rupture testing showing the impact of δ content on the deformation mechanism on Hot Rolled IN718. Left – Low δ content material showing no grain deformation resulting from grain boundary sliding and twinning. Right – 5% δ content showing heavy grain deformation from dislocation slip. Images taken from (Jinhui et al., 2017b)

The balance between the positive and negative effects of δ precipitation is determined by the volume fraction of δ present in the material, with diminishing benefits as the volume fraction

increases beyond a certain point. As δ content increases the increase in stress rupture crack initiation sites (Jinhui et al., 2017b; X. Lu et al., 2014) and the decrease in precipitation hardening possible (Saied Azadian et al., 2004) start to degrade the mechanical properties of the material, reducing creep and stress rupture life (Jinhui et al., 2017b; C.-M. Kuo et al., 2009) as well as room temperature properties.

2.3.2.2.2.3.2 Environmental factors

While the condition of the material itself plays a vital role in the creep properties of IN718 it is not the only factor. Previous research has reported that environmental factors have a dramatic effect both on the life and failure mechanism. The rate of creep crack growth was found to be two orders of magnitude faster in identical material coupons tested in air vs those tested in a vacuum, showing the dramatic negative effects of oxidation on the materials (Stucke et al., 1984). The oxidation and creep cracks were found to form preferentially at the grain boundaries where the increased vacancy density provides both a faster diffusion path for oxygen and a weaker interface for crack propagation. The oxidised material can contribute to crack growth either by forming a weak interface with the material or by the formation of microcracks which propagate back through the material to a crack tip and lengthen the creep crack (Ghonem & Zheng, 1991). A result of this oxygen dependent grain boundary weakening is that the failure mode of the material in the two different tests was different. Coupons treated in air showed exclusively intergranular cracking whereas the coupons tested in a vacuum failed in a transgranular fashion (Stucke et al., 1984).

2.3.2.2.2.3.3 Grain Size

Another microstructural factor which can contribute to the creep behaviour of a material is its grain size. The grain size of a material determines the grain boundary area per unit volume contained within it, and it is those grain boundaries which influence creep.

Generally, as a result of grain boundary strengthening from the Hall-Petch relationship, the strength, both room and elevated temperature, of a material is inversely proportional to its grain size. Smaller grains result in greater density of grain boundary area within the material. These grain boundaries act as barriers to the movement of dislocations through the material. The plot in Figure 13, for 316LN Stainless Steel, clearly shows this relationship at both 25 °C and 600 °C (Y. S. Lee et al., 2001). Grain boundary strengthening has been reported to decrease the creep rate during the primary phase of creep (Y. S. Lee et al., 2001).

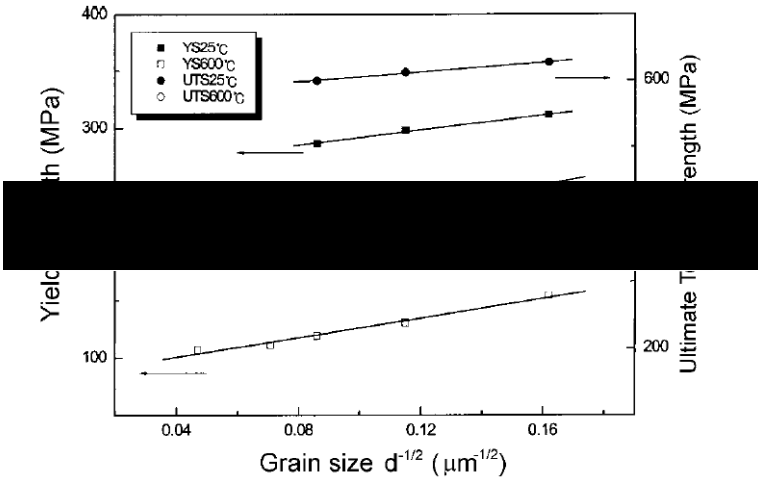

Figure 13 - Plot showing the inverse relationship between tensile strength and grain size (316L SS) (Y. S. Lee et al., 2001)

This initial, simple relationship however does not continue, with the same paper reporting that in the secondary phase of creep, steady state, an intermediate grain size yielded the lowest creep rate (Y. S. Lee et al., 2001). The impact of grain size on the creep properties is therefore not a straightforward relationship.

As previously discussed, different mechanisms of creep take place under different conditions, temperature and applied stress. This further complicates the issue of the influence of grain size. Thebaud et al (Thébaud et al., 2018) examined the performance of a fine and coarse grained Ni superalloy under different temperature and stress conditions. When the test was conducted at a higher temperature, 850 °C the coarse grained material displayed far superior properties (~40x better creep strength), this was attributed to the prevalence of grain boundary sliding and Coble creep as the deformation mechanism, something which would be exacerbated by the high grain boundary area of the fine grained material. When the temperature was lowered to 700 °C the performance difference between fine and coarse grains was drastically reduced, suggesting that the grain size was no longer a limiting factor on the creep performance.

Other factors about the grains and the boundaries can also influence the creep properties. As was mentioned in relation to the influence of δ precipitates, the morphology of the grain boundaries themselves can have an effect. It has been reported in various Ni superalloys that the formation of serrated grain boundaries can help to arrest the propagation of intergranular cracks during creep and improve the properties (Wisniewski & Beddoes, 2009; Yeh et al., 2011).

In summary the influence of grain size on the creep properties of a material is a complex and multivariate subject depending on the precise material and test conditions. Grain boundaries

can act both as barriers to dislocation movement, slowing the rate of creep and extending the life of the material, but also as sources of dislocations, reducing the creep life. It is important for the material to achieve the correct balance of grain size to resist the specific types of creep required (Pollock & Tin, 2006).

2.3.2.2.2.3.3.1 Grain Boundaries – Directional Solidification

Considering the potential influence of grain boundaries as sources and paths for intergranular cracking there are some alternative processing methods which are used in certain applications to create Ni superalloy components with improved creep life.

Directional solidification (DS) is a technique primarily used in the manufacture of gas turbine blades. The process works from the theory that by orienting the grains of the material in such a way that there are minimal boundaries perpendicular to applied stress, or even eliminating the boundaries altogether, the creep properties can be greatly improved.

DS is a refined method of casting where the mould, containing molten metal, is withdrawn slowly from the furnace. This slow withdrawal created a constant thermal gradient from the melt pool still within the furnace and the solidified material, outside. The constant thermal gradient causes the grains to grow in one constant direction parallel with the thermal gradient (Pollock & Tin, 2006). Given the cubic symmetry of Ni superalloys, they favour the growth of dendrites oriented along the <001> direction and so this DS process results in columnar grains predominantly with <001> orientations (Pollock & Tin, 2006). A further refinement can be applied to DS to allow grain boundaries to be altogether removed from the component, creating a single crystal alloy where the entire component is made up of one large grain of material.

A single crystal alloy is created by introducing a seed grain at the base of the mould. The seed grain is created using grain selection where a pig tail section is created at the bottom of the mould. As the material solidifies through this section competitive growth automatically results in only a single grain of the preferred <001> orientation reaching the bottom of the part mould (Esaka et al., 2005a; W. Yang et al., 2019). The same directional solidification process then leads to the entire part growing from that seed grain into a single crystal (Esaka et al., 2005b).

These processes reduce or eliminate grain boundaries within the material and therefore minimise or remove the possibility of grain boundary sliding or Coble creep, improving the creep life of the component. This process is however not suitable for all applications as it isn't possible to create certain components using these methods or the anisotropy of mechanical properties created from the aligned <001> grains might not be suitable if loading in multiple stress axes is required (W. Yang et al., 2019).

2.3.2.2.2.3.3.2 Grain Boundaries – Coincidence Site Lattice

Where two grains meet, they form a grain boundary. At this point, the crystal lattices of the two grains must join. In most cases, this results in some degree of misorientation, resulting in stored energy and vacancies where the lattices do not meet perfectly. The greater the angle of misorientation, the greater the stored energy. In crystallography, generally grains meeting with a misorientation of 15 ° or less are referred to as low angle. They have minimal misalignment between them and little stored energy. Above 15 ° the boundaries are referred to as high angle. These boundaries are deleterious to the material and provide an easier route for dislocations to travel through during material failure, or a lower energy location for segregated elements to reside (in the larger number of vacancies). There are however some special cases of higher angle grain boundaries where, although the misorientation angle is high, due to geometric alignment, the misfit of the two lattices is much lower, these are Coincidence Site Lattice (CSL) boundaries, or just special grain boundaries. Coincidence site lattice (CSL) boundaries occur as a result of lattice geometry, they are boundaries which occur at specific misorientation axis angles where points on the two meeting lattices overlap and are coincident (Brandon, 1966; Chong et al., 2014). This coincidence will recur every certain number of lattice points. CSL boundaries are expressed by a Σ symbol followed by a number which represents how often the coincident sites occur, for example a Σ3 boundary is one where coincidence occurs every 3 lattice point (Chong et al., 2014).

The coincidence of the lattice points reduces the misfit of the two lattices and reduces the free energy of the boundary. CSL boundaries are high angle random grain boundaries but with lower boundary energy, more like a low angle boundary. As the regularity of the coincidence decreases the reduction in free energy is reduced, so generally CSL boundaries are only considered special up to Σ29, with lower numbers being preferred (K et al., 2018).

CSL boundaries have been found to have many special properties however they have also been investigated regarding creep life. It is reported that in material where the presence of low Σ CSL boundaries is increased there is a reduction in both primary and steady state secondary creep rate (Lehockey & Palumbo, 1997). This is attributed to the decreased likelihood of void formation along the lower energy CSL boundaries, there are few places in the material for cracking to occur easily (Boehlert et al., 2008; K et al., 2018; Watanabe{ & Tsurekawa, 2008).

2.3.2.2.2.4 Novel Methods of improving stress rupture in Nickel Superalloy

Other methods have been investigated for improving the creep strength of nickel superalloys. One such example is the work of Weili Ren et. Al (Ren et al., 2018) who found that the application of a magnetic field to the material during directional solidification of a single crystal part lead to

an increase in creep life. The cause of this improvement is a combination of effects that the magnetic field have on the molten material. The magnetic field has a damping effect on the turbulent material flow within the melt, helping to reduce levels of macro segregation, cracking and inclusions. The result was material with better solute distribution and smaller strengthening phase precipitates more coherent with the y matrix. The use of such a magnetic field led to a reduction in the quantity of dislocations present in the material during creep and a maximum of a 5x increase in stress rupture life of the material (Ren et al., 2018).

2.3.2.2.2.5 Improving stress rupture by alloying element modification

Investigations have also been made into the effect of altering the proportion of different alloying elements. This is useful both for the development of new alloys but also the optimisation of existing ones. While the proportions of different alloying elements are determined by existing standards there is usually a range of acceptable element weights, therefore it is possible to slightly increase or decrease certain elements to improve the properties of the alloy.

Typically, the investigations look at trace elements in the alloy, for example phosphorus, which makes up a maximum of 0.015% of both IN625 and IN718. Typically P is considered a harmful impurity which degrades mechanical properties however in wrought Ni based super alloys like IN718, IN625 and others investigations have found the opposite to be true, that increasing P content can yield useful positive effects (Guan et al., 2016).

It was reported by Cao et al (W. Cao & Kennedy, 1994) that increasing the P content over what is found in standard commercial alloys, to 0.022% can result in up at a 100% increase in stress rupture life time. Similar improvements have also been reported for a variety of nickel based superalloys (Guan et al., 2016; X. Liu et al., 1999; Sun et al., 1998, 1997; M. Wang et al., 2015) This improvement is attributed to a solution hardening effect from the P atoms, which can act as barriers to dislocations (W. Cao & Kennedy, 1994). As well as an increase in rupture life, it is also reported that greater P content leads to decreased levels of intergranular cracking, suggesting that segregation of P to the grain boundaries results in a strengthening effect (W. Cao & Kennedy, 1994). This apparent strengthening of the grain boundaries could also contribute to the improved stress rupture properties, slowing crack propagation and forcing fractures to occur transgranularly instead. It has also been reported to reduce the impact of environmentally assisted cracking. Crack initiation was observed to move from the coupon surface to the coupon centre as P content was increased. This suggests that the P atoms segregated to the grain boundary act to slow the diffusion of O atoms. A link between P and the δ phase is also reported, with an inverse relationship between P content and δ precipitation.

With the benefits of both δ and P resulting from their grain boundary segregation their effects are intertwined and where P content is too high (~0.02% up to 0.05% have been reported) a decrease in stress rupture life results (M. Wang et al., 2015).

Modification of other elements such as the Al/Ti ratio has also been investigated, it is widely reported that this ratio is critical in determining the amount of γ' precipitation, which determines the level of strengthening γ' precipitation. In superalloys such as IN615 and IN718 the strengthening comes primarily from γ'' precipitates instead, so Al/Ti content is much lower so such modifications are less impactful (W. D. Cao & Kennedy, 2001).

2.3.2.2.3 Stress Rupture and Creep Performance of SLM Nickel Based Superalloy

As has previously been discussed in 2.1, the excellent high temperature properties of nickel-based superalloys are a primary driver in their selection for many applications, especially in the hot section of aerospace gas turbine engines.

Also discussed has been the many, practical geometric, efficiency and design freedoms which are brough about by manufacturing using additive manufacturing, more specifically SLM. The drawbacks of the SLM method have also already been discussed and can be, for many aerospace applications, ignored or worked around. There is however one remaining disadvantage of SLM superalloy material which is a critical stumbling point for its further adoption. It has been found, through industrial experimentation, that the high temperature performance, more specifically the stress and creep rupture life, are below that of conventionally manufactured material Figure 14. This difference in performance in present even following the application of a set of standard heat treatment routes.

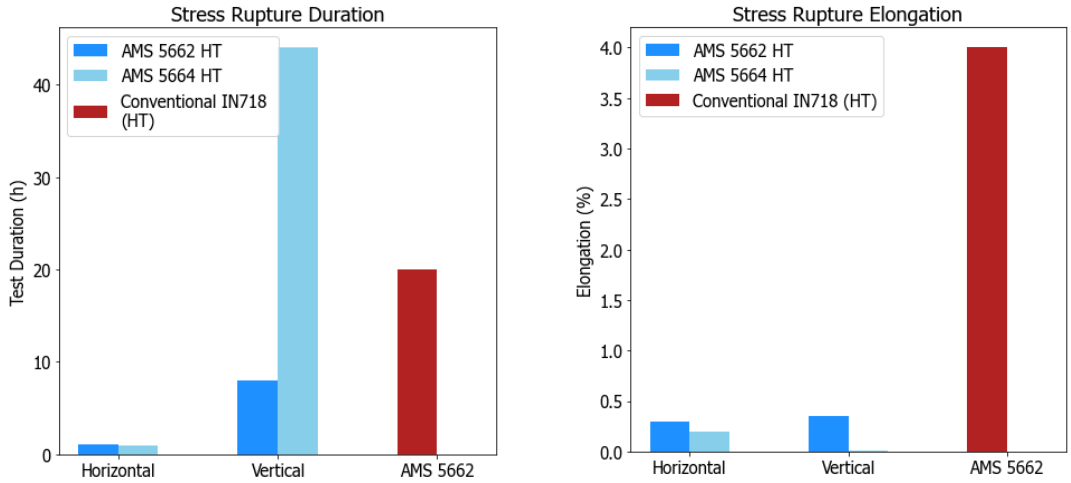

Figure 14 - Graph showing the stress rupture performance of SLM produces IN718 material. Both rupture life and elongation at rupture are plotted after the application of standard heat treatment routes intended to maximise performance. Data obtained from an industrial source not publicly available.

This shortcoming of the material prevents SLM superalloy being considered as a viable material, it fails to pass certain criteria to be put into production. This shortcoming of the standard heat treatment routes, designed for conventional material, raises the need for a specific route to be developed, optimised for SLM material.

Over and above this, as has already been discussed in section 2.2.3.3, the process parameters selected for SLM can have a significant influence on the material produced. This raises the need, not only for a novel heat treatment route for SLM material, but a novel heat treatment route for a specific set of processing parameters.

Such a heat treatment route should be designed with the aim of transforming the unique microstructure created by the SLM process into material which meets the theoretical criteria for material with good stress rupture performance, as outlines in section 2.3.2.2.2.3.

2.4 Powders as Raw Feedstock Material

2.4.1 Introduction

SLM is a powder bed fusion process which use a powdered metal as their raw material feedstock. As with any manufacturing process proper control of the raw material is essential to ensure that finished components meet design criteria. The use of powders introduces an additional level of complexity to this process on top of the usual material factors such as porosity or chemical homogeneity. Powders are a mixture of solid particles and the fluid medium between them, with properties of both being important. The control and characterisation of these properties is one of the primary challenges faced by users looking to implement ALM in any capacity but especially for commercially serviceable components in demanding applications.

2.4.2 Powder Requirements During ALM

The flow characteristics of the powder feedstock become a factor whenever the powder is required to move. In the SLM process there are several stages where this is important:

When loading the powder into the hopper or cassette inside the ALM machine. It is important at this stage that the powder packs closely and uniformly together, any significant air gaps could lead to a lack of powder being delivered to the build plate which could lead to pores or defects in the layer or even complete build failure. It is possible for the machine operator to have some input to this process, compacting the powder at this stage although it is still preferable to have a powder which will achieve good packing on its own.

The layer deposition or recoating process is the most critical stage of the process where good powder flow is required. As the powder is swept over the build plate it needs to flow underneath

the recoating arm and form a uniform layer on the build plate. Any failure to flow during this stage will have a direct impact on the quality of the layer and the build.

The final stage of the process where powder flow is required is powder recycling. Once the build is completed the unsintered powder can be collected and sieved to be reused. Powders that are too cohesive will be more difficult and time consuming to sieve. Although this does not have an impact on the build itself it is still a significant factor for the operation of ALM machines.

2.4.3 Powder Properties

There are several different properties which can be measured and characterised about any powder. They can be broadly divided into two categories, morphology or rheology. Morphology refers to the shape and size of the individual particles within the powder and rheology refers to the flow characteristics of the powder, how the stress on the powder relates to the deformation or flow that takes place (Tabilo-Munizaga & Barbosa-Cánovas, 2005).

The overall morphology is an inherent physical property of the powder. It will be determined by the history of the powder, the manufacturing method used to produce it and whether the powder has been recycled from previous builds where it has been used but not sintered. Morphology can generally be measured or characterised quantitatively using a variety of methods (discussed in section 3.1.2). Rheology is a more complex topic and more difficult to quantify. It has been reported that the flow behaviour of a powder can change depending on the conditions under which it is tested, both the consolidation of the powder prior to testing and the stress state during the test (Clayton, 2019; Freeman, 2007; Krantz et al., 2009; Spierings et al., 2015; Teunou & Fitzpatrick, 2000).

2.4.3.1 Forces of Powder Flow

Powder flow, as with any system in motion, is always a balance between the driving and opposing forces. Considering SLM and EBM specifically the force driving flow is always the powder particles weight due to gravity. Even the recoating stage, where a moving blade pushes powder across the build plate to deposit a fresh layer, the flow is taking place in the accumulated powder in front of the blade, particles are pulled to the bottom of the pile where they then pass under the blade and become deposited. The sideways force from the blade only serves to move the powder pile in its entirety, not causing any flow.

There are several forces opposing flow in a powder. The morphology of the powder contributes to mechanical resistance forces like surface friction and mechanical interlocking. Surface friction is of course dependent on the surface roughness of individual powder particles with rougher

surfaces leading to more friction and more resistance to flow, whereas mechanical interlocking is caused by irregularly shaped particles which can get caught on each other (Freman, n.d.). The condition of the powder can also contribute to flow resisting forces in the form of liquid bridging and electrostatics. Liquid bridging occurs where moisture content in the powder is high enough that particles can become stuck together via the surface tension of the liquid on their surfaces (Hotta et al., 1974). Electrostatic forces result from charges accumulating on the powder particles, eventually leading to attraction forces large enough to cause agglomeration, where multiple particles stick together and act as one large, irregularly shaped particle (Feng & Hays, 2003a; Freman, n.d.). Electrostatic forces can build up due to external electric fields or through contact and movement between particles within the powder (Feng & Hays, 2003a).

The final forces opposing the flow of powders are interparticle forces. The most significant interparticle force being the Van der Waals force, which has been reported to make up 80 – 90 % of all interparticle force (Krantz et al., 2009). The Van der Waals forces results from the atoms and molecules that make up the material altering their electronic configuration when they come into close proximity to each other (Visser, 1989), this rearrangement of electrons causes the molecule to become more negatively charged on one side leading to a dipole effect. This dipole effect means that although the particle has no net charge it can be attracted, similar to electrostatic force, to other particles (Feng & Hays, 2003a; Hamaker, 1937). The Van der Waals forces become less significant as the size of powder particles, and therefore their weight force due to gravity, increases, published literature puts the crossover point where gravity becomes more significant than Van der Waals forces at particle diameters around 10 µm (Feng & Hays, 2003a; Visser, 1989).

2.4.4 Powder Production Methods

Metal powders can be produced by several methods. For an end user, the practical difference between the methods is in the regularity of the powder particles they produce.

An example of a powder production technique which produces very irregular powders is hydride-dehydride (HDH) or ball milling. In HDH a hydrogen sensitive metal (Ti, V, Zr, Ta) is heated in a hydrogen rich environment, encouraging the formation of brittle hydrides. These hydrides are then crushed and milled into a powder which can then be vacuum heated to liberate the hydrogen and create a dehydride powder (Bolzoni et al., 2014; McCracken et al., 2011; Mitkov & Bozˇić, 1996). The edges of the particles are created by the fractures of the brittle hydride material, this creates irregular, jagged shapes of particles which will have significant surface friction and mechanical interlocking during any kind of flow, evident in their

low tapped density measurements (McCracken et al., 2011). These powders are more suitable for processes like press sintering or metal injection moulding, where an external force is applied to consolidate the particles together. No such force is present in SLM or EBM which would lead to gaps in the powder bed, translating to porosity in the finished material. A study into a similar irregular powder, created via ball milling, found density drop from 99.5% to 95% when a more irregular powder was used (Attar et al., 2015).

There are then atomisation processes, these processes melt the material in a vacuum furnace and pass the liquid in a stream through a nozzle. Upon exiting the nozzle, the flow of liquid metal will be broken up, or atomised, by a stream of high velocity fluid. The atomised droplets cool quickly and solidify, falling to the bottom of the chamber where they can be collected. The desired size distributions can be extracted from the atomised powder using differently graded sieves. Different atomisation methods are differentiated by the medium they use for atomisation. Water atomisation gives very fast cooling and less regular morphology powders, it is only suitable for use with unreactive metals (Mostafaei et al., 2018). Gas atomisation gives a slower cool with a regular spherical morphology, although some satellite or non-spherical particles have been observed, Figure 15. Plasma atomisation works slightly differently, with plasma being used to melt and atomise a wire feedstock to create very regular, spherical morphology powders.

Gas atomisation is the most commonly used powder production method for ALM applications, giving an acceptably regular spherical morphology at a lower cost than plasma methods (Mostafaei et al., 2018; Slotwinski & Garboczi, 2015).

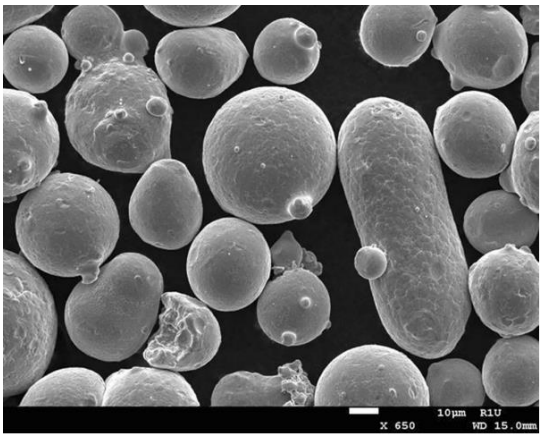

Figure 15 – Scanning Electron Microscope image showing the particles of a gas atomised metal powder. The image shows the general spherical nature of the particles produced but also the content of satellite and irregularly shaped particles which can occur (Slotwinski & Garboczi, 2015)

2.4.5 The need for standardisation of powder characterisation methods for Additive Manufacturing

Powder characterisation is a well established field of study and there are a wide range of characterisation methods and equipment available designed for a range of applications from pharmaceuticals and food to powdered paint and sintering materials. There is also a wide range of potential ways to interpret the results from these methods, as has already been discussed, the apparent properties of a powder can change depending on the conditions in which it is tested.

When using metal powders for certified, serial production this broad range of potential methods and outcomes presents an issue. The aim of a manufacturing process, critically so in industries such as aerospace, where nickel-based superalloys are targeted, is to create consistent, predictable and reliable parts every time. Without a good understanding of powder behaviour or an established standard procedure to characterise it, it is impossible to ensure long term consistency between different users or the production of confident, repeatable or correct results (Cooke & Slotwinski, 2015; Slotwinski & Garboczi, 2015). For this reason investigations have been conducted into the standardisation of powder metrology (as well as metrology of the manufactured material) to identify the key issues which need to be addressed (Jurrens & Energetics Incorporated, 2013; Metal AM, 2014; Slotwinski & Garboczi, 2015). Several groups are working towards developing such standards for powder characterisation such as ASTM F42 and ISO Technical Committee 261: Additive Manufacturing, with 37 standards either published or in progress (Manufacturing, n.d.).

Several key issues have been raised (Slotwinski & Garboczi, 2015)

- The complexity of the process and the large number of possible variables makes it difficult to identify and understand the root cause of machine-to-machine or day-to-day variations
- Many metrology methods developed for other processes are not suitable or practical for additive manufacturing applications (Krantz et al., 2009).
- No standardised methods exist for repeatable material testing between different users
- Lack of in-situ measurements for process control (Jurrens & Energetics Incorporated, 2013)

Further investigations of powder metrology methods and their applicability to additive manufacturing material are required in order to develop these standard practices and improve understanding of how they influence the additive manufacturing process. There is currently a

lack of any literature looking at the characteristics of metal powders and relating the results to the processability of the powder in SLM or in the quality of the material that it produces.

This task is further complicated by the fact that powder changes its properties depending on how it is processed. This means that there will not be a 'one size fits all' solution to the problem, with methods having to be established based on specific SLM machine models (since powder delivery and recoating mechanisms vary between machines).

Establishing a link between powder characteristics and the processability of a powder in SLM as well as determining a suitable method for making such a characterisation will be a focus of the first section of this thesis. This knowledge will be useful to industrial users of SLM who want to better understand how they can control their manufacturing process and monitor and minimise batch to match consistency of their powders.

2.5 Summary

Reviewing the published literature and knowledge surrounding nickel-based superalloys and their production via SLM has raised three areas suitable for further investigation. These three areas form the basis of the motivation behind this work and are outline below in the order in which they are addressed in this thesis.

The first of these areas relates to the quality, control and understanding of the raw metal powders used as feedstock material for the process. While a range of methods exist for characterising these powders, the topic is complex, and investigations must be directly linked to specific machine architectures (powder handling and recoating systems). This topic has not yet been fully investigated and there is no literature published linking the characteristics of a powder placed into an SLM machine and its processability or quality of finished material it will produce.

The second gap in current knowledge identified through the literature review is the potential for in-situ control or modification of the microstructure of nickel-based superalloy material in SLM. There is a wide range of literature investigating certain specifics of the microstructure of material produced by SLM however nothing yet exists to link these findings to potential productivity improvements or application specific process parameters which might make a material more responsive, even slightly, to post process heat treatments for example.

The third and final topic identified as requiring further investigation is the development of a post process heat treatment route specifically targeted at nickel-based superalloy. There is evidence showing that the as fabricated material does not respond well to standard heat treatment routes

however no literature addressing the development of a new route targeting properties critical to aerospace applications. High temperature properties such as stress rupture life have been shown to be significantly worse in SLM material compared to conventional even after heat treatment, making it clear that a new route is required. Based on the knowledge of how specific process parameters can modify the microstructure of material produced by SLM, it is unlikely that such a standard route can exist for all SLM material, so this topic will be investigated for a single set of process parameters.

3 Experimental Methodology

In this chapter the experimental method followed while conducting the work contained in this thesis is given. This is intended to allow the reader to understand the work that has been carried out and enable the reproduction of any of my experiments or results.

The details given focus on the work unique to my experiments with some more general procedures, such as sample cutting and polishing, or SEM microscope techniques omitted.

3.1 Investigation of Powder Characteristics and Metrology Methods for Application in Selective Laser Melting

3.1.1 Powders

In order to determine the effect of power characteristics on the SLM process it was necessary to compare a selection of different powders. Three powders were selected in total supplied by two different suppliers. The powders were all IN625 powders produced by gas atomisation (GA) and information is given about them in Table 6 below.

Table 6 – Table containing the naming convention for the three powders characterised in this chapter as well as their PSD as measured by laser particle analysis, expressed as d10, d50 and d90.

Powder	Supplier	d10	d50	d90
Powder 1 (P1)	A	20.0	33.0	55.4
Powder 2 (P2)	B	5.3	6.4	8.7
Powder 3 (P3)	B	22.5	32.7	47.7

3.1.2 Powder Rheology Characterisation Equipment

3.1.2.1 Carney Flow Test

Carney flow testing is conducted using a funnel of standard dimensions through which powder can flow. The time the powder takes to flow through the funnel is recorded. The standard dimensions of a carney flow funnel are illustrated in Figure 16. For each test a 100g sample of powder is taken and loaded into the funnel with the orifice covered preventing powder from passing through. The orifice is then uncovered, and the time taken for the powder to flow through completely is recorded. Each powder is measures 3 times to ensure repeatability. Where a stable flow could not be obtained, some mechanical agitation of the funnel was used.

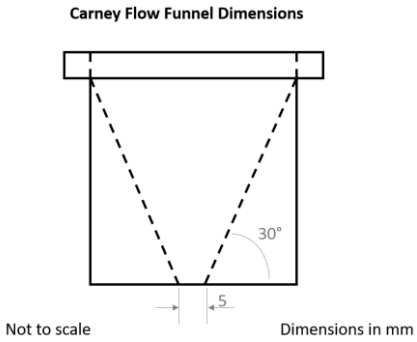

Figure 16 – Schematic illustration showing the standard dimensions of a funnel used for Carney flow powder rheology testing.

3.1.2.2 Tapped Density Test

Tap density testing is another, more manual test used to assess powder flowability. The test monitors the bulk density of the powder to assess how well the particles flow over each other.

To perform the test a sample of 100 g of powder loaded into a graduated cylinder using the Carney flow funnel from above. Once in the cylinder the volume level of the powder is used to calculate the bulk density. Several different sizes of graduated cylinder, 17 and 20 mm diameter, to investigate whether this had any effect on the results, but no significant difference was found, results are presented from the 17mm cylinder.

The cylinder is mechanically tapped at 5 Hz, to consolidate the powder particles. After 500 taps the tapped density is calculated from the new volume and used to calculate the Hausner Ratio, Equation 6.

$$H_r = \frac{\rho_T}{\rho_B}$$

Equation 6 – Equation for the calculation of Hausner ratio, H_r. ρ_T is tapped density, ρ_B is bulk density.

3.1.2.3 Freeman Technology 4 Powder Rheometer (FT4)

Using the FT4, a twisted blade is rotated and pushed through a cylinder containing a 25 ml volume of powder at different vertical speeds while the torque and height of the blade are recorded. This data is used to calculate work done or total flow energy. The FT4 test is illustrated below in Figure 17.

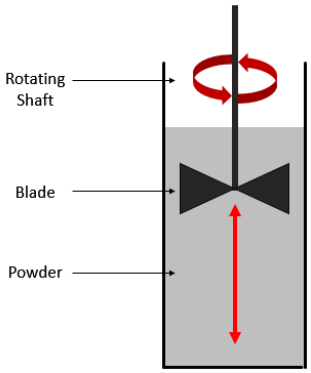

Figure 17 – Schematic illustration of test equipment used during a powder rheology rest with the freeman technology 4 FT4.

The full test consists of 7 repeated cycles of the blade traversing vertically down and then up through the powder sample producing several useful results:

- Normalised Basic Flow Energy (NBFE): The total flow energy of the downward stroke of the 7th run cycle. This gives an indication of the powders flow under compression (from the blade) and restriction (from the cylinder walls and bottom). This figure is normalised to account for the weight of powder in the test volume.
- Stability index (SI): The ratio between NBFE on the 1st and 7th test cycle. This gives an indication of whether the powders flowability has changed throughout the test.
- Specific Energy (SE): The equivalent to NBFE but measured on the upward test cycle. This gives a measure of the powders unconfined flow and its level of cohesion and mechanical interlocking forces.

During FT4 testing each powder was tested four separate times with the cylinder being emptied, cleaned and filled with a new sample of powder each time.

3.1.2.4 Rotating Powder Analysis (RPA)

Rotating powder analysis was conducted using a Revolution Powder Analyzer from Mercury Scientific. The RPA consists of a cylindrical drum with glass sides which allow the 'cross section' of the powder inside to be viewed, illustrated in Figure 18 (Pleass & Jothi, 2018). For the test a fixed volume of powder was loaded into the drum and rotated at 0.3 RPM. During the tests the integrated digital camera observes the powder and records data about when the free surface of the powder collapses in an 'avalanche'. Each test runs for 150 avalanches and is repeated 3 times for each powder.

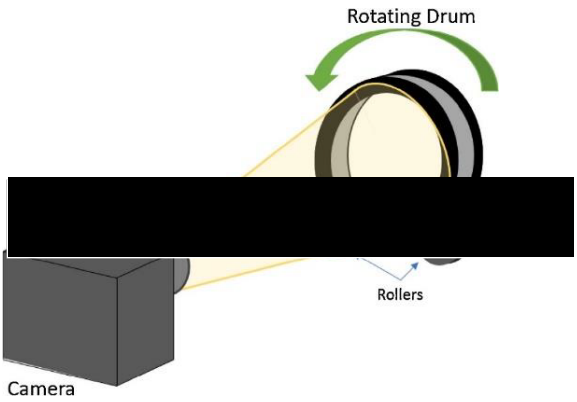

Figure 18 – Schematic illustration of the equipment set up to perform revolution powder analysis (RPA) (Pleass & Jothi, 2018).

The test produces several useful metrics of powder flowability:

- Avalanche and rest angle: The angle between horizontal and the linear best fit of the powder free surface immediately before or after an avalanche. The more flowable a powder is, the lower these angles will be as a less severe angle can be supported by the powder.
- Time between avalanches: The time, in seconds, between consecutive avalanches.
- Surface fractal (avalanche and rest): This is a measure of the linearity or 'smoothness' of the powder free surface. Calculated as the ratio between the linear distance between the top and bottom of the slope and the actual distance over the powder surface, illustrated in Figure 19(Pleass & Jothi, 2018)

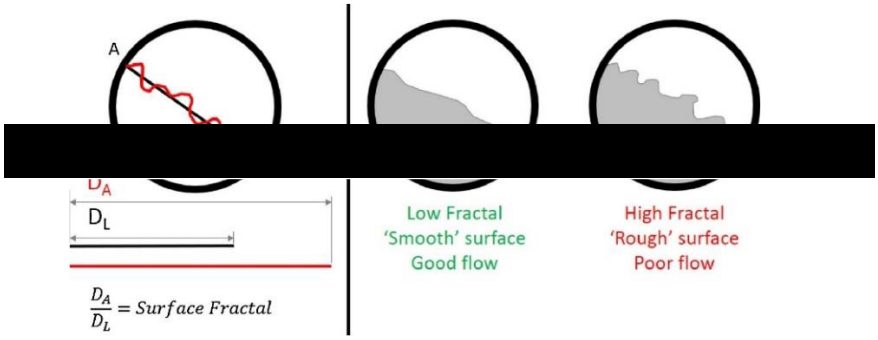

Figure 19 - Schematic illustration of surface fractal calculation. The illustrations shows how a powder surface might display different surface fractal values (Pleass & Jothi, 2018).

3.1.3 Coupon Manufacturing

To assess processability and the quality of material produced, a Trumpf TruPrint 1000 SLM machine was used to manufacture coupons with the three powders. The processability of the

powders during the SLM process was qualitatively assessed by observing the first 15 layers of powder deposition.

The quality of manufactured material was measured from the coupons produced. To account for any differences between the powders, 3 coupons were produced from each with different levels of energy input. Coupons were cut and polished to reveal cross sections of the central section of the coupon. These cross sections were imaged using an optical microscope to measure the porosity levels before being tested for hardness to determine mechanical properties. Porosity can be more accurately measured using equipment such as a Helium Pycnometer or an Archimedes balance, however these methods do not provide information on the morphology or distribution of the porosity, which was of more interest to this investigation.

The hardness test conducted for these samples was Rockwell C, this differs from other samples in this work as a whole. The reason for this difference is that it was desired to place the highest load possible, 150 kgf, on these samples in order to get the best indication of macroscopic properties throughout the materials. 9 indentations were made across the cross sections of materials avoiding edges.

3.2 The influence of Selective Laser Melting Process Parameters on Microstructural and Mechanical Properties of IN625

3.2.1 Coupon Manufacture

Coupons for this portion of the work were manufactured using an EOS M290 DMLS machine. All coupons were manufactured as 15mm cubes from IN625 powder (P1) in the previous chapter.

3.2.2 Process parameters

The investigation of process parameters is divided into two sections, contour parameters and in-skin parameters. These are the parameters used to can the outer edge of the bulk material of the samples respectively.

Throughout this work, where process parameters are given the have been encoded into levels, either 1, 2, 3, 4, 5 or low, medium and high.

3.2.2.1 Contour Parameters

Contour parameters were investigated with the aim of improving the surface finish of the material directly from the machine. The process parameters investigated are given below in Table 7. For each set of parameters, the area energy density of the parameters is calculated and given in J/mm^2. This provided for reference but is just a result of the parameters selected rather than a parameter input into the machine.

*Table 7 - Details of contour process parameters used to produce coupons for the investigation of contour parameters and surface roughness. *Area energy density of the coupons is provided for reference only and is not a set process parameter*

#	Laser Power	Scan Speed	*Area Energy Density (J/mm²)*
S1	3	5	*5*
S2	3	5	*5*
S3	2	1	*25*
S4	1	4	*5*
S5	3	5	*5*
S6	1	4	*5*
S7	2	1	*25*
S8	3	3	*15*
S9	5	2	*35*
S10	2	1	*25*
S11	4	1	*30*

3.2.2.2 In-skin Process parameters

The investigation of the in-skin process parameters was more in depth with the need to consider a greater number of variables. For these coupons a Tagchi Design of Experiments (DOE) approach was employed. Taguchi DOE is a form of fractional factorial experimental design where many factors can be tested with a smaller number of tests by accepting some confounding of interactions. The details of the process parameters selected are given below in Table 8 with process parameters set at one of three levels, low, medium or high (1, 2, 3 respectively). The Taguchi Orthogonal array was constructed using the statistical analysis software Minitab.

Due to the constraints of the material and machine time available, it was not possible to test all possible processing parameters. One significant omission was the investigation of different layer thicknesses. Thicker or thinner layer can have a significant effect on the productivity of the process as well as layer to layer fusion.

*Table 8 - Table showing the process parameter level selections for the initial L18 Taguchi DOE array. Levels low, medium and high are coded to 1, 2, 3 respectively. * Energy density column is included for reference only; this was not a process parameter included in the L18 array.*

#	Exposure Strategy	Laser Power (W)	Scan Speed (mm/s)	Hatching Distance (mm)	*Energy Density * (J/mm³)*
M1	1	1	1	1	*75*
M2	1	1	2	2	*30*
M3	1	1	3	3	*15*
M4	1	2	1	1	*100*
M5	1	2	2	2	*40*
M6	1	2	3	3	*20*
M7	1	3	1	2	*65*
M8	1	3	2	3	*35*
M9	1	3	3	1	*85*
M10	2	1	1	3	*25*
M11	2	1	2	1	*60*
M12	2	1	3	2	*25*
M13	2	2	1	2	*50*
M14	2	2	2	3	*30*
M15	2	2	3	1	*65*
M16	2	3	1	3	*45*
M17	2	3	2	1	*105*
M18	2	3	3	2	*45*

Following this initial Taguchi DOE investigation of the process parameters an additional 7 coupons were manufactured for microstructural investigation to further investigate the individual process parameters. The details of these coupons are given below in Table 9.

*Table 9 - Table giving details of 7 additional coupons produced for further microstructural investigation of individual process parameters. *Energy density is included for reference only and was not a process parameter set for these coupons*

#	Exposure Strategy	Laser Power (W)	Scan Speed (mm/s)	Hatching Distance (mm)	*Energy Density* (J/mm³)*
M19	1	1	2	1	*120*
M20	1	2	2	1	*140*
M21	1	3	3	1	*110*
M22	2	3	3	1	*110*
M23	2	2	1	2	*70*
M24	1	3	2	1	*170*
M25	1	3	1	1	*260*

3.2.3 Coupon Analysis

3.2.3.1 Porosity Measurement

As with the previous chapter, measurements of porosity were conducted using an optical microscope. Several images were taken and stitched together with the level of porosity being determined using a simple Python script to count the number of black pixels compared to white.

3.2.3.2 Surface roughness measurement

Surface roughness measurements were collected using a contact profilometer with a diamond tipped stylus. The stylus was drawn 10 mm in the build direction over the side of the manufactured coupon. The height difference along this distance is logged and the arithmetic mean deviation from the mean line of the surface is calculated to give a surface roughness measurement in µm, this is the most common type of surface roughness measurement, R_a. Two perpendicular sides of each coupon were measured with 5 profiles being taken from each. The results were combined to obtain a mean roughness value for each coupon.

This testing was only applied to coupons S1 – S11, Table 7 for the analysis of the influence of the contour parameters.

3.2.3.3 Hardness Testing

As with the previous chapter Rockwell C hardness with a 150 kgf load was used to characterise the mechanical properties of the samples. As previously, this method was selected for this analysis as it applies the largest load possible, giving a good indication of the macroscopic properties of the material rather than just the surface region. This was important in order to see the effects of porosity and defects within the material.

3.2.3.4 *Microstructural Characterisation*

Coupons M19 -M25 were manufactured to assess the microstructural effects of the process parameters. These coupons were sliced to reveal the ZX (side) plane of the material, prepared and characterised using scanning electron microscopy (SEM), energy dispersive spectroscopy (EDS) and electron backscatter diffraction (EBSD).

These techniques allow for the microstructure of the material to be viewed as well as quantitative measurements of features such as grain size, elongation and chemical segregation. In each case where grain size or elongation is measured, the results are collected macroscopically, incorporating over 3000 grains in the data to get a statistically significant result.

Where appropriate, samples with significant findings were remanufactured and repeat samples were characterised to confirm that the process and observations were reliable and repeatable.

3.3 The Influence of Post Process Heat Treatments on Microstructure and Mechanical Properties.

3.3.1 Coupon Preparation

For this investigation, cylindrical samples were manufactured from IN718 using an EOS M290 DMLS SLM machine. All samples were produced in a single build with the same process parameters applied to all.

These cylindrical coupons were then cut into semi cylindrical sections to reveal a ~10mm square section of the XZ plane of the sample which could then be heat treated and/or mounted and polished for analysis. This is illustrated in Figure 20 showing both a schematic illustration of the cutting procedure and an example of the original SLM fabricated cylinder, cut specimens and mounted specimens.

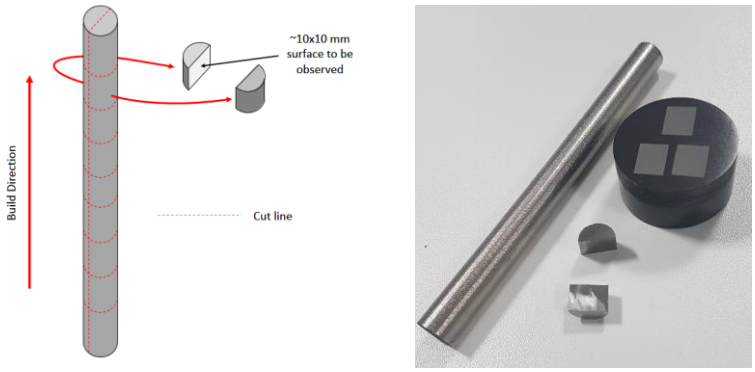

Figure 20 – (Left) Schematic illustration showing coupons being cut from a cylindrical specimen to expose the desired face. Right) Image of cylindrical specimen, cut coupons and full polished sample holder.

3.3.2 Heat Treatment

3.3.2.1 Heating and Coupon Insertion

All heat treatments, homogenisation and aging, were performed using a Carbolite Tube furnace with the treatments being conducted in an inert Argon gas atmosphere to minimise the risk of oxidation of the material. Due to the equipment available and the cooling required for the samples, some level of oxygen exposure while at high temperatures was unavoidable. Minimising contact time combined with removing the top layer of the sample during sample polishing and preparation was deemed sufficient to remove any surface oxidation (verified using EDS scanning of the treated samples). Prior to sample insertion the furnace was purged for 5 minutes with Argon after which the flow was reduced to 4L/min and maintained throughout the treatment. For every treatment the furnace was brought to temperature and verified using a thermocouple inside the furnace. Samples were always inserted into the furnace at the correct temperature.

3.3.2.2 Homogenisation Treatments

Different homogenisation treatments were applied to the material in order to establish the materials response. The different profiles are given below in Table 10. In all cases the cooling selected was a water quench (WQ). This was done to rapidly cool the samples and freeze the microstructure with no secondary precipitation or evolution taking place. The temperatures were selected to cover a broad range of temperatures from below the δ solvus temperature up to much higher temperatures certain to dissolve all phases present. The intervals between temperatures are not even, with smaller gaps providing increased resolution in the area most likely to be of interest (900 – 1060 ^{o}C) while still providing some information about higher temperatures. Homogenisation treatments were carried out for 1 hour each with a small subset of temperatures selected for additional 2 hour treatments to assess the time dependency of the treatment.

Highlighted in Table 10 in the 'Repeat' column are the treatments which were repeated across different coupons to study reliability. Due to material availability, it was not possible to repeat all treatments. To mitigate for this, and to qualify the repeatability of the treatments, as wide a range of temperatures as possible was repeated with particular focus being placed on the three treatments deemed most important to the conclusions of the work.

Table 10 – Details of homogenisation heat treatments applied as part of this investigation. All treatments feature a water quench (WQ) cooling. The repeat column indicates which of these tests were repeated across different coupons.

Temperature (°C)	Dwell Time (Hours)	Cooling	Repeat
900	1	WQ	
930			
950			
980			Yes
1000			
1030			Yes
1050			Yes
1060			Yes
1100			Yes
1180			Yes
1250			Yes
980	2		
1060			
1100			
1180			
1250			

3.3.2.3 Aging treatment

To conduct aging of the material a standard duplex aging procedure was applied, given in Table 11. The two temperatures, 720 and 625 °C are chosen to precipitate the strengthening phases γ'' and γ' respectively. The furnace cooling between the two temperatures is specified to cool in roughly 2 hours, bringing the total treatment time to 18 hours. The furnace was programmed and verified to be able to achieve this precise cooling rate by slowly decreasing the power of the heating elements. The standard aging procedure was applied to minimise the number of variables being investigated, with the focus of the study being on optimising the homogenisation treatment for SLM IN718 material. The standard treatment should be suitable for correctly homogenised SLM material as the material should be returned to a homogenous condition, like that of conventionally manufactured material.

Table 11 – Details of the duplex aging treatment applied to the SLM IN718 coupons.

Temperature 1 (°C)	Time (Hours)	Cooling	Temperature 2 (°C)	Time (Hours)	Cooling
720	8	FC (0.8 °C/min)	625	8	AC

Once again, due to material availability, it was not possible to repeat all the aging treatments. In total, four material conditions were selected for repeat testing. Repeats consisted of material from different coupons being homogenised and then aged again, with the results compared to show repeatability of the results. The samples selected are given in Table 12 and represent a repeat of directly aged as fabricated (AF) material, to confirm the baseline material performance, along with the three most promising homogenisation treatments selected based on the initial results.

Table 12 – Details of samples selected for repeat testing of their aging response. In each case samples from different manufactured material were put through the same heat treatment route to confirm the repeatability of the materials response.

Homogenisation Temperature (°C)	Dwell (Hours)
AF	-
1030	1
1050	1
1060	1

3.3.3 Material Characterisation

The microstructural evolution of the material in the post heat treatment condition (post homogenisation or post aging) homogenised condition was assessed using microscopy techniques (SEM, EDS and EBSD) of mounted and polished samples. This gave visual information about the grain structure and segregation/precipitates as well as some quantitative measurements of grain size and misorientation angles.

The mechanical properties of the samples were also measured using a Vickers hardness test. Due to material availability and size/shape, this was the best method to get an indication of properties and the effect of heat treatments. Ten indents were made in each sample and where possible, repeated samples were tested to confirm the results.

3.4 Investigation of Microstructural Evolution of Selective Laser Melted IN718 During High Temperature Homogenisation Treatments at 1250 °C

This investigation was carried out as an extension of the initial homogenisation investigation based on interesting observations. Coupons were taken from those manufactured in the same build as the initial investigation.

3.4.1 Homogenisation Treatment

The process of heat treatment was identical to the previous section 3.3.2 focusing on smaller increments of time at 1250 °C, detailed below in Table 13, note that the dwell times are now given in minutes.

There were no repeat tests of individual treatments in this investigation however the results of incrementally increasing dwell time showed consistent behaviour indicating good repeatability.

Table 13- Details of homogenisation heat treatments conducted for investigation of material behaviour and evolution during high homogenisation heat treatments. 1250 °C was selected based on the outcome of the previous set of heat treatments.

Temperature (°C)	Dwell (Minutes)	Cooling
1250	7.5	WQ
	15	
	30	
	45	
	60	
	120	

3.4.2 Material Characterisation

Material characterisation focussed on the microstructural evolution taking place using similar microscopy techniques to section 3.3. The major difference in the characterisation performed was the use of quasi in-situ EBSD (QIEBSD).

3.4.2.1 QIEBSD

QUEBSD is a process through which it is possible to view the grain structure changes taking place in a specific region of the material during heat treatment. It involves performing an EBSD scan if the exact same region of material both before and after the treatment is applied.

This is accomplished by polishing a sample, without mounting, in the as fabricated condition and creating a registration mark using a small Vickers hardness indent. And EBSD scan is then made,

using the hardness indent as a reference point to locate the same section of material (the scan needs to be performed far enough away from the indent so that no strain in the material is present to distort the results). The sample is then heat treated and repolished, taking care to remove as little material as possible. A second EBSD scan is performed of the same region and the two can be overlaid and compared.

This process was conducted on the 7.5 minute treated sample from Table 13 to capture the material in the process of its major microstructural evolution.

3.5 Summary

This chapter outlines the experimental method followed during investigation in this work. In some cases, the availability of materials or equipment has restricted the number of repeat experiments carried out however the test which are repeated should be appropriate to ensure that the material and results produced in this work are repeatable and representative of the true behaviour of the material. The repeat tests carried out focus on first confirming the repeatability of the SLM manufacturing process being used and then confirming any key results central to the outcomes of the work.

4 Results and Discussion

4.1 Investigation of Powder Characteristics and Metrology Methods for Application in Selective Laser Melting

4.1.1 Powder Processability

Processability of the powders was determined by observing how well they distributed layers on the powder bed. This was accompanied by general observation of ease of handling throughout testing.

The images in Figure 21 show how the powders behaved during deposition over the build plate. Images are from the 1st, 7th and 15th layers. It is difficult to make any distinction between P1 and P3, both can be seen to successfully deposit uniform layers of powder over the build plate with little qualitative difference visible between A) and C), D) or F) and G) or I). P2 on the other hand can be clearly seen to be unusable. The powder fails to deposit onto the build plate over any of the first 15 layers. The only difference between B), E) and I) being the powder trapped around the edge of the build plate where the powder is physically trapped due to the lowering of the build pate with each layer.

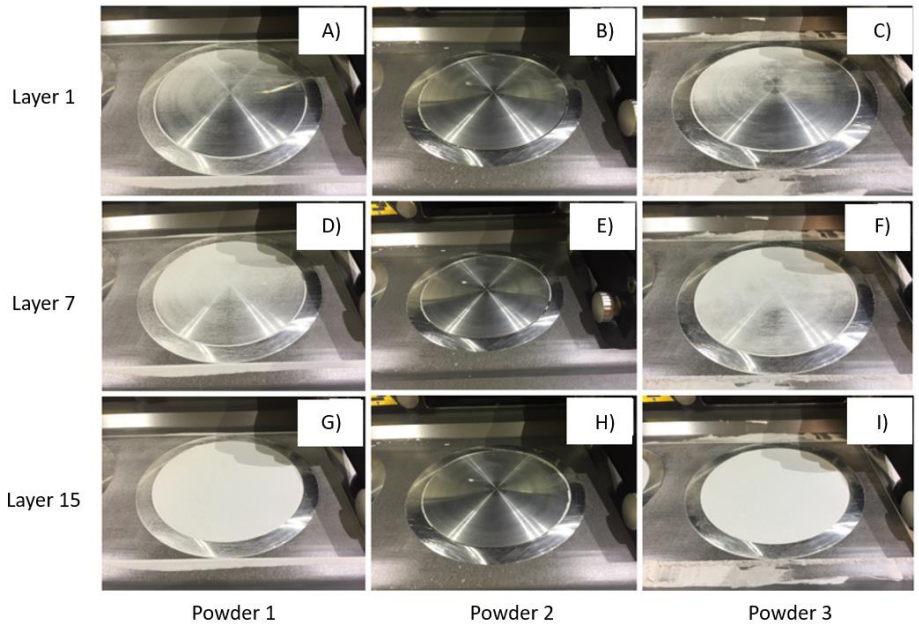

Figure 21 - Layer deposition during the first 15 layers of the SLM process. Powder 1, A), D), G). Powder 2 B), E), H). Powder 2 C), F), I). layer 1, 7 and 15 respectively. These images show the processability of the powders during the SLM process. Powder 2 fails to deposit a layer of powder on the build plate altogether. Powder 2 is not processable by selective laser melting.

This recoating and layer distribution process is an essential part of the SLM process, the quality of layers directly corresponds to the quality of parts produced. Any gaps in the powder bed will correspond to gaps in the finished material. From these results It can be concluded that there is

no significant difference in the processability of P1 and P3, both depositing uniform layers whereas P2 was entirely impossible to process.

4.1.1.1 Processability of P1 and P3

Qualitatively there is no significant difference which can be detected between these two powders in Figure 21. For a quantitative comparison, the quality of the manufactured coupons from these powders is considered.

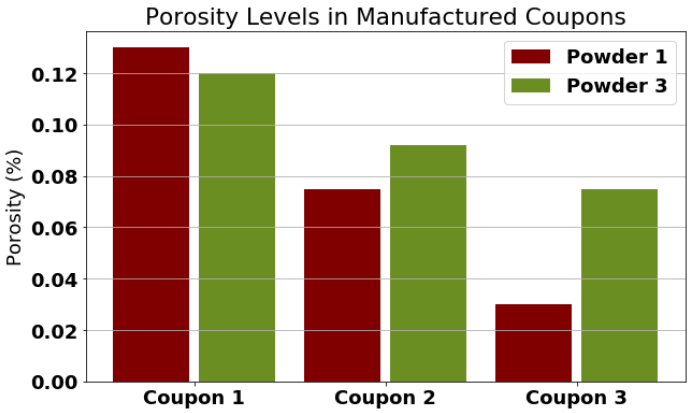

Figure 22 – Graph showing the porosity of coupons manufactured using Powder 1 and Powder 3. There is a general decrease in the porosity levels measured in the coupons from 1 to 3. There is no consistent trend for either powder to produce lower porosity coupons although powder 1 achieves the lowest porosity from all the coupons.

The porosity results in Figure 22 indicate that both powders were successful in producing almost fully dense material with no significant difference between them. The results also show that the increase in energy input from the process parameters, incrementally from coupons 1 – 3 had a far greater effect on the manufactured material than the powders themselves.

Figure 23 – Plot showing the measured hardness (Rockwell C) of the test coupons produced using both powders. These results show that the hardness does not vary significantly between the coupons manufactured. Powder 1 produces consistently harder material than powder 3 in all the coupons.

Hardness tests performed on the coupons revealed no significant difference between the two powders. Assessing P1 and P3 for their SLM processibility reveals that there is no significant difference between them which is large enough to yield a difference in material after the additional potential variables of the SLM process.

4.1.1.2 Processability of P2

The processability of P2 was found to be very poor. As images B, E and H in Figure 21 indicate, it was not possible to deposit any layers of this powder on the build plate. To confirm these results a further test was carried out to confirm that all over parts of the recoating process were operating correctly. The recoating process was stopped halfway, and the recoating arm was moved back to its home position. This test, pictured in Figure 24, showed that the recoating arm was picking up enough powder from the hopper for each layer. The problem is attributed entirely to the powder itself.

Figure 24 – Image demonstrating the behaviour of powder 2 during SLM layer deposition. Recoating direction right to left. This image shows the cohesion of the powder observed during characterisation and how this effects layer deposition. This cohesion prevents any particles from flowing under the recoating arm and being deposited on the build plate.

Figure 24 shows the cohesive tendency of P2. The powder particles stick together strongly and form agglomerations, preventing any particles from flowing under the recoating blade and becoming deposited on the build plate. The sheer sided walls of the line of powder pictured in Figure 24 show that the cohesive forces within the powder are stronger than the weight force due to gravity acting on the individual powder particles, preventing them from falling or flowing out of shape.

Since P2 is unable to deposit any powder material onto the build plate it is not possible to perform any SLM process successfully and it is therefore not processable. This is a clear and extreme demonstration of how powder characteristics can have a significant influence on the SLM process and why powder characterisation is necessary.

4.1.1.3 Mechanism of Powder Processability

From the previous discussion it can be concluded that P1 and P3 possess desirable characteristics for SLM processability while P2 does not. The mechanism responsible for this difference can be traced back to the characteristics of P2.

A powder can be measured to behave differently depending on the conditions under which it is tested (Clayton et al., 2015; Krantz et al., 2009). Although the behaviour of the powder may change, the root cause is always the same, the morphology of the powder particles. In section 2.4.3.1 the many different types of forces which can contribute to a powder flowability were discussed, friction, interlocking, interparticle forces and liquid bridging. When applied to the powders in this study several of these forces can be negated. The powders were all dried prior to testing and stored in airtight containers, this removes the influence of liquid bridging. The powders are all gas atomised and should have a predominantly spherical and uniform morphology. This was confirmed with SEM observations of the powders in Figure 25. This removes the chances mechanical interlocking and should provide a roughly equal contribution of friction. This leaves interparticle forces as the only remaining variable.

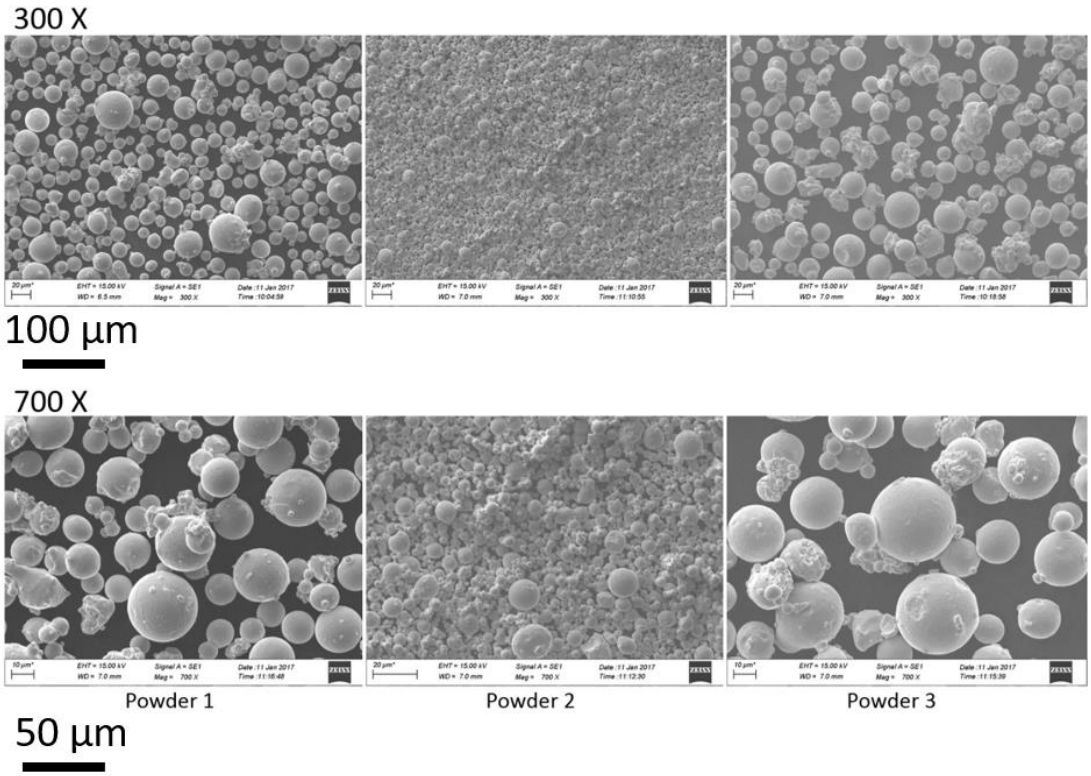

Figure 25 – SEM images of the three powders at low, 300X and high 700X magnification. These images show a qualitative comparison of the different powders making the differences in size between them clear. All powders are spherical with a small number of satellite particles.

The interparticle forces of interest here are Van der Waals forces which result from the atoms that make up the material altering their electronic configuration when they come into close proximity to each other. The rearrangement of electrons causes the molecule to become more negatively charged on one side, and more positively charged on the other. This leads to an overall di-pole effect on the powder particle. This happens in all the powder particles and results in attractive forces between them. This attractive force is relatively weak.

As the size of a powder particle increases, its weight increases, proportional to the cube of its radius (r^3), assuming a spherical particle. This increase in weight force quickly becomes much larger than the attractive Vander Waals forces. Van Der Waals forces are reported to only be a significant in powder particles up to 10µm (Feng & Hays, 2003b; Hamaker, 1937; Visser, 1989), above this size the weight of the particle can easily overcome the attractive force.

This explanation fits well with the measured powder characteristics of P2 as well as the observed behaviour. The PSD of the powders was given in Table 6 and P2 can be seen to have a d90 measurement <10 µm. This means that almost all of the particles present are small enough to strongly feel the effects of the Van Der Waals forces. The behaviour of P2 also clearly demonstrates the presence of strong cohesive forces, not only during layer deposition Figure 24, but also during different powder metrology methods in the following section 4.1.2.2.

This is the mechanism responsible for the difference in behaviour of P2. In P1 and P3 where particles are much larger, with d10 > 10 µm, the flowability of the particles is improved as their weight force is large enough to render the Van Der Waals forces insignificant.

4.1.2 Powder Rheology Methods

Following the assessment of the manufactured material quality and the layer deposition performance of the powders, a discussion can be made to consider the different powder metrology methods used, and their suitability for SLM powders. Where appropriate this discussion will also cover practical limitations or problems encountered during testing.

4.1.2.1 Powder Morphology

The assessment of the three powders processability revealed the importance of particle size distribution (PSD) with respect to determining the significance of inter particle Van der Waals forces. As has already been observed and discussed, this effect diminishes as the powder particles get larger and above the ~10 µm threshold. Another potential way in which the PSD of the powder is observed to affect the powders behaviour is in relation to the random close packing (RCP).

RCP dictates the packing density which the powder is able to achieve. The RCP or packing density dictates the density and uniformity of each build layer during manufacturing, with the potential to introduce defects or porosity into the build.

The mathematical theory behind PSD and its influence on RCP has been studied both experimentally and through simulation. It is reported that the greatest influencing factor is dispersity, Đ, calculated in Equation 7. A higher calculated dispersity means a greater range of particle sizes present, where smaller particles can fill the gaps left between larger particles thus increasing the packing density, illustrated in Figure 26. Another influencing factor on RCP is the skew of the PSD with more positively skewed (greater number of larger particles) mixtures with a given Đ achieving better packing density (Desmond & Weeks, 2014).

Equation 7 - Equation to calculate the dispersity (Đ) of a powder. Radius of particles = r

$$Đ = \frac{\sigma_r}{\bar{r}}$$

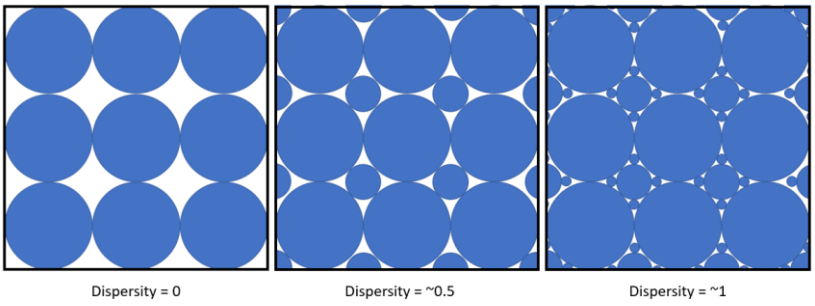

Figure 26 – Schematic Illustration of the effect of dispersity on RCP of uniform spheres. As dispersity increased, the theoretical maximum packing density increases.

To compare this theoretical effect to the observations made during practical testing the dispersity of the three powders are calculated below in Table 14. From this we can see that P1 and P2 have a greater dispersity value than P3. This difference is reflected in the results of tap density testing,

	Mean Radius (µm)	Standard Deviation	Dispersity
Powder 1	35.95	15.25	0.42
Powder 2	7.06	2.90	0.41
Powder 3	34.20	10.34	0.30

Table 15, where both bulk and tapped densities give a measure of the powders ability to pack together under its own weight and with mechanical agitation respectively. In both bulk and tapped density P3 is observed to achieve lower densities than P1, demonstrating its lesser ability to RCP.

Table 14 - Mean and standard deviation of radius calculated from measured PSD measurement using laser diffraction and the resulting calculated dispersity of the three powders.

	Mean Radius (µm)	Standard Deviation	Dispersity
Powder 1	35.95	15.25	0.42
Powder 2	7.06	2.90	0.41
Powder 3	34.20	10.34	0.30

Table 15 - Tap density testing results of the three powders. Results for Powder 2 are not present due to the inability of this powder to perform the test.

	Density (g/cm^3)		Hausner Ratio
	Bulk	Tapped	
Powder 1	4.46	5.05	1.13
Powder 2	NA	NA	NA
Powder 3	4.12	4.85	1.18

P2 in this case is an example of how other factors present in practical experiments can prevent theoretical effects from being observed. According to the dispersity value calculated it should achieve similar RCP performance to P3. In practice this is not observed, the cohesive nature of P2 prevents the free movement of the particles, preventing them from achieving their theoretical packing density.

4.1.2.2 Powder Flowability

While the root cause of a powders flowability is its particle morphology this is not always adequate. When an existing powder is known to perform well it might be sufficient to control subsequent batches by measuring PSD and ensuring compliance however it is much hard to perform this task in the opposite direction for a new powder. Where a new powder needs to be validated it will be required to directly measure the rheological properties. Several different methods of rheological assessment of the powders were applied during this study and their suitability for the SLM process will be discussed in this section.

It has been reported that the rheological properties of a powder are not fixed, but instead vary depending on the stress state in which characterisation is performed, whether the powder is confined or free, forced to flow or not. During this discussion, each of the rheology methods tested will be likened to some stage of the SLM process to determine where its results might best be applied.

4.1.2.2.1 Carney Flow Testing

Carney flow testing is a simple method of assessing flowability, requiring minimal equipment or time to perform. The results from the three powders in this study, given in Table 16, show that only one of the powders, P1, was able to produce usable test results. Although the standard operating procedure does allow for some mechanical agitation of the funnel to encourage powders to flow, this was not able to produce steady flow in either P2 or P3, making the collection of representative data impossible.

Table 16 - Carney flow testing results of the three powders. P2 and P3 results are missing due to them being unable to perform the testing in any repeatable way. These results do not provide much useful comparative information on the three powders.

	Mean	Deviation
Powder 1	10.3 s	0.2 s
Powder 2	NA	NA
Powder 3	NA	NA

These results indicate that Carney flow is not a suitable characterisation method for SLM. Most significantly, its results do not give any indication of suitability of a powder for SLM giving only a binary 'flow' or 'no flow' assessment. These assessments themselves, as well as lacking resolution, are not a good analogue to the SLM process, characterising the perfectly processable P3 and 'no flow'.

4.1.2.2.2 FT4 Testing

FT4 testing removes a great deal of human influence from the measurement process and captured the rheological properties with much greater accuracy. In comparison to the previous methods the FT4 is also capable of measuring a much greater range of rheological properties. The test programme used in this study alone can give some indication of powder packing properties, stability, restrained and unrestrained powder flowability.

The FT4 testing method proves itself to be more robust by being able to successfully process all three powders despite their great range in properties. This is an immediate advantage over previous methods as the difference between all the powders can now be quantified.

The main results from the FT4 testing in this study are given in Figure 27 however there is additional information recorded as part of the test programme which can be useful in gathering information on the powders. An example of this is the powder mass information. All the tests are conducted using a glass tube of constant volume which is filled with powder in a repeatable manner, and differences in the powder mass contains within that volume therefore give an indication of the packing density of the powder, in the same way as bulk density in tapped density testing.

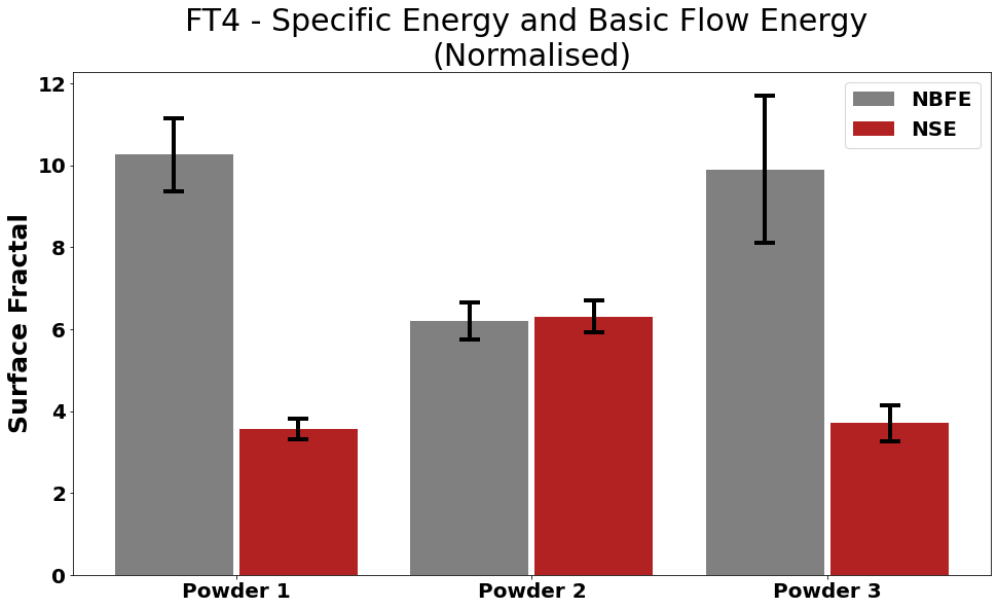

Figure 27 – Plot of normalised specific energy and basic flow energy collected from the three powders during FT4 testing. The results show an unexpected result of powder 2 appearing to be the best flowing powder, contrary to observations made up to this point.

Stability index, (SI), given in Table 17, can be thought of as analogous to HR in tapped density testing. Stability gives the ratio between the first and final (7^{th}) test cycle. Between these two cycles, the powder has been subjected to significant mechanical agitation which can allow the powder to flow to a denser packing structure, closer to its maximum or tapped density. The stability values for P1 and P3 agree with the HR measurements, with P1 outperforming P3, with 1.02 to 1.08, closer to 1.00 indicating perfect stability. The P2 stability measurement however demonstrate a shortcoming of this measure of powder flowability. P2 achieved a stability ratio of 1.00 but only because its packing was consistently poor. The cohesion of the powder particles due to Van der Waals inter particle forces was such that the mechanical agitation was not able

to increase the packing density of the particles. They can maintain their initial structure, containing large voids where no powder is present, as discussed in relation to the powder sample mass.

Table 17 – Numerical results of FT4 testing showing Powders 1 and 3 performing very similarly.

	SI	NSE (mJ/g)	NBFE (mJ/g)
Powder 1	1.02	3.56	10.26
Powder 2	1.00	6.31	6.20
Powder 3	1.08	3.71	9.90

The results presented in Figure 27 show the mean energy required to move the powder particles in either restrained (NBFE) or unrestrained, free surface (NSE) conditions. Lower required energy input indicates particles that can be made to flow more easily, a desirable property. Excluding the results for P2 (these will be discussed subsequently), there is a clear trend for NBFE results to be significantly higher than SE, this is due to the test conditions under which each measurement is conducted and gives a clear illustration of the dependence of a powder flowability on it stress state, as has been reported in (Clayton et al., 2015; Krantz et al., 2009). The NBFE measurements are taken during the downward cycle of the test. The blade forces the powder down and into the bottom surface of the glass tube. Under these conditions the bottom surface of the powder is restricted and cannot move, the powder particles all experience much greater forces and therefore friction forces are higher, and the energy required to displace them over each other is increased. Conversely, the NSE measurements are captured on the upward cycle and the top surface of the powder is unrestrained. Under these conditions only forces from the particles themselves, most notably friction, interparticle forces and any mechanical interlocking are the contributing factors to flowability.

From this understanding of the two measurements, it is possible to explain the different characteristics of the P2 results. Most notably the NBFE result, the restrained flow, is much lower than P1 or P3, indicating far superior flowability, inconsistent with any other observations up to this point. This result can be explained by referring to the mass of powder in the test volume and the voids present. These voids mean that even when measured on the downward cycle of the FT4 the powder particles have enough empty space to move into that they experience no restriction by the bottom of the glass tube. Since the powder experiences no restriction during the downward, NBFE, cycle this also explains why the result is so similar to the upward, NSE,

cycle, they are both measuring the same properties. The one property which is measured correctly is the NSE, which, as a measure of the interparticle forces. In agreement with all the previous observations and measurements, this is significantly higher than that of either P1 or P3. In order to get a true measure of the NBFE of P2 the powder loading method would need to be modified to include a compacting stage to ensure that the test volume is sufficiently free of voids. Doing so would likely produce a much higher energy requirement for the blade as it would need to contest with both the significant interparticle forces as well as the increase friction from the restricted powder.

The NSE and NBFE results for P1 and P3 show no significant difference, both recording ~3.6 and ~10 mJ/g for NSE and NBFE respectively. This result is expected, due to their similar PSD however does not provide any means to determine which powder is best suited to SLM application however as has already been discussed, both are adequate.

One inherent issue with the FT4 test procedure is that the conditions under which it assesses the powders are not easily linked to the SLM process itself, specifically the recoating process with its free surface, unforced flow of heaped powder. As has already been discussed, it is essential that powders are measured or assessed in conditions as close to their final use application as possible. Since the FT4 process is unable to achieve this as closely as other methods, it is not an ideal method for SLM application.

4.1.2.2.3 RPA Testing

The final results presented are those from revolution powder analysis, RPA. In this test the powder is in a free surface state with only the weight of the powder particles responsible for driving flow. RPA testing most closely resembles the recoating stag of the SLM process and the condition of the powder during it.

The first results presented from this method are the mean avalanche angles, Figure 28, with a lower mean angle indicating a more freely flowing powder. The results agree with all previous observations and measurements of the powders. The results clearly show the significance of the interparticle cohesive forces in P2 and how they allow the powder to achieve an avalanche angle near vertical, 86°, confirmed in the image in Figure 29. The results also display the similarity of P1 and P3, 41° and 50° respectively, while maintaining the resolution to detect a difference between them. The mechanism behind this difference in avalanche angle could be traced back to the PSD of these two powders, Table 6. P1 was found to have a larger d90 value, therefore a greater proportion of larger particles. During RPA testing the only force driving the flow or avalanche of the powder is their weight force due to gravity. The larger the particle is, the

greater this weight force will be and therefore the greater the force present to initiate the avalanche. All else being equal, as the morphology of the powder particles has been observed to be very similar, Figure 25, this will lead to avalanches occurring at lower angles in P1.

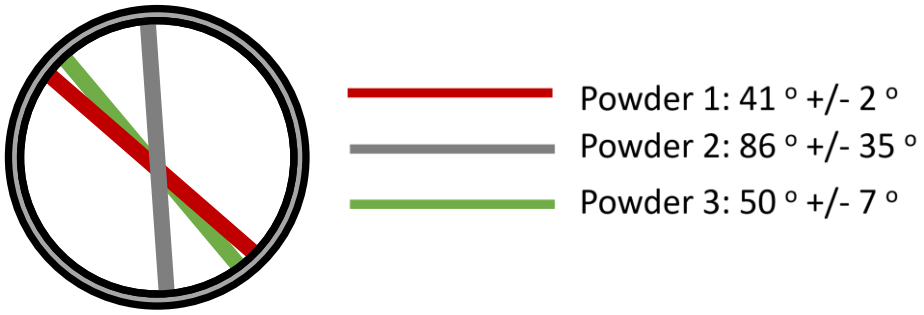

Figure 28 - Illustration of mean avalanche angles of the three powders collected during RPA testing. These results show how the cohesive nature of powder 2 negatively effects its flowability, maintaining much higher avalanche angles than either powder 1 or 3. Between powder 1 and 3, there is a small difference with powder 1 showing superior flow characteristics and a lower avalanche angle.

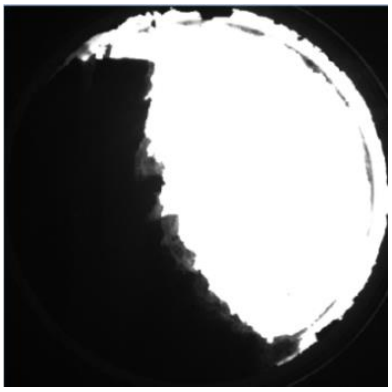

Figure 29 – Image of Powder 2 during RPA testing showing near vertical avalanche angles and nonlinear powder surface. This image confirms the results displayed in Figure 28 of an avalanche angle near 90 ° and removes any doubt that this could be a measurement error.

This single measurement of mean avalanche angle alone can replace nearly all the results from the previously tested methods while providing conditions more analogous with the target SLM process, a very important feature of any powder rheology method.

Mean avalanche angle, although very useful for SLM application, is not the only data available during RPA testing. Figure 30 shows a plot of the mean time between avalanches. This is useful data to consider as it gives an indication of the consistency of the avalanches. For example, the same mean avalanche angle could be produced by one powder repeatedly avalanching at the same angle, or another alternating between a high angle and a low angle. Looking at the time between avalanches and the deviation from the mean would reveal this difference. In Figure 30 there is a large difference between both the time and deviation between P1 and P3 with P1

having shorter times between avalanches, ~4s compared to ~6s, and a smaller deviation from this mean, +- ~2.2s compared to +- ~3s. This could be an indication of a contributing factor to P3's failure to flow consistently during carney flow testing, Table 16. The more consistent behaviour of P1, a result of its superior flow characteristics, is more desirable for the recoating stage of SLM and will likely contribute to more uniform distribution of powder as it flows under the recoating arm.

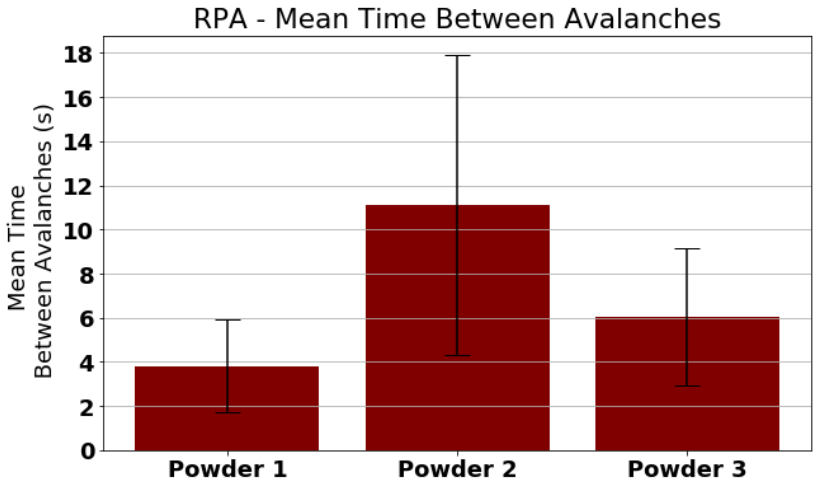

Figure 30 – Plot of mean time between avalanches of the three powders during RPA testing. The greater time between avalanches in powder 2 and the much greater variance demonstrates the inconsistency of the powder's behaviour. Powder 1 achieves the best flowability in this test with the shortest mean time and a smaller variance in the mean.

The mechanism behind the differing consistency could be attributed to the surface fractal results presented in Figure 31. The ratio between the physical distance over the powder surface and the linear distance from the top to bottom gives the fractal with smooth surfaces coming closer to linearity and a fractal of 1.

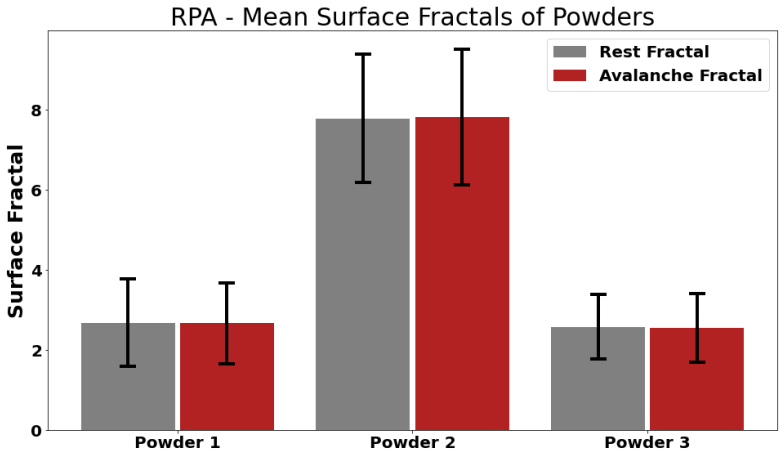

Figure 31 – Plot of mean rest and avalanche surface fractals of the three powders during RPA testing. These results show how linear the powder surface is during avalanche testing (value of 1.0 indicates perfect linearity). Powder 2 demonstrates poor flowability again with a highly irregular powder surface, imaged in Figure 29. Powder 1 is once again the best flowing powder with a powder surface closest to linearity although the avalanche results of powder 3 are similar.

The fractal measurements are taken immediately before and after an avalanche, giving avalanche or rest fractals respectively. Where roughness is present on the powder surface this introduces small sections of the surface which are at a greater angle than the overall powder slope. These small sections may collapse earlier than the powder slope as a whole, with the potential for this small avalanche to trigger the entire powder slope to avalanche, the formation of the surface roughness is random and therefor this effect is inconsistent. A smoother surface with a lower fractal is less likely to experience this phenomenon. This could account for the difference in consistency between P1 and P3 seen in Figure 30 however the results in Figure 31 show no significant difference between them. The much higher fractals measured in P2, Figure 31, and the large variation in its mean avalanche time, Figure 30, are a much clearer illustration of this.

An additional benefit of RPA testing is the number of tests which can be performed, for this study 150 avalanches were recorded for each powder sample, with three powder samples for each powder giving a total of 450 results. Compared to the manual methods such as Carney flow or tapped density where tests are time and labour intensive where only 3 tests were performed. This allows RA testing to produce a much greater sample size of results which helps to detect the minor differences between very similar powders such as P1 and P3 in this test.

4.2 The influence of Selective Laser Melting Process Parameters on Microstructural and Mechanical Properties of IN625

4.2.1 Repeatability of IN625 produced by SLM

As with any additive manufacturing process, SLM is notorious for being a variable process which can result in two different coupons built with the same processing parameters being different in their structure or properties. Since this section relies on comparing the differences between different processing parameters it is important to understand how reliable or repeatable the process is.

Due to material availability not all the investigations contained in this section were repeated, however work was done to ensure that the SLM process being used produced repeatable reliable material.

Firstly, a number of separate coupons, manufactured with the same process parameters, were compared to each other. Images from one such set of coupons is given below in Figure 32 and Figure 33. Figure 32 shows the macroscopic grain structure of the material, both coupons, produced in different builds look the same. This alone is not enough to confirm that the process is reliable however, as the columnar grain structure is typical of any SLM process. For a better idea of the whether there is any difference in thermals between the two builds a higher magnification image is used to observe the segregation distribution in the two coupons. These images are given in Figure 33. The formation of this segregation is discussed and investigated in more detail later in this section, however the similarity between the two coupons is an excellent indicator that the thermals experiences by the material is consistent between builds.

A) Sample 1 – Grain Structure

B) Sample 2 – Grain Structure

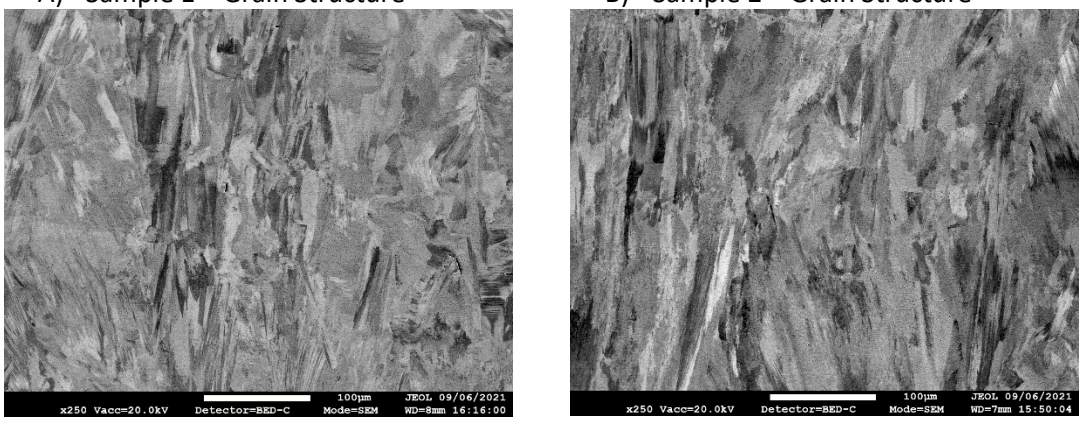

Figure 32 – Low magnification SEM images comparing material from two different coupons produced with the same processing parameters. This macroscopic view of the material reveals that the grain structure produced by the SLM process, across two different builds, is the same.

A) Sample 1 – Segregation Structure

B) Sample 2 - Segregation Structure

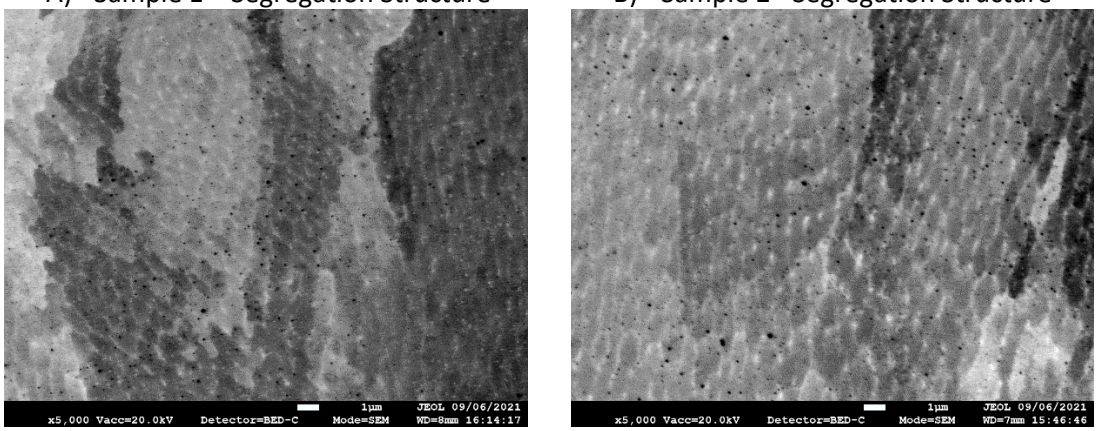

Figure 33 -High magnification SEM images of two different coupons produces with the same processing parameters. This microscopic view reveals that the formation of segregation structures in the material is the same between builds. This is a good indicator that the process thermals are well controlled and consistent.

These observations provide good evidence of the repeatability of the results obtained during this investigation however some repeat tests were still carried out. As already discussed, due to material availability it was not possible to repeat all test, however those deemed most important

to the conclusions of the work, namely those relating to the laser scan speed investigation, were remanufactured and measured from two different samples.

Additional images showing both high and low magnification SEM images of original and remanufactured, repeat coupons, from the laser scan speed investigation can be found in the appendix, section 6.1.

4.2.2 Macrostructure and Defects

Initial investigations of the process parameters were carried out with the aim of determining the role of different processing parameters in eliminating macroscale defects, such as lack of fusion, porosity and cracking. Any large defects such as these are well known to be severely detrimental to the serviceability of the material, reducing the mechanical properties and acting as sites for crack initiation and propagation leading to premature failure (S. G. Lee & Gokhale, 2006; Y. Liu et al., 2017; Q. . Wang et al., 2001; Zhao et al., 2011).

A clear link is shown in Figure 34 between the combined, volumetric energy density of the processing parameters and the porosity formed within the samples in both XY and XZ planes. Higher energy density combinations of processing parameters produce material with lower porosity content. The morphology of the porosity found within some of the samples is shown in Figure 35 in the form of an optical micrograph. An important observation of the porosity is its distribution in horizontal bands in the XZ plane, perpendicular to build direction.

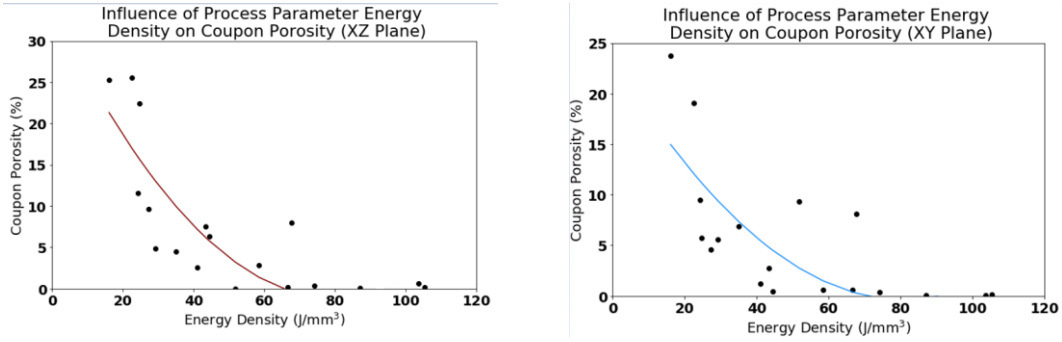

Figure 34 – Plots showing the relationship between the volumetric energy density of the processing parameters and the porosity measured in the manufactured material. Data collected from both XZ and XY planes are shown for comparison. The plots show that as energy density is increased the porosity found in the sample decreased.

The mechanism responsible for the formation of the most severe porosity is lack of fusion. During manufacturing the processing parameters are inadequate to generate a large enough melt pool. In the Z direction this means that the melt pool does not penetrate deeply enough into the substrate material to fully fuse the previously deposited material.

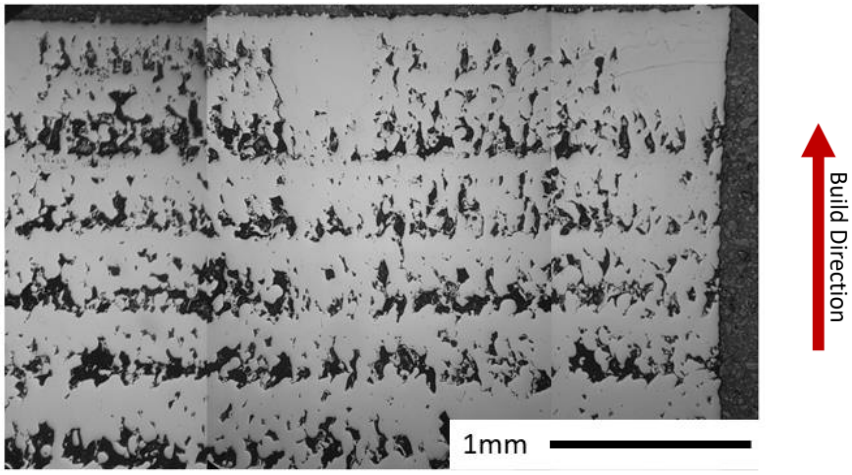

Figure 35 – High magnification image of the most severe porosity found in the coupons in the XZ plane. This reveals in more detail the morphology of the pores. They appear to show the remnants of un-melted powder particles with distinctive round edges among the irregular partially melted pores.

Considering the formation mechanism of the porosity, the importance of the energy density of the processing parameters becomes clear. The greater the energy density of the parameters, the more energy is input into the melt pool, this results in an increase in melt pool size, in length, wide and depth (Beuth & Klingbeil, 2001; Kusuma, 2016). A larger melt pool fuses a larger region of material and will reduce the amount of porosity within the material. This is the trend shown in Figure 34, where, as the volumetric energy density is increased the porosity within the sample is decreased. The energy density initially has a large effect on porosity levels where significant lack of fusion defects can be removed for significant improvements. Once the melt pool is adequate to remove these large defects the benefit of increasing energy density is diminished, eventually reaching a stable state around 0 – 0.5% porosity. In these samples the process parameters produce a melt pool large enough to fully fuse the material and the remaining porosity results from other sources, such as gas entrapment, shrinkage or non-uniform powder distribution. Changes to the processing parameters are unable to remove this final amount of porosity.

4.2.2.1 The influence of defects on material hardness

The hardness of the coupons was measured to quantify the mechanical properties. Although not as useful as tensile testing, hardness testing allows for some quantification of the mechanical properties with much smaller material coupons.

When plotted against the energy density of the processing parameters, Figure 37, hardness is found to display an identical relationship as was observed with porosity Figure 34. When plotted directly against each other, Figure 37, it becomes clear that this relationship is linear, with hardness inversely proportional to porosity. This relationship is a result of the structural

weakness introduced into the material by the porosity. Where defects are present in the material the effective cross-sectional area of the material is reduced. This increases the stress induced by loading during hardness testing and leads to greater levels of deformation and therefore a softer material. This same effect would take place during a tensile test however additional factors such as the abundance of crack initiation sites and the ease of crack propagation would also contribute to the materials deteriorated properties.

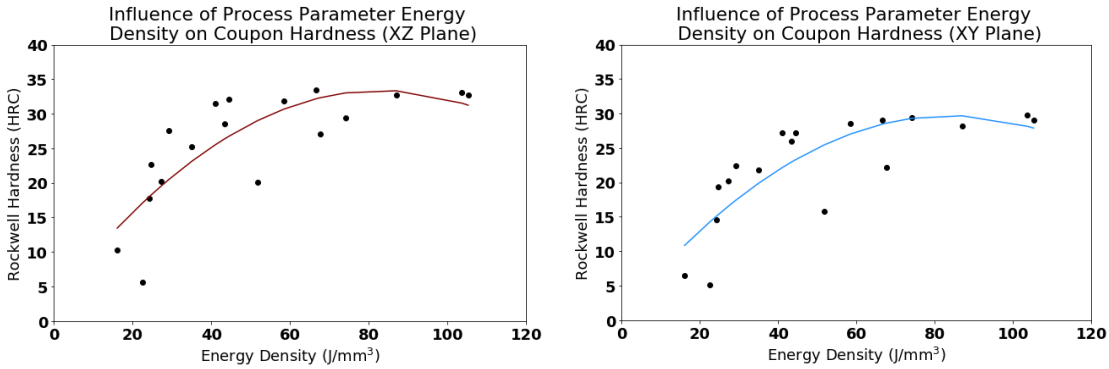

Figure 36 – Plots showing the relationship between the volumetric energy density of the processing parameters and the Rockwell C (HRC) hardness measured in the manufactured material. Data collected from both XZ and XY planes for comparison. The plots show that as energy density is increased the hardness of the coupons increases to a maximum value. There is also an observable difference between the hardness values measured in the XZ and XY planes with the XY plane being consistently softer.

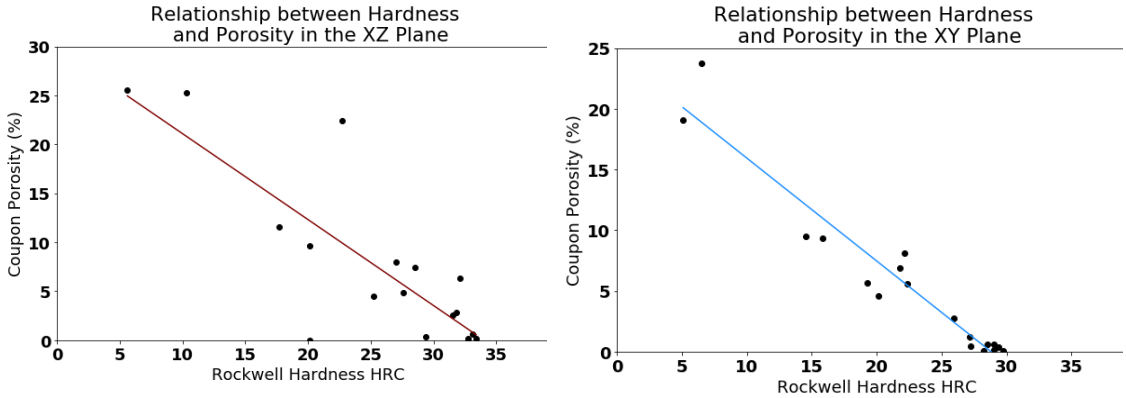

Figure 37 – Plots showing the relationship between the measured porosity and the hardness of the material in the XZ and XY planes. These plots show a strong linear relationship between hardness and porosity with decreasing porosity yielding an increasing hardness value.

A difference in hardness between the values measures from the XZ plane and the XY plane was also noted in the results in Figure 36 and Figure 37. The XZ plane was consistently harder. This is attributed to the anisotropy of both the microstructure and defects within the manufactured coupons. The defects primarily form as a result of lack of fusion between the layers due to insufficient melt pool penetration. This has been observed to create large, interconnected pores

perpendicular to the build direction, show in Figure 35. The hardness test in the XY plane will involve compressing the material in the vertical direction. Such a test direction only has a relatively thin layer of material below it with a high volume fraction of defects present. This can be visualised from Figure 35, where the hardness indenter can be imagined to apply load in the vertical axis of the image. This makes the material much less resistant to deformation and therefore softer. Tested in the XZ plane the test is instead pressing into the page in the image in Figure 35. In this direction there is much more fused material available to bear the load of the test.

4.2.3 Influence of Contour Scanning Parameters on Coupon Surface Roughness

Surface finish of the manufactured material is an important property. If the finish of the manufactured material can be improved by altering processing parameters, then some cases it may be possible to avoid the need for post processing operations or allow certain components to be manufactured which were not before possible due to the need for impossible internal post processing.

In order to alter the surface roughness of the manufactured material the contour scanning parameters were altered. Since these parameters are only responsible for fusing the outermost layer of material, they can be changed with little effect on the bulk microstructure or mechanical properties of the coupon. The results in Figure 38 show the effect of changing contour line energy density on the coupons surface roughness. It was observed that the surface roughness can be improved significantly in this manner. Roughness was measured to reduce from ~15 R_a down to ~5 R_a. The data also shows a clear optimal setting for the energy density, at 23 J/mm^2, above or below which the roughness of the surface is measured to increase.

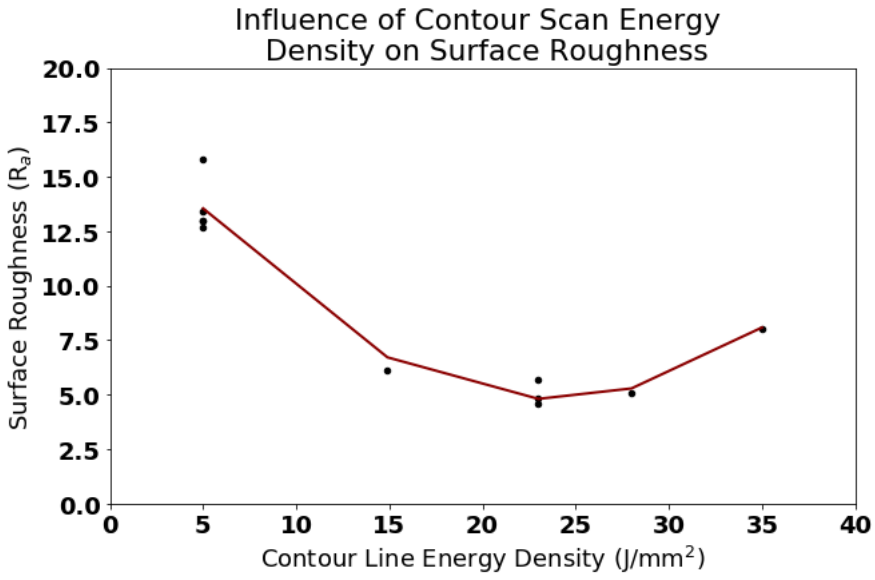

Figure 38 – Plot of showing the relationship between linear energy density and the surface roughness R_a of the manufactured material coupons. The trend displayed shows surface roughness reducing with the initial increase in energy density, 5 – 23 J.mm^2 and reaching a minimum value of roughness, ~5 R_a. When energy density is increased beyond this level the surface roughness is seen to increase again

The reason for this relationship was further investigated by observing the surfaces of a high and low roughness coupon. These images are presented in Figure 39 and reveal the cause of the roughness of the surface. The high roughness coupon, Figure 39 A) and C), is observed to be uniformly covered with partially melted powder particles. These particles are partially melted to the coupon surface, margin them positively affixed but not fully incorporated into the surface. On the low roughness coupon, Figure 39 B) and D), shows fewer of these particles, and the morphology of the particles on the surface is notably less spherical.

A) High Surface Roughness – 100x

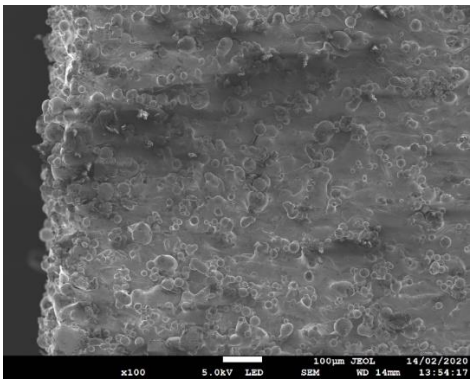

B) Low Surface Roughness – 100x

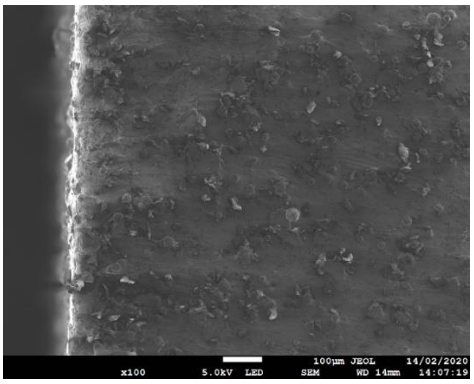

C) High Surface Roughness – 150 x

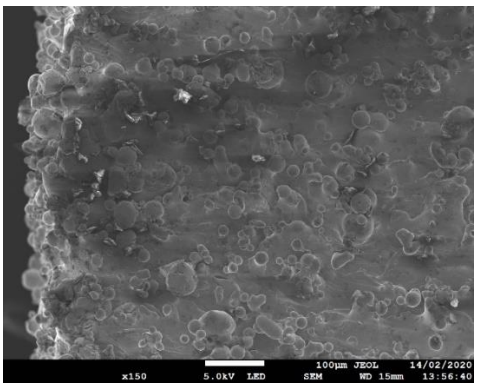

D) Low Surface Roughness – 150 x

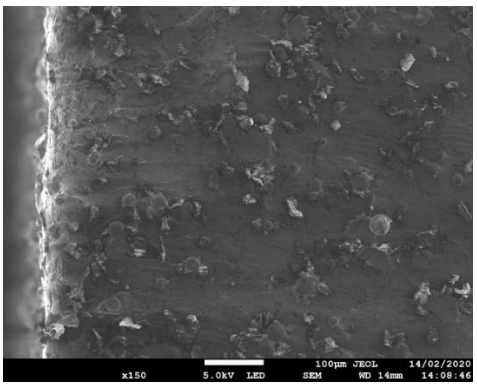

Figure 39 – Scanning electron microscope images showing the surface of two coupons, one with high surface roughness, A and C and one with low surface roughness B and D. Two magnifications are provided to show more detail on the surfaces. These images show that the roughness on the surface is comprised of almost spherical particles. The amount of these particles is reduced on the surface of the coupon with lower surface roughness.

The partial sintering of the powder particles to the high roughness coupon is due to the heat affected zone (HAZ) surrounding the melt pool of the contour scan. The melt pool temperature exceeds the melting temperature of the powder and fully melts its contents. Around the melt

pool however, there is a continuous reduction in temperature down to ambient. The result of this is that in the region immediately adjacent to the melt pool, the temperature is high enough to partially melt powder particles. These particles become partially sintered to the powder surface but are not liquid for sufficient time to conform to the surface. This results in the structure observed in Figure 39 A) and C). This partial melting of the powder particles occurs during the laser passes for the in-skin scanning, prior to the contour scan being applied. The aim of the contour scan is to remelt these partially sintered particles to conform them to the surface. This remelting must be done while avoiding the sintering of new particles from the powder bed to the coupon surface. Any new particles sintered to the surface would just recreate the original surface roughness issue.

A contour scan can achieve this because the particles are partially sintered to the part surface and therefore have superior heat conduction compared to the loose powder bed. The superior heat conduction into these partially sintered particles means that the contour scan can remelt them at much lower laser powers and energy densities than are required for the loose powder bed. The lower energy scan has a much smaller HAZ and is therefore less susceptible to partially sintering additional particles from the powder bed to the part surface, recreating the roughness.

The trend seen in Figure 38 can be explained with this mechanism. The lowest energy contour scans do not provide enough energy to remelt any of the particles, therefore the roughness is unchanged. As the energy density is increased the roughness decreases and a greater proportion of partially sintered particles are remelted and conform to the surface. When the energy density is increased beyond the optimal value, ~23 J/mm^2, the HAZ of the laser pass increases in size and starts to repeat the partial sintering process. A similar trend and smoothing effect has been reported by Koutiri et al (Koutiri et al., 2018).

The ideal contour scanning parameters are a balance between providing enough energy to remelt the partially sintered particles without creating a HAZ large enough to partially sinter new particles.

4.2.4 The influence of individual process parameters on microstructure

The link between energy density and hardness or porosity already discussed in the previous section gives an indication of the process parameters which should be selected for the best properties. Energy density is maximised by slower scan speeds, higher laser powers and shorter hatching distances.

In this section the effects of individual processing parameters will be investigated in more detail. A second set of coupons was manufactured for this investigation. As was previously observed,

once process parameters reach and adequate level to fully fuse the material, a hardness test no longer has the resolution to determine differences between coupons. To investigate the material further, microstructural characterisation was performed.

4.2.4.1 Chemical Segregation

Some degree of chemical segregation, visible as lighter, white regions in the BSD images, was observed within all the test coupons manufactured for this study. Two examples of this are shown in Figure 40 and Figure 41. The two coupons shown were selected to show the effects of process parameters on the segregation. One coupon was manufactured with a set of low energy density parameters and the other with high energy density parameters, coupons M23 and M25 respectively. The composition of these segregated regions was measured using EDS and is plotted in Figure 42, showing the segregation to be enriched with Nb in both samples.

A) – Low Energy Density (M23) B) – High Energy Density (M25)

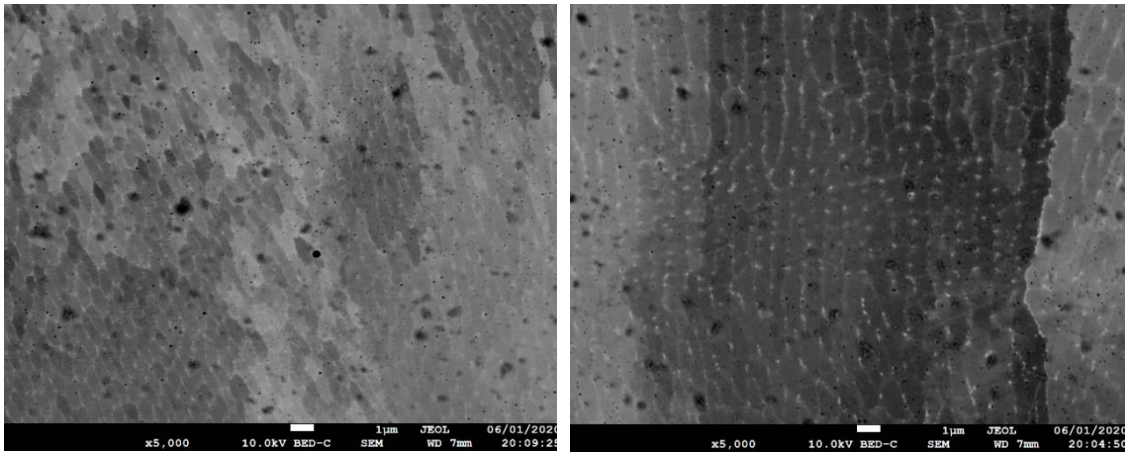

5 µm

Figure 40 – Back scattered electron images captured from test coupons manufactured with low or high energy density process parameters. The white, dendritic structure shows the location of areas of chemical segregation. The two images show differences in the morphology of the segregation which forms in each coupon. Smaller, closed cells in A) and more elongated, dendritic structure in B).

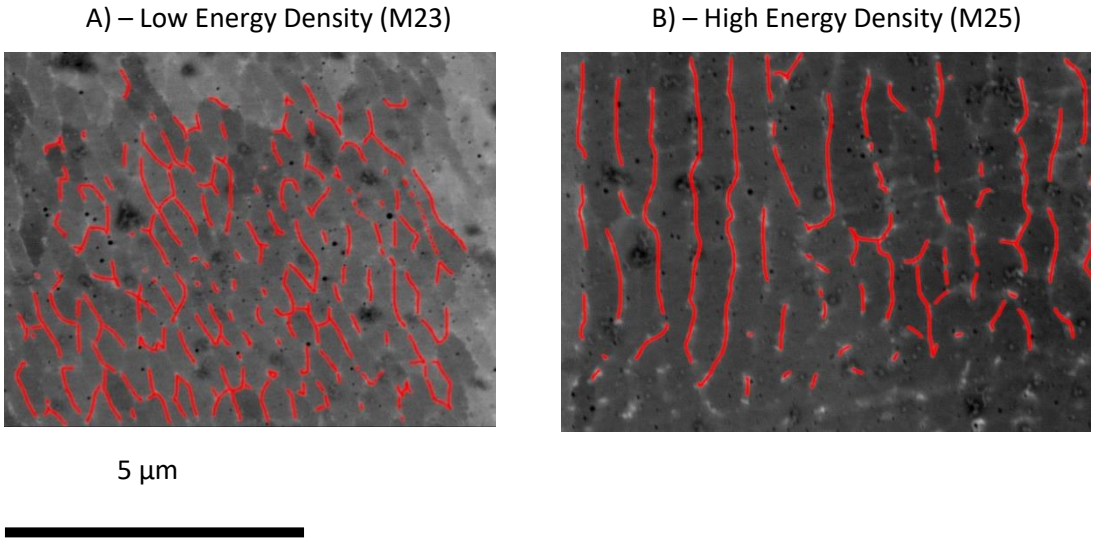

Figure 41 – Enlarged regions of the images shown in Figure 40 with the segregation structure highlighted in red to make them easily visible. These images clearly illustrate the difference in morphology of the segregation in the two samples. Low density sample A) has an interconnected network of smaller cells where the high energy density sample produces a more elongated structure in the build direction.

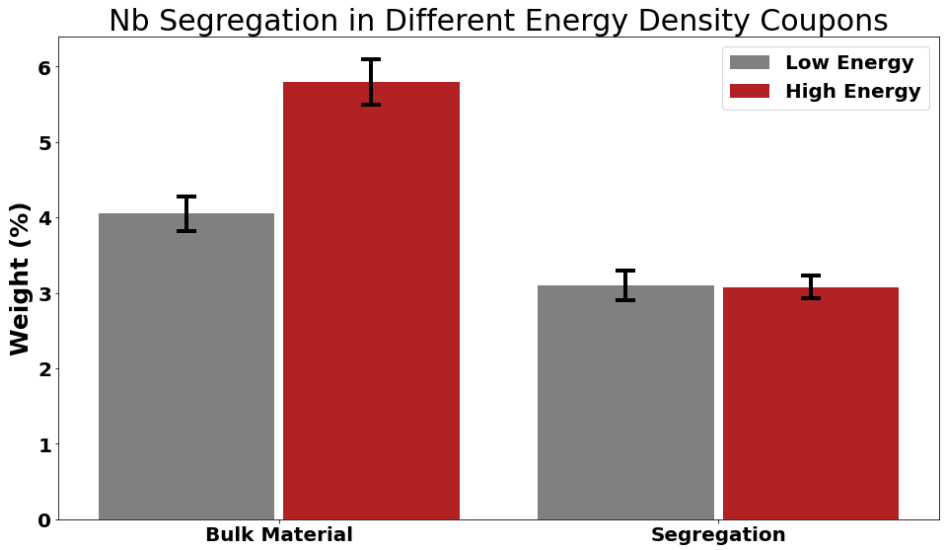

Figure 42 – EDS results comparing the chemical weight (%) content of the segregation found within the samples to the bulk, unsegregated material in the same area. These results show that in both samples, high and low energy density, the segregated regions are enriched with Nb however the enrichment is much greater in the high energy density coupon.

The two images given in Figure 40 show a clear visible difference resulting from the different processing parameters. The morphology, or structure, of the segregated regions forming in the material is very different between the two coupons. The high energy density coupon shows a large scale, elongated and build direction aligned structure whereas in the low energy density

coupon there is less interconnectivity of the segregated regions and less indication of alignment with the build direction.

Another difference between the segregation is observed in Figure 42. Although the primary segregating element, Nb, is the same across both coupons, there is a significant difference in the severity of the segregation occurring. In the low energy density coupon, the mean Nb weight present in the segregated region was only ~4%, compared to ~5.8% in the high energy density coupon. In both cases this Nb content was significantly higher than that of the bulk γ matrix material, which was measured (by the same EDS technique) to be only 3.1% in both coupons. As well as displaying the influence of the processing parameters on the segregation behaviour of the material, the results in Figure 42 also reveal that the segregation which takes place, regardless of severity, only has a short-range influence. Nb is depleted in the material immediately surrounding the segregation however the levels in the bulk material are unaffected.

The presence of Nb enriched areas of segregation in IN625 manufactured by SLM has been previously reported (Anam et al., 2014; Shuai et al., 2016). The segregation forms as a result of the poor solubility of Nb in the bulk γ matrix during solidification and cooling. This poor solubility is a result of the size difference between Nb and the other main alloying elements (Ni, Fe, Cr, etc.). As the material cools from a liquid and solidifies, the first transformation is from a liquid to a γ + liquid mixture. As the γ phase forms it preferentially rejects the larger, poorly soluble Nb atoms. This process leaves the remaining liquid, between the formed solid dendrites, enriched with Nb, which continues throughout the entire solidification process (Knorovsky et al., 1989). Once solidified, there is still the potential for the movement of atoms via diffusion however the relatively large size of Nb makes this process slow, meaning that little to no solid solute redistribution of Nb, to move towards an equilibrium distribution, occurs, following the Scheil equation (Auburtin et al., 1997; DuPont et al., 2009). This process of segregation results in the structures observed in Figure 40 and Figure 41 which show the solidification sub grains (SSG). Structure such as this are observed, do differing degrees, in all samples, more examples can be seen in the images provided in appendix section 6.1. These SSG have minimal misorientation between them but are easily distinguished by the Nb rich regions surrounding them (DuPont et al., 2009).

Understanding the mechanism for the formation for the Nb enriched regions of segregation allows for an explanation for the influence of process parameter energy density, both morphology and segregation.

The morphology of the segregated regions suggests that the SSG's in the high energy density coupon are more elongated in the build direction. Far more of the solidification sub grain boundaries (SSGB) would be aligned with the build direction rather than perpendicular to it. This would leave more segregated Nb located along these length-wise boundaries rather than width-wise ones, exactly the structure which is observed in Figure 40 and Figure 41 B). The morphology of the SSG's can be explained by the process parameter energy density. It has been reported that a higher energy density during SLM results in an increased melt pool temperature, yielding a larger melt pool, length, width and depth (Cheng & Chou, 2015; Ding et al., 2019; Hussein, Hao, Yan, & Everson, 2013; Promoppatum et al., 2017; Sadowski et al., 2016). A larger melt pool provides a larger volume of liquid and therefore the potential for larger SSG's to form. The opposite effect occurs with reduced energy density. The smaller melt pool yields shorter SSG's, giving the more cellular structure shown in Figure 40 and Figure 41 A).

Another feature of the low energy density coupon is that its segregation is not aligned perfectly with the build direction. This could be due to slight differences in heat flow direction throughout the melt pool. The boundary between the melt pool and the substrate material is semi-circular, with heat travelling outwards into the substrate. Near the edges of this melt pool the local heat flow direction, dictating the growth of the SSG's, may be different from the build direction.

The difference in segregation severity can also be explained by considering the influence of the processing parameters on the solidification process. As has already been established, higher energy densities create larger melt pools and larger SSG's. The larger melt pool, being a higher temperature and containing a greater amount of energy, takes longer to cool down. The influence of solidification and cooling rates on levels of segregation in Nb containing Ni superalloys has been reported (Chen, Lu, et al., 2016; LONG et al., 2016; Sivaprasad & Ganesh Sundara Raman, 2008; Y. C. Zhang et al., 2013) with a faster cooling rate being found to reduce the severity of segregation. The results in Figure 42, showing a greater weight % of Nb in the segregated regions within the high energy density coupons, correlate well with this. The greater energy input into this coupon leads to a slower cooling rate and increased levels of segregation.

Figure 42 also shows that the Nb content in the bulk material was the same in both high and low energy density coupons, despite the difference in severity of the segregation. This is a result of a lower extent of diffusion of the large Nb atoms. The segregation is only able to incorporate the Nb atoms in its immediate local area. Regardless of the energy density, the material does spend enough time at a sufficiently high temperature for longer range diffusion of Nb atoms to take place.

4.2.4.1.1 Influence of segregation on mechanical properties

Segregation within the material can have a significant effect on the mechanical properties of the material. Nb enriched areas can accommodate the precipitation of detrimental secondary phases such as the Ni_3Nb Laves phase. At the interface between the laves phase and the bulk γ matrix there is a point of weakness where cracks can more easily initiate or propagate. This introduction of a preferential crack path will manifest most significantly during fracturing or failure.

The morphology of the segregation can be considered first. If the segregated regions represent paths where cracks might easily propagate, due to the presence of weak interfaces with secondary phases, then the low energy density coupon should be affected more detrimentally. The segregations are interconnected and run in all directions, creating a path through the material along which a crack would be able to propagate with minimal change of direction. The high energy density coupon, with its fewer instances of interconnection of segregated regions, provides fewer of these crack paths to a crack travelling perpendicular to the build direction, which would have to traverse through bulk material in order to connect adjacent segregated regions. Cracks travelling parallel to the build direction however have a clear path to follow of almost uninterrupted segregation. This should make the mechanical properties, such as tensile strength and fracture stain, of the high energy density material highly anisotropic depending on whether the stress axis is aligned perpendicular or parallel to the build direction.

The severity of the Nb segregation is another consideration for the degradation of the mechanical properties. The greater the weight of Nb within the segregated regions, the more Nb must have been removed from the surrounding area. This lack of Nb reduces the ability of secondary strengthening phases, such as γ'' to form. In a solid solution strengthened material like IN625 this is a more minor effect than in an age hardened alloy (such as IN718). The high energy density coupon, with its more severe segregation, would suffer more from mechanical property degradation in this manner.

4.2.4.2 Grain Structure

4.2.4.2.1 General Grain Structure of SLM Material

Throughout all the microstructural investigations of the manufactured material produced with different processing parameters the same general microstructure was observed. The structure of the material is anisotropic, with significant differences between the structure viewed in the XY plane, Figure 43 A), and the XZ plane (parallel to the build direction), Figure 43 B).

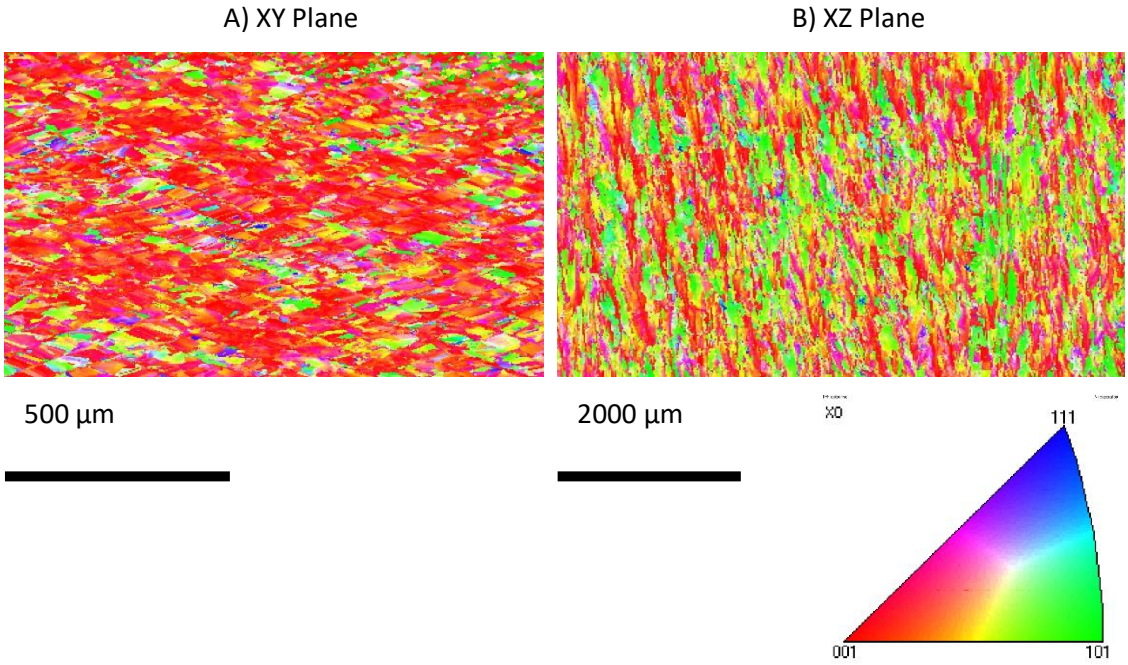

Figure 43 – IPF coloured maps (with orientations relative to the build direction, out of the page in XY plane and vertically in XZ plane) of EBSD data displaying the general characteristics of all the samples microstructures. Both XY (Top) A) and XZ (side) B) plane are shown. These images show the general microstructure observed in all the test coupons manufactured in this section. Specifics of the microstructure are seen to change however the general structure remains the same.

In the XZ plane the structure is comprised of columnar grains elongated in the build direction, running over multiple build layer heights. The XY plane appears much closer to an equiaxed structure.

This structure has been previously observed and reported in SLM manufactured material. The columnar structure visible in the XZ plane is a result of partial remelting of previously deposited material and the epitaxial dendrite growth. This allows the grains to grow over greater distances than a single build layer height (Amato et al., 2012; Anam et al., 2014; Niendorf et al., 2013; D. Zhang et al., 2018). The equiaxed structure visible when observing the material in the XY plane is the result of the truncation of these columnar grains revealing their cross-sectional area. This idea is visualised in Figure 44.

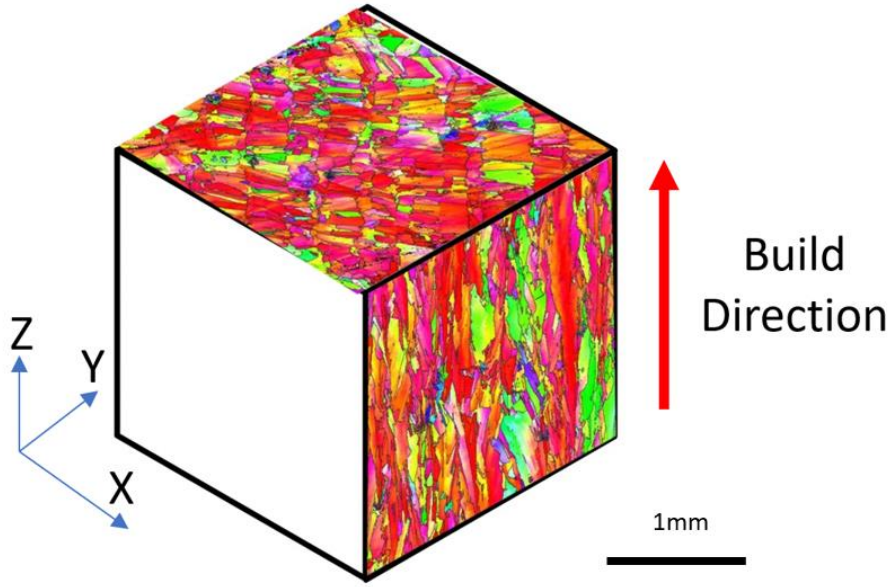

Figure 44 – Rendering of what the general microstructure observed in SLM IN625 would look like viewed in three dimensions. This image illustrates how the equiaxed grains, visible in the XY plane are a result of the truncation of the columnar grains visible in the XZ.

While different process parameters combinations did result in evolutions of the manufactured materials microstructure, which will be addressed in the following sections, the same general grain structure was present in all the samples. This indicates that, while process parameters do have an observable effect on the microstructure of SLM material, they cannot be manipulated to remove this characteristic SLM microstructure altogether.

4.2.4.2.2 Influence of Individual Processing parameters on manufactured material grain structure

The data collected for this microstructural evolution analysis is presented as a plot of mean grain diameter and mean grain aspect ratio. This data was collected from a macro scale EBSD data set collected from each coupon, covering a ~5mm^2 area of material and containing over 3000 grains. This data is preferred over images of the structure as it provides the means to quantitatively compare the structures. The size of the sample of grains collected in this manner also makes the results statistically significant and representative of the material as a whole, something which might not be possible through images alone.

In all cases the size of the main y matric grains is measured. This is done to give an indication of the macroscopic grain structure of the material. In the manufactured material, minimal levels of other phases are present, with other microscopic changes, such as to levels of Nb segregation have been discussed previously in section 4.2.4.1.

Within each processing parameter investigation, the multiple coupons were produced using the same set of processing parameters with only the individual parameter under investigation being altered between several levels.

4.2.4.2.3 Influence of Energy Density on Grain Structure

Although not an individual process parameter, the results comparing energy density provide a good starting point to examine how process parameters can influence the microstructural evolution of the manufactured material.

The results in Figure 45 show that both grain size (diameter) and elongation (aspect ratio) increase as the energy density of the parameters is increased. This can be explained by considering the effect of energy density on the material previously discussed. Higher energy density parameters input greater energy into the same unit volume, resulting in higher melt pool temperatures and an increase in melt pool size (Cheng & Chou, 2015; Ding et al., 2019; Hussein, Hao, Yan, & Everson, 2013; Promoppatum et al., 2017; Sadowski et al., 2016). This larger melt pool will allow grain growth to take place over a greater distance, as there is a larger liquid region present. As melt pool depth increases and there is greater penetration into previously deposited substrate material, the grains can grow further in the build direction, increasing elongation and aspect ratio. The same is true with melt pool width, with the greater area of liquid present in axis perpendicular to the build direction allowing grains to coarsen further in these directions.

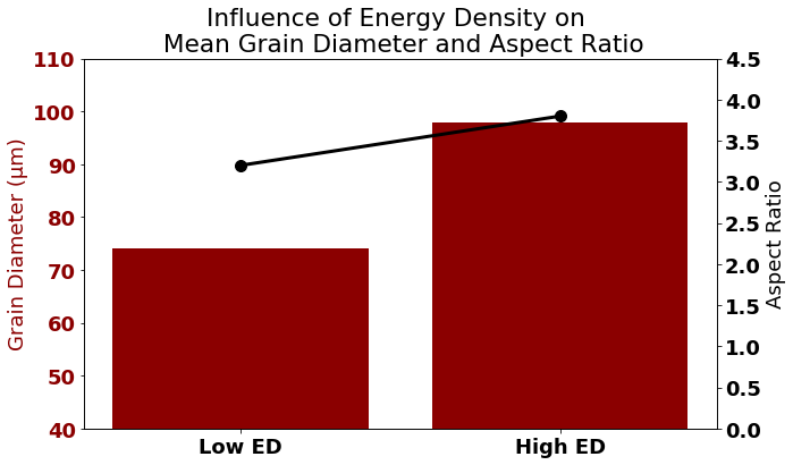

Figure 45 – Plot of the mean grain diameter and aspect ratio measured, via EBSD, within samples produced with high or low energy density parameters (samples M23 and M25 respectively, Table 9). This shows that the higher energy density sample produces material with larger, more elongated grains.

To confirm the link between energy density and melt pool size, measurements of the melt track width were taken from a selection of manufactured test coupons. The melt tracks were measured via optical microscopy of the top surface of the sample, where individual laser passes

can be observed. Due to the overlap of the scan tracks this method is not entirely accurate, however for the purposes of giving an approximation of melt track width it is adequate. The results, Figure 46, show the expected trend that increasing energy density yields a wider melt track, indicating a larger melt pool. This confirms the previously published theory and provides good evidence that these larger melt pools are responsible for the grain coarsening observed in these samples.

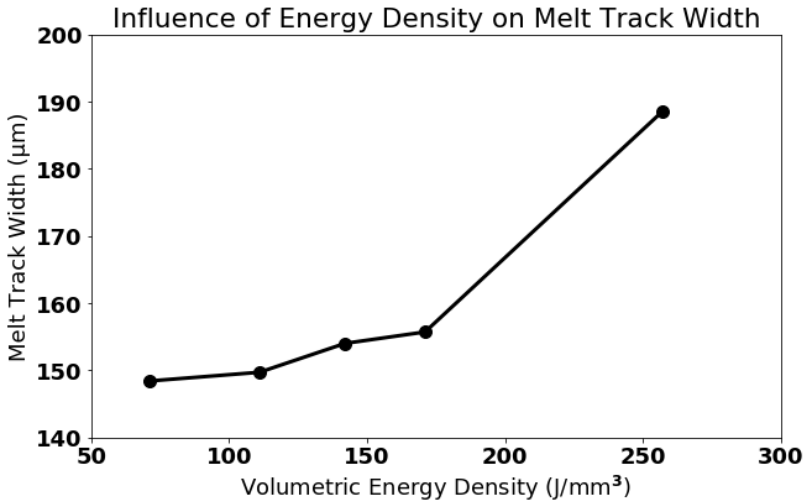

Figure 46 – Plot showing how the volumetric energy density of the processing parameters influences the melt track width. Melt track width was measured from the top surface of manufactured samples from optical microscopy images. The plot shows the trend for melt track width to increase as energy density of the process parameters is increased.

The link between the grain size and energy density had already been investigated by Ding et al (Ding et al., 2019) in the context of individual melt tracks. Although these findings relate to IN718 material being manufactured by electron beam melting, the mechanics of grain growth should be comparable with that of this study, IN62 and SLM. Ding et al report no profound link between the energy density and the grain structure, either grain area or aspect ratio. These results seem to contrast with the findings of this study. The reason for the difference in results can most likely be attributed to the difference between the process of grain growth in a single melt track compared to a complete build. On the scale of a single melt track there is little opportunity for the grains to exhibit extensive growth, with only a single heating pass and the area of one melt track in which to grow. When an entire coupon is manufactured there are repeated instances of heating and penetration between subsequent build layers which allow the process of epitaxial grain growth to take place over a greater distance, both in the build direction and perpendicular. This can be seen in structure visible in Figure 44 where the grains are clearly seen to grow to a much greater length than a single melt track can provide.

Control of the size of the melt pool is the primary mechanism through which the process parameters can influence the evolution of the microstructure created. This will recur throughout the proceeding sections of analysis of the process parameters in this study.

4.2.4.3 Influence of Laser Rastering Strategy on Microstructure

The plot in Figure 47 shows the details of the microstructure of two samples produced with identical process parameters but different laser rastering strategies. These results are interesting because there is a clear difference between the two samples despite the identical energy input of the process parameters themselves. The chessboard strategy coupon was measured to have ~20% larger mean diameter grains with ~25% more elongation as measures by their mean aspect ratio, a significant difference.

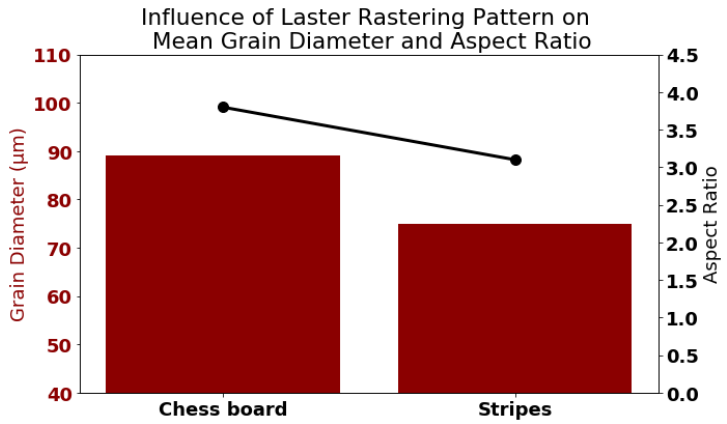

Figure 47 – Plot showing the mean grain diameter and aspect ratio, measured using EBSD in two coupons produced with identical processing parameters but different laser rastering patterns. This shows the chess board rastering pattern to produce larger grains with higher aspect ratios, indicating greater elongation.

The explanation for this difference in microstructure can be found by examining the rastering patterns more closely and considering their effect on the material during manufacturing. The chess board strategy is comprised of 5 mm^2 squares which are arranged over each layer to fill the desired cross section. The striped rastering strategy uses 7mm wide stripes, running the length of the cross section to fill the area, both strategies are pictured in Figure 48. For both strategies the laser spot traverses the rastering pattern in a width wise direction moving by a single hatching distance with each adjacent laser pass. The difference between these two strategies is the width of the pattern, known as the scan vector length.

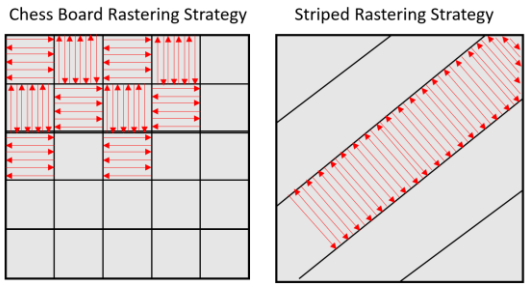

Figure 48 – Illustration of striped and chess board rastering strategies showing the direction of laser spot travel.

With all other parameters fixed, the beam travels at the same speed for both strategies and inputs the same amount of energy per unit time. When the scan vector length is increased, as it is in the striped strategy compared to the chess board, this means that the laser spot takes longer to travel the width of the pattern. By extension this means that the time between a point of the material being exposed for the first time, and then reheated by the laser spot passing nearby on the adjacent scan vector, is increased as the scan vector length is increased. The result of this difference is that the initially exposed point of material has longer to cool down between heating. This effect has been reported in literature where Kruth et al report a link between scan vector length and melt pool temperature (J. P. Kruth et al., 2004b). This increase in temperature should also result in an increase in the size of the melt pool itself.

As was previously discussed, the size of the melt pool is responsible for facilitating the growth of larger, more elongated grains during manufacturing. The shorter scan vector length of the chess board strategy yields a larger, higher temperature melt pool in the same way that an increased energy density might, resulting in the formation of larger grains.

This finding exposes a shortcoming in the use of energy density as a way of summarising SLM processing parameters as it makes no account of the scan strategy.

4.2.4.4 Influence of Laser Scan Speed on Microstructure

The results given in Figure 49 shows how a changing laser scan speed influenced the microstructure of the material. These results show the medium scan speed producing significantly smaller grains with less elongation than either the slow or fast scan speed. As these results were deemed to be most significant to the conclusions of this investigation, these three samples were remanufactured and the test repeated, and the results presented below are the average from measurements taken across two coupons in each case. The error bars show the standard deviation of the two tests.

For additional information, SEM images of both the original and remanufactured, repeat coupons, are provided for the readers reference in the appending, section 6.1. the images show the repeatability of the microstructure created in the material by the SLM process.

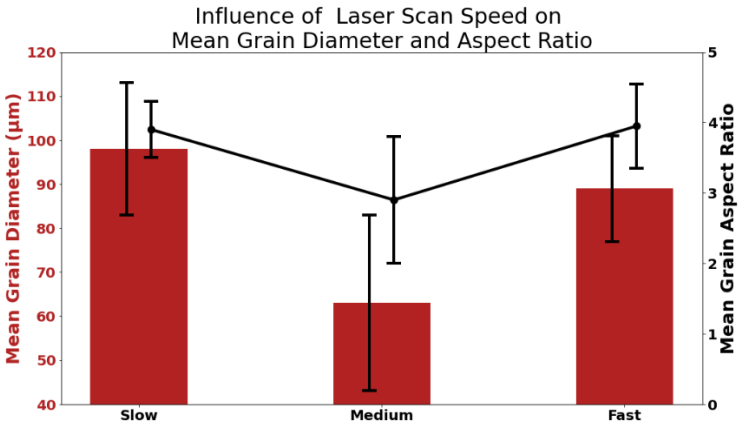

Figure 49 – Plot showing the mean grain diameter and aspect ratio, measured using EBSD data, in samples produced with identical processing parameters, with only laser scan speed being varied over 3 levels, slow, medium and fast. Both mean grain diameter and aspect ratio show nonlinear responses to the laser scanning speed. Both diameter and aspect ratio were at a minimum in the sample produced with medium laser speed, being higher in both slow and fast scanning coupons.

As has been observed in previous sections the size of the grains which form in the material and their elongation is dependent on the temperature and size of the melt pool during manufacturing, which is in turn dependent on the energy density of the process parameters. The results in Figure 49 appear to contradict this. Energy density is inversely proportional to the laser scan speed, with higher speeds yielding lower energy density. The expected trend for Figure 49 would be for grain size to decrease as laser speed increased, with grains also becoming less elongated as the higher speed laser input less energy and create a smaller melt pool (section 4.2.4.2.3). This is not what is found experimentally as grain size starts to increase again at higher speeds.

To explain the trend, which is observed experimentally, the medium speed producing smaller grains than both lower and higher speed scans, more factors must be considered than simply energy density in isolation. It has already been discussed how scan vector length can alter the microstructure of the material by reducing the time between adjacent laser scans therefore reducing the cooling time. It is possible that the laser scan speed can have a similar effect to this. For a fixed scan vector length (as is the case in the three samples measured in Figure 49) increasing the laser scan speed will reduce the time between a point of material being melted and subsequently re-heated by the adjacent scan track.

Unlike the scan vector length however, which only influences the time between adjacent laser passes, laser scan speed also alters the amount of energy input into each point of the material, as calculated by the energy density. Considering both these effects combined it is possible to present a scenario in which the results in Figure 49 are obtained. With the slow laser scan speed, energy input is sufficient to create a large melt pool, creating large, elongated grains. At the highest laser scan speed, the material does not receive as much energy during its initial scan, however the beam returns to an adjacent track so quickly that minimal cooling takes place. This results in the formation of larger grains than the energy density alone might suggest. For a medium laser scan speed there will be a crossover between these two effects, potentially resulting in a beam with too little energy to create a large melt pool, but also moving too slowly to minimise cooling between adjacent tracks, resulting in smaller grains.

This study only investigated three different laser scan speed settings; this was enough to reveal a potential trend however further investigations with a greater range of laser scanning speeds would be required. Extra investigations would allow for the interaction between scan speed and grain size to be investigated and the cross over point to be identified. Other factors such as scan vector length and hatching distance (the distance between adjacent scan tracks) would also have a significant influence on this process, changing the time between adjacent scan tracks and the degree of overlap and reheating experienced during manufacturing. Some basic thermal modelling of the interaction is conducted later in this chapter to investigate this from in a theoretical manner.

4.2.4.5 Influence of Laser Power on Microstructure

Results for the influence of laser power on the microstructure of the material are presented in Figure 50. Interestingly, these results show no relationship between the power and either the size (mean diameter) or elongation (mean aspect ratio) of the grains present in the manufactured material.

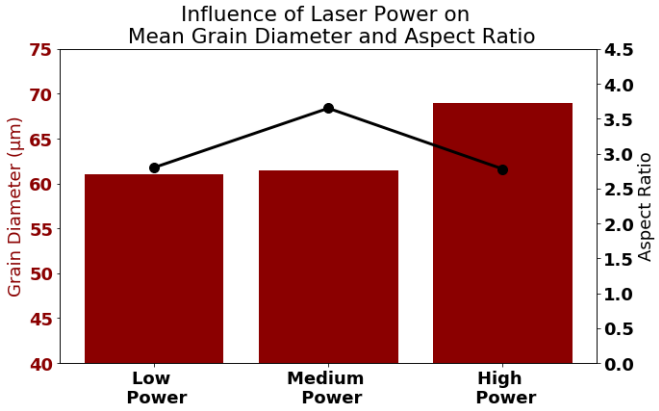

Figure 50 – Plot of the mean grain diameter and aspect ratio measured, via EBSD, in samples produced with different laser power settings. This shows linear trend in the grain diameter or aspect ratio as laser power is changed although the highest power sample does produce the largest grains. The most elongated grains, largest aspect ratio, are produced by the medium power setting.

There is little difference between the mean grain diameter in the low and medium power coupons however the grains become more elongated with medium laser power. The high laser power coupon is measured to have a greater mean grain diameter, ~70 µm compared to ~62 µm in low or medium laser power coupons, but less elongation, with its mean aspect ratio being similar to that of the low power coupon.

These results seem to contradict the observations of previous process parameters and the mechanisms proposed to explain them. As the laser power is increased, the temperature and size of the melt pool should be increased during manufacturing resulting in coarser, more elongated grains.

Assuming that these results are significant (which would require additional remanufactured coupons to investigate), one possible reason for this contradiction could be the specific process parameters selected for these coupons, compared to others in this study. Although between the low, medium and high laser power coupons all parameters are fixed, due to the design of the experiment, they are not the same as those used in scan speed, rastering strategy or energy density tests. It is possible that the parameters selected for these laser power coupons are not appropriate to reflect the influence of changing laser power. One observation of the process parameters selected for these coupons is that the laser scan speed was the same as the medium speed coupon in the previous section, noted to produce smaller grains, there is a possibility that this medium speed and the time between adjacent laser scan passes was sufficient to negate the effects of laser power changes in some samples. Further research and investigation of this

phenomenon would be necessary to confirm the reason for these results and to fully understand the mechanism responsible.

4.2.5 Thermal Modelling

To further investigate the interesting finding relating to laser scan speed and its influence on microstructure observed in 4.2.4.4 further theoretical tests were conducted. This involved modelling the thermals of the SLM process to determine the validity of the proposed mechanism of grain coarsening.

The mechanism proposed in 4.2.4.4 was that there is a point at which laser scan speed can be increased enough to negate the reduction in energy input. The increased laser scan speed allows the laser spot to return to the adjacent scan track quickly enough to reheat previous scanned material and maintain a higher average temperature, and larger melt pool, despite the decreased energy input that results from a faster scan.

4.2.5.1 Constructing the Thermal Model

The computational model was created from scratch using Python. The SLM process, when considered as an entire system, is complicated with many potential variables, so many assumptions or simplifications are made in the model. The aim of the model is to generate a better understanding of the effect of scan speed on melt pool temperatures rather than generate accurate temperature predictions of the SLM melt pool. The trends of change in temperature should be accurate even if the precise values are not.

The model has several process parameters incorporated into it, laser power, hatching distance, spot size and scan vector length, however the only parameter investigated for its effect is laser scan speed.

4.2.5.1.1 Laser Beam

The laser beam traverses the surface of the 3D material mesh in an alternating pattern corresponding to what occurs during SLM. The gaussian power distribution of the laser beam over the surface is calculated using Equation 8 below (Khan et al., 2018; Majeed et al., 2019).

$$q = \frac{2\varepsilon P}{\pi R^2 S} \times e^{\frac{2\left[(x-x_L)^2+(y-y_L)^2+(z-z_L)^2\right]}{R^2 S}}$$

Equation 8 – Calculation of gaussian distribution of laser power over the material surface. Where q is the energy input from the laser, ε is absorption coefficient of the material, P is laser power, R is the beam spot radius, S is the penetration depth of the beam. X, Y and Z represent locations on the materials surface either of the point of interest or of the laser.

4.2.5.1.2 Heating and Cooling of Material

The temperature change created by the beam passing over the material surface is calculated using thermally dependent specific heat capacity as well as latent heat of fusion (Khan et al., 2018).

Heat transfer through the material, accounting for the heating and cooling of different regions of the material, is divided into different mechanisms, conduction, radiation and convection. Conduction of heat away from the laser beam spot over time is calculated using Equation 9.

$$\frac{\delta T}{\delta t} = \frac{k}{\rho C}\left(\frac{\delta^2 T}{\delta x^2} + \frac{\delta^2 T}{\delta y^2} + \frac{\delta^2 T}{\delta z^2}\right)$$

Equation 9 - Equation for heat conduction in 3D. K is the thermal conduction of the material, ρ is material density and C is specific heat capacity which would encompass both specific heat capacity and latent heat of fusion in the model.

This considers heat conduction over a defined period of time, δt and is calculated based on the temperature of the neighbouring points of material and simulates how the temperature dissipates.

Radiative cooling from the material surface is calculated with Equation 10.

$$q_{rad} = \sigma T^4 A$$

Equation 10 - Equation for radiative cooling from the material surface. σ is the Stefan-Boltzman constant, T is the material temperature in K and A is the surface area of the body.

Convection heat loss occurs between the top surface of the material and the atmosphere within the SLM machine. The equation for this heat transfer is given below

$$q_{conv} = h_c A \partial T$$

Equation 11 - Convective cooling equation. h_c is the convective cooling coefficient, and δT is the difference in temperature between the material and the atmosphere.

4.2.5.1.3 Assumptions and Simplifications

As stated previously, the SLM process is complex with many potential variables and physical processes taking place. Modelling this accurately is a difficult task and beyond the scope of this work. For this reason, several assumptions or simplifications about the process are made in order to simplify this model.

One feature of the SLM process not represented in this model is the difference in thermal properties between a loose powder bed and melted, solidified substrate material. Since the loose powder bed contains a significant amount of space between particles it demonstrates superior insulation properties to solid material, the thermal conductivity properties have been reported to be almost independent of the material (Roberts et al., 2009; Rombouts et al., 2005), with conductivity increasing as powder bed porosity is decreased (Andreotta et al., 2017). This will alter the amount of heat retained in the edges of the material being scanned as well as the amount absorbed and conducted during laser scanning. To simplify this for the current model, the material is treated as a solid substrate with the thermal properties of the solid material regardless of whether the material has been scanned and melted by the laser (Andreotta et al., 2017; Hussein, Hao, Yan, & Everson, 2013; Roberts et al., 2009).

Another feature not included in the current model are the properties of the melt pool. In the real world process the melt pool, containing liquid can experience several different effects which can significantly alter the temperature distribution or melt pool geometry. Convection currents in the melt pool due to thermals and Marangoni flow due to surface active elements and the keyhole melting mode are examples of these (Andreotta et al., 2017; Dai et al., 2018; Khairallah et al., 2016; Le & Lo, 2019). A major simplification made in the current model is that the material is never treated as a liquid, although the latent heat of melting is considered, the material above its melting temperature still behaves as a solid. For this reason, although the high temperature region predicted by the model can be considered similar to the melt pool, it is not an accurate representation of the true melt pool geometry which might occur in the real-world process.

Considering the simplifications and assumptions made, the intention of the model created in this chapter is to gain some insight into the general response of the temperature profile of the material during SLM to changes in the processing parameters. This is done to provide further insight into the findings and proposed mechanisms from investigations in chapter 4.2 beyond what is possible using available practical equipment. For this reason, the results presented will not feature the precise numbers calculated, with only the melting temperature T_m indicated.

4.2.5.2 Results and Discussion

The graph plotted in Figure 51 shows the predicted temperature of a single point in the material and how it varies during three adjacent laser passes, as calculated using the thermal model.

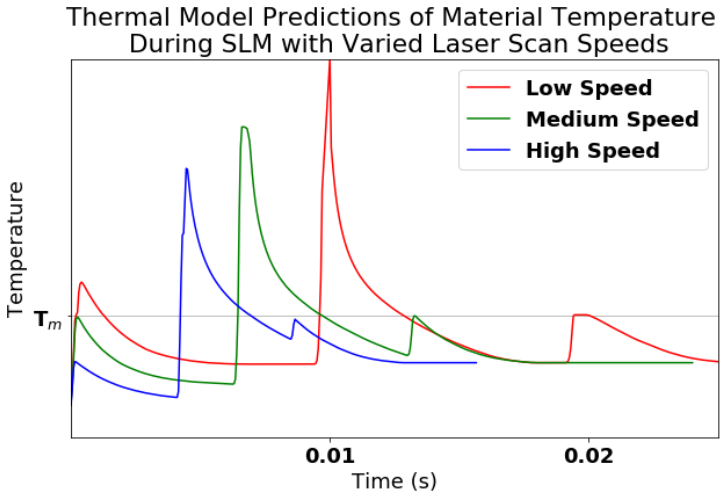

Figure 51 – Plot showing the predicted temperature profile of a single point in material SLM manufacturing. Three different laser scan speeds were used in order to study how the heating and cooling of the material is affected. The results show that as laser scan speed is increased the peak temperature is decreased but the time and cooling between adjacent laser scan tracks is reduced.

This model is intended to provide some evidence to validate the explanation previously proposed in 4.2.4.4 for the microstructural evolution as a result of changing laser scan speed. The proposed mechanism was that increasing laser scan speed can have a secondary effect beyond simply reducing the melt pool temperature and size. The reduction in time between adjacent laser scan tracks reduced the cooling of the material and maintains a higher temperature in the material for longer, allowing more time for grain growth to occur during manufacturing.

The results of the model show the expected trend, increased laser scan speeds yield a lower peak temperature in the melt pool as less energy is directly input by the beam spot. This correlates well with previously published literature (Kusuma, 2016; Lynch, 2013; Majeed et al., 2019). This is reflected in the largest, central peak for each laser scan speed, which increases in temperature as the laser scan speed is slowed.

The temperature distribution over the surface at any given moment can also be plotted to give an indication, although not a perfect model, of the melt pool geometry. This is presented in Figure 52. These results also give credit to the model being a reasonable approximation of the SLM process. When compared to findings of previously published literature focusses specifically on modelling the SLM process, with the width and temperature of the melt pool responds correctly to changes in laser scan speed. Lower speeds yielding a wider, shorter melt pool (Kusuma, 2016; Lynch, 2013; Majeed et al., 2019; Sadowski et al., 2016).

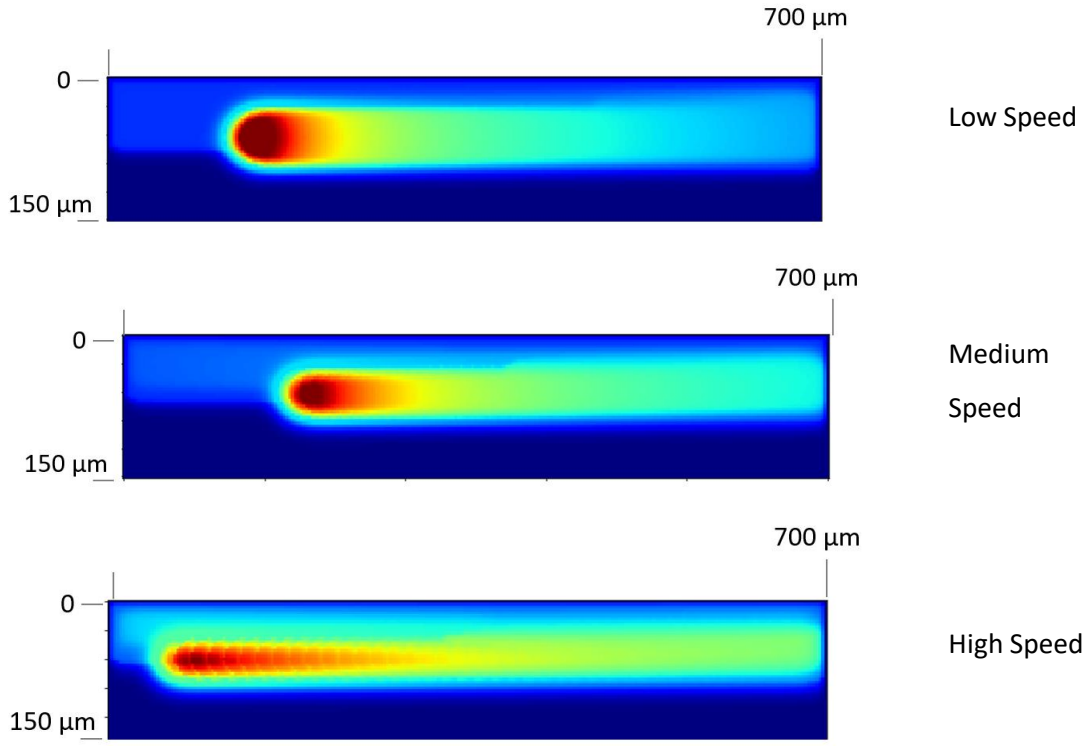

Figure 52 – Plots of the predicted temperature profile over the material surface during SLM processing with different laser scan speeds. The results show the difference in the geometry of the high temperature region, decreasing in width but increasing in length as the laser scanning speed is increased.

The most important results from this modelling relate to the cooling between scan passes. The region of interest in Figure 51 is materials temperature between the second and third peak, the initial melting of the material when the laser is directly incident on it and the laser passing by on the adjacent laser scan track respectively.

Comparing this region on the medium and high laser scan speed results, they can both be seen to cool to below T_m before being reheated by the adjacent laser pass. Despite this however, there is a difference in the lowest temperature that each material reaches. Although the medium scan speed material starts from a higher peak temperature, in the time between initial melting and reheating it is shown to cool to a lower temperature compared to the higher speed material. This results in both materials reheating to very similar temperatures at their third peak. These predictions provide evidence that faster laser scan speeds have the potential to maintain a higher average temperature in the material by limiting cooling, despite the reduced peak temperatures they induce.

Due to the simplifications and assumptions made in the thermal model it is likely that the temperatures it predicts are not accurate to the real-world process. The general trends

displayed however, cooling rates and time between laser passes, should be representative of what happens during the process. It is possible, for example, that with improved insulating properties of a powder bed rather than a solid substrate (as the scanned material was modelled), the high-speed laser scan could maintain the temperature of the material above the melting temperature between two adjacent laser scan tracks. Even if this is not the case, and the material is not maintained in its liquid state, it is still possible for solid state grain coarsening to take place at an accelerated rate at higher temperatures.

4.3 The Influence of Post Process Heat Treatments on Microstructure and Mechanical Properties.

4.3.1 Repeatability of As Fabricated Material

Additive manufacturing is notorious for producing anisotropic material with variation between builds and slightly different material properties. The first stage of this investigation was to establish whether the as fabricated material manufactured for this work was repeatable. This was done using SEM to observe both the grain structure and the structure of any segregation present in the material to ensure that it was consistent between different samples. The images showing this are given in Figure 53.

The as fabricated (AF) material displayed the same structure between multiple coupons from the build. Figure 53 A) shows the grain structure of the material, a typical columnar grain structure with grains elongated in the build direction (left to right in the image). This is caused by the partial remelting of the substrate material and resulting epitaxial grain growth (Dinda et al., 2009; Y. Lu et al., 2015; Tao et al., 2019; D. Zhang et al., 2018). The grains grow in the opposing direction of heat flow, which is predominantly vertically down from the melt pool into the substrate material (D. Zhang et al., 2018). There is no sign of the grains being inclined at an angle to the build direction as a result of laser scanning direction, as has been observed in some other studies. This indicates that the rotation of the laser rastering pattern between each layer has been effective in mitigating this, as has been previously observed (Dinda et al., 2009). This structure was confirmed to be present in multiple different coupons manufacture in the same build. This provides evidence that the SLM process being used is at least repeatable within a single build (as was used to manufacture all the coupons for this work). This provides a consistent starting point for all following heat treatments and a strong likelihood of repeatable representative results.

A) B)

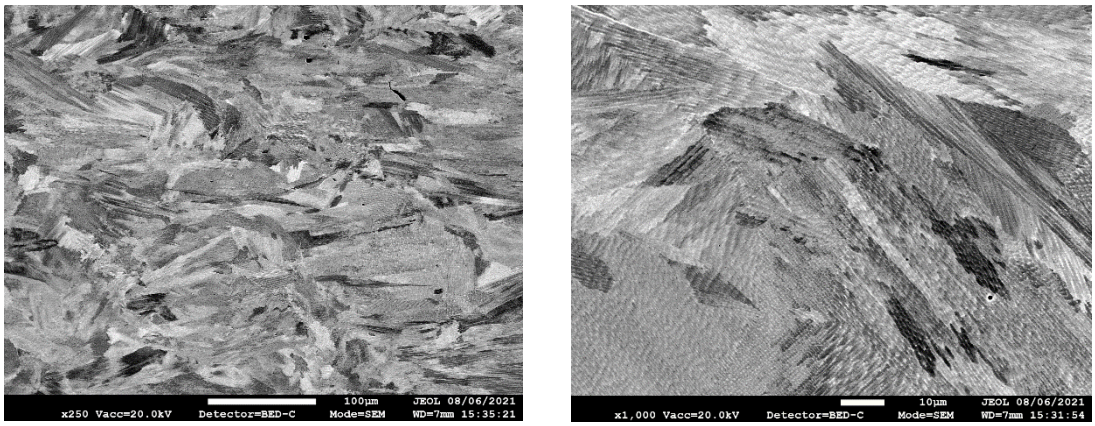

Figure 53 – SEM images of as fabricated material showing the grain structure (A) and the distribution of segregation (B). Similar images were collected from multiple different coupons from the build in order to verify that the structure present was the same throughout the build.

As well as within build consistency of material, further imaging was undertaken to investigate the 'within sample' consistency of the material. Coupons were all manufactured as tall ~100mm cylinders, there was therefore the potential for variations in the structure of the material from top to bottom. Sections were cut from the top, middle and bottom of a single coupon and imaged to investigate this. In general, the material was found to be identical in structure regardless of its position within the sample, confirming that coupons can be cut from anywhere and assumed to be representative.

One major finding of this work is presented in Figure 54. The image shows the edge of the coupon, there is a clear band of finer grains present within ~10 um of the edge. This is likely due to the ramping up/direction change of the laser during processing of this area leading to a different thermal experience of the material. This finding indicates that the structure of the material around the extreme edges is not representative of the bulk structure as a whole. As a result of this, the extreme edges of the sample were excluded from any images or data gathered from heat treated samples.

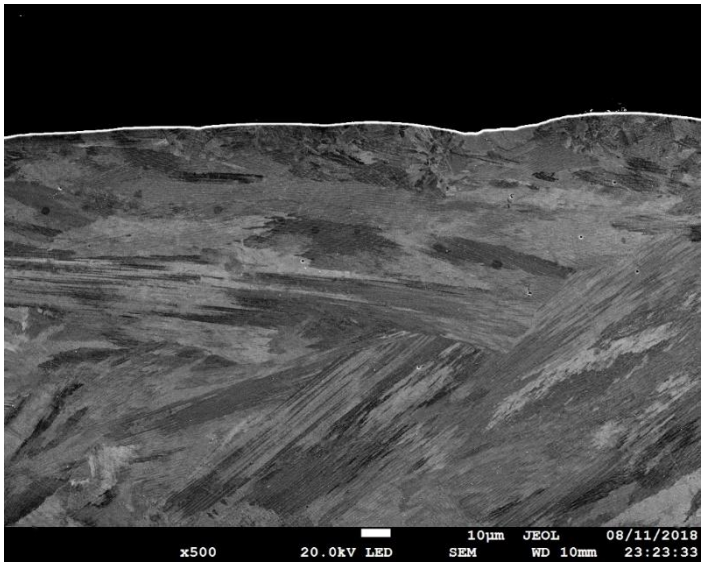

Figure 54 – SEM image taken from near the edge of a coupon. There is a clear change in structure within ~10 um of the coupons side surface. This indicates that the material in the outer region of the coupons is not representative and should not be included in any investigations or data analysis.

4.3.2 Microstructure

4.3.2.1 Grain Structure

To establish the grain structure of the material in the homogenised condition SEM images were taken of the material. The key finding from these images can be seen in the two images presented below in Figure 55. At 1100 °C the structure of the material can be seen to be visually identical to what was observed in the AF condition, elongated columnar grains in the build direction (left to right). In contrast, the material homogenised at 1180 °C shows a significantly evolved structure. Grains have undergone coarsening. These images are consistent with what was observed in the other samples, all those treated at or below 1100 °C maintained their same grain structure and those treated at or above 1180 °C exhibited coarsening (additional images showing a selection of different homogenisation treatments are provided in the appendix, section 6.2). This indicates the presence of some 'threshold' temperature for grain coarsening between these two temperatures. This shows that SLM IN718 is capable of maintaining its fine structure at higher temperatures than have been reported to trigger recrystallisation (RX) in wrought IN718 material, with some degree of RX being reported from 950 °C (Azarbarmas et al., 2016; Guest & Tin, 2012). This indicates that the residual stress in SLM material is much lower, being unable to drive RX at these lower temperatures. A consequence of this finding is that any improvement in the material achieved by these heat treatments below 1100 °C, such as reduction of segregation or secondary phase precipitation, are achieved without losing the fine AF microstructure of the material. This means that the improved mechanical properties of a fine

grain structure, such as tensile and fatigue properties (D et al., 1997; Popovich et al., 2017a; D. Zhang et al., 2018).

A) 1100 °C B) 1180 °C

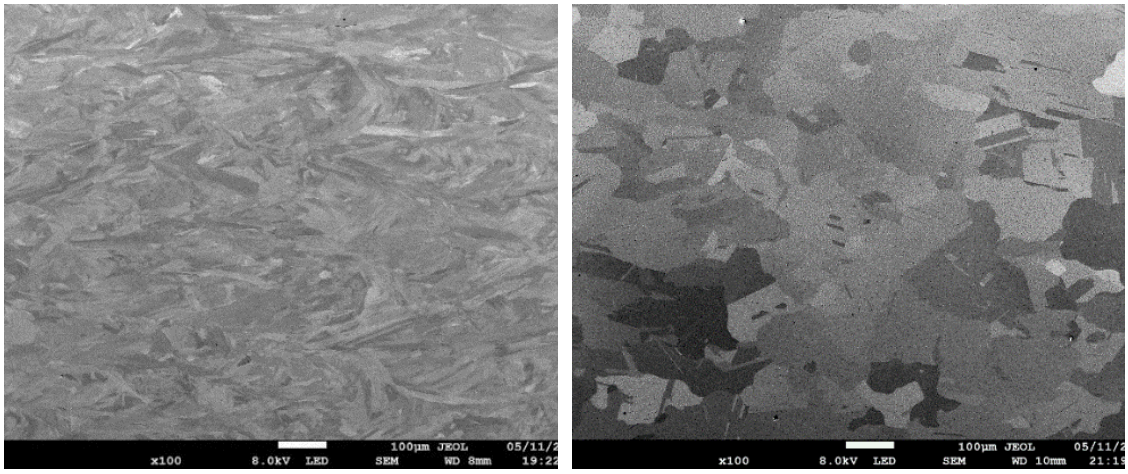

Figure 55 – SEM images showing the grain structure of homogenised material. The temperatures pictured show treatments either side of an apparent threshold temperature at which grain structure evolution and coarsening take place.

To quantify this threshold and the effect it has on grain morphology, EBSD data was used to plot Figure 56. The coarsening and equiaxing threshold is clearly visible as a dramatic increase in grain diameter and a reduction in aspect ratio in the 1180 °C and 1250 °C samples. A range of temperatures is plotted as well as 1 and 2 hour treatments to establish any influence of time on the results. The coarsening seems to be exclusively dependent on temperature with no consistent difference between 1 and 2 hour treatments. The specific point of this grain coarsening is not captured by the temperatures selected. The temperatures were initially selected to cover a range of temperatures from the delta dissolution temperature up to an extreme high. Grain coarsening is a result of homogenisation at a temperature too high to be useful for the purposes of this thesis. The specifics of the grain coarsening were however found to eb interesting with relation to the mechanism responsible, this is investigated in greater detail in section 4.4.

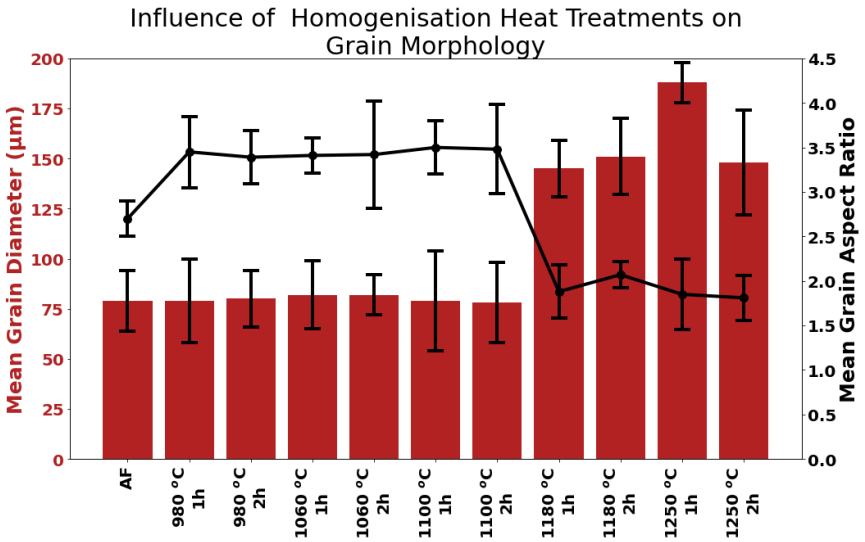

Figure 56 - Plot of grain morphology data obtained from EBSD scans. Grain size is plotted as grain diameter with morphology being captured as aspect ratio. For each homogenised condition the data is made up of >3000 grains of data, making the results statistically significant, error bars show the standard deviation of the data.

4.3.2.2 Misorientation Angle Evolution

Figure 57 and Figure 58 show the misorientation angle distribution measured in the homogenised coupons and compares them to the AF material. The results are divided over 2 plots, 980 – 1100 °C and 1180 – 1250 °C for ease of reading with the AF results being present in both for comparison.

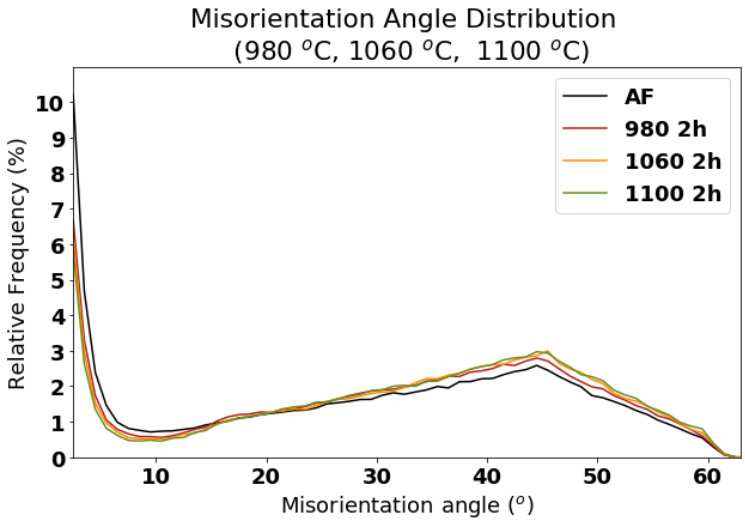

Figure 57 – Plot showing misorientation angle distribution within the coupons, plotted from EBSD scan data. AF material is shown and compared to material treated at 980 °C – 1100 °C. This shows the similarity in misorientation angle distribution between the AF material and homogenised coupons. The size of the initial low angle peak is reduced by homogenisation.

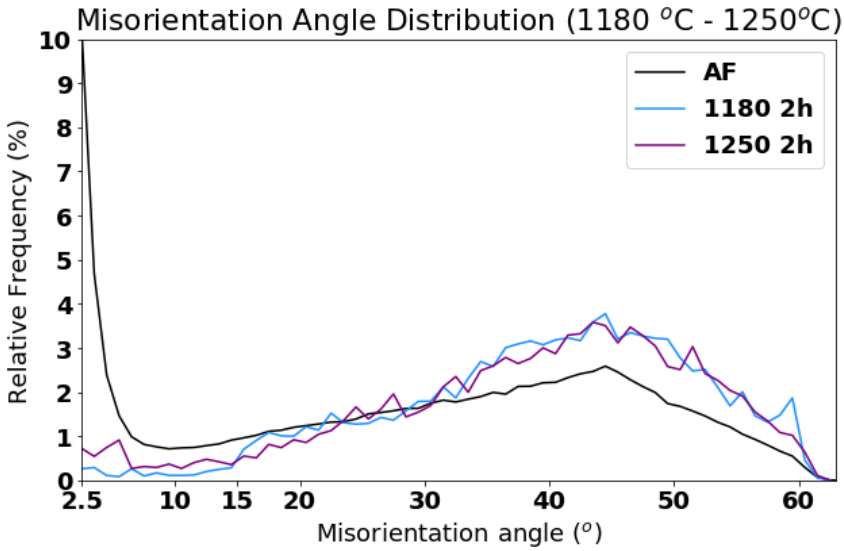

Figure 58 – Plot showing misorientation angle distribution within the coupons, plotted from EBSD scan data. AF material is shown and compared to material treated at 1180 °C – 1250 °C. This shows how the homogenisation treatements in this temperature range completely remove the initial low angle misorienation peak found in the AF material. The removal of these low angle misorientations results in the high angle boundaries and the secondary peak around 45 ° contributing a greater proportion of misorientations in the material, hence increasing in frequency.

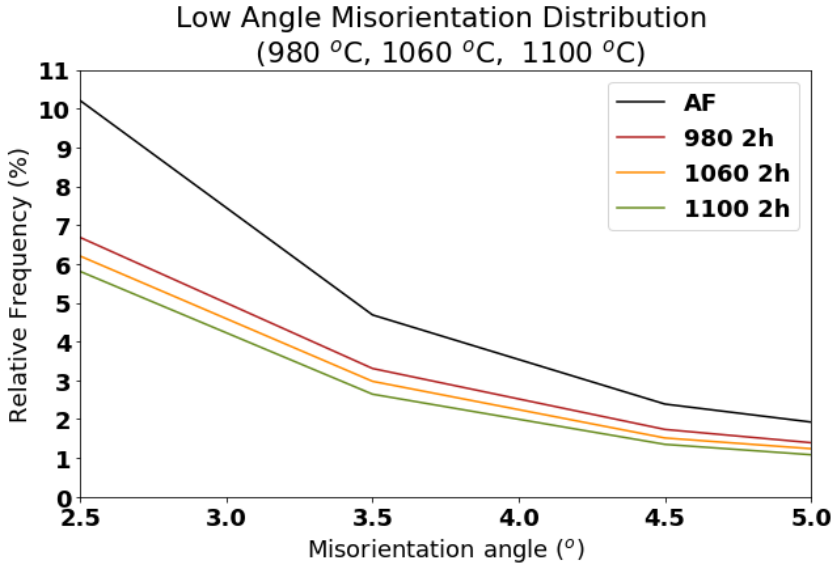

Figure 59 – Plot showing the low angle region of Figure 57 allowing for the difference between the homogenised coupons to be seen. This shows that as the homogenisation temperature was increased, within this temperature range, the size of the initial low angle misorientation peak is reduced and the frequency of low angle misorientations throughout is reduced.

The material in the AF condition displays a characteristic distribution of the misorientations angles, visible in the black lines plotted in both Figure 57 and Figure 58. The main feature of the material is the high frequency of low angle misorientations present, between 2 ° and 10°. This high frequency peak has been previously observed within IN718 material and has been attributed to the presence of local lattice misorientations within the material (Rahimi et al., 2017), which in SLM material is due to residual thermal stresses built up in the material as a result of rapid heating and cooling during manufacturing.

In Figure 57 the misorientation angle distribution in coupons homogenised at 980°C, 1060°C and 1100°C is plotted. These display similar distributions of misorientation angles, with a significant high frequency peak in misorientations between 2° and 10° followed by a smaller secondary peak at ~45°. The lack of evolution in the higher angle misorientations, representing grain boundaries, supports the previous observations where no change in the morphology of the grain structure was observed during homogenisation in this temperature range. Although the same initial low misorientation angle peak is still present in the homogenised coupons its height, or frequency, is reduced. This is shown in greater detail in Figure 59 where only misorientation angles between 2.5 ° and 5 ° are plotted. From this it is apparent that the frequency of low angle misorientations is reduced by increasing homogenisation temperature. The frequency of the initial peak is reduced from ~10 % in the AF coupon down to 6.7%, 6.2% and 5.9% in the 980 °C, 1060 °C, and 1100 °C coupons respectively. This difference is maintained throughout the region plotted although the lines converge as misorientation angle increased. This suggests that the lower angle boundaries are most susceptible to change during the homogenisation treatments and most temperature sensitive.

The reduction of the frequency of the low angle misorientations is due to the recovery process. At elevated temperature the dislocations become more mobile and can rearrange themselves. In some cases, this results in dislocations annihilating in pairs, to minimise their stored energy, in others they simply take the most efficient arrangement. Recovery is known to occur at lower temperatures, leaving the structure and orientation of the material largely unchanged, as is observed in previously published literature (Callister & Rethwisch, 2014; Guy, 1976; Mercier et al., 2002). The process reduces the density of dislocations in the material and relieves the residual stress stored in the material. The lower angle misorientations require less energy to become mobile, explaining the converging lines in Figure 59 as misorientation angles increase.

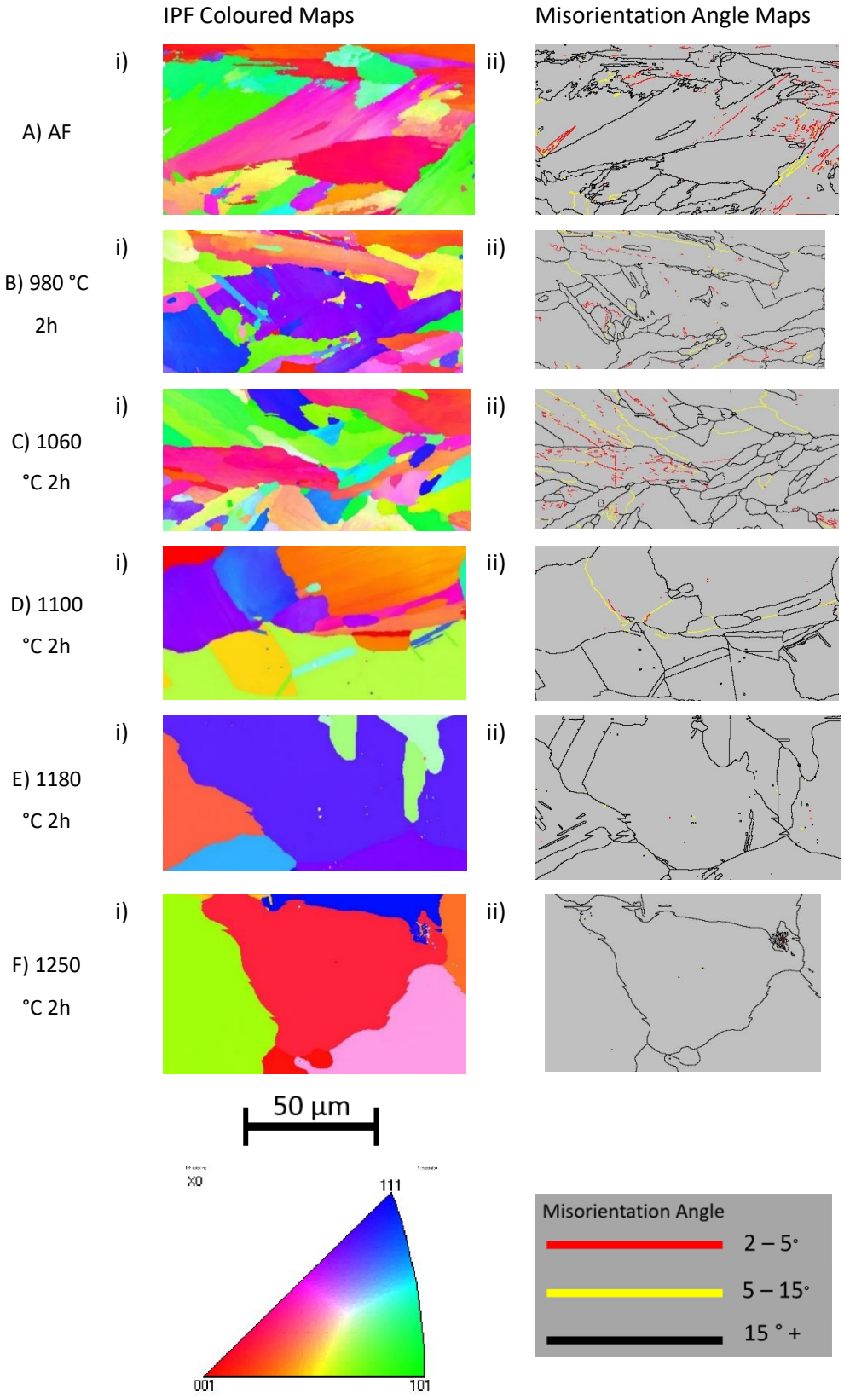

Figure 60– High magnification detailed EBSD data captured from the homogenised material. IPF coloured maps are included for reference, column i), as well as the misorientation angle maps, coloured according to their boundary angles, column ii). These images shoe the characteristics of the boundaries present changing during homogenisation, with low angle boundaries moving and relieving some of the strain and free energy in the material.

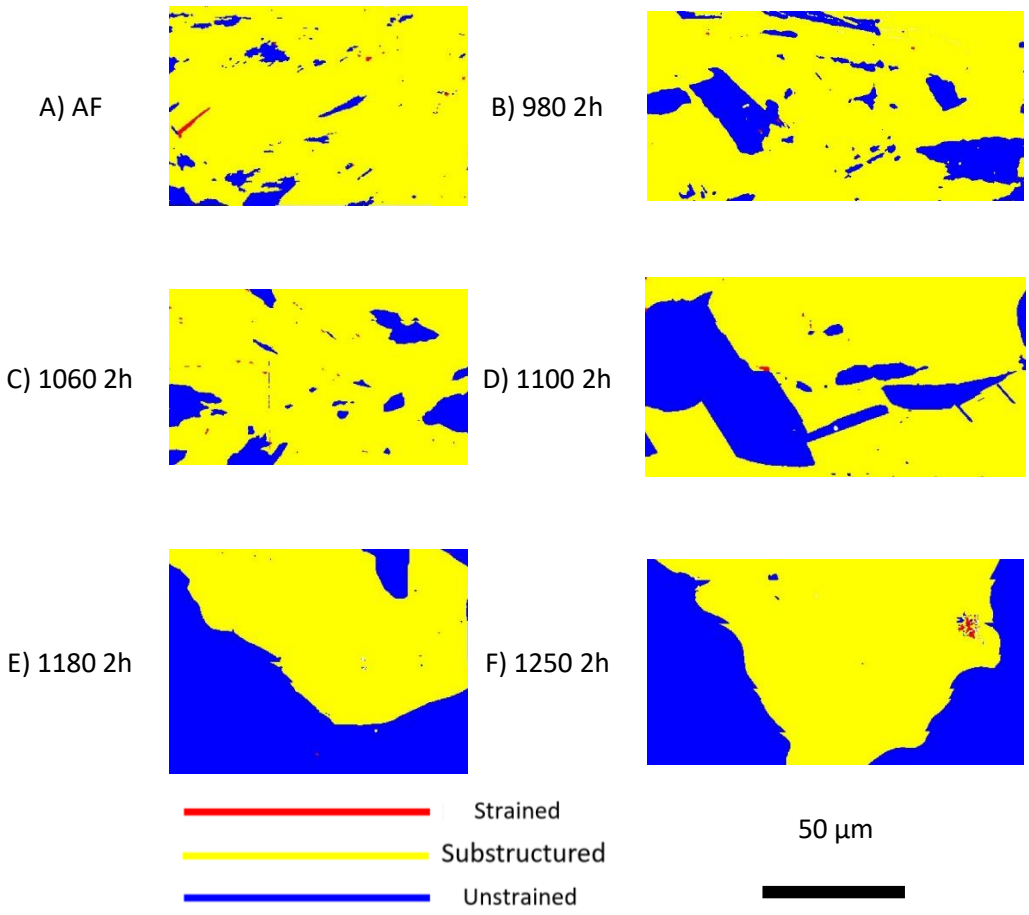

Figure 61– Images produced from EBSD scan data showing the nature of grains present within the homogenised material. Grains are coloured according to their structure, either strained, substructured or not strained.

The low angle misorientations and their recovery was observed in the higher magnification, more detailed, microscale EBSD scans of the material shown in Figure 60. This contains an image where the grain boundaries are plotted with coloured lines corresponding to their misorientation angle. In the AF material, Figure 60A) i), on the right-hand side of the misorientation angle map, there are several grains which display a clear pattern of red, 2 – 5° boundaries creating a sub grain structure. The grains containing these networks can also be seen in the coloured IPF coloured map, Figure 60A) ii), where a marbling if the colour of these grains indicates slight differences in orientation throughout the grain. Once the material has been heat treated at 980 °C it can be observed that there are fewer instances of these sub grain low angle misorientations due to the recovery process taking place. In the material treated at the highest temperature, 1250 °C for 1h, there are no sub grain low angle misorientations remaining, suggesting that complete recovery and relaxation if the residual stresses and dislocation has taken place. This removal of the intragranular misorientation is also illustrated well in Figure 61 where the grains are determined to be strained, substructured or unstrained depending on their internal misorientations. These images clearly illustrate the recovery process taking place as a

greater volume fraction of unstrained grains can be seen as homogenisation temperature is increased. Interestingly there is never a complete removal of substructured grains from the material regardless of the homogenisation treatment applied. This could be due to the rapid cooling of the coupon during water quenching after homogenisation, this could introduce some small amount of residual thermal stress back into the coupon.

This recovery process takes place during all the different homogenisation treatments as the temperature is sufficient to allow the lower angle boundaries and dislocations to move within the material and achieve a more thermodynamically efficient arrangement. This is confirmed by the images presented in Figure 61where the grains are labelled visually to show the presence of unstrained grains. There is a reduction of strain within the grains at all homogenisation temperatures, regardless of whether the grain structure morphology changed visually.

4.3.2.3 Chemical Segregation and Precipitation

Backscattered electron images (BSE) of the as fabricated material, Figure 62, show an intragranular, dendritic structure of brighter material, similar segregated areas have been observed and highlighted in a previous section, Figure 40 and Figure 41. The results of the EDS comparing these bright regions to the bulk matrix, given in Figure 63, find that the most significant difference was an increase in the % wt content of Nb from ~5% in the bulk matrix to ~18%. This shows that, in this SLM IN718 material, Nb is the major alloying element most susceptible to segregation.

The dendritic segregation of Nb observed in the as fabricated material in Figure 62 is a result of the solidification of the material during the SLM process. Relative to the other alloying elements Nb atoms are large, this size differential slows down the diffusion process. During solidification of IN718 the first reaction which takes place is the liquid – γ transformation, forming a dendrite. This solidification process preferentially includes the faster moving alloying elements more soluble in the γ matrix, this leaves the liquid between dendrites, the interdendritic region, enriched with Nb (Cieslak et al., 1989; Deng, 2018). This process continues, further enriching the interdendritic regions until the cooled material is left with the Nb segregation observed in Figure 62.

The distribution Nb is of critical interest in IN718 because it plays a major role in the mechanical properties of the material, being a key component in the γ'' (Ni_3Nb) phase. This phase is the primary strengthening mechanism of IN718, providing coherency strain hardening. The distribution of Nb therefore directly controls where and how much γ'' can form. The segregation of Nb is also often associated with the formation of the brittle intermetallic Laves phase (of (Ni,

Fe, $Cr)_2$(Nb, Mo, Ti) (Guo et al., 2017; Ma et al., 2015; Ch. Radhakrishna et al., 1995; Schirra et al., 1991)). The interface between the laves phase and the bulk γ matrix also introduces a weak point which can act as a preferential site for cracks to nucleate and propagate (Mills, 1984; CH Radhakrishna & Prasad Rao, 1997; Schirra et al., 1991) further degrading mechanical properties such as room and high temperature tensile, low cycle fatigue and impact toughness (Shi et al., 2018; Sui et al., 2017). This dendritic structure of Nb segregation is the primary reason to employ a homogenisation heat treatment, to reset the material and improve its aging response.

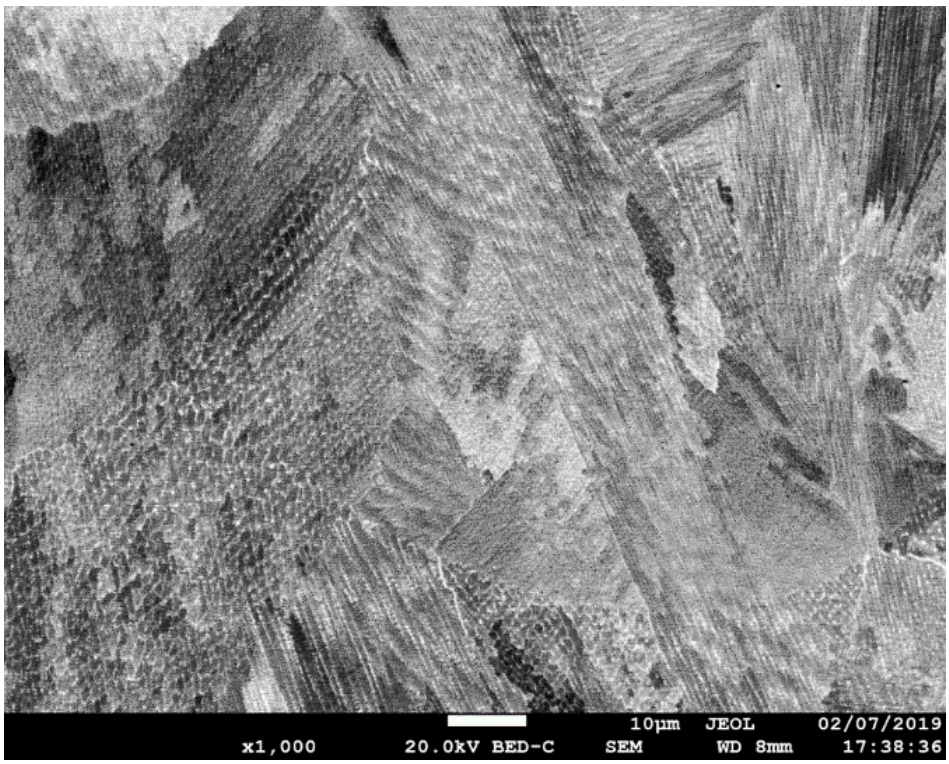

As Fabricated Material

Figure 62 - Back scatter electron image showing segregation morphology present in the as fabricated SLM material. Bright regions are the segregated material, forming an interdendritic pattern throughout the material as a result of rapid cooling of the material.

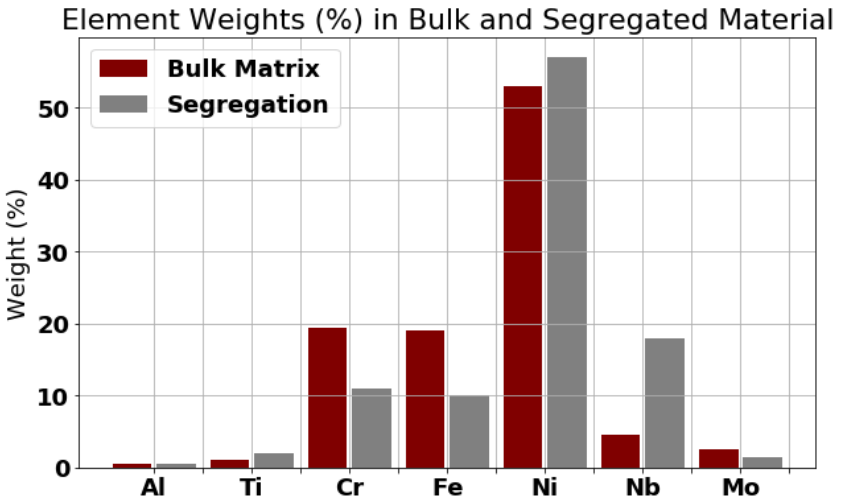

Figure 63 – Energy dispersive spectroscopy data plotted to compare the chemical composition of the bulk matrix material to segregated material. This shows that the segregated regions are enriched with niobium and depleted of other elements such as chromium and iron.

At the highest homogenisation temperature, 1250 °C, a significant change in the segregation behaviour of the material was observed. At this temperature irrespective of dwell time, the segregation of Nb in the material becomes more severe, Figure 64, Figure 65 and Figure 66 show several examples of segregation found in the material. The Nb rich regions all have an irregular morphology with jagged edges with sizes in the 5 – 25 µm range. The areas of segregation do not show a preference for any particular locations within the material, grain boundaries or pores. They are observed uniformly throughout the material. There also appears to be no dependence on the homogenisation hold time. From 15 minutes to 120 minutes the size, and morphology of the segregate regions visible is very similar. There appears to be no evolution over time.

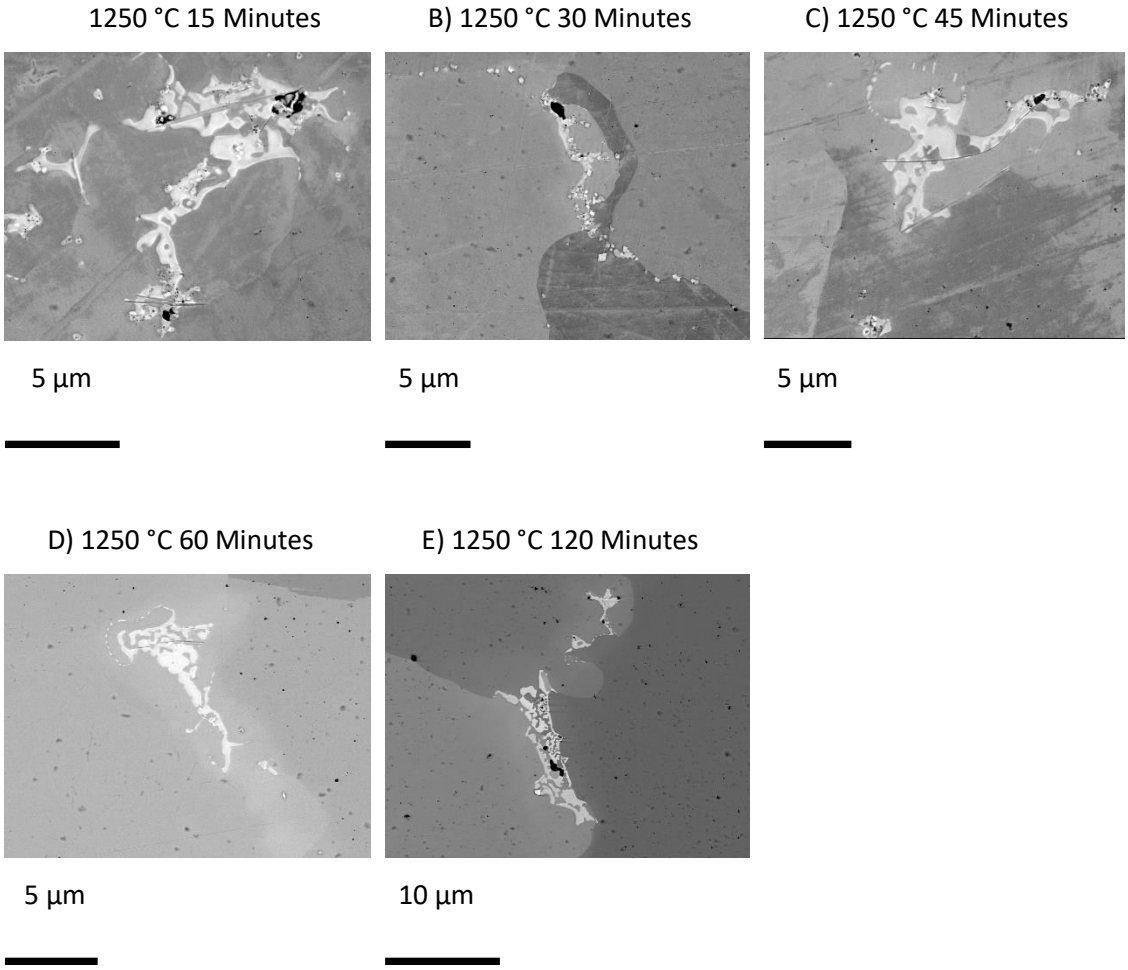

Figure 64 – Backscattered electron images showing instances of Nb segregation in material heat treated at 1250 °C. These images show that the morphology of the segregation is significantly changed from the as fabricated material. In all instances the segregated regions are irregularly shaped with no consistent features. The formation of these features is similar in all the homogenisation times tested.

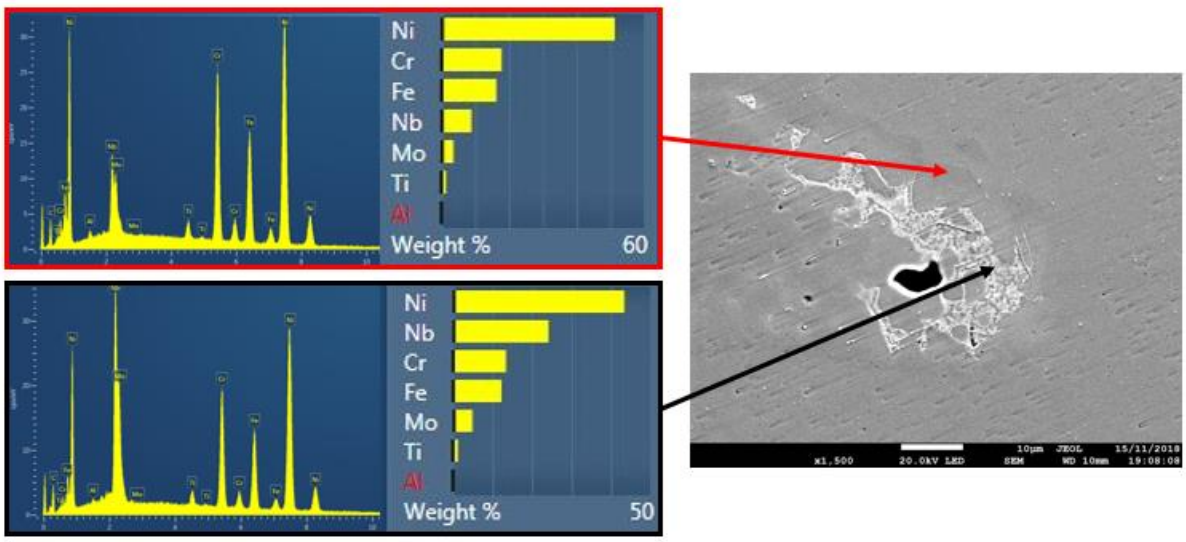

Figure 65 – EDS results comparing the chemical composition between the bulk matrix of the material and the segregation. These results confirm the large instances of segregation observed in the material homogenised at 1250 °C to be enriched with Nb as is seen in the as fabricated material.

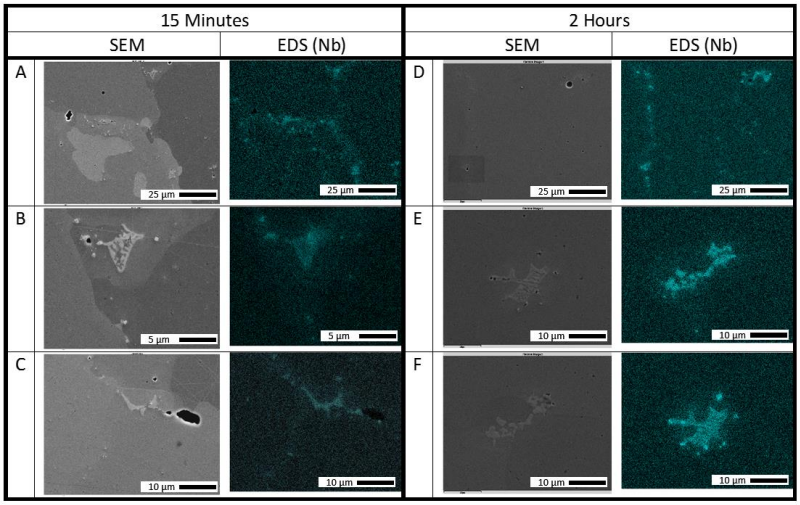

Figure 66 – Scanning electron microscope (SEM) images of the segregations found in material homogenised at 1250 °C for 15 minutes (A – C) and 2 hours (D – F) and energy dispersive spectrocopty (EDS) maps showing the enrichment of Nb in these regions. These images show that these segregated regions form in all the coupons regardless of homogenistion time. There is little difference in the morphology of the segregated regions ebtween the two different treatmetns shown, indicatign a lack of any relation to homogenisation time, only temperature.

These segregated regions are formed by a process of incipient melting. In IN718 incipient melting takes place when the material is heated to high temperatures, causing the laves phase to undergo sub solidus melting (Huang et al., 2019; MIAO et al., 2011; WD et al., 1991). Similar morphology regions of Nb enrichment have been reported and identified as laves phase in IN718 by Xu et al (Xiangfang Xu et al., 2018). The incipient melting temperature (IMT) has been measured in wrought IN718 to around 1170 °C (MIAO et al., 2011; Y. Yang et al., 1994). It has

also been reported that the IMT of IN718 material can vary significantly depending on the initial condition of the material and the morphology of the laves phase present, (F. Liu et al., 2011). Where the laves phase present has a finer structure the IMT will be increased (Y. Yang et al., 1994), for example Cao et al. found that the IMT of cast IN718 was increased from ~1170 °C to 1230 °C following a homogenisation treatment which greatly reduced laves content in the material (WD et al., 1991), Liang et al. reported similar findings, with an increase from ~1170 °C to 1205 °C following homogenisation (Y. Yang et al., 1994). Lui et al report that, in laser rapid formed IN718, due to a lack of laves formation, no incipient melting was observed at all at 1250 °C (F. Liu et al., 2011).

During SLM the IN718 material undergoes rapid solidification and cooling. This restricts the formation of the laves phase, limiting the volume and size of precipitation, which will in turn increase the IMT. This is confirmed by Huang et al. who reported no incipient melting occurring in as fabricated SLM IN718 at 1230 °C, instead requiring 1260 °C before the process began (Huang et al., 2019). The IMT of SLM IN718 is slightly lower than this, clearly occurring in the coupons in this study treated at only 1250 °C.

The heavily segregated incipient melting zones present in the material treated at 1250 °C will be deleterious to mechanical properties of the material. This can be attributed to two mechanisms. The first is that the heavy Nb segregation depletes the γ matrix of a vital component required to pre precipitate strengthening phases during subsequent aging treatments (Amato et al., 2012; Saied Azadian et al., 2004; S. Li et al., 1994). The second reason is the weak interface between the incipient melted area and the γ matrix, which will act as easy crack initiation and propagation sites in the material. Considering this, suitable homogenisation treatments for SLM IN718 should take place below the IMT of the material, which appears to be between 1230 °C, where no incipient melting has been observed (Huang et al., 2019), and 1250 °C.

Comparing the morphology of the segregations found in the following the 15 minutes treatment with those found after 120 minutes, Figure 66, reveals that they both appear very similar, both on a macro and microscopic scale. There is no significant difference in size between the different hold times. This suggests that once the initial incipient melting process has taken place and the segregation has formed in the material, there is little to no diffusion of the Nb out of these areas. This behaviour can be attributed to the slow and difficult diffusion of Nb in the γ matrix of IN718. The Nb rich segregations provide a preferential site for the Nb atoms to remain, the driving force created by the concentration gradient between these areas and the γ matrix is clearly not sufficiently strong to overcome this.

4.3.2.3.1 Modification and removal of chemical segregation during homogenisation heat treatments

The segregation and its evolution was investigated in all homogenised samples however only samples treated between 900 °C and 1060 °C are selected for discussion here. This temperature range represents the most interesting and promising result for creating an improvement in aging response and mechanical performance of the material.

To aid with the analysis of the images in this section, differential scanning calorimetry (DSC) was performed on a sample of AF IN718 material, shown in Figure 67. The peaks in the heating curves indicate phase changes in the material with the beginning, peak and end of each indicating the temperature at which 99% precipitation, fastest precipitation and onset of precipitation would occur respectively. In Figure 67 the peaks have been labelled to indicate the phase change they are associated with.

While the precise temperature of each phase change varies slightly with the heating rate the temperatures for each can be approximated as 620 °C, 800 °C and 1100 °C for γ', γ'' and δ respectively. This information is critical in analysing the response of segregation observed after different homogenisation treatments.

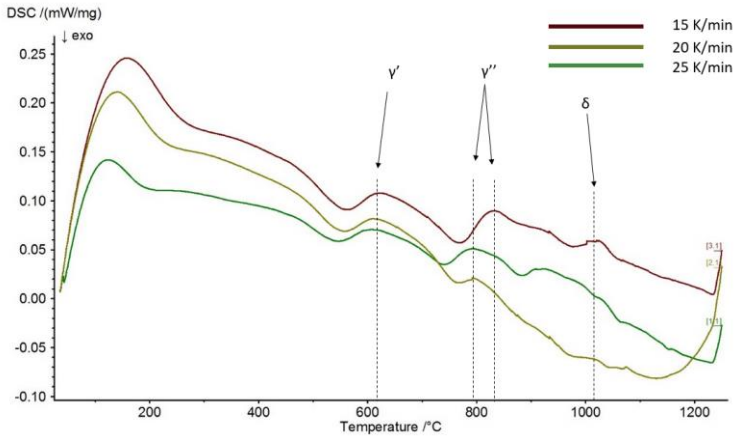

Figure 67 - DSC results for SLM IN718 showing 3 different heating rates 15, 20 and 25K/min. Peaks for the three phases of IN718 are indicated. These results indicate the rough temperatures at which the different phases of IN718 can be expected for precipitate or dissolve in the SLM material.

4.3.2.4 900 °C – 980 °C

Between 900 and 980 °C, Figure 68 B) – E) the segregated material visible in the AF material is transformed to discrete precipitates distributed throughout the material. These results agree well with similar heat treatments conducted by Li et al. (J. Li et al., 2019) who observed similar needle shapes precipitates forming during heat treatment (homogenisation, 940 °C followed by

aging).These precipitates have a needle shaped morphology which is more clearly visible in the higher magnification images shown in Figure 69. The length of the precipitates was also measured to aid in identification. This was accomplished using the SEM images of the samples in Figure 68 and image analysis tools. The sample size is small, however the results are still useful in building understanding of the precipitates. Precipitates were found to be a mean of ~1 µm in length, Figure 70.

The morphology of these precipitates strongly suggests that they are the Ni_3Nb δ phase. The δ phase can be observed in two morphologies, either a globular, spheroidal precipitate or a needle shaped precipitate. The precipitates present in 900 – 980 °C 1h treatments display this second morphology. Although it is often referred to as needle shaped, these precipitates are likely to in fact be plate like when viewed in 3D with only the thin ~0.1 µm edge and one longer side visible in Figure 68 and Figure 69 (Desvallees et al., 2006).

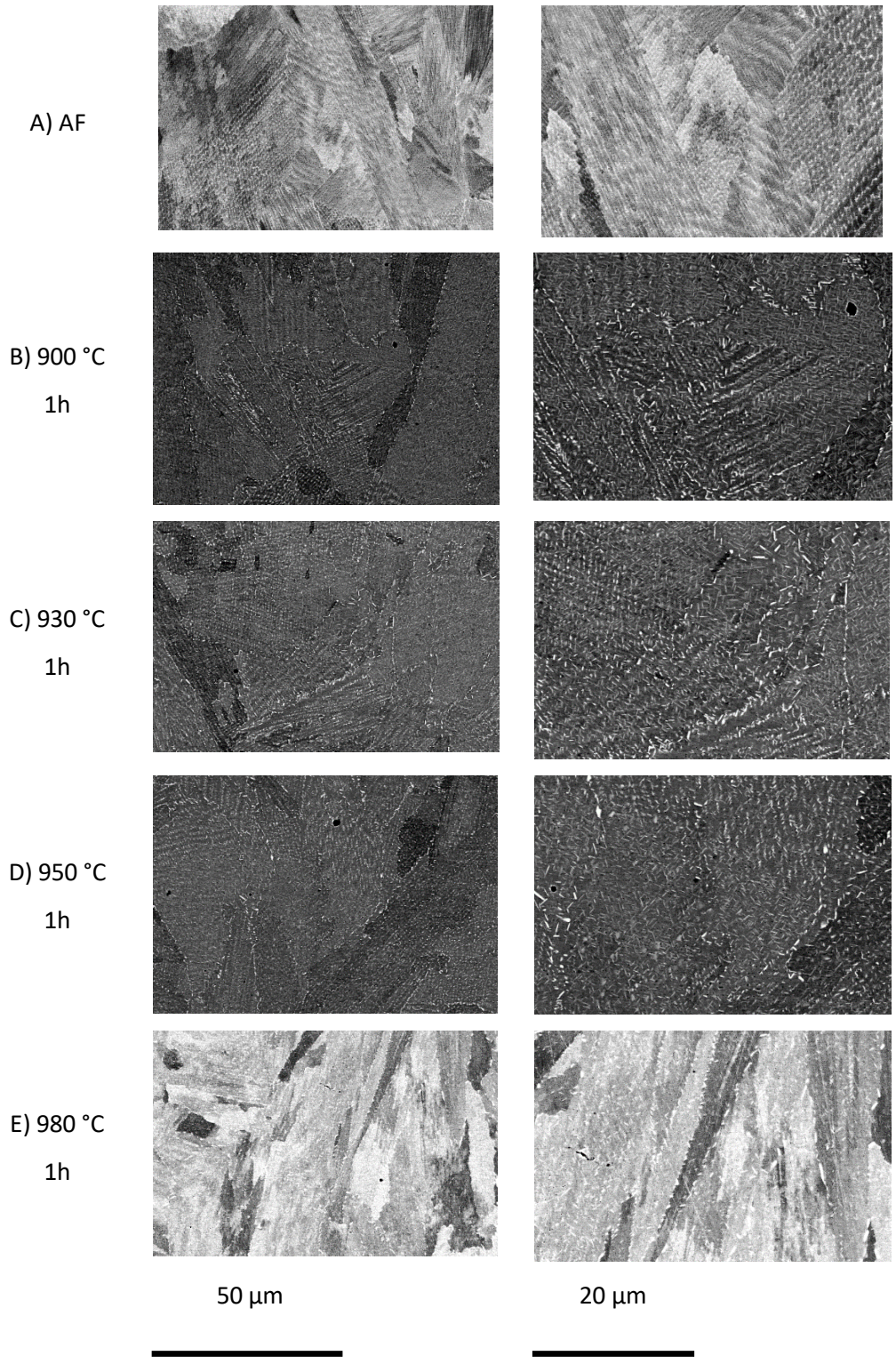

Figure 68 - Backscattered electron images showing segregation within the homogenised coupons. These images show the evolution of the morphology and distribution of the segregated grains within the material. Homogenisation between 900 °C and 980 °C B) – E) shows the formation of needle shaped precipitates, initially throughout the material but moving preferentially to the grain boundaries as the temperature is increased.

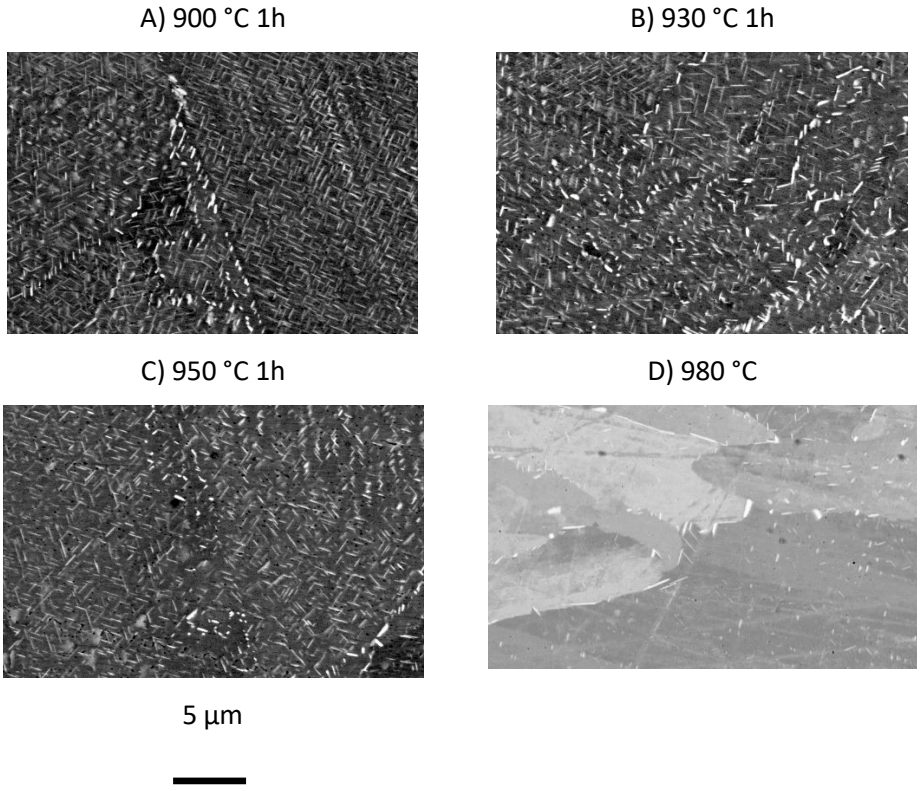

Figure 69 – High magnification images showing the morphology of needle shaped precipitates found in coupons homogenised between 900 °C and 980 °C. The needle morphology is observed in all the coupons with the length of the precipitated forming remaining similar throughout regardless of homogenisation temperature in this range.

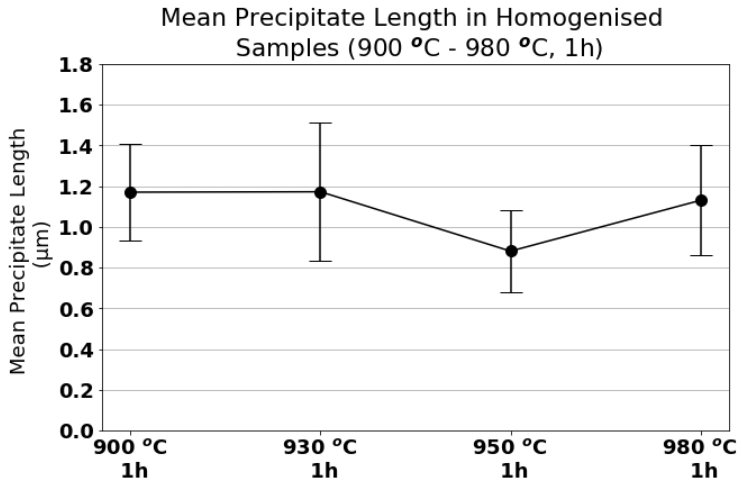

Figure 70 - Mean precipitate length (µm) measured in homogenised coupons between 900 and 980 °C. These result show that there is no significant change in the size of precipitated forming in the material as the homogenisation temperature is increased.

As well as the morphology of the precipitates, the homogenisation temperature at which they formed are strong evidence to identify them as δ phase. From the DSC results obtained from AF material, presented in Figure 67, the precipitation of δ phase in this SLM IN718 material occurs

up to and around the temperature range of these homogenisation treatment. Previously published literature confirms this, stating that within the 900 – 1000 °C temperature range the γ'' phase is readily transformed to its stable, equilibrium form δ (W. D. Cao & Kennedy, 2004; Kañetas et al., 2015; X. Xie et al., 2005). This transformation of the γ'' to the δ phase can also explain the distribution of the precipitates in the material. The δ phase in IN718 typically begins its precipitation at the grain boundaries, growing outwards (S. Azadian et al., 2001; Saied Azadian et al., 2004). This is not the behaviour visible in Figure 68 B) – E) and Figure 69, therefore another mechanism of formation must be taking effect. The transformation of γ'' to δ and the precipitation of δ at stacking faults in the γ'' precipitates have both been reported (S. Azadian et al., 2001; Saied Azadian et al., 2004) and would account for the intergranular distribution of the δ phase observed in these coupons. Although it has also been proposed that the δ phase is able to grow directly from the γ matrix without an intermediate γ'' phase (Dehmas et al., 2011), this is less likely as it is reported that AF SLM IN718 material, even prior to aging, does contain some γ'' precipitation (Chlebus et al., 2015; Huang et al., 2019; Tucho et al., 2017), also evidenced by the loss of mechanical properties through homogenisation treatments and dissolution of strengthening phases observed later in this section in Figure 81. Another mechanism for the precipitation of δ in the grain interiors seen in these coupons is simply a coarsening of existing δ precipitates already present in the interdendritic regions of the AF material, which have been reported by Kuo et al (Y.-L. Kuo et al., 2017).

From the images in Figure 69 and the plot in Figure 70 it can be observed that the length of the δ precipitates in these coupons does not change as a results of homogenisation temperature, staying consistently close to 1 µm. Previous papers have observed δ precipitates of much greater length than 1 µm following longer heat treatments (S. Azadian et al., 2001; Saied Azadian et al., 2004). This indicates that the controlling factor of δ phase length is heat treatment time rather than small variations in temperature. The growth of the δ phase might be slowed by Nb depleted regions surrounding other δ precipitates where such a high-volume fraction of δ is present. This effect is well known and is often observed preventing the formation of γ'' strengthening phase around δ precipitates (Amato et al., 2012; Saied Azadian et al., 2004; S. Li et al., 1994). This may only allow the δ precipitates to coarsen to a short length before encountering the Nb depleted zone of another δ particle, slowing its elongation.

4.3.2.5 1000 °C – 1060 °C

Between 1000 and 1060 °C, Figure 71 B) – E) a different behaviour of the δ precipitates is observed. At 1000 °C there is a significant reduction in the volume fraction of δ overall and an almost complete removal of δ from the grain interiors. This coupon is characterised by the

abundance of δ present, decorating the grain boundaries with a mostly needle or plate shaped morphology. This removal of δ from the grain interiors, which continues to completion at 1030 °C+, Figure 71 C) – E), represents the crossing of the dissolution temperature of δ phase. This correlates well with the temperature indicated in Figure 67, where the onset of the δ peak happens at ~1000 °C. The dissolution of the intragranular δ prior to the grain boundary δ is expected as precipitation of δ during solidification is known to start at the grain boundaries at higher temperatures, being eventually proceeded by the formation of δ in grain interiors (Anderson et al., 2017; Saied Azadian et al., 2004). The lack of any intragranular δ phase in the 1000 – 1060 °C homogenised coupons indicates that the water quench cooling, applied following homogenisation treatments to cool the coupons to room temperature, is successful in cooling the material rapidly enough to suppress any further precipitation of δ during cooling.

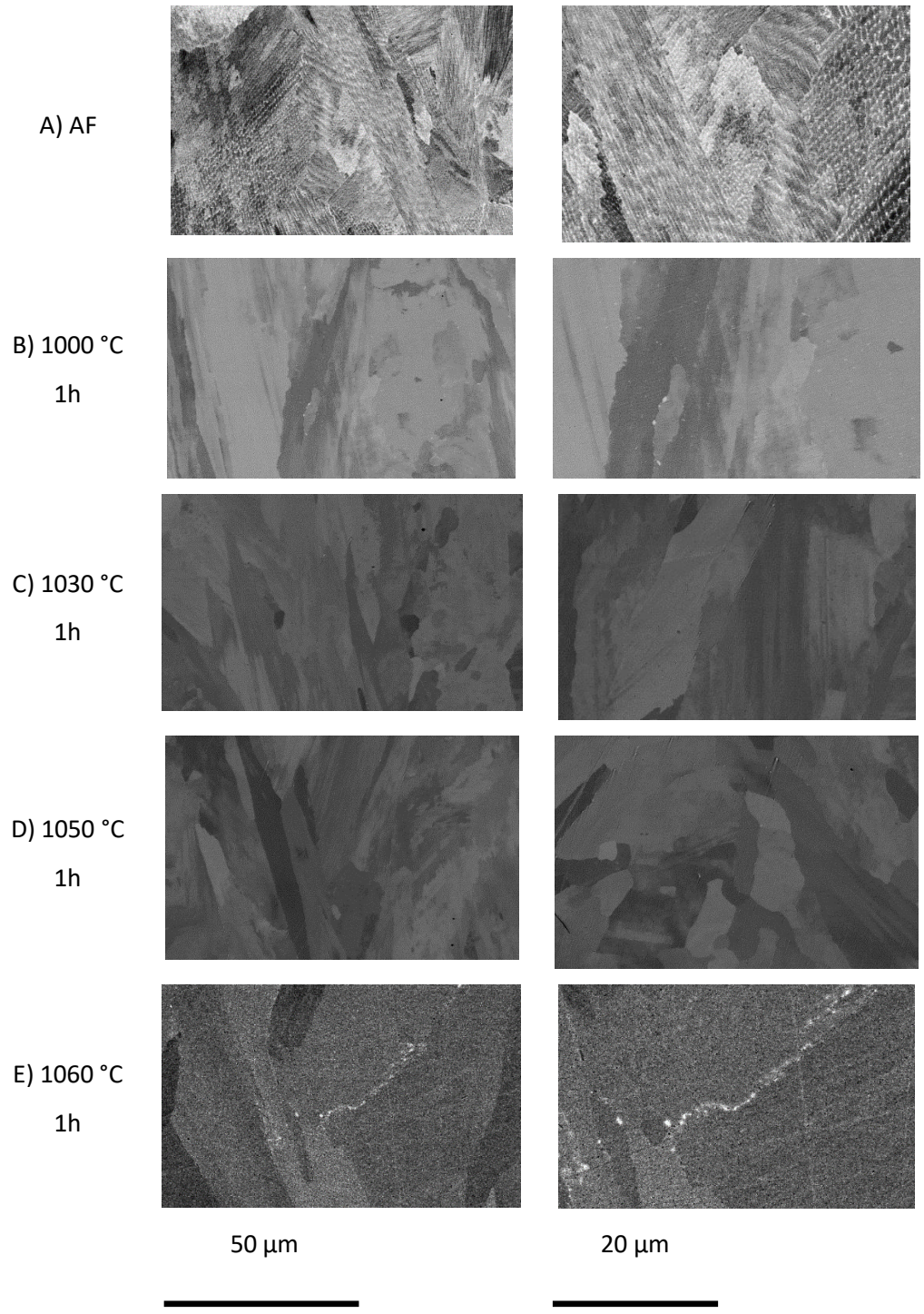

Figure 71- Backscattered electron images showing segregation within the homogenised coupons treated between 1000 °C and 1060 °C. These images show the evolution of the morphology and distribution of the segregated grains within the material. Above 1000 °C B) – E) there is a reduction in the content of any segregation.

As temperature is increased from 1000 °C, Figure 71B) – E) two further evolutions of the intergranular, grain boundary δ phase takes place. The morphology of the precipitates changes from needle like to globular and the volume fraction is reduced. In the 1000 °C homogenised coupon precipitates can be seen along all grain boundaries however at increased temperatures

the instances of δ become fewer and are only found along a small number of boundaries. This is a result of the increasing rate of δ dissolution at these higher temperatures, the grain boundary precipitates begin to dissolve. The nature of the grain boundaries which retain their δ precipitates to higher temperature is investigated in Figure 72. These images show several grain boundaries, one of which is decorated with δ precipitates, found in a coupon homogenised at 1030 °C for one hour. The locations of the precipitates are indicated in Figure 72 A) and are seen to lie across the same grain boundary, Figure 72 B) and C). The other grain boundary shown in this image is found not to feature any δ precipitation. The significant difference between these two boundaries is their misorientation, with the boundary retaining precipitates having a much greater misorientation, 30 – 50 ° compared to 15 – 20 ° of the 'clean' boundary. At a boundary with higher misorientation the density of lattice defects and vacancies is increased due to the misfit between the two crystal structures meeting (Alabbad & Tin, 2019; Hiroshi, 2014). These defects provide lower energy locations for the δ precipitates to reside in, making them more resistant to heating. This difference between grain boundaries and grain interiors is the reason the δ precipitates remain at boundaries at higher temperatures, as well as why higher misorientation boundaries retain δ precipitates for longer and at higher temperatures than lower angle boundaries (Alabbad & Tin, 2019; McDevitt, 2010).

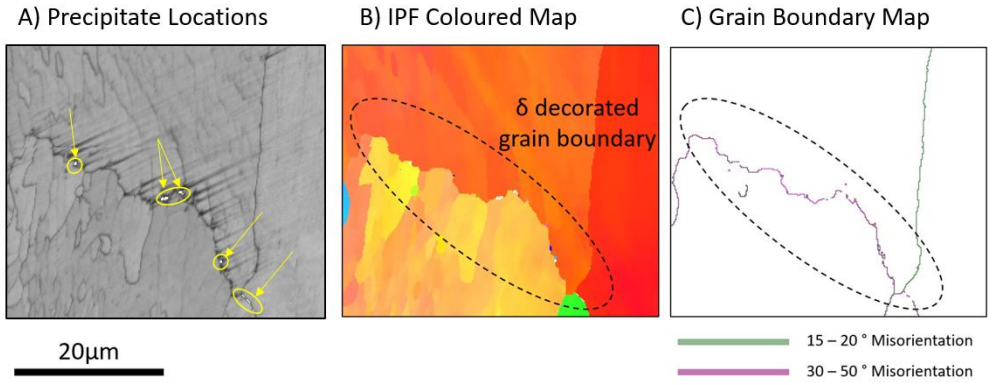

Figure 72 – Images of a δ precipitate decorated region of material following homogenisation at 1030 °C for 1 hour. A) shows the precipitate locations, B) shows an IPF coloured map making the different grains present easily distinguishable, C) plots the grain boundaries coloured according to their misorientation angles. These images reveal the nature of grain boundaries which retain their δ precipitated to higher homogenisation temperatures. The higher angle boundaries are more stable locations for δ precipitation.

The change in morphology from needle to globular δ between 1000 °C, Figure 71 B) and 1030 °C+ Figure 68 C) – E) represents an important transition. Previously published literature has investigated the effect of the δ phase on the high temperature properties of IN718 material and found not only an influence of the volume fraction of δ present but also of the morphology. It is

reported that the globular form of δ is preferable for improved stress rupture, high cycle fatigue and creep behaviour (S. Li et al., 1994) while the needle shaped form has been noted to provide preferential sites for the cavity formation and growth (Desvallees et al., 2006). This change of the δ phase morphology which occurs between 1000 °C and 1030 °C is an important observation for targeting homogenisation treatments to improve the stress rupture life of SLM IN718.

4.3.2.6 1100 °C +

As has already been observed, the segregation and subsequent delta precipitates are seen to almost completely dissolve into the bulk matrix after treatment at 1060 °C. This was consistent with the observation that there were almost no precipitates observed in the material treated above this temperature. Very small, globular precipitates were present in limited locations in the 1100 °C treated material and no precipitates were present at 1180 °C, pictured in Figure 73.

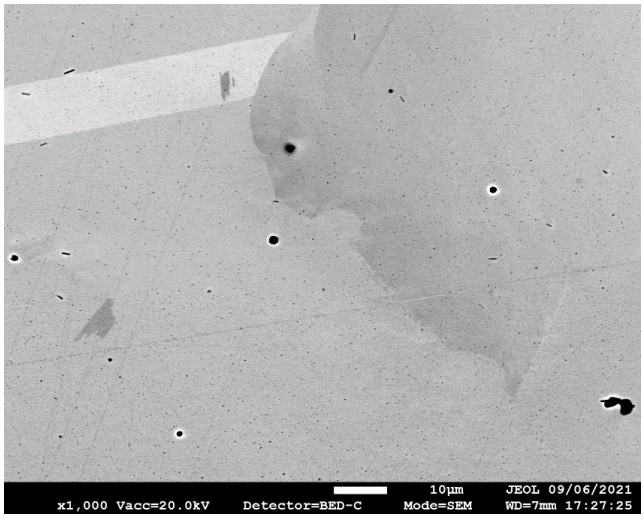

Figure 73 - SEM image of material treated at 1180 °C for 1 hour. No precipitates are now visible anywhere in the material.

There was also a significant difference in the segregation structure of material treated at 1250 °C however discussion of this is reserved for investigation in section 4.4, where this treatment and the material behaviour is investigated in much greater detail.

4.3.3 Macrotexture

The pole figures in Figure 74 provide a snapshot of the texture evolution throughout the homogenisation temperatures. The temperatures selected cover with side of the previously identified grain coarsening threshold. The 1250 °C coupon is selected for the coarsened samples to represent the most significant change in macro grain structure possible. The AF material, Figure 74 (A) does not display a strong texture, with a max MUD less than 2.0. This indicates that

despite the epitaxial and competitive growth of the grains during manufacturing there is no significant texture dominating the material and preferentially growing. SLM material is commonly observed to display a fibre texture with the preferred crystal direction, <100> aligned parallel to the build direction (Kunze et al., 2015; Thijs et al., 2013; Zhou et al., 2015). This texture is not present in these coupons due to the rotation of the rastering pattern between subsequent layers. This rotation changes the local direction of heat flow throughout the coupon and weakens the crystallographic texture (Thijs et al., 2013; Zhou et al., 2015). Throughout homogenisation treatments at different temperatures this remains true. None of the homogenised coupons in Figure 74, where above or below the grain coarsening threshold, shows the development of a strong texture component.

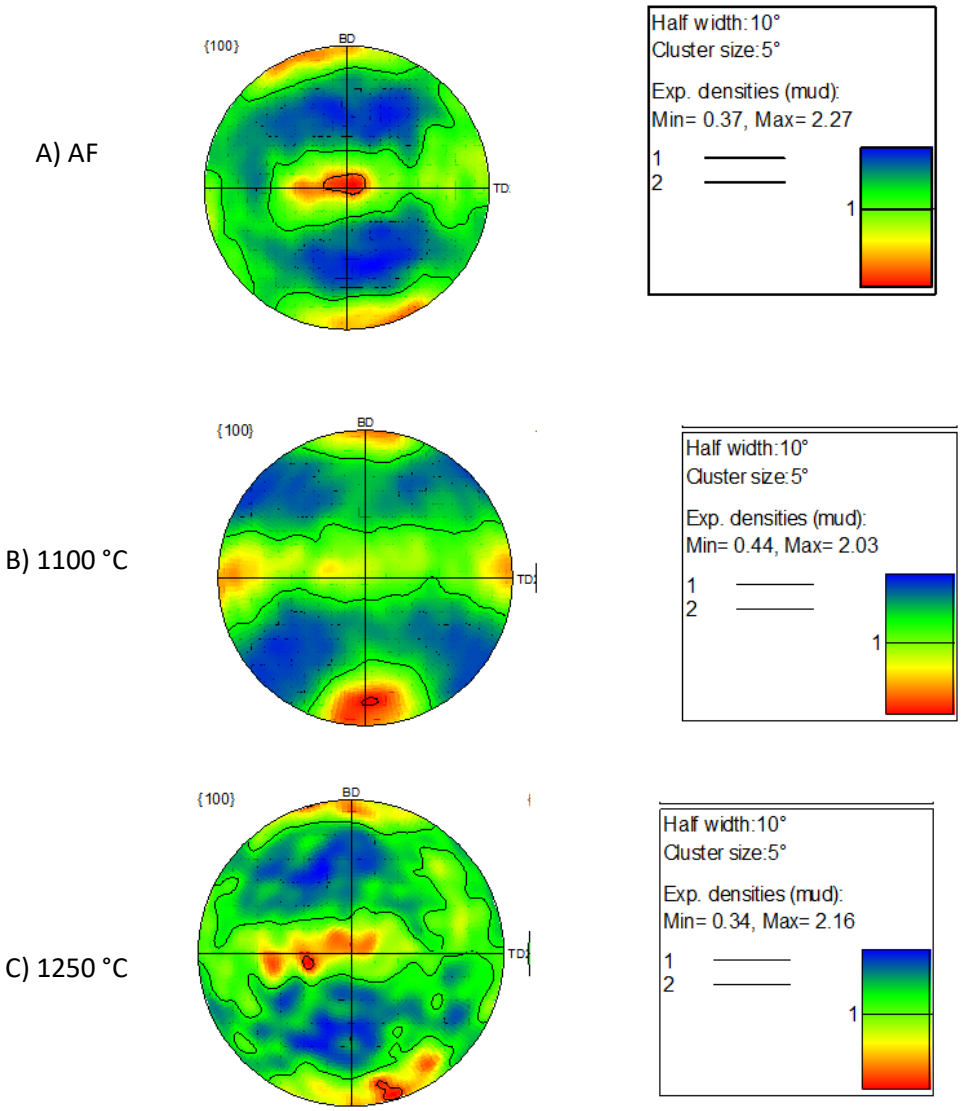

Figure 74 – {100} Pole figures plotted from EBSD data captured from as fabricated (AF) and homogenised material. Temperatures are selected to show samples homogenised either side of the grain coarsening threshold. The pole figures show that all the material, AF and homogenised, displays a weak texture. The figures also show how there are similarities in the texture displayed in all coupons.

Although weak, the texture present in the AF coupon, Figure 74A) can be seen to have several distinct regions of higher intensity, most notably along the build direction (BD) axis. These same regions can be observed throughout the pole figures in Figure 74 B) and C), although they become more diffused, as the contour lines can be seen to dissipate around them. These same texture components being discernible following all heat treatments provides evidence of a link between the microstructure of all the coupons. This is expected in the lower temperature homogenised material below the coarsening threshold, where no microstructural evolution is

observed, however at 1250°C, where extensive grain structure coarsening and evolution is observed this indicates that the grains present are evolutions of the AF structure rather than newly nucleated random grains. This will be seen in greater detail in the following section.

4.3.3.1 Subset Macrotexture

The pole figures in Figure 74, made using the entire EBSD data set shows only a weak texture with low intensity components, this makes it difficult to observe its evolution over the homogenisation treatments. To make the texture components easier to discern, the data is divided into subsets and replotted. These subsets were created based on the crystallographic orientation of the grains, with similar orientation being grouped together, giving a detailed idea of their texture and how it changes through the homogenisation treatment. Selections of grains were made around the three orientations, <001>, <110> and <111> with up to 18 ° of misorientation allowable in each case. Inverse pole figures showing the orientations included in each subset are given in Figure 75, being labelled subset A, B and C for 001, 101 and 111 respectively. There is also a fourth subset included, subset D, which contains the remaining grains which did not fall into A, B or C.

An example of an EBSD data set divided into these subsets is given below in Figure 76 where an IPF coloured map is shown of the complete and subset data. The subsets allow for the volume fraction and morphology of the differently oriented grains to be analysed for any response to homogenisation. The subsets also display stronger macrotexture, making its evolution more easily visible.

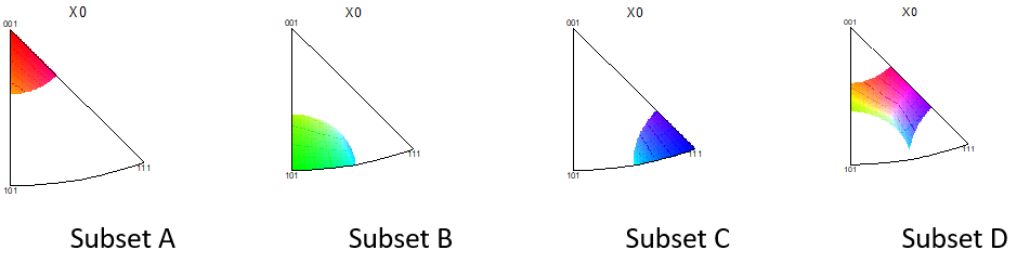

Figure 75 – Inverse pole figures showing the orientations, with respect to the build direction, of grains included in each subset A – D

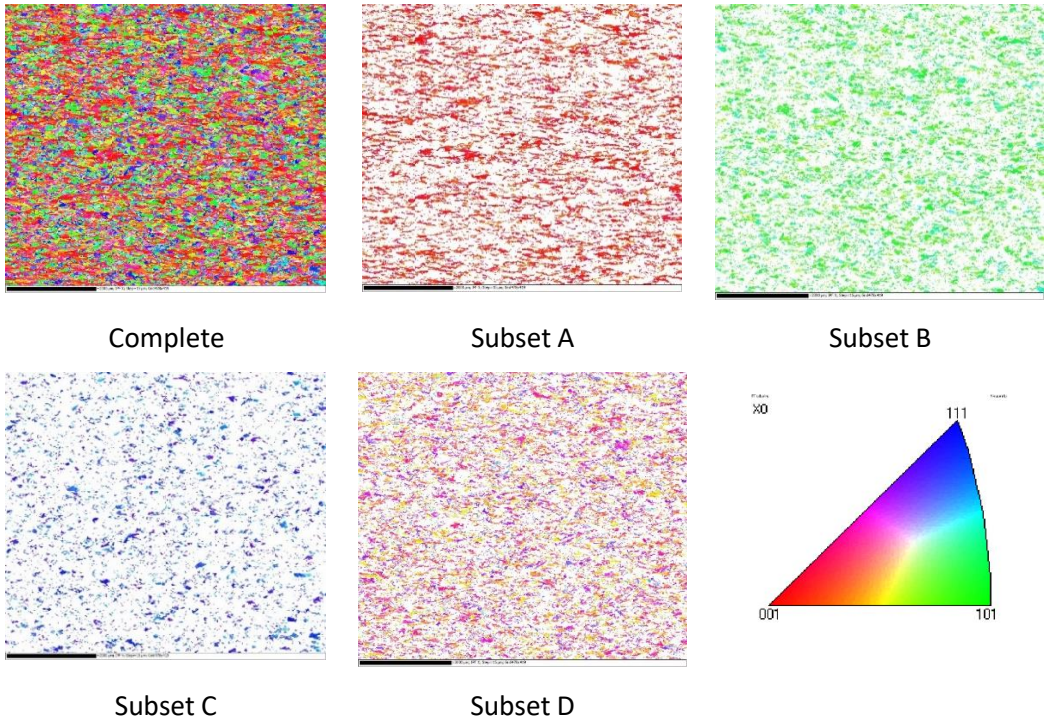

Figure 76 – Inverse pole figure colours maps of an example EBSD data set. The images show how the grains contained in different subsets can be analysed independently of one another, revealing more information about the evolution of the material. The images are for illustration of the subsets created; data shown is from the as fabricated condition.

The utility of this method is seen in Figure 77 where pole figures are plotted from each subset of the AF material. Within the subsets, texture components are much more clearly visible, even though they are weak and poorly defined when combined.

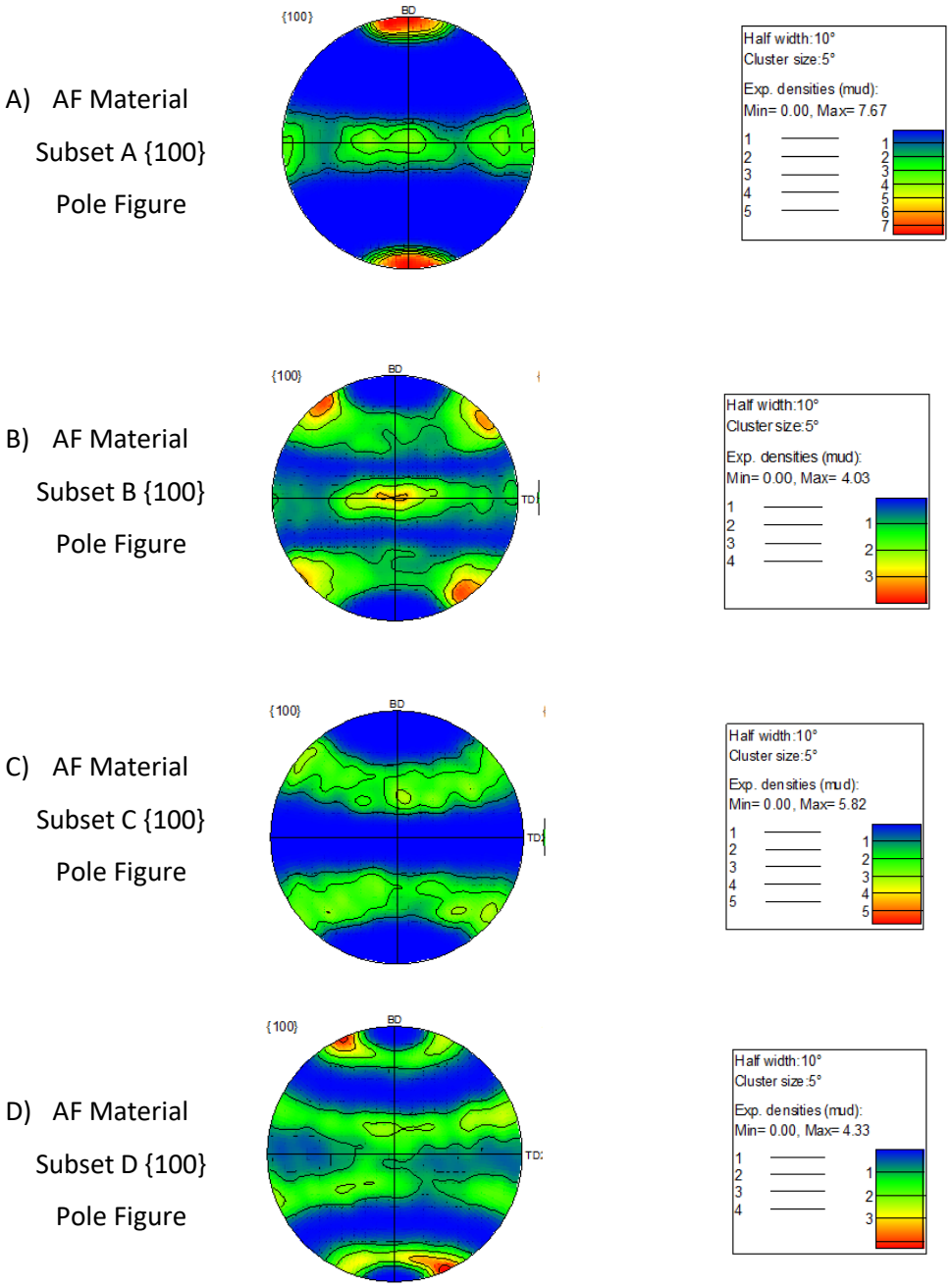

Figure 77 {100} Pole figures from as fabricated material separated into the subsets illustrated in Figure 75 and Figure 76. These pole figures illustrate how examining the different subsets of grains individually makes the texture components present much easier to see.

Subset A in the AF material coupon, Figure 77 A) and Figure 78 A) displays a fibre texture. The texture component is seen to rotate around the BD axis, creating dispersed intensity along the TD axis. This type of fibre texture has been reported in other SLM manufactured material and is a result of the directional solidification of the material. This causes the FCC crystals preferential growth direction, <100>, to be aligned parallel to the build direction while randomly oriented around this axis (Kunze et al., 2015; Thijs et al., 2013; Zhou et al., 2015). The reason that this

texture is not stronger in the complete data set is due to the rotation of the rastering strategy between layers. A rotation of 67 ° was reported by Zhou et al to significantly reduce the texture strength of SLM CoCrMo (Zhou et al., 2015).

A) AF – Subset A Grains {100} Pole Figure

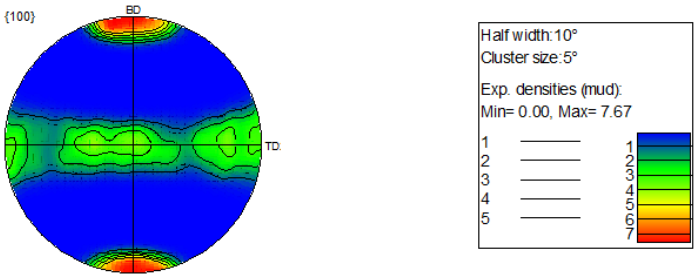

B) 1100 °C – Subset A Grains {100} Pole Figure

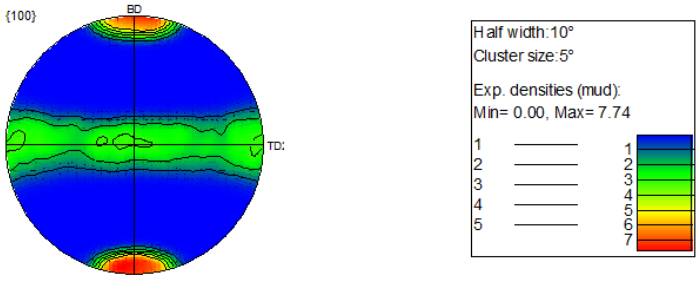

C) 1250 °C – Subset A Grains {100} Pole Figure

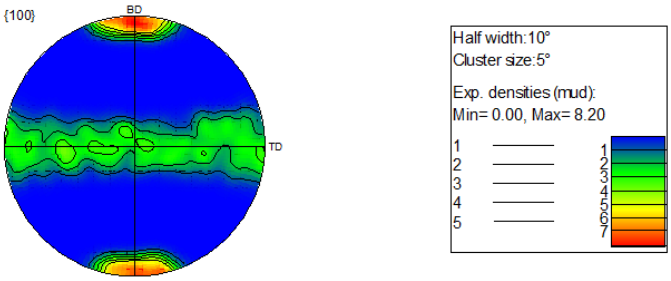

Figure 78 – {100} Pole figures plotted from EBSD data collected from Subset A in AF, 1100 °C and 1250 °C coupons. These pole figures show the evolution of the texture in the grains in Subset A. the same characteristic texture is visible throughout all homogenised conditions, indicating that the significant evolution of grain structure seen at 1250 °C is not a complete replacement of the original structure, instead an evolution.

The same texture can be clearly observed in the homogenised material, Figure 78 B) and C). The same points of high intensity at the top and bottom of the BD axis are present in all coupons with similar intensities, ~8.0 MUD. The homogenised coupons also all display the same dispersed intensity along the TD axis, indicating rotation, with little discernible difference between even the highest temperature 1250°C 2h homogenised coupon, Figure 78 C) and the AF material, Figure 77 A) and Figure 78 A). The same textural evolution is observed in other subsets. Pole figures for Subset B are given in Figure 79 and the initial cubic texture in the AF material coupon

can be seen to rotate into a fibre as homogenisation is applied. In all conditions there is a similar texture visible in the material.

A) AF – Subset B Grains {110} Pole Figure

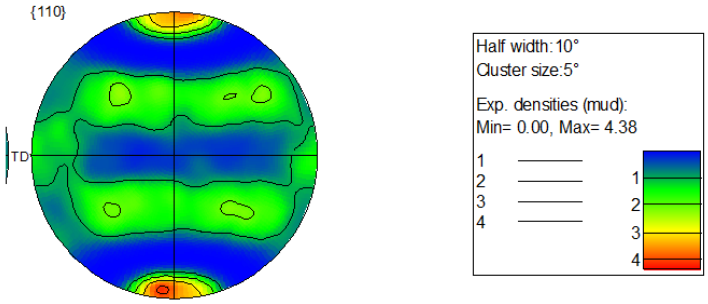

B) 1100 °C – Subset B Grains {110} Pole Figure

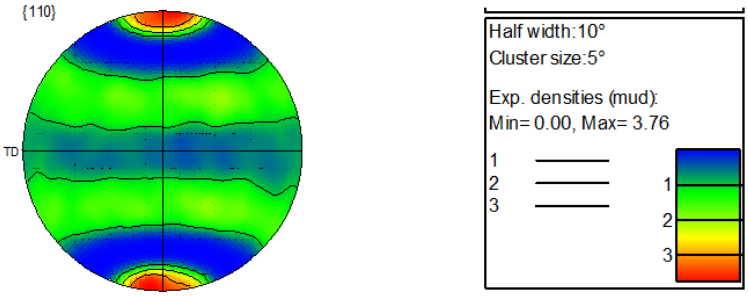

C) 1250 °C – Subset B Grains {110} Pole Figure

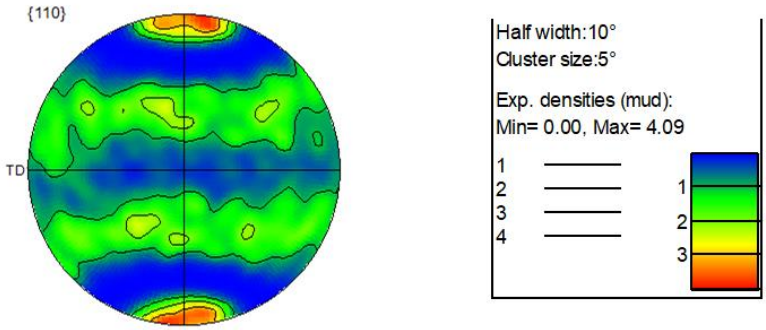

Figure 79 – {110} Pole figures plotted from EBSD data collected from Subset B in AF, 1100 °C and 1250 °C coupons. These pole figures show the evolution of the texture in the grains in Subset B. Once again, these pole figures indicate the same texture components being present in all samples. This shows that the structure is never completely removed and replace, only evolved.

This agrees with the observations made about the weak texture observed in the pole figures from the complete grain set. There is no significant or measurable evolution of the microtexture of the material throughout any of the homogenisation treatments applied during this study. Regardless of whether macro scale grain coarsening takes place, there is always a strong presence of the AF material texture. This indicates that the changes to grain structure may occur from grain coarsening rather than a recrystallisation and nucleation of a new, undeformed set of grains. This will be discussed in greater detail in section 4.4.3.

4.3.4 Aging

It was already observed in the homogenised material that treatment below ~1180 °C results in no change in the macroscopic grain structure of the material. The duplex aging treatment is conducted at a much lower temperature (720 °C and 625 °C) and therefore results in no grain structure evolution.

The aged material was also imaged using the same SEM techniques to study the precipitate/segregation structure within the material, Figure 80. The material showed no evolution from the homogenised condition with the same dendritic structure visible in the directly aged AF material, the same needle shaped delta forming and eventually precipitates disappearing altogether at 1100 °C and up. As the samples used for aging were cut from different SLM manufactured coupons and put through the same homogenisation treatment, these results can be used as a 'quasi repeat' of the initial homogenisation treatments (although with an additional aging treatment on the end). They show how the material responds in the same way, forming the same precipitates at the same temperatures. This is evidence that the results of the homogenisation investigation, even for treatments which were not repeated individually, are repeatable and representative of the material behaviour.

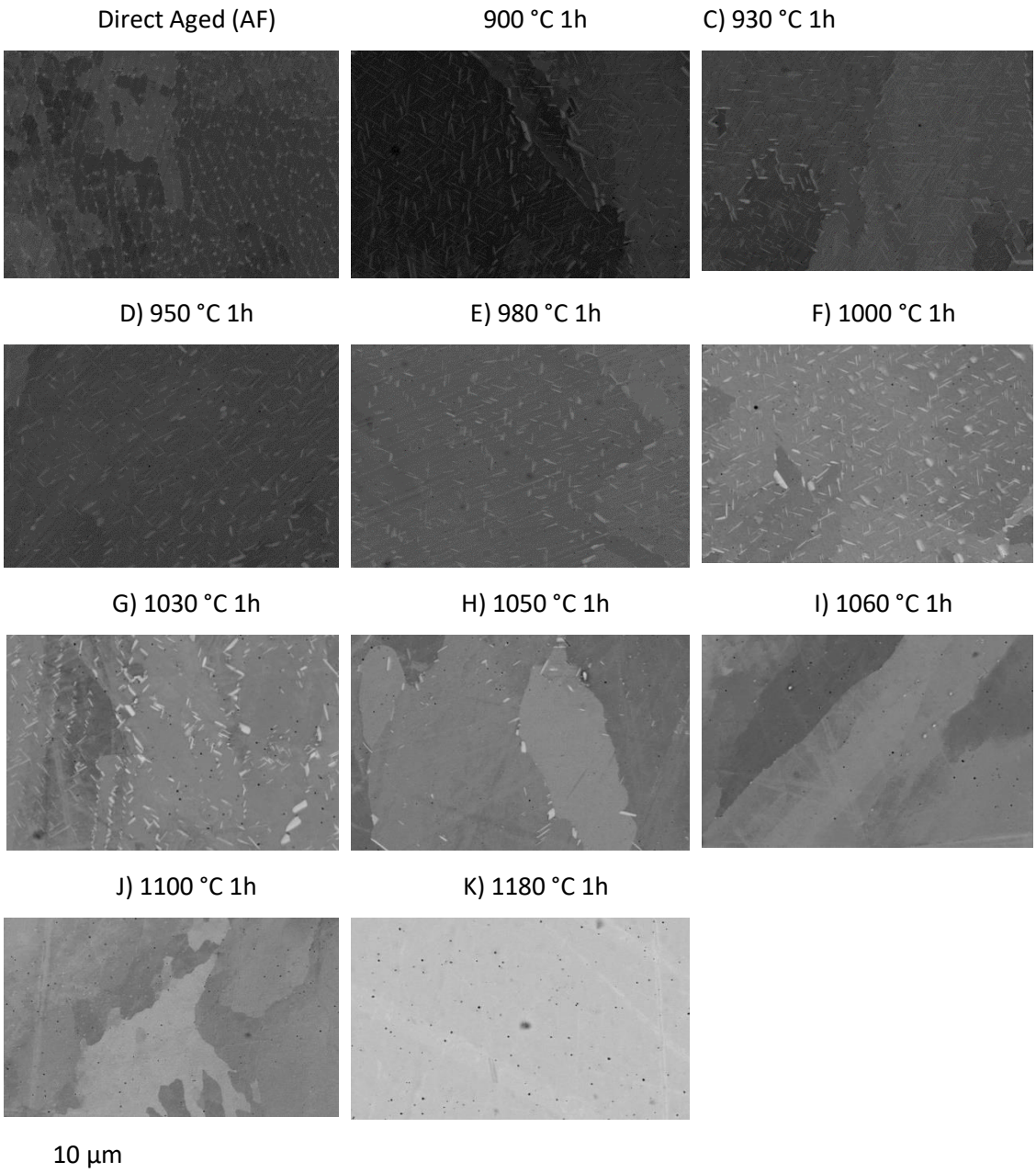

Figure 80 –Back scattered electron images of the coupons in their aged conditions. The precipitate phases in the material following aging are no different to those seen in the homogenised material. This indicates that aging has no influence on the presence of these precipitate phases or segregation structure.

These findings support the previous discussion where the precipitates present from 900 – 1060 °C were identified as δ phase. Their lack of response to aging confirms this, since the maximum aging temperature being selected purposefully outside the range in which δ phase precipitates form and coarsen quickly.

Another change in microstructure taking place in these coupons which is not visible in the images is the formation of the γ'' strengthening phase (and some amount of γ' phase). These

precipitates are typically much smaller than phases such as δ or Laves and as a result are more difficult to image. Their content and precipitation can instead only be inferred from other changes in the material which will be discussed in the following section.

4.3.5 Material Hardness

The mechanical properties of the material in both homogenised and aged conditions were characterised using a hardness test with the results being extrapolated to estimate their influence on tensile or high temperature stress rupture properties using theory and previously published literature. This approach is not ideal, and it would be preferable to directly measure the mechanical properties of interest. Unfortunately, due to material availability and coupon geometry, it was not possible to perform these tests. Hardness and theory are used as a basic indicator in this work.

4.3.5.1 Homogenised Material

The properties of the AF and homogenised material are plotted as the red line in Figure 81. The AF material represents the starting point for SLM IN718. It has already been established that this condition is not ideal for high temperature properties or aging response however it is an important reference point to which other treatments can be compared.

The hardness of the AF material was measured at 350 HV5, significantly higher than any of the homogenised coupons. Even when the grain structure of the material appears very similar, as it does with all treatments below 1180 °C, the material achieves a significantly lower hardness measurement. The highest hardness occurred in the lowest temperature homogenisation treatment, 900 °C coupon, 980 °C 1h, although this still shows a ~10% reduction from the AF condition.

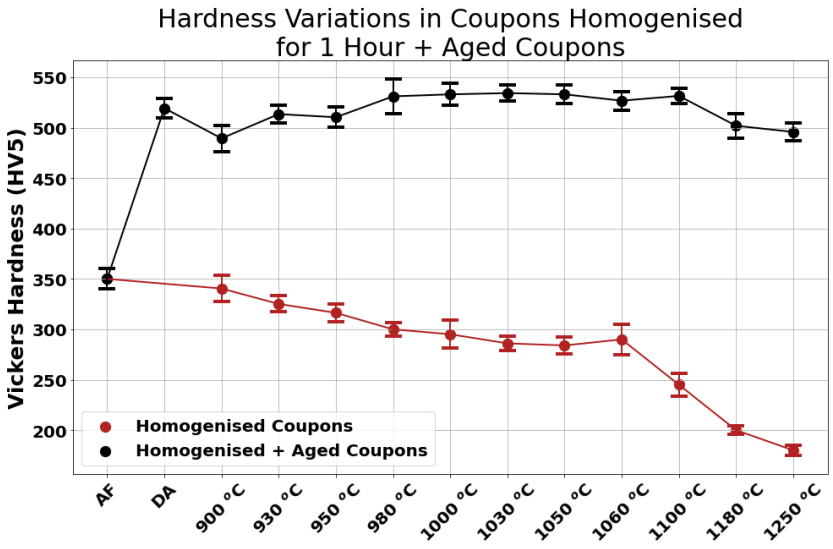

Figure 81 – Plot of mean Vickers hardness (HV5) measured in the coupons after aging. Also plotted are the hardness values measured in the material prior to aging. These results show the significant effect of aging the material and the large increase in hardness that it yields. Error bars show the standard deviations of repeat measurements of the samples.

The primary mechanism responsible for the reduction in hardness, and other mechanical properties, in all the homogenised coupons is the dissolution of strengthening precipitate phases, predominantly the γ'' phase. Previous papers report that the volume fraction of γ'', the main strengthening phase in IN178, will start to reduce significantly at 850 – 900 °C due to a combination of dissolution and transformation to the equilibrium, stable δ phase (Saied Azadian et al., 2004; Mei et al., 2015; Oradei-Basile & Radavich, 1991). This process has been reported to take less than 30 mins at 870 °C (Oradei-Basile & Radavich, 1991) so for even the lowest homogenisation temperature of 900 °C this process will have had a significant effect after an hour, removing the strengthening provided by the γ'' phase. The γ'' phase usually provides a barrier to the movement of dislocation through the material required for it to deform, the reduction or removal of these phases and the increase freedom of the dislocations to move through the material led to the loss of mechanical properties. The development of this effect can be seen in the most clearly in the difference in yield strength of the different homogenisation temperature coupons. Between 900°C and 1100°C the yield stress reduces as the temperature increases. As these coupons were all homogenised for equal time, this shows how the dissolution of strengthening phases happens more quickly as the temperature is increased.

Another contributing factor in the difference in hardness as homogenisation temperature is increased could also be the recovery process taking place and the reduction of sub grain misorientations. These sub grain networks of dislocations and misorientations act similarly to

strengthening precipitate phases, providing barriers to the movement of the dislocations required to induce permanent, plastic deformation in the material. As the amount of these sub grain dislocations is reduced the material will become les resistant to deformation and therefore softer.

In the coupons homogenised at 1180 °C and 1250 °C there is an additional mechanism acting in the material to further reduce the yield strength of the material over and above the previously discussed strengthening phase dissolution and strain recovery. The grain structure in these coupons was observed to coarsen significantly. This contributes to Hall-Petch softening. The grain boundaries within the material are areas of dislocation, these act in the same way as the sub grain low angle misorientations previously discussed, providing barriers to the movement of dislocation through the material. The coarser grain structure, and more equiaxed morphology, of these two coupons contains a reduced grain boundary length compared to the AF material. With fewer grain boundaries, the dislocations encounter fewer barriers to their movement as can move more easily through the material, degrading yield strength.

The reduction is mechanical properties of the material in the homogenised condition does not represent a failure of the treatments to improve the material. This is the desired effect from the treatment. The aim of a homogenisation treatment is to dissolve the precipitate phases and redistribute any segregated elements uniformly through the bulk matrix. As has already been observed, this has taken place in many of the samples. This brings the material to a good condition from which a subsequent aging treatment, as is discussed in the following section, can be applied with improved results. The only coupons which are likely to have been permanently degraded by the homogenisation treatments are the two treatments above the grain coarsening threshold, 1180 °C and 1250 °C. In these samples the fine grain structure of the AF material has been lost and will not be recovered through aging. This will result in lower mechanical properties even after precipitation of strengthening γ'' phase.

4.3.6 Aged Material

The hardness results from the material in the aged condition are plotted in Figure 81 as the black line. This time these results are representative of the final, serviceable condition of the material. Following an aging treatment, the material is at its peak strength and generally the highest hardness will be desired for most applications as an indication of the optimal mechanical properties.

There is a large increase in the hardness of all the coupons following aging. This hardening of the material is excellent proof of the precipitation of the strengthening γ'' phase precipitates in

the material. All the coupons display the ability to harden significantly during aging, indicating that none of the segregation or other material conditions observed in the homogenised material are severe enough to negate this effect. These results also show that, while it was not possible to image with the SEM, the γ'' strengthening phase is indeed present in the aged samples.

The peak hardness of the homogenised material coupons is seen to depend on the temperature of homogenisation. The trend follows an arc with hardness initially increasing as homogenisation temperature is increased before reaching a peak and eventually reducing again.

The lower temperature homogenisation treatments at 900 °C, 930 °C and 950 °C yield a hardness lower than that of the directly aged (DA) material. An explanation for this can be found in the images in Figure 80 B) – D) and the precipitates which are observed therein, identified as needle shaped δ. It was previously proposed, based on literature, that these δ precipitates deplete the region of material around them of the Nb required to precipitate γ'' (Radavich, 2004; Rahimi et al., 2017; Sundararaman & Mukhopadhyay, 1993). This is the reason for the decrease in hardness compared to DA material. The large volume fraction of δ present in these coupons is preventing sufficient γ'' from forming to harden the material.

This same mechanism can be applied to explain the increase in hardness that takes place from 900 °C up to 1030 °C. As has been observed and is visible in Figure 80 B) – G), as homogenisation temperature is increased, the volume fraction of δ phase present is reduced. As the homogenisation temperature is increased in this range is exceeds the dissolution temperature of the δ phase and begins to reduce the volume fraction (Cai et al., 2007; Desvallees et al., 2006). As the δ content is reduced there is an increase in γ'' precipitation during aging as more Nb is available in the matrix. This results in the corresponding increase in hardness.

Although the material reaches its peak hardness at 1030 °C with 535 HV5 and then reduces as homogenisation temperature is increased, the hardness is measured to remain around a similar level from 1000 °C up to 1100 °C, varying only by ~5 HV5. This is a result of this temperature range being above the solvus temperature of the δ phase and resulting in similar, low levels of δ being present each of the coupons. They each undergo very similar levels of γ'' precipitation.

At the highest two temperatures there is a significant decrease in hardness to 500 HV5 and 495 HV5 in 1180 °C and 1250 °C coupons respectively. A large proportion of this decrease can be attributed to the Hall-Petch softening effect of the grain coarsening observed in these coupons as previously discussed. The further decrease in hardness of 5 HV5 measured in the 1250 °C coupon could be attributed to the additional effect of the severe segregation observed in the

material which will be discussed in greater detail in section 4.4. These areas of segregation, being found to be enriched with Nb, may behave similarly to the δ phase in depleting the γ matrix of the Nb required to uniformly precipitate γ'' strengthening phase.

An important result shown in Figure 81 is that several of the homogenised + aged coupons, 1000 °C – 1100 °C achieve a higher hardness value than the direct aged (DA) coupon. This is significant firstly because it proves that the segregation structure found in the AF material is deleterious to mechanical properties, causing a significant and measurable reduction in the materials ability to undergo age hardening. It also proves that homogenisation treatments at a suitable temperature are an effective method of recovering this lost hardening potential. The hardening potential can also be recovered while still maintaining the unique fine-grained columnar structure produced by SLM.

4.3.7 Homogenisation Temperature to Target High Temperature Mechanical Properties

While no direct tests of high temperature mechanical properties were conducted, for reasons already explained, is it possible to propose which homogenisation heat treatments might be optimal to improve them.

Several of the homogenised material conditions were observed to respond significantly better to aging than the as fabricated material being directly aged. The best performing material conditions were those treated between 980 °C and 1100 °C where peak hardness was significantly increased.

These hardness responses combined with the observations of precipitate distribution and morphology seen in Figure 72, suggest that material treated between 1030 °C and 1060 °C presents a promising prospect for the improvement of SLM IN718, especially for high temperature applications. This new post processing heat treatment route could enable SLM IN718 material, and the associated benefits of additive manufacturing (geometric freedom, no need for tooling, fast route from design to manufacture etc.) to be applied to demanding applications such as jet engine hot section components.

4.3.8 Repeatability of Heat Treatment Response

Having identified these temperatures (1030 °C, 1050 °C and 1060 °C) as the most promising for the aim of this work repeats tests were performed. New samples were cut from different material coupons from the same build and the entire heat treatment process, homogenisation and aging, was repeated to validate that the material responded in the same way. A second AF sample was also directly aged to confirm that the baseline aging response of the material was a

reliable result. In the case of all samples repeated, the results were found to correlate well with those obtained in the first round of tests. Where these repeat tests were performed the results presented in Figure 81 are a mean of the measurements taken from both samples along with the error bars showing standard deviation.

4.4 Investigation of Microstructural Evolution of Selective Laser Melted IN718 During High Temperature Homogenisation Treatments at 1250 °C

4.4.1 Evolution of Grain Structure

In order to determine the mechanism of microstructure evolution at work during homogenisation of SLM IN718 first the characteristics of the evolution will be assessed.

The grain structure evolution visible in the coupons treated at 1250 °C is clear to observe in Figure 82 and Figure 83, there is a clear increase in the size of the grains present and an equiaxing of their morphology, removing the characteristic columnar structure seen it the AF material. In Figure 83 it can be observed that neither mean grain size nor mean aspect ratio in any of the homogenised coupons shows any significant change in correlation to the homogenisation hold time. This suggests that the evolution of grain structure is completed fully within the first 15 minutes and undergoes no further significant change.

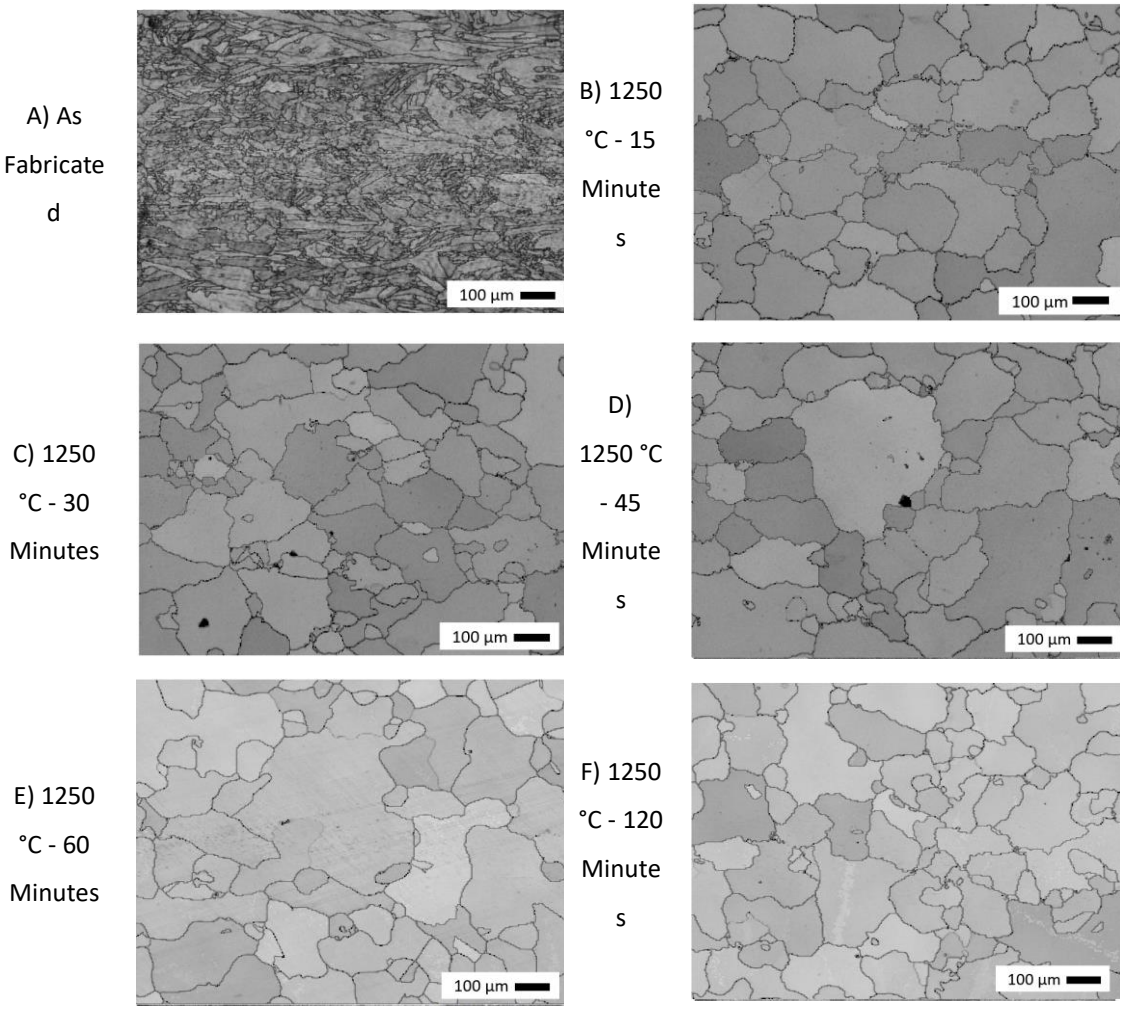

Figure 82 – SEM images showing evolution of the grain structure over time during homogenisation at 1250 °C. The build direction in these images runs along the horizontal, X axis. These images show how the evolution appears to be complete during the first 15 minutes of homogenisation.

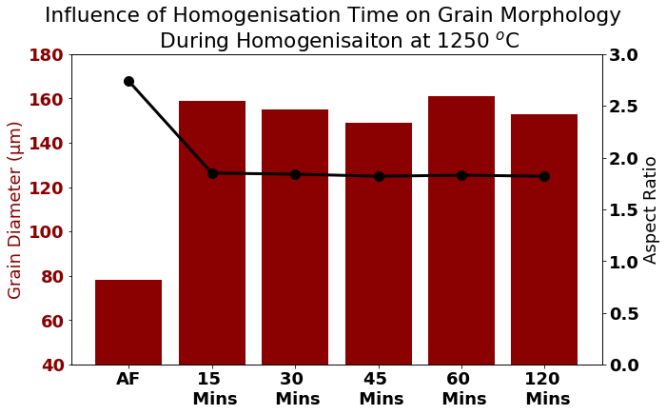

Figure 83 - Plot of mean grain diameter and mean grain aspect ratio measured from macro scale EBSD data from coupons following homogenisation at 1250 °C with different hold times. This shows how all homogenised coupons, regardless of hold time, show significant increase in grain size and reduction in grain elongation. All the hold times produce very similar grain size and aspect ratio values.

In Figure 82 the structure of all the homogenised coupons, B) – F) can be seen to dominated by coarser grains with a small number of fine grains interspersed between them. This observation is quantified in Figure 84 and Figure 85 where is can be observed that, numerically, the fine grains outnumber the coarse grains ~3:1 in the homogenised material (Figure 84) however they only account for 30 – 40 % of the total grain area.

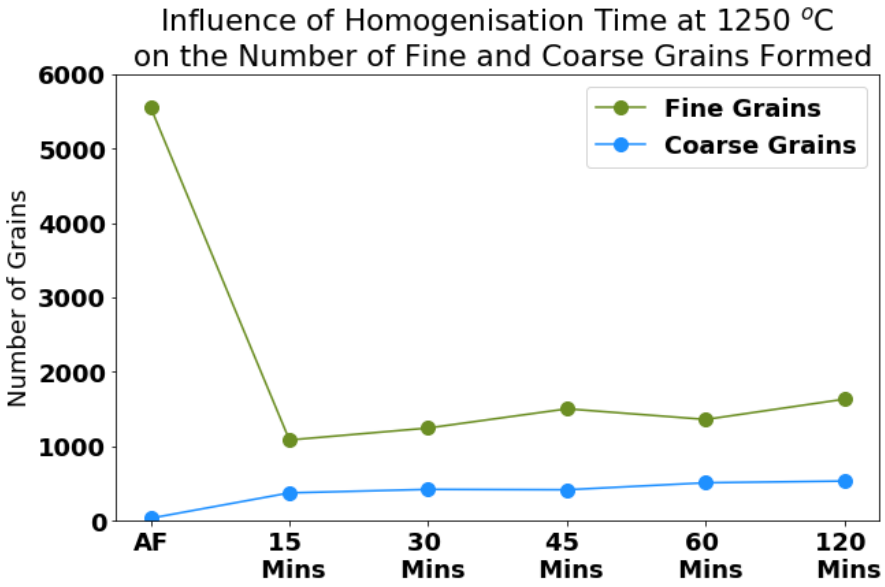

Figure 84 – Plot showing the evolution in the count of fine (>200 µm) and coarse (<200 µm) grains present in the material following homogenisation at 1250 °C. Following homogenisation, the number of fine grains is greatly reduced, and the number of coarse grains is increased. All the homogenised coupons display an overall reduced number of grains with the proportion of coarse grains being increased. By number, the fine grains still represent the majority of all the homogenised coupons.

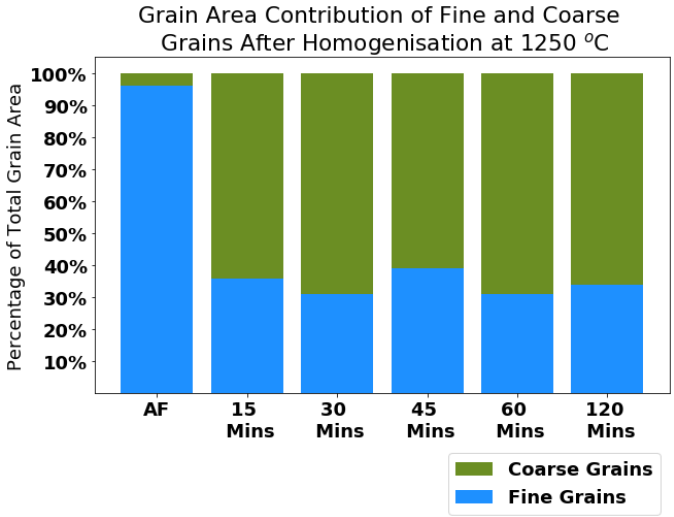

Figure 85 – Plot showing the total combined grain area contribution of both fine and coarse grains following different homogenisation times at 1250 °C. This shows the increase in proportion of coarse grains in the homogenised material which varies little with different homogenisation hold times.

Besides their size, there was no other morphological difference observed between the fine and coarse grains left in the material following homogenisation. Considering their elongation and mean aspect ratio, given in Figure 86, both fine and coarse grains achieve near identical levels of equiaxing. This suggests that, despite their size, the fine grains have still undergone a process of evolution from the AF material.

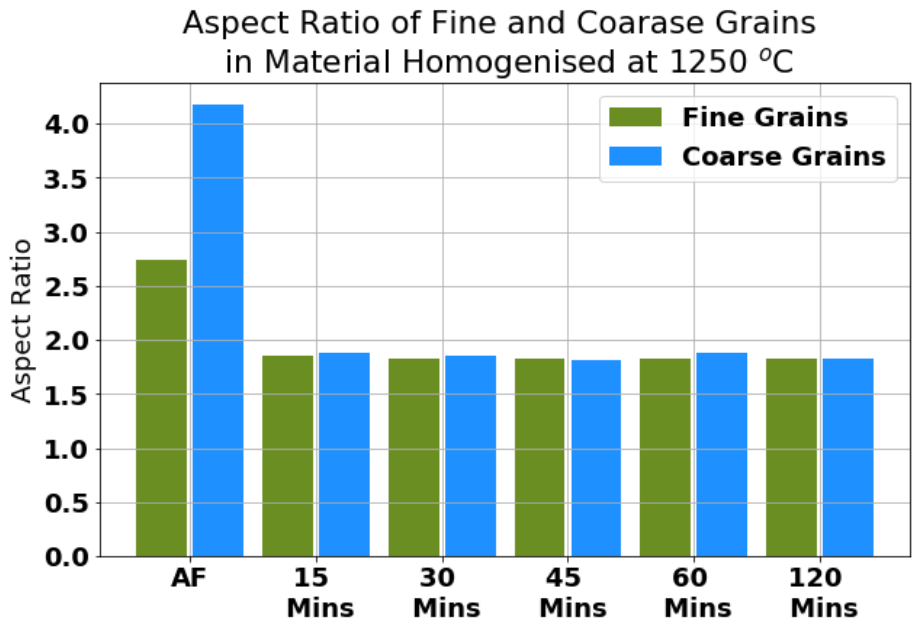

Figure 86 – Plot investigating the dependence of mean grain aspect ratio on the grain size in coupons homogenised at 1250°C. This plot shows the significant dependence of grain aspect ratio on the grain size in the AF material. This is not present in the homogenised coupons where both fine and coarse grains are measured to have near identical aspect ratio. The duration of homogenisation is shown to have no influence on this, with all the coupons having very similar mean aspect ratios.

4.4.1.1 *Influence of Crystallographic Orientation on Grain Evolution*

Further detail about the characteristics of the evolution taking place during homogenisation can be obtained by looking at some of the microstructural features of the material. Crystallographic orientation of grains within a material can often have a significant effect on the speed of their growth. This was investigated with respect to the grain coarsening process to determine whether certain orientations dominate the process.

Grains were divided into subsets by the same method as is illustrated in Figure 75 and Figure 76, grouped by their crystallographic orientation. In Figure 87 a clear preference, in the AF material coupon, for the grains in Subset A, aligned closely to the <001> direction with respect to the build direction, to achieve greater aspect ratios, therefore elongation, compared to any of the other subsets is shown. The grains in Subset A are oriented close to the preferred and fastest growth direction for FCC material such as IN718 (Kunze et al., 2015; Thijs et al., 2013; Zhou et

al., 2015). During the SLM process the grains grow competitively in the direction of heat transfer, the result of this is that the grains which grow the fastest, <100> oriented grains, dominate and reach greater elongation. Also shown in Figure 87 is the fact that following homogenisation, and the change in grain structure which occurs as a result, this trend is lost, the different subsets in the homogenised coupons no longer display any significant difference between them, all being measured at ~1.85 aspect ratio with a deviation of 0.03 either way. This suggests that during the change in grain structure there is much less or no emphasis on the competitive, unidirectional growth of the grains. Since during homogenisation there is not a single dominant direction of heat flow the grains are freer to grow in all directions.

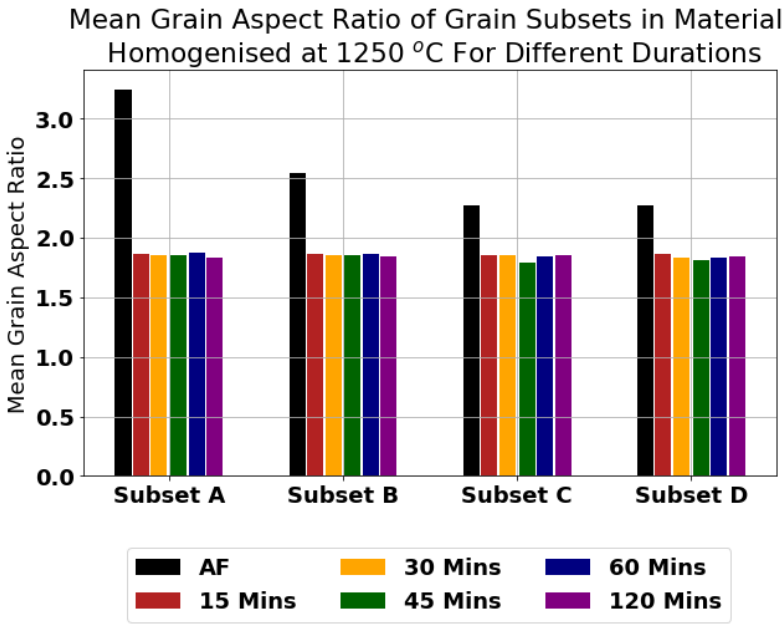

Figure 87 – Plot showing the aspect ratio of grains contained within the different subsets. This plot shows that in the AF material the aspect ratio of grains has some dependence on the different subsets with Subset A producing significantly greater aspect ratios. In the homogenised material coupons this is lost, all subsets from all durations of homogenisation produce nearly identical aspect ratios.

The change in grain structure is also examined in Figure 88, where the volume fraction of grains contained within each of the different subsets is plotted. The results shown agree with the previous statement that during homogenisation and the grain structure evolution taking place there is not a significant process of competitive growth. The volume fractions of the different subsets, although changing slightly, remain ranked in the same order, Subset D is the largest throughout all homogenisation conditions. As it has already been observed that the morphology of all the grains is changing, these results indicate that the grains from all the subsets grow at a more or less equal rate. It is possible, if the grains grow along their preferred orientation, that

in the homogenised material the result of Figure 88 might appear different if the coupon was viewed in a different plane.

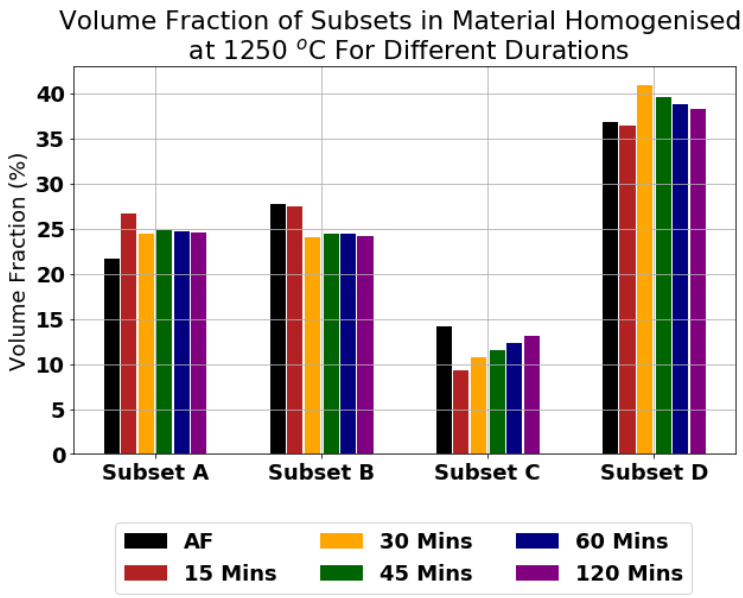

Figure 88 – Plot showing the evolution of different subsets of grains within the material. The plot shows that Subset D (section 4.3.3.1) contributes the largest volume fraction of grains to the material regardless of homogenisation condition. Homogenisation does influence the other subsets. A and B become very similar in volume following any homogenisation and Subset C is seen to initially reduce in volume followed by a steady recovery as homogenisation duration is increased.

All the data from this subset analysis supports the idea that the majority of the grain structure evolution seen to occur in these homogenisation treatments happens quickly during the first 15 minutes. In Figure 88 and Figure 87 there is very limited change observed to take place over time beyond the first 15 minutes of homogenisation.

4.4.2 Evolution of Misorientation During Homogenisation at 1250 °C

Misorientations within the material are indications of both grain boundaries and deformation. Figure 89 shows the relative frequency of different misorientation angles within the material. Compared to the AF material the significant difference occurs in the very low angle misorientations between 2 ° and 10 °. These low angle misorientations are generally associated with deformation and residual stress contained within the grains. In the case of SLM material this will be almost entirely as a result of residual thermal stresses caused by the rapid cooling during manufacturing. Following homogenisation, all the coupons can be seen to dramatically reduce the frequency of these misorientations, from a peak of ~10 % in AF material down to < 1% in the homogenised coupons. This suggests that through the homogenisation process and the grain coarsening which occurred, almost all the residual stress and deformation stored

within the grains has been removed. The small amount remaining may be due to the rapid cooling as a result of the water quench cooling of the coupon after homogenisation inducing some mild residual thermal stress.

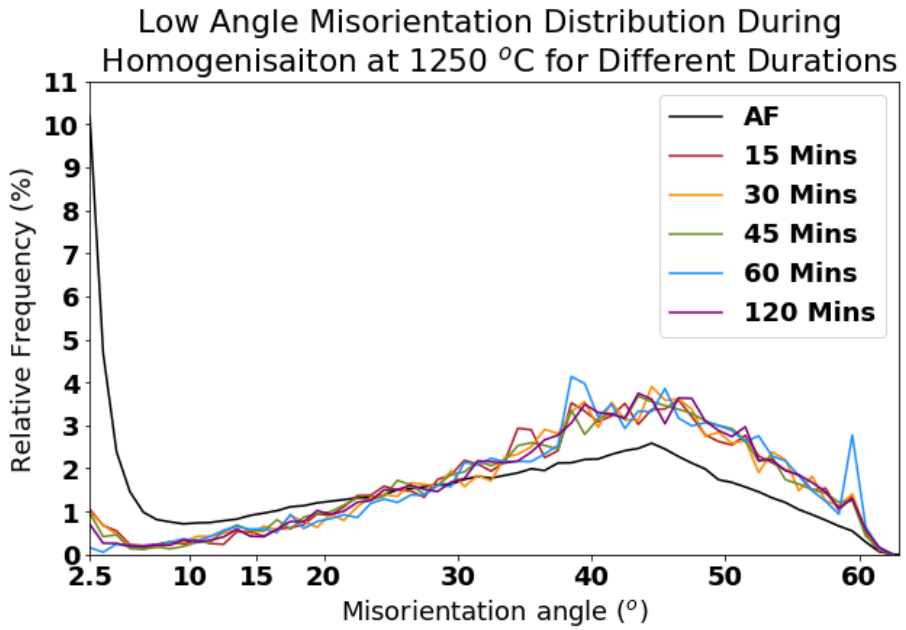

Figure 89 – Plot showing how the relative frequency of misorientations angles within the material coupons and their evolution over homogenisation at 1250 °C for different durations. The plot shows how the high frequency peak in 2.5 ° - 10 ° misorientations present in the AF material is removed in the homogenised coupons. All the different homogenisation durations produce very similar profile to each other.

At higher misorientation angles, more indicative of grain boundaries in the material, both the AF and homogenised material follow a similar trend with a rise to a peak around 45 °. The homogenised material shows a higher relative frequency of these boundaries due to the removal of a large number of misorientations at lower angles. This reduces the overall number of misorientations present within the coupons, resulting in those remaining now contributing an increased percentage of the overall total.

Once again when comparing the different homogenisation hold times, the coupons show little to no difference between them. All the lines from the homogenised coupons in Figure 89 overlap each other over the entire plot, supporting the theory that all, or the vast majority, of the structural evolution is completed iniital 15 minutes of homogeniation, with little further changes takeing place thereafter.

4.4.3 Mechanism of Grain Coarsening

Considering the nature of the evolution which takes place in the material the physical mechanism behind it can be proposed. The general evolution of the structure, coarsening and

equiaxing of the grains has been previously observed in published literature (Amato et al., 2012; Kreitcberg et al., 2017; C. Li et al., 2017; Tucho et al., 2017; Y. Zhang et al., 2017) and referred to as recrystallisation however this does not seem to be applicable to the current work. Considering the behaviour observed and the characterisation performed, the process is different.

4.4.3.1 Recrystallisation

The recrystallisation (RX) process is driven by energy stored in the material as residual stress. The process replaces a deformed grain structure with newly nucleated, strain free, equiaxed grains (Callister & Rethwisch, 2014; Guy, 1976; Mercier et al., 2002). The new grains initially form with a small size, growing by short range atomic diffusion across the boundary to consume the initial structure. It is reported that the RX process will not take place, irrespective of time or temperature of heat treatment, if the degree of cold work in the material is below ~20 % (Callister & Rethwisch, 2014; Guy, 1976). RX initially leaves the material with a refined grain structure although holding at temperature leads to coarsening of the new structure over time.

Several characteristics of this definition do not adequately describe the observed behaviour observed in the 1250 °C homogenised material in this chapter. The AF material contains some amount of residual thermal stress and stored deformation, this can be seen in the peak in low angle misorientations in Figure 89, however this is a far lower amount of deformation than might be present in a forged or rolled microstructure. This lack of stored deformation energy limits the driving force available to trigger the RX process.

The grain morphology following homogenisation is also inconsistent with RX. After the shortest treatment the overall structure is dominated by grains much coarser than those of the AF material with some instances of fine grains between them. These fine grains show no sign of further coarsening that might be associated with the growth of newly nucleated, RX, grains as they replace the deformed structure. They remain of a similar size, shape and number regardless of homogenisation time.

Considering these observations and inconsistencies with the RX process a different mechanism responsible for the microstructural evolution will be proposed.

4.4.3.2 Other Mechanisms of Thermally Activated Microstructural Evolution

It is known that there are three stages of thermally activated processes of microstructural evolution which occur when the temperature of a material is raised above ~1/3 T_m (in K), these are recovery, recrystallisation and grain growth. All these processes operate in order to bring the material closer to its thermodynamic equilibrium state, releasing and minimising stored

energy in the material. Recrystallisation has already been discussed and its characteristics are not clearly visible in the material in this chapter (although differentiating between the different thermally activated processes can be difficult to do precisely), this leaves recovery and grain growth.

The structure of the material after short hold times of 15 or 30 minutes, Figure 82 and Figure 83, is made up of roughly equally sized grains with an equiaxed morphology. After longer hold time treatments from 45 minutes and up the grains continue to evolve, with the structure now dominated by mostly large grains with a few smaller ones still present between them.

These observations indicate that the process of microstructural evolution can be divided into 2 stages. The first stage is an equiaxing of the structure, where the material loses much of its directionality and characteristic columnar morphology, this process happens quickly, being mostly complete by 15 minutes. The second stage of the evolution is an overall coarsening of the grains, this happens after longer hold times, 45 minutes and on.

4.4.3.2.1 Recovery

Recovery is a process which can begin to take place from lower temperatures than grain growth or RX. It is the process of rearranging the dislocations within the material into a more thermodynamically efficient configuration.

The dislocations present within the AF material can be clearly seen in Figure 89 with the large content of <10 ° misorientations (Brewer et al., 2006; Fang et al., 2018; D. Zhang et al., 2015). These are induced by residual thermal stress from the rapid cooling of the material during the SLM process. These dislocations form a subgrain structure where the crystal lattice is slightly misaligned, seen in section. As the temperature of the material is increased the subgrain structures cells of dislocation become more mobile and they can further rearrange themselves and, through short range dislocation interactions minimise their potential energy, either through the annihilation of dislocation di poles or through arranging themselves in a lower energy configuration (Kestens & Pirgazi, 2016). It is possible for the recovery process to take place at much lower temperatures than grain growth, leaving the structure and orientation of the material largely unchanged however it continues to happen even as the temperature is increased to grain growth levels (Callister & Rethwisch, 2014; Guy, 1976; Mercier et al., 2002). This is the reason that the low angle misorientations, seen in the AF material, were observed to reduce in Figure 57, section 4.3.2.2, and why they are almost entirely removed in the 1250 °C homogenised coupons in Figure 89 (Brewer et al., 2006; Fang et al., 2018; D. Zhang et al., 2015).

4.4.3.2.2 Grain Growth

Due to their misorientation the atoms at grain boundaries to not meet perfectly, this results in some interfacial free energy. The greater the grain boundary area (or grain boundary length) the more of this free energy there is present in the material (Callister & Rethwisch, 2014). To minimise the amount of free energy stored the material undergoes a process of grain boundary area reduction, known as grain growth. During grain growth the grain boundaries in the material migrate via a process of short range atomic diffusion across the boundary, with the direction of atomic and boundary movement being opposite (Callister & Rethwisch, 2014). Recrystallisation and grain growth are similar processes, both relying on the migration of grain boundaries, however the driving force behind each is different. Whereas recrystallisation is driven by strain energy, as previously discussed, grain growth is driven by the free energy stored at grain boundaries (Guy, 1976; Mercier et al., 2002). This means that grain growth can occur in undeformed materials, or materials with much lower levels of deformation.

4.4.3.3 Proposed Mechanism of Grain Coarsening

Considering both recovery and grain growth mechanisms a mechanism of grain coarsening can be proposed which more closely matches the observations which are made.

At 1250 °C both recovery and grain growth can take place simultaneously, the recovery takes place to almost completely remove the sub grain dislocation structures present in the AF material. This results in entirely undeformed grains without substructure, removing any small amount of the driving force that might drive RX.

The grain growth process is then responsible for the major change in grain morphology which are observed. With the aim of minimising grain boundary length, the grain growth mechanism alters the grains in two ways. Firstly, the equiaxing of the grains, this transforms the grains closer to a circle and provides a reduced grain boundary length for any given area, compared to the elongated columnar grains of the AF material this represents a reduction in stored energy. The next phase is then for the grains to grow, coarsening and absorbing other smaller grains and reducing the total grain boundary area within the coupon (Callister & Rethwisch, 2014).

The data presented in Figure 82 to Figure 89 support that both of these processes happen rapidly, begin fully completed within the first 15 minutes of homogenisation at which point they have already reached equilibrium and show no further signs of evolution.

It is also observed that the grain coarsening process affects all orientations equally. The volume fraction of grains strongly oriented in each of the primary direction with respect to the build

direction, Figure 88, is seen to remain unchanged following homogenisation. The morphology of the differently oriented grains is also equalised during the coarsening process, Figure 87. This is attributed to the nature of heating during homogenisation compared to manufacturing. During SLM heat flows in one direction and all grains compete to grow in that direction, those which are oriented in a preferred direction relative to heat flow have an inherent advantage, shown by the greater elongation and aspect ratio of <100> grains shown in Figure 87. This competitive unidirectional growth is not present during heat treatment, the material is heated and cooled uniformly in all directions. This means that grains are free to grow in any direction and each grain, this reduces competition and nullifies the advantage of grains in the preferred orientation with respect to the build direction.

4.4.4 Analysis of Quasi in Situ Electron Backscatter Diffraction

A process of quasi in situ electron backscatter diffraction (QIEBSD) was used to investigate further the grain coarsening mechanism taking place during these homogenisation treatments. The material was homogenised at 1250 °C for 7.5 minutes in an attempt to capture the material at its transition stage between the as fabricated structure and the homogenised, coarsened structure.

The images in Figure 90 demonstrate that the method employed, detailed in section 3.4.2.1, was successful in locating and imaging the same region of material between heat treatments, with the same pore type feature being visible in both images. Figure 91, Figure 92 and Figure 93 demonstrate that the homogenisation time selected as correct to allow for some amount of the grain coarsening process to take place, notably coarsening two grains in the observed area, labelled location 1 and 2 in Figure 93 B).

A) As Fabricated

B) 1250 °C 7.5 Minutes

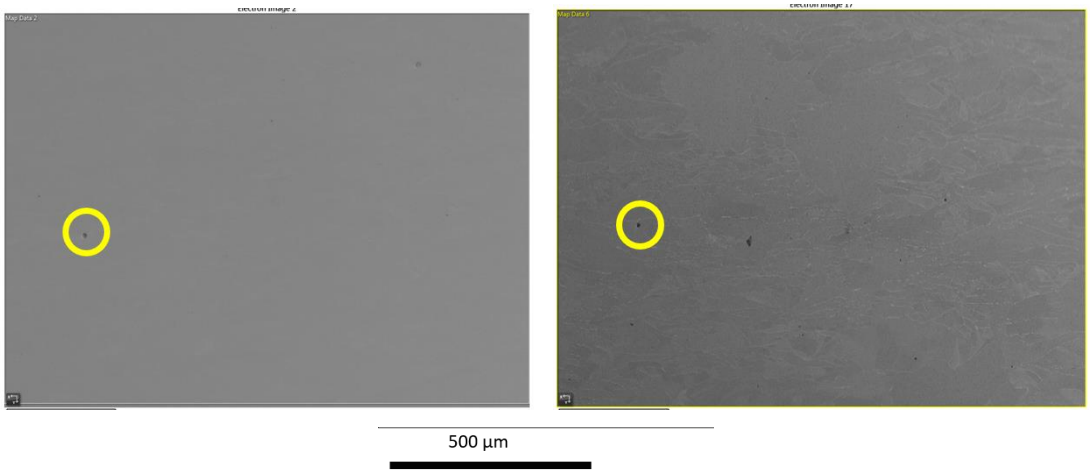

Figure 90 – Scanning Electron Microscopy images of the regions of the material scanned for quasi in situ electron back scatter diffraction before and after homogenisation at 1250 °C for 7.5 minutes A pore type defect is highlighted in both images to demonstrate that the same region is captured in both.

A) As Fabricated – Grain Boundaries

B) 1250 °C 7.5 Minutes – Grain Boundaries

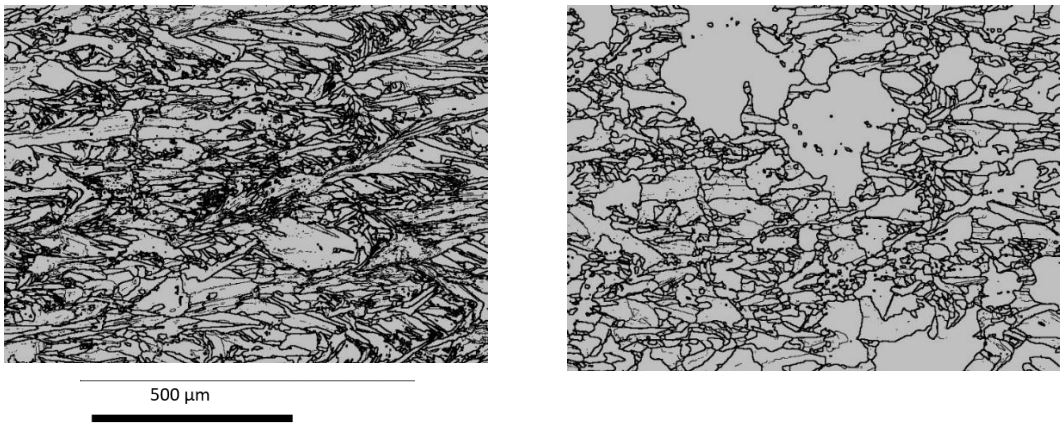

Figure 91 – Images showing the location of grain boundaries in the material before and after homogenisation at 1250 °C for 7.5 minutes. These images demonstrate that the short homogenisation treatment applied is sufficient to begin the process of grain coarsening with two larger grains visible. The homogenised material, B), still retains a structure of fine, elongated, columnar grains between the few instances of coarsened grains. These fine grains are similar in morphology to those in the as fabricated material, A).

A) AF – IPF Colour

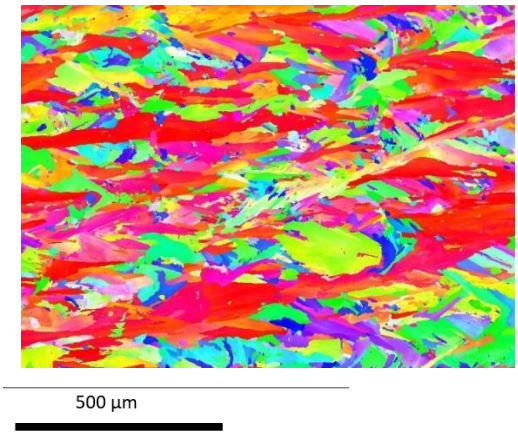

B) 1250 °C 7.5 Mins - IPF Colour

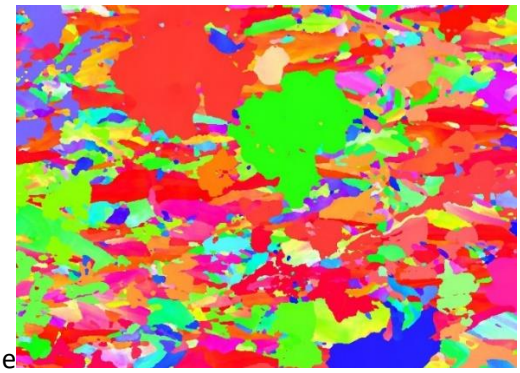

C) AF – Euler Space Colour

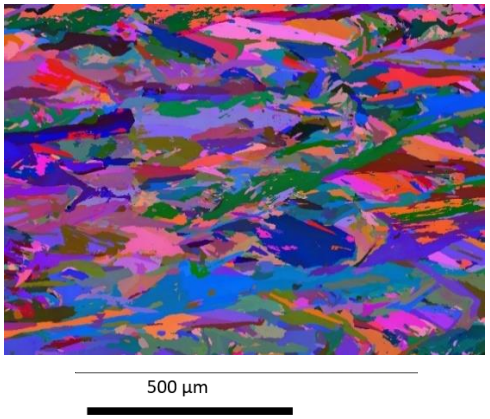

D) 1250 °C 7.5 Mins – Euler Space Colour

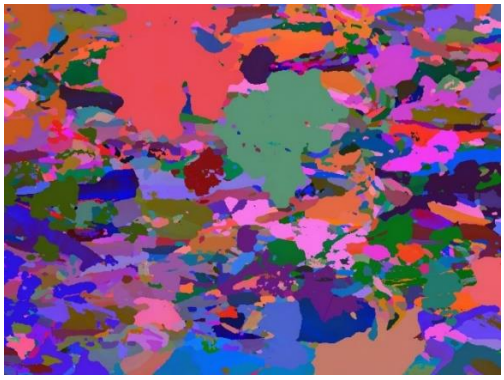

Figure 92 – Maps of electron back scatter diffraction data plotted with different colourings. A), B) are plotted with inverse pole figure colouring with orientations relative to the coupon build direction (horizontally in the image). C), D) is plotted with colouring according to the grain's orientation in Euler space. The images show that there is no relationship or similarity between the orientations of the two coarsened grains visible in the homogenised material, B) and D).

A) AF B) 1250 °C 7.5 Minutes

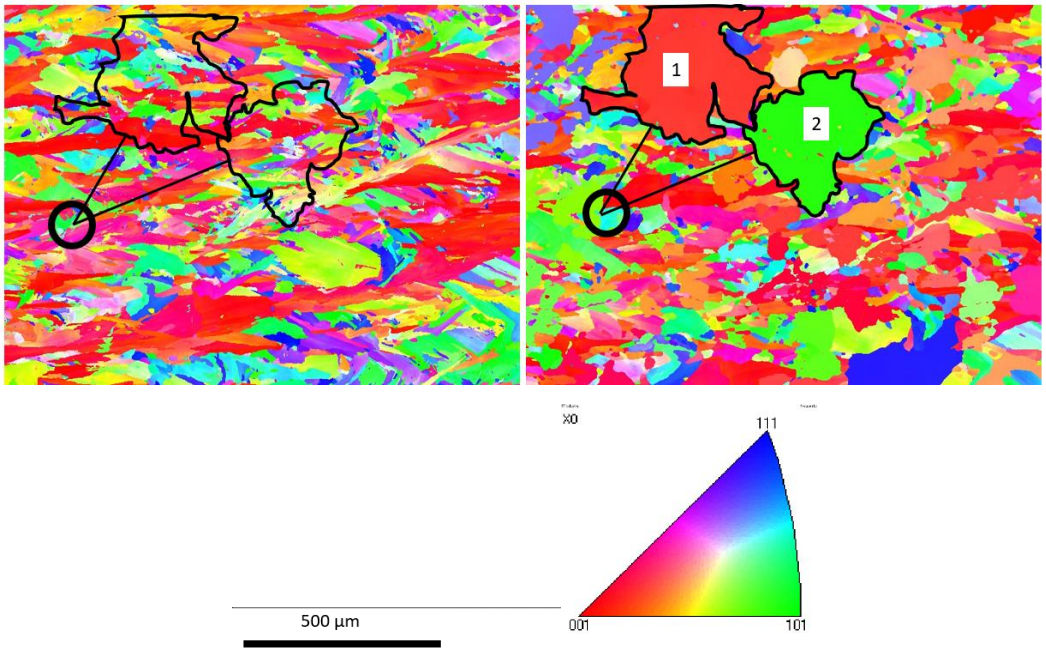

Figure 93 – Areas of interest in the material. The locations of the two grains observed to undergo coarsening during homogenisation are highlighted and superimposed over their locations in the as fabricated (AF) material. Coarse grain locations are determined by distance from the pore defect and labelled 1 and 2.

4.4.4.1 Grain Structure Evolution

The Images in Figure 91 and Figure 92 provide useful information on the grain coarsening process taking place. In the material in its partially grain coarsened state in Figure 91 B) and Figure 92 B), it can be observed that other than the two significantly coarsened grains, much of the grain structure from the as fabricated material is retained. These finer grains can still be seen to display some elongation in the build direction (horizontally in the image), however much of the angular nature of the as fabricated grains has been lost.

This observation confirms that IN718 produced by SLM does not contain sufficient residual thermal stresses to trigger a recrystallisation process. If recrystallisation was to take place it would require the nucleation of a new set of undeformed grains which would be visible in the 7.5 minute treated material. The details on mean grain aspect ratio, given in Figure 83, measure the aspect ratio of grains in the homogenised coupon. This found a reduction from 3.3 in the as fabricated material to 2.4 after the 7.5 minute homogenisation. This shows that the grains present are undergoing a process of equiaxing during this initial treatment. This equiaxing demonstrates the grain boundary area reduction mechanism occurring prior to significant grain coarsening. The mean grain aspect ratio measured after homogenisation for 7.5 minutes demonstrates that the grain structure evolution process was successfully stopped before completion, the mean aspect ratio of 2.4, although smaller than that of the as fabricated

material, is not down to the 1.75 measured in material homogenised for longer (15, 30, 45, 60 or 120 minutes), Figure 83.

4.4.4.2 Selection of grains for preferential coarsening

The aim of performing QIEBSD was to view which specific grains are preferred for grain coarsening and determine the reason for this preferential selection.

To accomplish this several different pieces of data are considered, examining the grains which are selected for grain coarsening, those which are absorbed into the coarsening grain and those which remain relatively unchanged throughout the process, remaining as sub-grains within the coarse grain.

4.4.4.2.1 Characteristics of Grains Rejected by Grain Coarsening

This discussion will first deal with the grains which are fully contained within the coarse grain forming at location 2 (Figure 93 B) in the homogenised material. These grains are rejected by the coarsening process and remain visible as sub-grains in the 7.5 minute homogenised condition.

These grains were isolated and are plotted in Figure 94, superimposed over the top of the same region of material in the as fabricated condition. The map is coloured with respect to the grain's orientation relative to the build direction. The grains not yet included into the coarse grain are all significantly smaller than they were in the as fabricated condition, this shows that as dominant grain coarsens it invades the surrounding grains. The small grains not yet included have only not been invaded due to the short treatment time. It is observed that these areas of material undergo little to no change in orientation throughout homogenisation. It can also be observed that they all display a range or orientations without indicating a preference one. From their orientations, these grains not yet included in the coarse grain cannot be considered to be similar. This indicates that a grains orientation is not a significant factor in determining whether it will be absorbed by a coarsening grain.

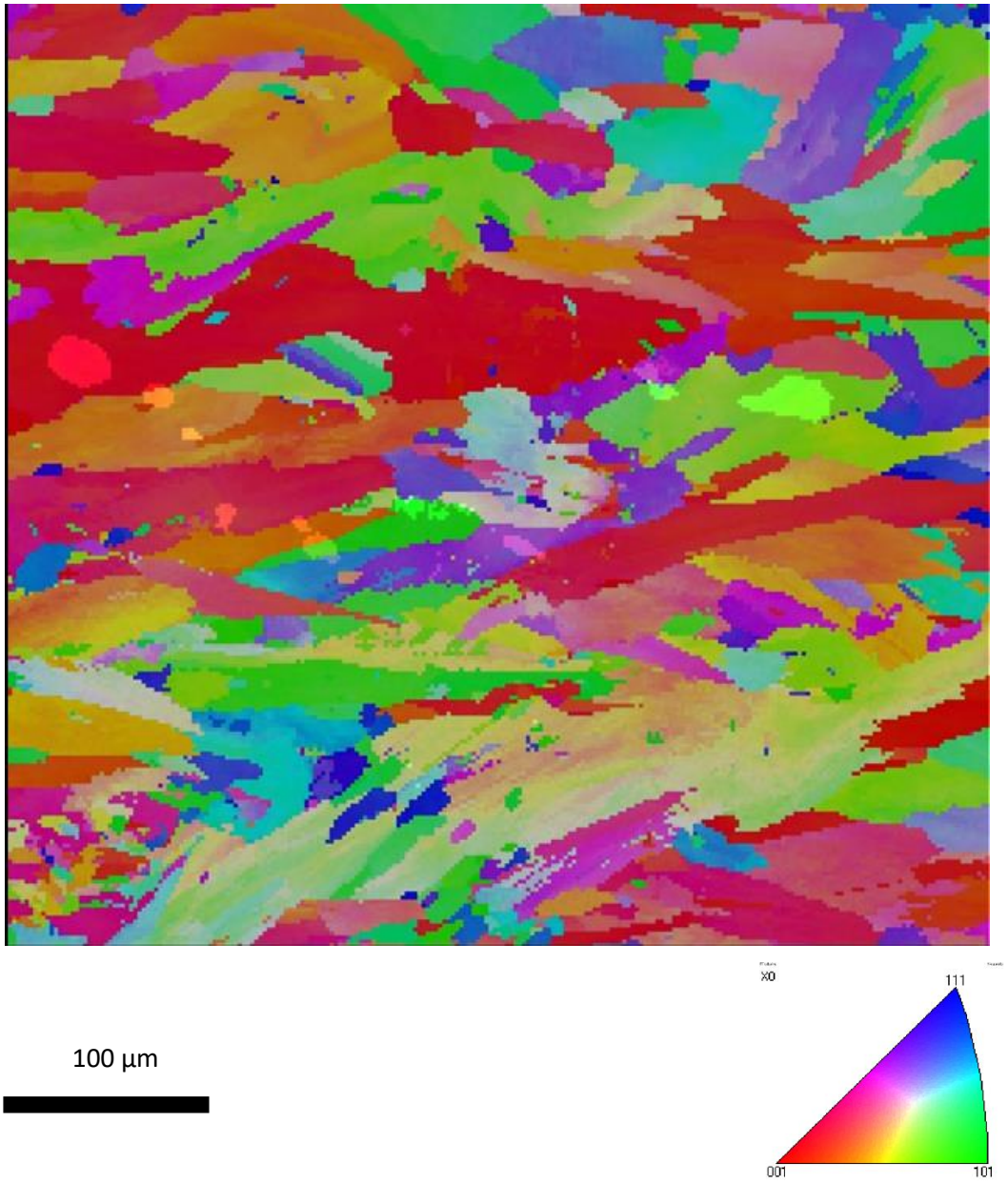

Figure 94 – Grains observed remaining within the coarse grain 2, Figure 93 are plotted using IPF colouring with respect to the build direction (horizontally in the image). The grains remaining after homogenisation are superimposed over the same region of material in the as fabricated condition. The grains are seen to reduce in size during homogenisation but not change in their orientation (indicated by their colour.

The second map of these sub-grains, presented in Figure 95, gives details of the misorientation angle between the sub grain and the coarse grain which has formed. They are all shown to have very high misorientation angles, above 30 °. This common feature between all the grains suggests that the misorientation between the sub-grain and the coarsening grain is the determining factor which makes its inclusion into the coarsening grain more difficult, requiring more time. Observations of the longer homogenisation treatments, 15+ minutes Figure 82, shows that most of these sub-grains are eventually absorbed by the coarsening grain. There are

however a few visible sub-grains remaining even after longer treatments, most notably Figure 82 C) and F) 15 minutes and 120 minutes respectively.

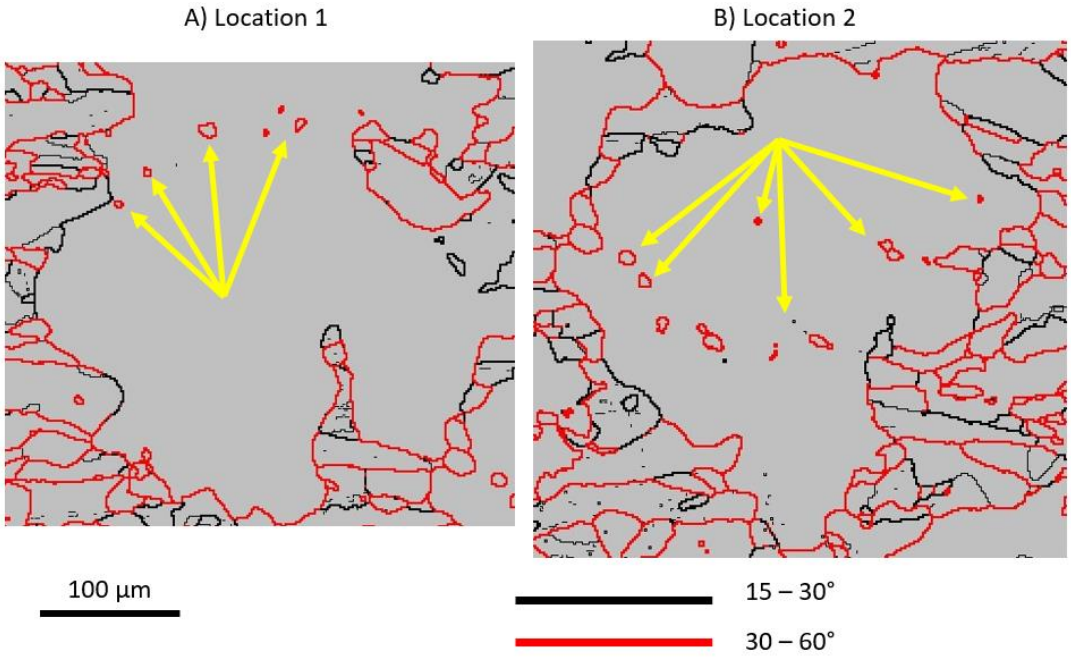

Figure 95 – EBSD Maps plotted with grain boundaries coloured with respect to their misorientation. The small grains not yet included into the coarsened grain all display a high misorientation angle above 30 °. Grains indicated by arrows.

4.4.4.2.2 Characteristics of Seed Grains and Grain Coarsening Behaviour

The grains identified in the as fabricated material to share the same orientation as the final, coarse grain are considered to be the seed grains for the coarsening process. It is assumed that these are the grains from which the coarse grain originated. Identifying the seed grains of the process is useful in helping to build a picture of how the coarsening process works. If it is possible to track where the coarsening begins, then this may help determine the reason for coarsening occurring in the way that it does.

The seed grains for the locations 1 and 2, (Figure 93 B), are highlighted in Figure 96 along with their crystallographic orientation. The orientation of the coarse grains, and therefore also their seed grains, shows no similarity or relation. Once again, as with the observations of the sub-grains in the previous section, these grains do not indicate any preference of the coarsening process for a particular grain orientation. These observations also agree with the results presented in Figure 88, where the volume fractions of different subsets were not noted to change with homogenisation. The coarsening process taking place is not significantly influenced by grain orientations.

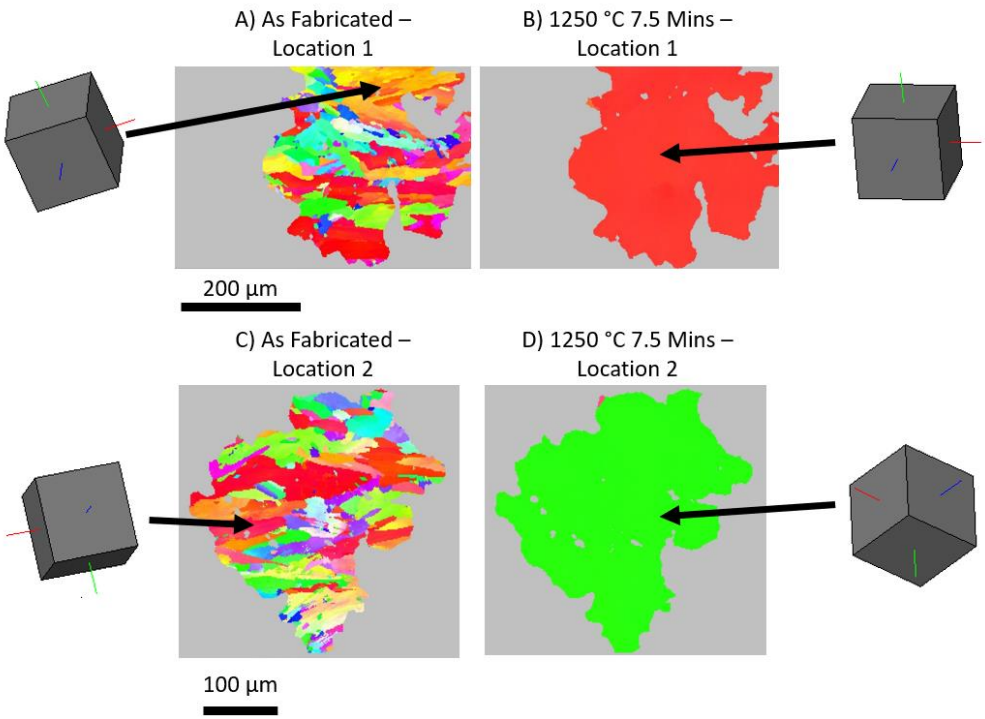

Figure 96 – IPF coloured maps of the two coarse grain locations showing the crystallographic orientation of the coarse grain forming and instances of this orientation in the as fabricated material. These images identify the seed grain in the as fabricated material which coarsened to form the grain present in the homogenised material.

As with the sub-grains, the misorientation angles and their distribution within the material are plotted in Figure 97 with the location of the seed grains in each case highlighted. The seed grains, in both locations, can be seen to be near a path of lower angle grain boundaries. As previously discussed, higher angle misorientations require greater energy input to move them, conversely lower angle misorientations require less energy. The path of lower angle misorientations near the seed grains may have provided the coarsening grain with a lower energy path to follow during its initial growth period. This would give the grain an initial advantage over the other grains enclosed by higher angle boundaries. This initial advantage places the seed grain at a competitive advantage and leads to its continued coarsening at the expense of other grains.

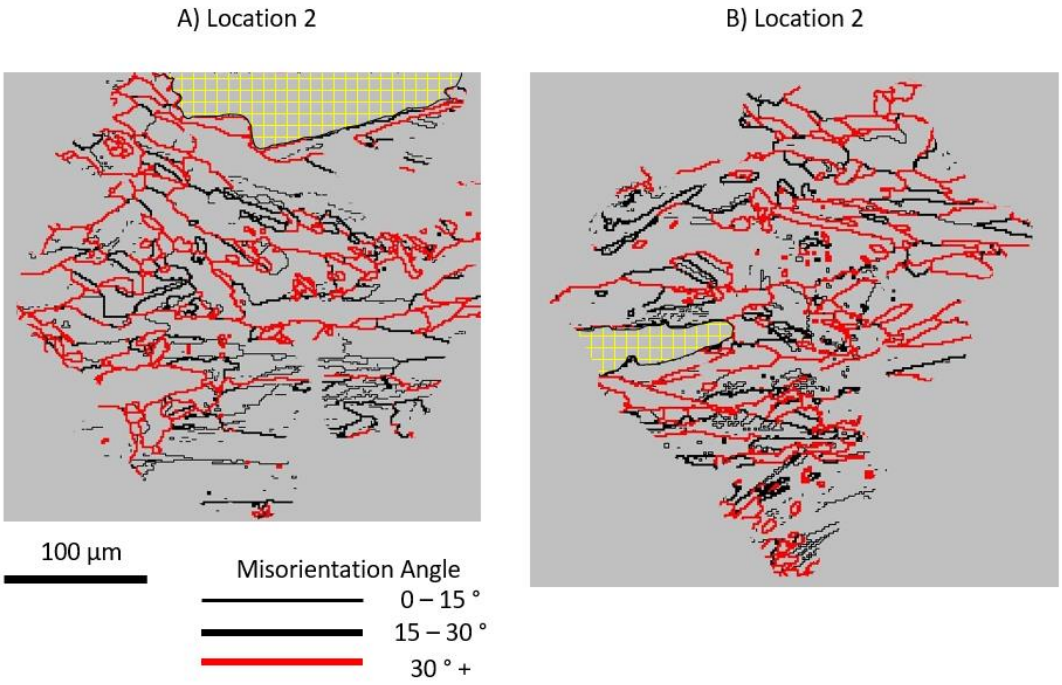

Figure 97 – Grain boundary maps of the two coarse grain locations in the as fabricated material. The seed grains identified in Figure 96 are highlighted to show their location. These seed grains can be seen to have instances of lower angle grain boundaries, <30 °, around them, more so than other grains present.

At both location 1 and 2 the direction in which the majority of the coarsening takes place could be said to be perpendicular to the build direction. The seed grains are located towards the edges of the final, coarsened grain rather than the top or bottom (relative to build direction, horizontal in the image). The reason for this is the aim of the grains to minimise their grain boundary area. The grains are initially elongated in the build direction meaning that any further coarsening in that direction would yield an increase in boundary area, increasing the free energy of the system. The grain coarsening in direction perpendicular elongation results in the grain becoming more equiaxed, reducing grain boundary length and decreasing the free energy stored in the system at the boundaries, the thermodynamically preferred state.

5 Conclusions

In this chapter the conclusions of the thesis are presented. The key and novel findings are listed first followed by a more detailed, section by section breakdown of all findings and conclusions.

The key findings of this work are as follows:

- For SLM processing IN625 powder having a significant content of particles <10 µm severely hinders processability, making it impossible to manufacture any coupon with during testing
- Revolution avalanche analysis is found to be the most suitable of the methods tested for characterising powders for SLM. It was able to quantitatively resolve differences between similar powders while still being able to process a wide range of powders, flowable or not.
- A theory is proposed for the influence of laser scan speed on the microstructure of SLM IN625. The microstructure is found not to respond linearly to changes in scan speed. Through a proposed reheating effect, higher laser scan speeds can maintain a higher average temperature in the material and therefore yield a coarser microstructure, similar to a much slower scanning laser.
- A novel heat treatment route is investigated aimed at recovering the high temperature mechanical properties in SLM IN718. Through a sequence of homogenisation and aging treatments, a material is obtained which appears to have favourable characteristics for high temperature properties. This treatment route is novel in its design specifically for SLM material and its unique as fabricated microstructure.
- The microstructural evolution of SLM IN718 during high temperature heat treatments, at 1250 °C, is investigated. A novel mechanism is proposed for the changes observed in this work when the material was observed quasi in-situ during heat treatment. It is proposed that a sequence of recovery, and grain growth is taking place rather than recrystallisation.

5.1 Investigation of Powder Characteristics and Metrology Methods for Application in Selective Laser Melting

- Investigation of powder characteristics and their influence on the SLM process revealed that the particle size distribution of a powder can significantly limit the processability of a powder. In powders where a significant proportion of particles present are below a threshold value, estimated to be 10 µm, the powder becomes impossible to process.

This is attributed to the significance of interparticle Van der Waals forces in comparison to the small weight force of individual particles.

- Of the powder rheology methods tested a rotating avalanche analysis approach was deemed to be most suitable for SLM application. This method was able to process all three powders in the study and find differences in the behaviour of similar powders. The method also most closely matches the stress state of the powder during the recoating process, critical for an accurate characterisation of the powder behaviour during the process.

5.2 The influence of Selective Laser Melting Process Parameters on Microstructural and Mechanical Properties of IN625

- The contour scan implemented during SLM, used to fuse the outer layer of material, was effectively manipulated to yield and improvement in as fabricated surface finish. By using lower energy parameters than the in-skin material the contour scan was found to be effective in remelting and smoothing loose powder particles which had become partially sintered to the material surface during in-skin scanning. A 66% reduction in surface roughness (R_a) was achieved using this method. Any improvement in surface roughness will open new applications for the material, reducing the number of operations, and by extension, cost per part for applications where such a finish is applicable. For other applications however such as critical mating faces or bearing journals, further finishing would still be required.
- Evolution of the microstructure was observed as a result of modifying in-skin processing parameters. Changes in mean grain size and aspect ratio resulted from different parameters. This was concluded to be a result of the process parameters effect on melt pool and material temperature during manufacturing. Process parameters expected to create higher temperatures were found to create a coarser grain structure with greater elongation. This was attributed to the changes in the size of the melt pool and therefore the volume of liquid material available to grow grains.
- A coarse microstructure was observed as a result of higher energy density processing parameters however also from parameters with shorter times between adjacent laser scan passes, e.g., higher scan speeds or shorter scan vectors. This is attributed to the reduced time between adjacent scan passes and a reheating effect. This work finds that this mechanism may be applicable to laser scan speed. High laser speeds were observed to create coarser microstructures, indicative of higher melt pool temperatures.

5.3 The Influence of Post Process Heat Treatments on Microstructure and Mechanical Properties

- It is proposed that heat treatments in excess of the δ phase dissolution temperature (measured to be ~1000 °C in this work), are proposed to be most beneficial for improving SLM IN718, especially elevated temperature properties such as stress rupture or notch sensitivity. Homogenisation temperatures of 1030 °C – 1060 °C are promising for creating material with an appropriately small, but not zero, δ precipitate content. This material condition, with an appropriate content of δ, is reported in literature, to be beneficial for properties such as improved stress rupture life to reduced notch sensitivity.
- Homogenisation between 980 °C and 1100 °C achieved superior hardness to direct aged material. Considering the previously observed microstructure and precipitate content it was concluded that the temperature range of 1030 °C – 1060°C is most promising for producing material with the best properties for demanding applications.
- A temperature of 1180 °C was identified as a threshold for triggering a large-scale grain structure evolution in the material. Above this temperature significant grain coarsening and equiaxing were observed, reducing the hardness of the material through the Hall-Petch mechanism.

5.4 Investigation of Microstructural Evolution of Selective Laser Melted IN718 During High Temperature Homogenisation Treatments at 1250 °C

- The grain structure of the coupons homogenised at 1250 °C was observed to be significantly coarser and more equiaxed in comparison to the as fabricated material. A mechanism is proposed for this evolution. The grains are observed to first equiax and then coarsen in order to reduce the total grain boundary area in the material. This differs from explanations in previously published literature but more closely explains the observations of this work.
- Investigations of specific grains which were observed to coarsen revealed that the process is not dependent on the orientation of the grains. It is proposed that grains are selected for coarsening based on the misorientation of their boundaries with neighbouring grains. Grains with paths of low misorientation boundaries <30 ° near them in the as fabricated condition were seen to be selected for coarsening due to the available path of least resistance.
- During 1250 °C the formation of large, irregular areas of segregation thought to be laves phase, were observed, it was concluded that these form as a result of incipient melting during the rapid heating at the start of the homogenisation process. These

regions are expected to be detrimental to material properties, restricting the formation of γ'' precipitates and providing a weak interface, susceptible to cracking during loading.

6 Appendix

6.1 Appendix I – The influence of Selective Laser Melting Process Parameters on Microstructural and Mechanical Properties of IN625

In section 4.2.4 the primary findings of interest related to the influence of laser scanning speed on the microstructure of the IN625 material produced. These samples were remanufactured in order to validate the results and the repeatability of the SLM process. This ensured that the results obtained were representative of the process.

The main results from this investigation are presented in 4.2.4.4 where the grain size and morphology was measured and averaged across both original and repeat coupons. These results quantify the change of microstructure however additional SEM images were captured as part of the investigation. These images are included in this appendix section to show the repeatability of the SLM process, as well as of the results relating specifically to laser speed and it influence on microstructure.

6.1.1 Slow Laser Scan Speed

The images below in Figure 98 compare both low and high magnification images of the original and remanufactured coupons for the slowest laser scan speed. At lower magnification the macro scale grain structure is clearly visible showing the same columnar grain structure. At higher magnification the interdendritic segregation is visible as a network of brighter white bands. These images illustrate the repeatability between samples from the SLM process used in this work. The grain structure is quantified in the main text.

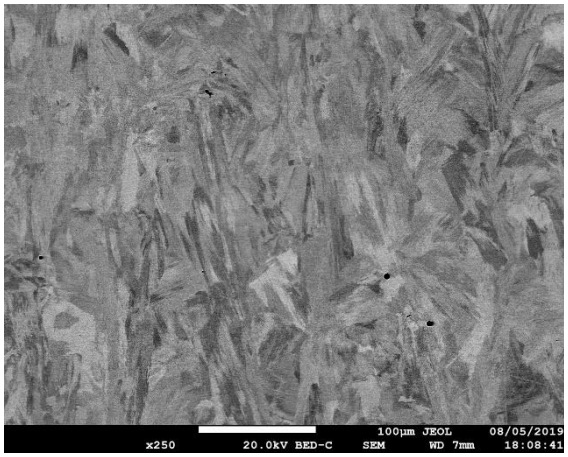

A) Original Sample Low Magnification

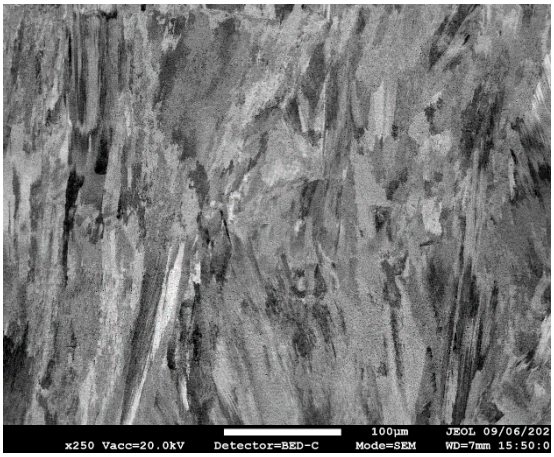

B) Remanufactured Sample Low Magnification

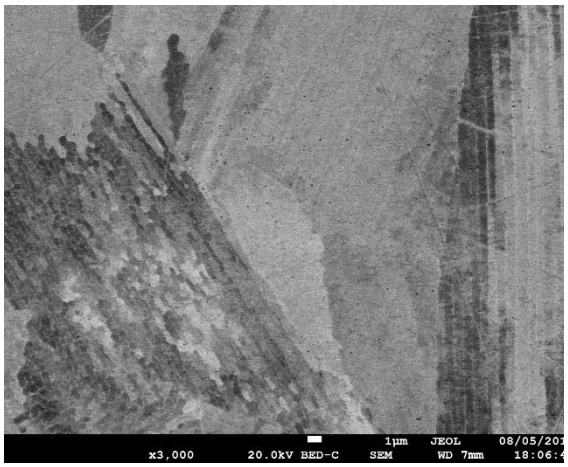

C) Original Sample High Magnification

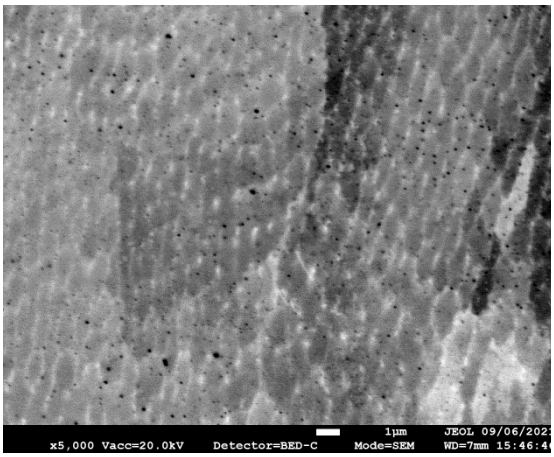

D) Remanufactured Sample High Magnification

Figure 98 - SEM images showing low and high magnification SEM images comparing originally manufactured coupons and remanufactured repeat coupons for a slow laser scan speed. These images show the similarity of both coupons, illustrating the repeatability of the process.

6.1.2 Medium laser Scan Speed

The images below in Figure 99 show the repeatability of the SLM process when using the medium speed laser scan speed. The macro scale images once again show the same columnar elongated grain structure and the higher magnification images show the interdendritic Nb segregation structure. There is a difference in the appearance of the Nb segregation structure compared to the slower scan speed. The reasons for this difference and quantifications of the difference between the microstructures created by different scan speeds is quantified in the main text in section 4.2.4.

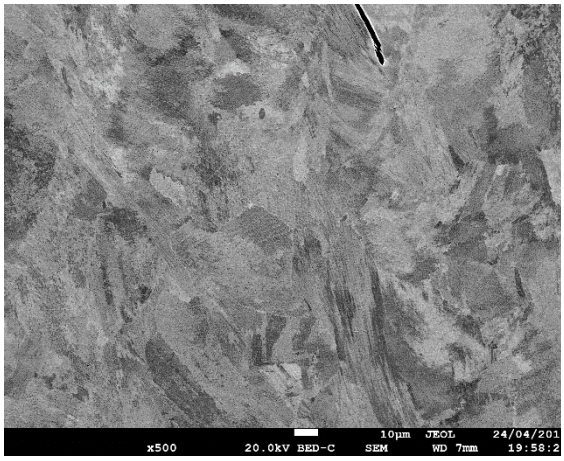

A) Original Sample Low Magnification

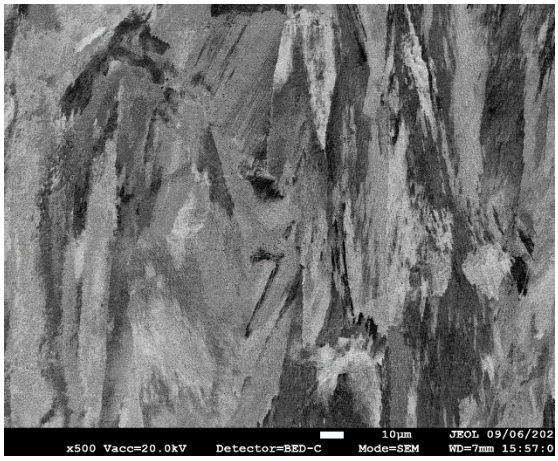

B) Remanufactured Sample Low Magnification

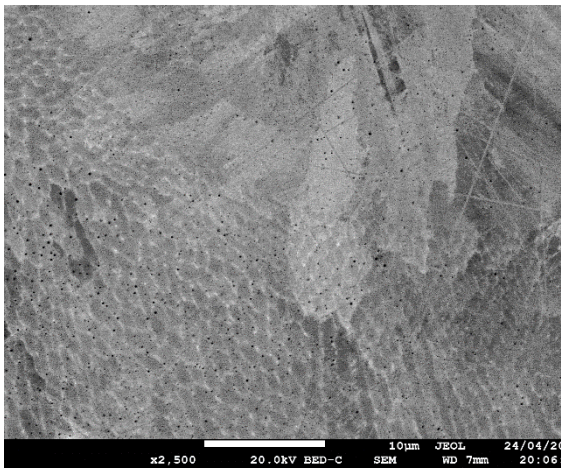

C) Original Sample High Magnification

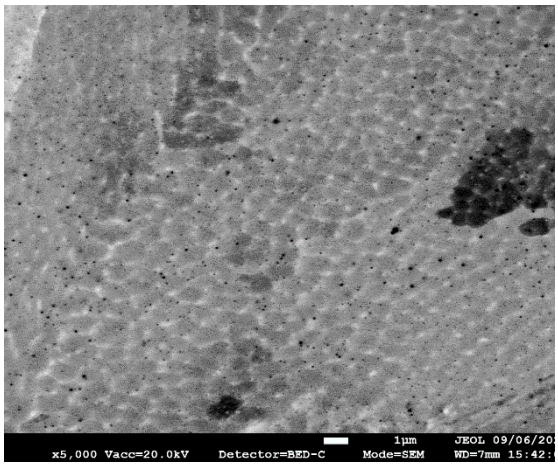

D) Remanufactured Sample High Magnification

Figure 99 - SEM images showing low and high magnification SEM images comparing originally manufactured coupons and remanufactured repeat coupons for a medium laser scan speed. These images show the similarity of both coupons, illustrating the repeatability of the process.

6.1.3 Fast Laser Scan Speed

The images below in Figure 100 show the microstructure of the SLM material produced at the fastest laser scan speed. At a macro level, the materials once again look similar with elongated columnar grains growing in the build direction (running vertically in the images). At higher magnifications the interdendritic Nb segregation structure is once again clearly visible. In these samples manufactured using the highest laser scan speed, there is a noticeable variation in the structure of the segregation, changing depending on proximity to the boundary of a melt pool in the material.

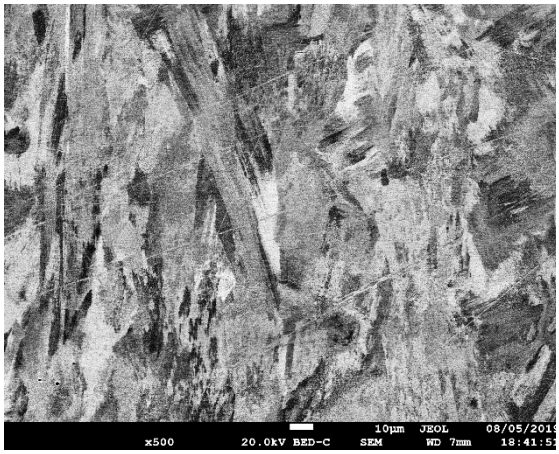

A) Original Sample Low Magnification

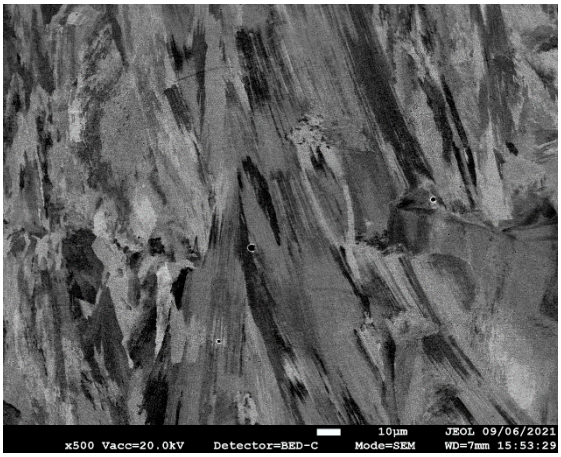

B) Remanufactured Sample Low Magnification

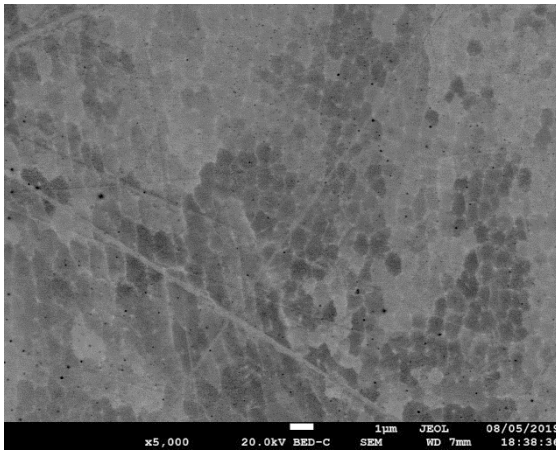

C) Original Sample High Magnification

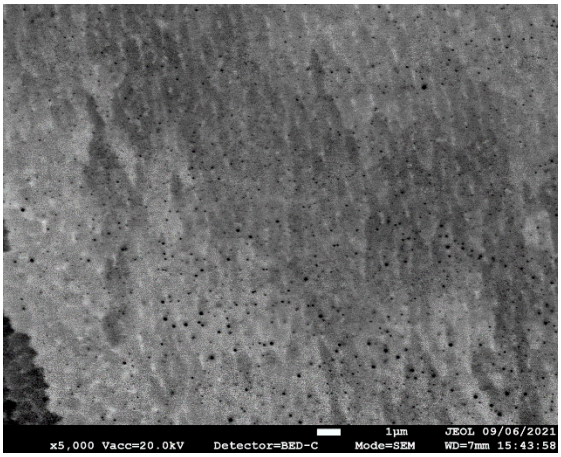

D) Remanufactured Sample High Magnification

Figure 100 - SEM images showing low and high magnification SEM images comparing originally manufactured coupons and remanufactured repeat coupons for a fast laser scan speed. These images show the similarity of both coupons, illustrating the repeatability of the process.

These images were included to illustrate the similarity between separate coupons manufactured using the same processing parameters. Although visually differences between the scanning speeds might not be obvious, the quantitative measurements included in the main text confirm the differences arising. These images demonstrate the repeatability of the process. These are used to prove the reliability of the laser scanning results and to provide evidence that other coupons from this work are also likely to be a repeatable and reliable representation of the SLM process.

6.2 Appendix II - The Influence of Post Process Heat Treatments on Microstructure and Mechanical Properties.

In section 4.3.2.1 the transition point for microstructure coarsening was observed to occur between 1100 °C and 1180 °C. Included below in Figure 101 are some additional images of

microstructures in materials homogenised both above and below this temperature. These SEM images show that, below the transition point, there is very little change to the microstructure visible at a macro level. These images also show a clear lack of any difference occurring from different hold times during homogenisation, either 1 or 2 hours. These results confirm the quantitative results presented in Figure 56.

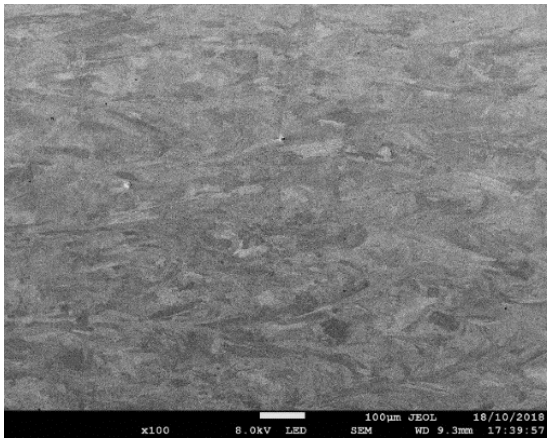

A) 980 °C 1h

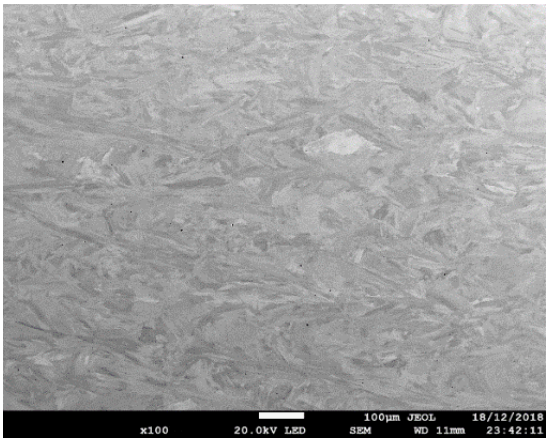

B) 980 °C 1h

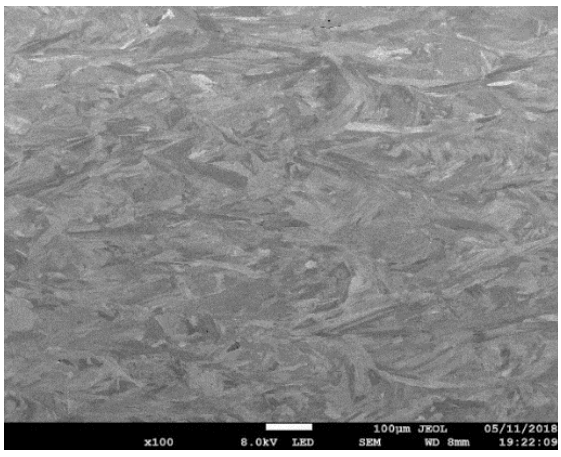

C) 1060 °C 1h

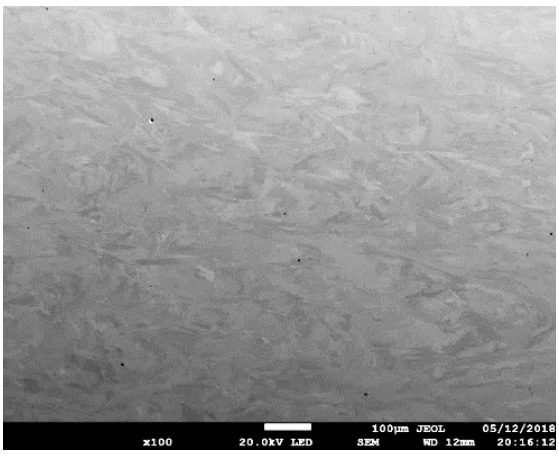

D) 1060 °C 2h

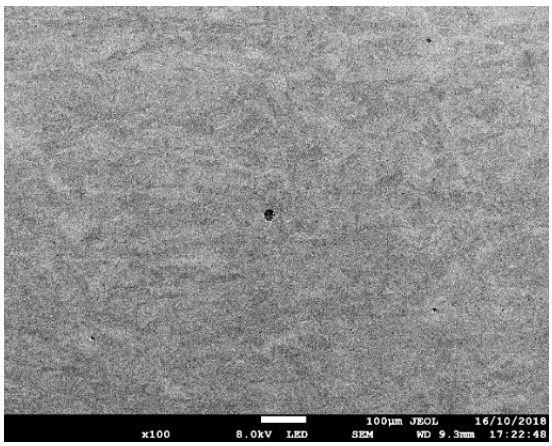

E) 1100 °C 1h

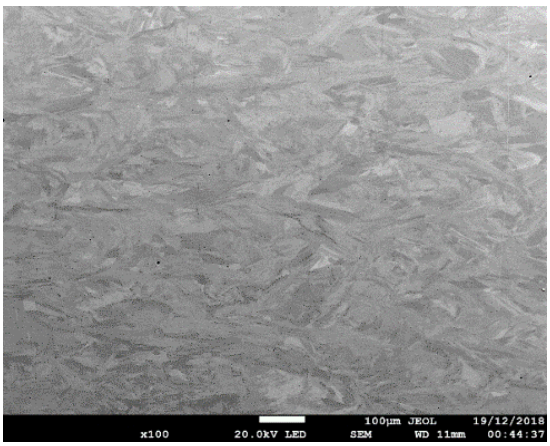

F) 1100 °C 2h

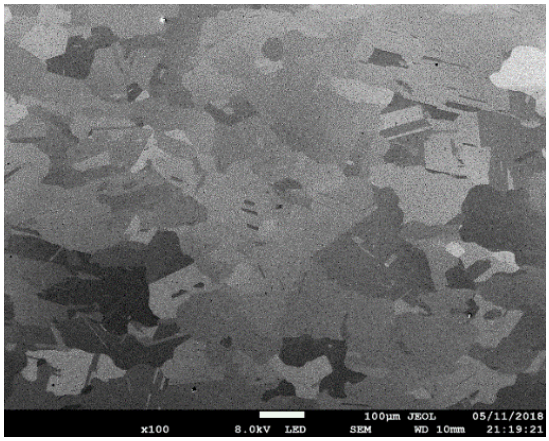

G) 1180 °C 1h

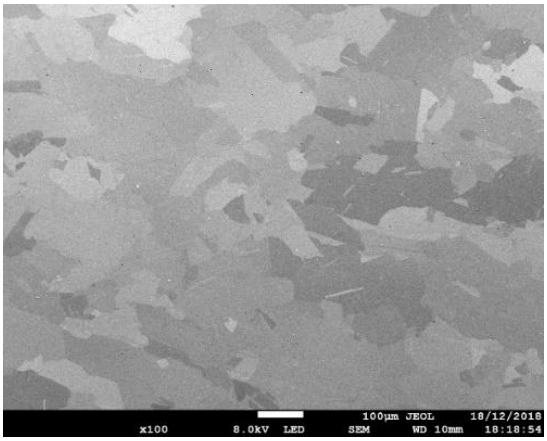

H) 1180 °C 2h

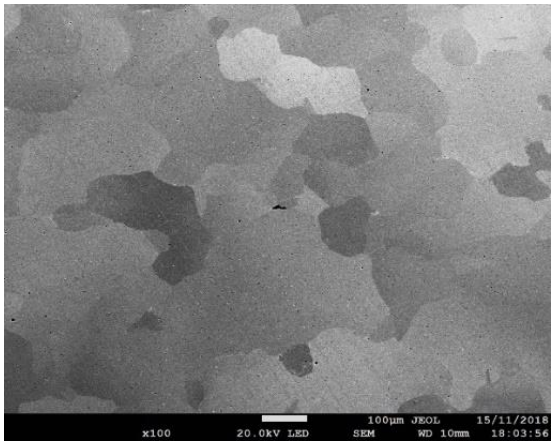

I) 1250 °C 1h

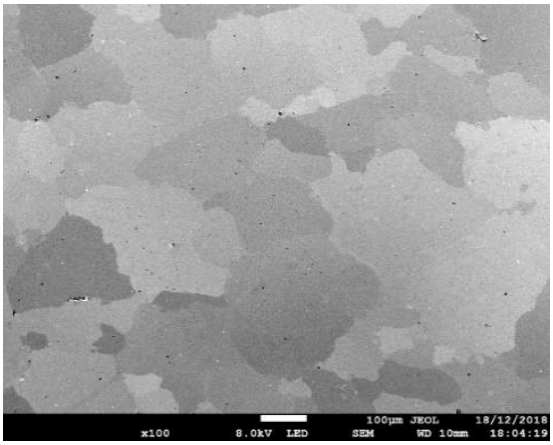

J) 1250 °C 2h

Figure 101 – Images comparing the microstructure of a range of samples following homogenisation. Both 1 and 2 hour homogenised samples are shown. These images illustrate the consistency of the microstructure of the material treated below the transition point for grain coarsening.

7 Abbreviations

ALM – Additive Layer Manufacturing

AM – Additive Manufacturing

DSC – Differential Spectroscopy Calorimetry

EBM – Electron Beam Melting

EBSD – Electron Backscatter Diffraction

E_d – Energy Density

EDS – Energy Dispersive Spectroscopy

FT4 – Freeman Technology 4

H_d – Hatching Distance

HR – Hausner Ratio

IPF – Inverse Pole Figure

L_p – Laser Power

LPA – Laser Particle Analysis

PBF – Powder Bed Fusion

QIEBSD – Quasi in Situ Electron Backscatter Diffraction

RPA – Revolution Powder Analysis

SEM – Scanning Electron Microscope

SLM – Selective Laser Melting

V_s – Laser Scanning Speed

δ – Delta (Precipitate Phase of IN625 and IN718)

γ – Gamma (Continuous Matrix Phase of IN625 and IN718)

γ’ – Gamma Prime (Strengthening Phase of IN625 and IN718)

γ’’ – Gamma Double Prime (Strengthening Phase of IN625 and IN718)

8 Bibliography

Age-hardenable nickel alloy. (1958). https://patents.google.com/patent/US3046108?oq=nickel

“Air Transport Action Group.” (2006). *Facts & Figures*. https://www.atag.org/facts-figures.html

Aircraft Materials. (n.d.). *Nickel Alloy 718 / Inconel 718 (UNS N07718)- Aircraft Materials*. Retrieved July 12, 2018, from https://www.aircraftmaterials.com/data/nickel/718.html

Airlines For America (A4A). (2010). *Policiy Priorities*. http://airlines.org/policy-priorities-learn-more/#energy

Alabbad, B., & Tin, S. (2019). Effect of grain boundary misorientation on η phase precipitation in Ni-base superalloy 718Plus. *Materials Characterization*, *151*(November 2018), 53–63. https://doi.org/10.1016/j.matchar.2019.02.038

Alfa Romeo Sauber. (n.d.). *Alfa Romeo Sauber F1 Team*. Retrieved July 24, 2018, from https://www.sauberf1team.com/news/the-sauber-f1-team-accelerates-3d-metal-printing

Amato, K. N., Gaytan, S. M., Murr, L. E., Martinez, E., Shindo, P. W., Hernandez, J., Collins, S., & Medina, F. (2012). Microstructures and mechanical behavior of Inconel 718 fabricated by selective laser melting. *Acta Materialia*, *60*(5), 2229–2239. https://doi.org/10.1016/J.ACTAMAT.2011.12.032

Anam, A., Dilip, J. J. S., Pal, D., & Stucker, B. (2014). Effect of Scan Pattern on the Microstructural Evolution of Inconel 625 during Selective Laser Melting. *International Solid Freeform Fabrication Symposium – An Additive Manufacturing Conference*, 363–376. https://doi.org/10.13140/2.1.1256.6089

Anderson, M., Thielin, A. L., Bridier, F., Bocher, P., & Savoie, J. (2017). δ Phase precipitation in Inconel 718 and associated mechanical properties. *Materials Science and Engineering A*, *679*, 48–55. https://doi.org/10.1016/j.msea.2016.09.114

Andreotta, R., Ladani, L., & Brindley, W. (2017). Finite element simulation of laser additive melting and solidification of Inconel 718 with experimentally tested thermal properties. *Finite Elements in Analysis and Design*, *135*, 36–43. https://doi.org/10.1016/J.FINEL.2017.07.002

Antonsson, T., & Fredriksson, H. (2005). The effect of cooling rate on the solidification of INCONEL 718. *Metallurgical and Materials Transactions B*, *36*(1), 85–96. https://doi.org/10.1007/s11663-005-0009-0

ASM International. (1996). Inconel 718. In *Heat Treater’s Guide: Practices and Procedures for Nonferrous Alloys* (pp. 41–58).

Attar, H., Prashanth, K. G., Zhang, L.-C., Calin, M., Okulov, I. V., Scudino, S., Yang, C., & Eckert, J. (2015). Effect of Powder Particle Shape on the Properties of In Situ Ti–TiB Composite Materials Produced by Selective Laser Melting. *Journal of Materials Science & Technology*, *31*(10), 1001–1005. https://doi.org/10.1016/J.JMST.2015.08.007

Auburtin, P., Cockcroft, S. L., Mitchell, A., & Schmalz, A. J. (1997). Center Segregation. Freckles and Development Directions for Niobium-Containing Superalloys. *Superalloys 1997*, 47–54. https://doi.org/10.7449/1997/superalloys_1997_47_54

Azadian, S., Wei, L. Y., Niklasson, F., & Warren, R. (2001). Precipitation in spray-formed in 718. *Proceedings of the International Symposium on Superalloys and Various Derivatives*, *1*, 617–626. https://doi.org/10.7449/2001/superalloys_2001_617_626

Azadian, Saied, Wei, L., & Warren, R. (2004). Delta phase precipitation in Inconel 718. *Materials Characterization*, *53*(1), 7–16. https://doi.org/10.1016/J.MATCHAR.2004.07.004

Azarbarmas, M., Aghaie-Khafri, M., Cabrera, J. M., & Calvo, J. (2016). Dynamic recrystallization mechanisms and twining evolution during hot deformation of Inconel 718. *Materials Science and Engineering: A*, *678*, 137–152. https://doi.org/10.1016/J.MSEA.2016.09.100

Bandyopadhyay, A., & Bose, S. (2015). *Additive Manufacturing: Pioneering Affordable Aerospace Manufacturing National*.

Beuth, J., & Klingbeil, N. (2001). The role of process variables in laser-based direct metal solid freeform fabrication. *Jom*, *53*(9), 36–39. https://doi.org/10.1007/s11837-001-0067-y

Biswas, S., Reddy, G. M., Mohandas, T., & Murthy, C. V. S. (2004). Residual stresses in Inconel 718 electron beam welds. *Journal of Materials Science*, *39*(22), 6813–6815. https://doi.org/10.1023/B:JMSC.0000045609.86430.19

Boehlert, C. J., Longanbach, S. C., & Bieler, T. R. (2008). Effect of thermomechanical processing on the creep behaviour of Udimet alloy 188. *Philosophical Magazine*, *88*(5), 641–664. https://doi.org/10.1080/14786430801944836

Boen, B. (2015). *NASA Tests Limits of 3-D Printing with Powerful Rocket Engine Check*. https://www.nasa.gov/exploration/systems/sls/3d-printed-rocket-injector.html

Bolzoni, L., Ruiz-Navas, E. M., & Gordo, E. (2014). Powder metallurgy CP-Ti performances: Hydride–dehydride vs. sponge. *Materials & Design*, *60*, 226–232. https://doi.org/10.1016/J.MATDES.2014.04.005

Brandl, E., Heckenberger, U., Holzinger, V., & Buchbinder, D. (2012). Additive manufactured AlSi10Mg samples using Selective Laser Melting (SLM): Microstructure, high cycle fatigue, and fracture behavior. *Materials & Design*, *34*, 159–169. https://doi.org/10.1016/J.MATDES.2011.07.067

Brandon, D. . (1966). The structure of high-angle grain boundaries. *Acta Metallurgica*, *14*(11), 1479–1484. https://doi.org/10.1016/0001-6160(66)90168-4

Brewer, L. N., Othon, M. A., Young, L. M., & Angeliu, T. M. (2006). Misorientation Mapping for Visualization of Plastic Deformation via Electron Back-Scattered Diffraction. *Microscopy and Microanalysis*, *12*(01), 85–91. https://doi.org/10.1017/S1431927606060120

Brooks, J. W., & Bridges, P. J. (1988). Metallurgical Stability of Inconel 718. *Superalloys*.

Cai, D., Zhang, W., Nie, P., Liu, W., & Yao, M. (2007). Dissolution kinetics of δ phase and its influence on the notch sensitivity of Inconel 718. *Materials Characterization*, *58*(3), 220–225. https://doi.org/10.1016/J.MATCHAR.2006.04.020

Callister, D. W., & Rethwisch, D. G. (2014). *Materials Science and Engineering* (Ninth Edit). Wiley.

Çam, G., & Koçak, M. (1998). Progress in joining of advanced materials. *International Materials Reviews*, *43*(1), 1–44. https://doi.org/10.1179/imr.1998.43.1.1

Cao, W. D., & Kennedy, R. L. (2001). Improving stress rupture life of alloy 718 by optimizing Al, Ti, P and B contents. *Proceedings of the International Symposium on Superalloys and Various Derivatives*, *1*, 477–488.

Cao, W. D., & Kennedy, R. L. (2004). Role of Chemistry in 718 Type Alloys - Allvac 718-Plus Alloy

Development. *Super Alloys (2004)*, *3*, 1–10.

Cao, W., & Kennedy, R. L. (1994). the Effect of Phosphorous on Mechanical Properties of alloy 718. *Superalloys 718, 625, 706 and Various Derivatives*, 463–477.

Carter, L. N., Martin, C., Withers, P. J., & Attallah, M. M. (2014). The influence of the laser scan strategy on grain structure and cracking behaviour in SLM powder-bed fabricated nickel superalloy. *Journal of Alloys and Compounds*, *615*, 338–347. https://doi.org/10.1016/j.jallcom.2014.06.172

CFM. (n.d.). *LEAP Engines – CFM International Jet Engines CFM International*. Retrieved April 12, 2018, from https://www.cfmaeroengines.com/engines/leap/

Chamanfar, A., Sarrat, L., Jahazi, M., Asadi, M., Weck, A., & Koul, A. K. (2013). Microstructural characteristics of forged and heat treated Inconel-718 disks. *Materials & Design (1980-2015)*, *52*, 791–800. https://doi.org/10.1016/J.MATDES.2013.06.004

Chan, K. S., Koike, M., Mason, R. L., & Okabe, T. (n.d.). *Fatigue Life of Titanium Alloys Fabricated by Additive Layer Manufacturing Techniques for Dental Implants*. https://doi.org/10.1007/s11661-012-1470-4

Chang, L., Sun, W., Cui, Y., & Yang, R. (2014). Influences of hot-isostatic-pressing temperature on microstructure, tensile properties and tensile fracture mode of Inconel 718 powder compact. *Materials Science and Engineering: A*, *599*, 186–195. https://doi.org/10.1016/J.MSEA.2014.01.095

Chastand, V., Quaegebeur, P., Maia, W., & Charkaluk, E. (2018). Comparative study of fatigue properties of Ti-6Al-4V specimens built by electron beam melting (EBM) and selective laser melting (SLM). *Materials Characterization*, *143*, 76–81. https://doi.org/10.1016/J.MATCHAR.2018.03.028

Chaturvedi, M. C., & Han, Y. (1983). Strengthening mechanisms in Inconel 718 superalloy. *Metal Science*, *17*(3), 145–149. https://doi.org/10.1179/030634583790421032

Chen, Y., Lu, F., Zhang, K., Nie, P., Elmi Hosseini, S. R., Feng, K., Li, Z., & Chu, P. K. (2016). Investigation of dendritic growth and liquation cracking in laser melting deposited Inconel 718 at different laser input angles. *Materials & Design*, *105*, 133–141. https://doi.org/10.1016/J.MATDES.2016.05.034

Chen, Y., Zhang, K., Huang, J., Hosseini, S. R. E., & Li, Z. (2016). Characterization of heat affected zone liquation cracking in laser additive manufacturing of Inconel 718. *Materials & Design*, *90*, 586–594. https://doi.org/10.1016/J.MATDES.2015.10.155

Cheng, B., & Chou, K. (2015). Melt Pool Evolution Study in Selective Laser Melting. *Conference: 26th Annual International Solid Freeform Fabrication Symposium*.

Chlebus, E., Gruber, K., Kuźnicka, B., Kurzac, J., & Kurzynowski, T. (2015). Effect of heat treatment on the microstructure and mechanical properties of Inconel 718 processed by selective laser melting. *Materials Science and Engineering A*, *639*, 647–655. https://doi.org/10.1016/j.msea.2015.05.035

Choi, J.-P., Shin, G.-H., Yang, S., Yang, D.-Y., Lee, J.-S., Brochu, M., & Yu, J.-H. (2017). Densification and microstructural investigation of Inconel 718 parts fabricated by selective laser melting. *Powder Technology*, *310*, 60–66. https://doi.org/10.1016/J.POWTEC.2017.01.030

Chong, Y., Liu, Z., Godfrey, A., Liu, W., & Weng, Y. (2014). The Application of Grain Boundary

Engineering to a Nickel Base Superalloy for 973 K (700 °C) USC Power Plants. *Metallurgical and Materials Transactions E*, *1*(1), 58–66. https://doi.org/10.1007/s40553-014-0009-6

Cieslak, M. J., Knorovsky, G. A., Headley, T. J., & Romig, Jr, A. D. (1989). *The Solidification Metallurgy of Alloy 718 and Other Nb-Containing Superalloys*. 59–68. https://doi.org/10.7449/1989/superalloys_1989_59_68

Clavel, M., & Pineau, A. (1978). Frequency and wave-form effects on the fatigue crack growth behavior of alloy 718 at 298 K and 823 K. *Metallurgical Transactions A*, *9*(4), 471–480. https://doi.org/10.1007/BF02646402

Clayton, J. (2019). An Introduction to Powder Characterization. In *Handbook of Pharmaceutical Wet Granulation* (pp. 569–613). Academic Press. https://doi.org/10.1016/B978-0-12-810460-6.00021-X

Clayton, J., Millington-Smith, D., & Armstrong, B. (2015). The Application of Powder Rheology in Additive Manufacturing. *Jom*, *67*(3), 544–548. https://doi.org/10.1007/s11837-015-1293-z

Climate Central. (2012). *Countries Embrace New Rules to Limit Airline Emissions*. https://www.climatecentral.org/news/countries-embrace-new-rules-airline-emissions-20007

Cooke, A., & Slotwinski, J. (2015). Properties of metal powders for additive manufacturing: A review of the state of the art of metal powder property testing. *Additive Manufacturing Materials: Standards, Testing and Applicability*, 21–48. https://doi.org/10.6028/NIST.IR.7873

D, G., Jha, S. N., & Dash, L. N. (1997). INFLUENCE OF MICROSTRUCTURE ON FATIGUE PROPERTIES OF ALLOY 718. *Superalloys 718,625,706 and Various Derivatives (1997)*, 567–573. http://www.ghbook.ir/index.php?name=فرهنگ و رسانه های نوین&option=com_dbook&task=readonline&book_id=13650&page=73&chkhashk=ED9C9491B4&Itemid=218&lang=fa&tmpl=component

Dai, D., Gu, D., Zhang, H., Xiong, J., Ma, C., Hong, C., & Poprawe, R. (2018). Influence of scan strategy and molten pool configuration on microstructures and tensile properties of selective laser melting additive manufactured aluminum based parts. *Optics & Laser Technology*, *99*, 91–100. https://doi.org/10.1016/J.OPTLASTEC.2017.08.015

Damon, J., Hanemann, T., Dietrich, S., Graf, G., Lang, K.-H., & Schulze, V. (2019). Orientation dependent fatigue performance and mechanisms of selective laser melted maraging steel X3NiCoMoTi18-9-5. *International Journal of Fatigue*, *127*, 395–402. https://doi.org/10.1016/J.IJFATIGUE.2019.06.025

Dawes, B. J., & Bowerman, R. (2015). Introduction to the Additive Manufacturing Powder Metallurgy Supply Chain: Exploring the production and supply of metal powders for AM processes. *JOHNSON MATTHEY TECHNOLOGY REVIEW Johnson*, *59*(3), 243–256.

Deckard, C. R. (1987). *Method and apparatus for producing parts by selective sintering* (Patent No. WO1988002677A2). https://patents.google.com/patent/WO1988002677A2/en

Dehmas, M., Lacaze, J., Niang, A., & Viguier, B. (2011). TEM Study of High-Temperature Precipitation of Delta Phase in Inconel 718 Alloy. *Advances in Materials Science and Engineering*, *2011*, 1–9. https://doi.org/10.1155/2011/940634

Deng, D. (2018). Additively Manufactured Inconel 718 : Microstructures and Mechanical

Properties. In *Additively Manufactured Inconel 718 : Microstructures and Mechanical Properties* (Issue 1798). https://doi.org/10.3384/lic.diva-144491

Deng, D., Moverare, J., Peng, R. L., & Söderberg, H. (2017). Microstructure and anisotropic mechanical properties of EBM manufactured Inconel 718 and effects of post heat treatments. *Materials Science and Engineering: A*, *693*, 151–163. https://doi.org/10.1016/J.MSEA.2017.03.085

Desmond, K. W., & Weeks, E. R. (2014). Influence of particle size distribution on random close packing of spheres. *Physical Review E - Statistical, Nonlinear, and Soft Matter Physics*, *90*(2), 1–6. https://doi.org/10.1103/PhysRevE.90.022204

Desvallees, Y., Bouzidi, M., Bois, F., & Beaude, N. (2006). Delta Phase in Inconel 718: Mechanical Properties and Forging Process Requirements. *Minerals, Metals & Materials Society*, 603–621.

Devaux, A., Nazé, L., Molins, R., Pineau, A., Organista, A., Guédou, J. Y., Uginet, J. F., & Héritier, P. (2008). Gamma double prime precipitation kinetic in Alloy 718. *Materials Science and Engineering: A*, *486*(1–2), 117–122. https://doi.org/10.1016/J.MSEA.2007.08.046

Dinda, G. P., Dasgupta, A. K., & Mazumder, J. (2009). Laser aided direct metal deposition of Inconel 625 superalloy: Microstructural evolution and thermal stability. *Materials Science and Engineering: A*, *509*(1–2), 98–104. https://doi.org/10.1016/J.MSEA.2009.01.009

Dinda, G. P., Dasgupta, A. K., & Mazumder, J. (2012). Texture control during laser deposition of nickel-based superalloy. *Scripta Materialia*, *67*(5), 503–506. https://doi.org/10.1016/J.SCRIPTAMAT.2012.06.014

Ding, X., Koizumi, Y., Wei, D., & Chiba, A. (2019). Effect of process parameters on melt pool geometry and microstructure development for electron beam melting of IN718: A systematic single bead analysis study. *Additive Manufacturing*, *26*, 215–226. https://doi.org/https://doi.org/10.1016/j.addma.2018.12.018

Du, J. H., Lu, X. D., Deng, Q., Qu, J. L., Zhuang, J. Y., & Zhong, Z. Y. (2007). High-temperature structure stability and mechanical properties of novel 718 superalloy. *Materials Science and Engineering: A*, *452–453*, 584–591. https://doi.org/10.1016/J.MSEA.2006.11.039

Dudzinski, D., Devillez, A., Moufki, A., Larrouquère, D., Zerrouki, V., & Vigneau, J. (2004). A review of developments towards dry and high speed machining of Inconel 718 alloy. *International Journal of Machine Tools and Manufacture*, *44*(4), 439–456. https://doi.org/10.1016/S0890-6955(03)00159-7

DuPont, J. M., Lippold, J. C., & Kiser, S. D. (2009). *Welding Metallurgy and Weldability of Nickel-Base Alloys* (1st ed.). Wiley.

Edwards, P., & Ramulu, M. (2014). Fatigue performance evaluation of selective laser melted Ti–6Al–4V. *Materials Science and Engineering: A*, *598*, 327–337. https://doi.org/10.1016/J.MSEA.2014.01.041

Eiselstein, H. L., & Tillack, D. J. (1991). The Invention and Definition of Alloy 625. *Superalloys 718, 625 and Various Derivatives (1991)*, 1–14. https://doi.org/10.7449/1991/Superalloys_1991_1_14

Ellyson, B., Brochu, M., & Brochu, M. (2017). Characterization of bending vibration fatigue of SLM fabricated Ti-6Al-4V. *International Journal of Fatigue*, *99*, 25–34. https://doi.org/10.1016/J.IJFATIGUE.2017.02.005

EOS. (n.d.). *EOS M 290 - industrial 3D printed parts from metal materials*. Retrieved September 11, 2018, from https://www.eos.info/eos-m290

Esaka, H., Shinozuka, K., & Tamura, M. (2005a). Analysis of single crystal casting process taking into account the shape of pigtail. *Materials Science and Engineering: A*, *413–414*, 151–155. https://doi.org/10.1016/J.MSEA.2005.08.154

Esaka, H., Shinozuka, K., & Tamura, M. (2005b). Analysis of single crystal casting process taking into account the shape of pigtail. *Materials Science and Engineering: A*, *413–414*, 151–155. https://doi.org/10.1016/J.MSEA.2005.08.154

Fang, X. Y., Li, H. Q., Wang, M., Li, C., & Guo, Y. B. (2018). Characterization of texture and grain boundary character distributions of selective laser melted Inconel 625 alloy. *Materials Characterization*. https://doi.org/10.1016/J.MATCHAR.2018.02.008

Feng, J. Q., & Hays, D. A. (2003a). Relative importance of electrostatic forces on powder particles. *Powder Technology*, *135–136*, 65–75. https://doi.org/10.1016/J.POWTEC.2003.08.005

Feng, J. Q., & Hays, D. A. (2003b). Relative importance of electrostatic forces on powder particles. *Powder Technology*, *135–136*, 65–75. https://doi.org/10.1016/J.POWTEC.2003.08.005

Ferrer, F., Pieraggi, B., & Uginet, J. F. (1991). Microstructural Evolution During Thermomechanical Processing of Alloy 625. *Proc. Superalloys 1991*.

Freeman, R. (2007). Measuring the flow properties of consolidated, conditioned and aerated powders — A comparative study using a powder rheometer and a rotational shear cell. *Powder Technology*, *174*(1–2), 25–33. https://doi.org/10.1016/J.POWTEC.2006.10.016

Freman, T. (n.d.). *Mechanicsms of Particle Interaction*. Retrieved October 5, 2017, from http://www.freemantech.co.uk/_powders/powder-flowability-mechanisms-of-particle-interaction

Gao, Y., Zhang, D., Cao, M., Chen, R., Feng, Z., Poprawe, R., Schleifenbaum, J. H., & Ziegler, S. (2019). Effect of δ phase on high temperature mechanical performances of Inconel 718 fabricated with SLM process. *Materials Science and Engineering: A*, *767*, 138327. https://doi.org/10.1016/J.MSEA.2019.138327

General Electric. (n.d.). *The FAA Cleared the First 3D Printed Part to Fly in a Commercial Jet Engine from GE - GE Reports*. Retrieved April 12, 2018, from https://www.ge.com/reports/post/116402870270/the-faa-cleared-the-first-3d-printed-part-to-fly-2/

Geng, L., Na, Y.-S., & Park, N.-K. (1997). Continuous cooling transformation behavior of Alloy 718. *Materials Letters*, *30*(5–6), 401–405. https://doi.org/10.1016/S0167-577X(96)00225-X

Ghonem, H., & Zheng, D. (1991). OXIDATION-ASSISTED FATIGUE CRACK GROWTH BEHAVIOR IN ALLOY 718-PART I. QUANTITATIVE MODELING. *Fatigue & Fracture of Engineering Materials and Structures*, *14*(7), 749–760. https://doi.org/10.1111/j.1460-2695.1991.tb00703.x

Ghosh, S., Yadav, S., & Das, G. (2008). Study of standard heat treatment on mechanical properties of Inconel 718 using ball indentation technique. *Materials Letters*, *62*(17–18), 2619–2622. https://doi.org/10.1016/J.MATLET.2008.01.001

Gong, H., Rafi, K., Gu, H., Starr, T., & Stucker, B. (2014). Analysis of defect generation in Ti–6Al–4V parts made using powder bed fusion additive manufacturing processes. *Additive Manufacturing*, *1–4*, 87–98. https://doi.org/10.1016/J.ADDMA.2014.08.002

Gu, D., & Shen, Y. (2009). Balling phenomena in direct laser sintering of stainless steel powder: Metallurgical mechanisms and control methods. *Materials and Design*, *30*(8), 2903–2910. https://doi.org/10.1016/j.matdes.2009.01.013

Guan, S., Cui, C., Yuan, Y., & Gu, Y. (2016). The role of phosphorus in a newly developed Ni-Fe-Cr-based wrought superalloy. *Materials Science and Engineering: A*, *662*, 275–282. https://doi.org/10.1016/J.MSEA.2016.03.069

Guest, R. P., & Tin, S. (2012). *The Dynamic and Metadynamic Recrystallisation of IN 718*. *1*, 373–383. https://doi.org/10.7449/2005/superalloys_2005_373_383

Guo, Y., Sun, M., Xu, B., & Li, D. (2017). A method based on semi-solid forming for eliminating Laves eutectic phase of INCONEL 718 alloy. *Journal of Materials Processing Technology*, *249*, 202–211. https://doi.org/10.1016/J.JMATPROTEC.2017.05.015

Guy, A. G. (1976). *Essentials of materials science*.

Hague, R. (2006). Unlocking the Design Potential of Rapid Manufacturing. In *Rapid Manufacturing* (pp. 5–18). John Wiley & Sons, Ltd. https://doi.org/10.1002/0470033991.ch2

Hamaker, H. C. (1937). The London—van der Waals attraction between spherical particles. *Physica*, *4*(10), 1058–1072. https://doi.org/10.1016/S0031-8914(37)80203-7

Hirata, T., Kimura, T., & Nakamoto, T. (2020). Effects of hot isostatic pressing and internal porosity on the performance of selective laser melted AlSi10Mg alloys. *Materials Science and Engineering: A*, *772*, 138713. https://doi.org/10.1016/J.MSEA.2019.138713

Hiroshi, N. (2014). Defects in Metals. *Physical Metallurgy*, 561–637. https://doi.org/10.1016/B978-0-444-53770-6.00006-X

Hong, H. U., Kim, I. S., Choi, B. G., Kim, M. Y., & Jo, C. Y. (2009). The effect of grain boundary serration on creep resistance in a wrought nickel-based superalloy. *Materials Science and Engineering: A*, *517*(1–2), 125–131. https://doi.org/10.1016/J.MSEA.2009.03.071

Hotta, K., Takeda, K., & Iinoya, K. (1974). The capillary binding force of a liquid bridge. *Powder Technology*, *10*(4–5), 231–242. https://doi.org/10.1016/0032-5910(74)85047-3

Huang, W., Yang, J., Yang, H., Jing, G., Wang, Z., & Zeng, X. (2019). Heat treatment of Inconel 718 produced by Selective Laser Melting: Microstructure and mechanical properties. *Materials Science and Engineering: A*, *750*, 98–107. https://doi.org/10.1016/j.msea.2019.02.046

Hull, C. W. (1984). *Apparatus for production of three-dimensional objects by stereolithography* (Patent No. US4575330A). https://patents.google.com/patent/US4575330A/en?q=stereolithography&before=priority:19900101&after=priority:19600101&sort=old

Hussein, A., Hao, L., Yan, C., & Everson, R. (2013). Finite element simulation of the temperature and stress fields in single layers built without-support in selective laser melting. *Materials and Design*, *52*, 638–647. https://doi.org/10.1016/j.matdes.2013.05.070

Hussein, A., Hao, L., Yan, C., Everson, R., & Young, P. (2013). Advanced lattice support structures for metal additive manufacturing. *Journal of Materials Processing Technology*,

213(7), 1019–1026. https://doi.org/10.1016/J.JMATPROTEC.2013.01.020

Inconel 625 (tm) Super Alloys [Altemp 625 (tm),Chronin 625 (tm),Custom Age 625 Plus Alloy (tm),HAYNES 625 alloy,Nickelvac 625 (tm),Nicrofer 6020 hMo (tm),Pyromet Alloy 625 (tm),Udimet 625 (tm),VLX625 (tm)] Material Property Data Sheet. (n.d.). Retrieved October 25, 2018, from https://www.suppliersonline.com/propertypages/Inconel625.asp

Janaki Ram, G. D., Venugopal Reddy, A., Prasad Rao, K., & Madhusudhan Reddy, G. (2004). Control of Laves phase in Inconel 718 GTA welds with current pulsing. *Science and Technology of Welding and Joining*, *9*(5), 390–398. https://doi.org/10.1179/136217104225021788

Jinhui, D., Xudong, L., Qun, D., & Ying, L. (2017a). Effect of Solution Treatment on the Microstructure and Mechanical Properties of IN718 Alloy. *Rare Metal Materials and Engineering*, *46*(9), 2359–2365. https://doi.org/10.1016/S1875-5372(17)30197-2

Jinhui, D., Xudong, L., Qun, D., & Ying, L. (2017b). Effect of Solution Treatment on the Microstructure and Mechanical Properties of IN718 Alloy. *Rare Metal Materials and Engineering*, *46*(9), 2359–2365. https://doi.org/10.1016/S1875-5372(17)30197-2

Jurrens, K., & Energetics Incorporated. (2013). Measurement Science Roadmap for Metal-Based Additive Manufacturing. *Additive Manufacturing*, 86. https://doi.org/10.1007/s13398-014-0173-7.2

K, R., E, N. K., R., J., G.D., J. R., & V., S. S. (2018). Effect of grain boundary character distribution on weld heat-affected zone liquation cracking behavior of AISI 316Ti austenitic stainless steel. *Materials Characterization*, *142*, 115–123. https://doi.org/10.1016/J.MATCHAR.2018.05.020

Kañetas, P. J. P., Osorio, L. A. R., Mata, M. P. G., Garza, M. D. La, & López, V. P. (2015). Influence of the Delta Phase in the Microstructure of the Inconel 718 subjected to "Delta-processing" Heat Treatment and Hot Deformed. *Procedia Materials Science*, *8*, 1160–1165. https://linkinghub.elsevier.com/retrieve/pii/S2211812815001819

Kestens, L. A. I., & Pirgazi, H. (2016). Texture formation in metal alloys with cubic crystal structures. *Materials Science and Technology (United Kingdom)*, *32*(13), 1303–1315. https://doi.org/10.1080/02670836.2016.1231746

Khairallah, S. A., Anderson, A. T., Rubenchik, A., & King, W. E. (2016). Laser powder-bed fusion additive manufacturing: Physics of complex melt flow and formation mechanisms of pores, spatter, and denudation zones. *Acta Materialia*, *108*, 36–45. https://doi.org/10.1016/J.ACTAMAT.2016.02.014

Khan, H. M., Dirikolu, M. H., & Koç, E. (2018). Parameters optimization for horizontally built circular profiles: Numerical and experimental investigation. *Optik*, *174*, 521–529. https://doi.org/10.1016/J.IJLEO.2018.08.095

Knorovsky, G. A., Cieslak, M. J., Headley, T. J., Romig, A. D., & Hammetter, W. F. (1989). INCONEL 718: A solidification diagram. *Metallurgical Transactions A*, *20*(10), 2149–2158. https://doi.org/10.1007/BF02650300

Kobayashi, K., & Yamaguchi, K. (2005). Fatigue Strength of Alloy 718 at High-Temperatures. *MATERIALS TRANSACTIONS*, *46*(4), 869–871. https://doi.org/10.2320/matertrans.46.869

Kong, Y. H., Liu, R. Y., Chen, G. S., Xie, L. X., & Zhu, S. G. (2013). Effects of Different Heat Treatments on the Microstructures and Creep Properties of GH4169 Superalloy. *Journal of Materials Engineering and Performance*, *22*(5), 1371–1377.

https://doi.org/10.1007/s11665-012-0422-x

Koutiri, I., Pessard, E., Peyre, P., Amlou, O., & De Terris, T. (2018). Influence of SLM process parameters on the surface finish, porosity rate and fatigue behavior of as-built Inconel 625 parts. *Journal of Materials Processing Technology*, *255*, 536–546. https://doi.org/10.1016/J.JMATPROTEC.2017.12.043

Krantz, M., Zhang, H., & Zhu, J. (2009). Characterization of powder flow: Static and dynamic testing. *Powder Technology*, *194*(3), 239–245. https://doi.org/10.1016/j.powtec.2009.05.001

Kreitcberg, A., Brailovski, V., & Turenne, S. (2017). Effect of heat treatment and hot isostatic pressing on the microstructure and mechanical properties of Inconel 625 alloy processed by laser powder bed fusion. *Materials Science and Engineering: A*, *689*, 1–10. https://doi.org/10.1016/J.MSEA.2017.02.038

Kruth, J.-P., Vandenbroucke, B., Vaerenbergh, J. Van, & Naert, I. (n.d.). *Rapid Manufacturing of Dental Prostheses by means of Selective Laser Sintering/Melting*. Retrieved April 25, 2017, from http://doc.utwente.nl/52914/1/Wa1025.pdf

Kruth, J. P., Froyen, L., Van Vaerenbergh, J., Mercelis, P., Rombouts, M., & Lauwers, B. (2004a). Selective laser melting of iron-based powder. *Journal of Materials Processing Technology*, *149*(1–3), 616–622. https://doi.org/10.1016/j.jmatprotec.2003.11.051

Kruth, J. P., Froyen, L., Van Vaerenbergh, J., Mercelis, P., Rombouts, M., & Lauwers, B. (2004b). Selective laser melting of iron-based powder. *Journal of Materials Processing Technology*, *149*(1–3), 616–622. https://doi.org/10.1016/J.JMATPROTEC.2003.11.051

Kunze, K., Etter, T., Grässlin, J., & Shklover, V. (2015). Texture, anisotropy in microstructure and mechanical properties of IN738LC alloy processed by selective laser melting (SLM). *Materials Science and Engineering: A*, *620*, 213–222. https://doi.org/10.1016/J.MSEA.2014.10.003

Kuo, C.-M., Yang, Y.-T., Bor, H.-Y., Wei, C.-N., & Tai, C.-C. (2009). Aging effects on the microstructure and creep behavior of Inconel 718 superalloy. *Materials Science and Engineering: A*, *510–511*, 289–294. https://doi.org/10.1016/J.MSEA.2008.04.097

Kuo, Y.-L., Horikawa, S., & Kakehi, K. (2017). The effect of interdendritic δ phase on the mechanical properties of Alloy 718 built up by additive manufacturing. *Materials & Design*, *116*, 411–418. https://doi.org/10.1016/J.MATDES.2016.12.026

Kusuma, C. (2016). *The Effect of Laser Power and Scan Speed on Melt Pool Characteristics of Pure Titanium and Ti-6Al-4V alloy for Selective Laser Melting*.

Larson, R. (1994). *Method and device for producing three-dimensional bodies* (Patent No. US5786562A). https://patents.google.com/patent/US5786562

Le, T.-N., & Lo, Y.-L. (2019). Effects of sulfur concentration and Marangoni convection on melt-pool formation in transition mode of selective laser melting process. *Materials & Design*, *179*, 107866. https://doi.org/10.1016/J.MATDES.2019.107866

Lee, S. G., & Gokhale, A. M. (2006). Formation of gas induced shrinkage porosity in Mg-alloy high-pressure die-castings. *Scripta Materialia*. https://doi.org/10.1016/j.scriptamat.2006.04.040

Lee, Y. S., Kim, D. W., Lee, D. Y., & Ryu, W. S. (2001). Effect of grain size on creep properties of type 316LN stainless steel. *Metals and Materials International*, *7*(2), 107–114.

https://doi.org/10.1007/BF03026948

Lehockey, E. M., & Palumbo, G. (1997). On the creep behaviour of grain boundary engineered nickel 1. *Materials Science and Engineering: A*, *237*(2), 168–172. https://doi.org/10.1016/S0921-5093(97)00126-3

Li, C., White, R., Fang, X. Y., Weaver, M., & Guo, Y. B. (2017). Microstructure evolution characteristics of Inconel 625 alloy from selective laser melting to heat treatment. *Materials Science and Engineering: A*, *705*, 20–31. https://doi.org/10.1016/J.MSEA.2017.08.058

Li, J., Zhao, Z., Bai, P., Qu, H., Liu, B., Li, L., Wu, L., Guan, R., Liu, H., & Guo, Z. (2019). Microstructural evolution and mechanical properties of IN718 alloy fabricated by selective laser melting following different heat treatments. *Journal of Alloys and Compounds*, *772*, 861–870. https://doi.org/10.1016/J.JALLCOM.2018.09.200

Li, R., Liu, J., Shi, Y., & Wang, L. (2012). *Balling behavior of stainless steel and nickel powder during selective laser melting process*. 1025–1035. https://doi.org/10.1007/s00170-011-3566-1

Li, R., Shi, Y., & Liu, J. (2009). *EFFECTS OF PROCESSING PARAMETERS ON THE TEMPERATURE FIELD OF SELECTIVE LASER MELTING METAL POWDER*. *48*(3), 186–195.

Li, S., Yang, J., Zhuang, J., Deng, Q., Du, J., Xie, X., Li, B., Xu, Z., Cao, Z., Su, Z., & Jiang, C. (1994). The Effect of Delta-Phase on Crack Propagation Under Creep and Fatigue Conditions in Alloy 718. *Superalloys 718, 625,706 and Various Derivatives (1994)*, 545–555. https://doi.org/10.7449/1994/superalloys_1994_545_555

Lingenfelter, A. (1989). Welding of Inconel Alloy 718: A Historical Overview. *Superalloys 718 Metallurgy and Applications (1989)*, 673–683. https://doi.org/10.7449/1989/Superalloys_1989_673_683

Liu, F., Lin, X., Yang, G., Song, M., Chen, J., & Huang, W. (2011). Microstructure and residual stress of laser rapid formed Inconel 718 nickel-base superalloy. *Optics and Laser Technology*, *43*(1), 208–213. https://doi.org/10.1016/j.optlastec.2010.06.015

Liu, W. C., Yao, M., Chen, Z. L., & Wang, S. G. (1999). Niobium segregation in Inconel 718. *Journal of Materials Science*, *34*(11), 2583–2586. https://doi.org/10.1023/A:1004648615561

Liu, X., Dong, J., Tang, B., Hu, Y., & Xie, X. (1999). Investigation of the abnormal effects of phosphorus on mechanical properties of INCONEL718 superalloy. *Materials Science and Engineering: A*, *270*(2), 190–196. https://doi.org/10.1016/S0921-5093(99)00153-7

Liu, Y., Kang, M., Wu, Y., Wang, M., Gao, H., & Wang, J. (2017). Effects of microporosity and precipitates on the cracking behavior in polycrystalline superalloy Inconel 718. *Materials Characterization*, *132*, 175–186. https://doi.org/10.1016/J.MATCHAR.2017.08.012

LONG, Y., NIE, P., LI, Z., HUANG, J., LI, X., & XU, X. (2016). Segregation of niobium in laser cladding Inconel 718 superalloy. *Transactions of Nonferrous Metals Society of China*, *26*(2), 431–436. https://doi.org/10.1016/S1003-6326(16)64131-6

Louis, E. H., & John, G. (1962). *Matrix Stiffened Alloy* (Patent No. US3160500A). https://patents.google.com/patent/US3160500A/en

Lu, X., Du, J., Deng, Q., & Zhuang, J. (2014). Stress rupture properties of GH4169 superalloy. *Journal of Materials Research and Technology*, *3*(2), 107–113.

https://doi.org/10.1016/J.JMRT.2014.03.003

Lu, Y., Wu, S., Gan, Y., Huang, T., Yang, C., Junjie, L., & Lin, J. (2015). Study on the microstructure, mechanical property and residual stress of SLM Inconel-718 alloy manufactured by differing island scanning strategy. *Optics and Laser Technology*, *75*(November 2016), 197–206. https://doi.org/10.1016/j.optlastec.2015.07.009

Lynch, S. (2013). Melt Pool Evolution Study in Selective Laser Melting. *Dynamical Systems with Applications Using MATLAB*, *53*, 1182–1194. https://doi.org/10.1017/CBO9781107415324.004

Ma, M., Wang, Z., & Zeng, X. (2015). Effect of energy input on microstructural evolution of direct laser fabricated IN718 alloy. *Materials Characterization*, *106*, 420–427. https://doi.org/10.1016/J.MATCHAR.2015.06.027

Mahobia, G. S., Paulose, N., Mannan, S. L., Sudhakar, R. G., Chattopadhyay, K., Santhi Srinivas, N. C., & Singh, V. (2014). Effect of hot corrosion on low cycle fatigue behavior of superalloy IN718. *International Journal of Fatigue*, *59*, 272–281. https://doi.org/10.1016/J.IJFATIGUE.2013.08.009

Majeed, M., Khan, H. M., & Rasheed, I. (2019). Finite element analysis of melt pool thermal characteristics with passing laser in SLM process. *Optik*, *194*, 163068. https://doi.org/10.1016/J.IJLEO.2019.163068

Manikandan, S. G. K., Sivakumar, D., Rao, K. P., & Kamaraj, M. (2014). Effect of weld cooling rate on Laves phase formation in Inconel 718 fusion zone. *Journal of Materials Processing Technology*, *214*(2), 358–364. https://doi.org/10.1016/J.JMATPROTEC.2013.09.006

Manufacturing, I. 261: A. (n.d.). *ISO/TC 261 Additive Manufacturing*. Retrieved February 21, 2020, from https://www.iso.org/committee/629086.html

Marchese, G., Lorusso, M., Parizia, S., Bassini, E., Lee, J.-W., Calignano, F., Manfredi, D., Terner, M., Hong, H.-U., Ugues, D., Lombardi, M., & Biamino, S. (2018). Influence of heat treatments on microstructure evolution and mechanical properties of Inconel 625 processed by laser powder bed fusion. *Materials Science and Engineering: A*, *729*, 64–75. https://doi.org/10.1016/J.MSEA.2018.05.044

MATTER, T. U. of L., & Andrew Green, T. U. of L. (2001, July 18). *Coherency Strain Hardening*. http://core.materials.ac.uk/search/detail.php?id=2618

McCracken, C. G., Barbis, D. P., & Deeter, R. C. (2011). Key characteristics of hydride–dehydride titanium powder. *Powder Metallurgy*, *54*(3), 180–183. https://doi.org/10.1179/174329011X13045076771849

McDevitt, E. (2010). Effect of temperature and strain during forging on subsequent delta phase precipitation during solution annealing in ATI 718plus® alloy. *7th International Symposium on Superalloy 718 and Derivatives 2010*, *1*, 307–319. https://doi.org/10.1002/9781118495223.ch23

McLaren. (2015). *McLaren Formula 1 - McLaren Deploys Stratasys Additive Manufacturing to Improve 2017 Car Performance*. https://www.mclaren.com/formula1/partners/stratasys/mclaren-deploys-stratasys-additive-manufacturing-improve-2017-car-performance/

Mei, Y., Liu, Y., Liu, C., Li, C., Yu, L., Guo, Q., & Li, H. (2015). Effects of cold rolling on the precipitation kinetics and the morphology evolution of intermediate phases in Inconel 718 alloy. *Journal of Alloys and Compounds*, *649*, 949–960.

https://doi.org/10.1016/J.JALLCOM.2015.07.149

Mercier, J.-P., Zambelli, G., & Kurz, W. (2002). High temperature Deformation. In *Introduction to Material Science* (p. 304).

Metal AM. (2014). *Properties of metal powders used for Additive Manufacturing to be described in proposed ASTM standard*. https://www.metal-am.com/properties-of-metal-powders-used-for-additive-manufacturing-to-be-described-in-proposed-astm-standard/

Miao, Z., Shan, A., Wang, W., Lu, J., Xu, W., & Song, H. (2010). Quantitative Characterization of Two-Stage Homogenization Treatment of Alloy 718. In *7th International Symposium on Superalloy 718 and Derivatives* (pp. 107–115). John Wiley & Sons, Inc. https://doi.org/10.1002/9781118495223.ch7

MIAO, Z., SHAN, A., WU, Y., LU, J., XU, W., & SONG, H. (2011). Quantitative analysis of homogenization treatment of INCONEL718 superalloy. *Transactions of Nonferrous Metals Society of China*, *21*(5), 1009–1017. https://doi.org/10.1016/S1003-6326(11)60814-5

Miller, M. ., Babu, S. ., & Burke, M. . (1999). Intragranular precipitation in alloy 718. *Materials Science and Engineering: A*, *270*(1), 14–18. https://doi.org/10.1016/S0921-5093(99)00235-X

Mills, W. J. (1984). Effect of Heat Treatment on the Tensile and Fracture Toughness Behavior of Alloy 718 Weldments. *Welding Research Journal*, 237-s-245-s.

MIT Technology Review. (n.d.). *Cleaner Jet Fuel from Coal*. Retrieved July 31, 2019, from https://www.technologyreview.com/s/417217/cleaner-jet-fuel-from-coal/

Mitkov, M., & Bozˇić, D. (1996). Hydride-dehydride conversion of solid Ti6Al4V to powder form. *Materials Characterization*, *37*(2–3), 53–60. https://doi.org/10.1016/S1044-5803(96)00061-7

Mostafaei, A., Hilla, C., Stevens, E. L., Nandwana, P., Elliott, A. M., & Chmielus, M. (2018). Comparison of characterization methods for differently atomized nickel-based alloy 625 powders. *Powder Technology*, *333*, 180–192. https://doi.org/10.1016/J.POWTEC.2018.04.014

Nelson, J. C., Vail, N. K., & Barlow, J. W. (1993). Laser sintering for composite materials. *1993 International Solid Freeform Fabrication Symposium*.

Newman John. (2011). *Koenigsegg Harnesses Additive Manufacturing for the One:1*. http://www.rapidreadytech.com/2014/04/koenigsegg-harnesses-additive-manufacturing-for-the-one1/

Nguejio, J., Szmytka, F., Hallais, S., Tanguy, A., Nardone, S., & Godino Martinez, M. (2019). Comparison of microstructure features and mechanical properties for additive manufactured and wrought nickel alloys 625. *Materials Science and Engineering: A*, *764*, 138214. https://doi.org/10.1016/J.MSEA.2019.138214

Ni, M., Chen, C., Wang, X., Wang, P., Li, R., Zhang, X., & Zhou, K. (2017). Anisotropic tensile behavior of in situ precipitation strengthened Inconel 718 fabricated by additive manufacturing. *Materials Science and Engineering: A*, *701*, 344–351. https://doi.org/10.1016/J.MSEA.2017.06.098

Niang, A., Viguier, B., & Lacaze, J. (2010). Some features of anisothermal solid-state transformations in alloy 718. *Materials Characterization*, *61*(5), 525–534. https://doi.org/10.1016/J.MATCHAR.2010.02.011

Niendorf, T., Leuders, S., Riemer, A., Richard, H. A., Tröster, T., & Schwarze, D. (2013). Highly Anisotropic Steel Processed by Selective Laser Melting. *Metallurgical and Materials Transactions B*, *44*(4), 794–796. https://doi.org/10.1007/s11663-013-9875-z

Ö. Poyraz, E. Yasa, G. Akbulut, A.Orhangül, S. P. (n.d.). *INVESTIGATION OF SUPPORT STRUCTURES FOR DIRECT METAL LASER SINTERING (DMLS) OF IN625 PARTS*. 560–574.

Office of Nuclear Energy. (2016). *NEET-ADVANCED METHODS FOR MANUFACTURING AWARD SUMMARIES*. https://www.energy.gov/sites/prod/files/2016/05/f31/2016 ADVANCED METHODS FOR MANUFACTURING AWARD SUMMARIES_0.pdf

Oradei-Basile, A., & Radavich, J. F. (1991). *A Current T-T-T Diagram for Wrought Alloy 718*. 325–335. https://doi.org/10.7449/1991/superalloys_1991_325_335

Periane, S., Duchosal, A., Vaudreuil, S., Chibane, H., Morandeau, A., Cormier, J., & Leroy, R. (2019). Machining influence on the fatigue resistance of Inconel 718 fabricated by Selective Laser Melting (SLM). *Procedia Structural Integrity*, *19*, 415–422. https://doi.org/10.1016/J.PROSTR.2019.12.045

Physical Sciences Inc. (2009). *PSI's Additive Manufacturing of Nuclear Grade Components | PSI - Physical Sciences Inc.* http://www.psicorp.com/content/psis-additive-manufacturing-nuclear-grade-components

Ping, D. H., Gu, Y. F., Cui, C. Y., & Harada, H. (2007). Grain boundary segregation in a Ni–Fe-based (Alloy 718) superalloy. *Materials Science and Engineering: A*, *456*(1–2), 99–102. https://doi.org/10.1016/J.MSEA.2007.01.090

Pleass, C., & Jothi, S. (2018). Influence of powder characteristics and Additive manufacturing process parameters on the microstructure and mechanical behaviour of Inconel 625 fabricated by Selective Laser Melting. *Additive Manufacturing*.

Pollock, T. M., & Tin, S. (2006). Nickel-Based Superalloys for Advanced Turbine Engines: Chemistry, Microstructure and Properties. *Journal of Propulsion and Power*, *22*(2), 361–374. https://doi.org/10.2514/1.18239

Popovich, V. A., Borisov, E. V., Popovich, A. A., Sufiiarov, V. S., Masaylo, D. V., & Alzina, L. (2017a). Functionally graded Inconel 718 processed by additive manufacturing: Crystallographic texture, anisotropy of microstructure and mechanical properties. *Materials & Design*, *114*, 441–449. https://doi.org/10.1016/J.MATDES.2016.10.075

Popovich, V. A., Borisov, E. V., Popovich, A. A., Sufiiarov, V. S., Masaylo, D. V., & Alzina, L. (2017b). Impact of heat treatment on mechanical behaviour of Inconel 718 processed with tailored microstructure by selective laser melting. *Materials & Design*, *131*, 12–22. https://doi.org/10.1016/J.MATDES.2017.05.065

Promoppatum, P., Yao, S.-C., Pistorius, P. C., & Rollett, A. D. (2017). A Comprehensive Comparison of the Analytical and Numerical Prediction of the Thermal History and Solidification Microstructure of Inconel 718 Products Made by Laser Powder-Bed Fusion. *Engineering*, *3*(5), 685–694. https://doi.org/10.1016/J.ENG.2017.05.023

Quist, W. E., Taggart, R., & Polonis, D. H. (1971). The influence of iron and aluminum on the precipitation of metastable Ni3Nb phases in the Ni-Nb system. *Metallurgical Transactions*, *2*(3), 825–832. https://doi.org/10.1007/BF02662742

Radavich, J. F. (2004). The Physical Metallurgy of Cast and Wrought Alloy 718. *Superalloys 718 Metallurgy and Applications (1989)*, 229–240. https://doi.org/10.7449/1989/Superalloys_1989_229_240

Radhakrishna, Ch., & Rao, K. P. (1994). Studies on creep/stress rupture behaviour of superalloy 718 weldments used in gas turbine applications. *Materials at High Temperatures*, *12*(4), 323–327. https://doi.org/10.1080/09603409.1994.11752536

Radhakrishna, Ch., Rao, K. P., & Srinivas, S. (1995). Laves phase in superalloy 718 weld metals. *Journal of Materials Science Letters*, *14*(24), 1810–1812. https://doi.org/10.1007/BF00271015

Radhakrishna, CH, & Prasad Rao, K. (1997). The formation and control of Laves phase in superalloy 718 welds. *Journal of Materials Science*, *32*(8), 1977–1984. https://doi.org/10.1023/A:1018541915113

Rahimi, S., King, M., & Dumont, C. (2017). Stress relaxation behaviour in IN718 nickel based superalloy during ageing heat treatments. *Materials Science and Engineering: A*, *708*, 563–573. https://doi.org/10.1016/J.MSEA.2017.09.116

Ram, G. D. J., Reddy, A. V., Rao, K. P., & Reddy, G. M. (2005). Microstructure and mechanical properties of Inconel 718 electron beam welds. *Materials Science and Technology*, *21*(10), 1132–1138. https://doi.org/10.1179/174328405X62260

Rao, G. A., Kumar, M., Srinivas, M., & Sarma, D. S. (2003). Effect of standard heat treatment on the microstructure and mechanical properties of hot isostatically pressed superalloy inconel 718. *Materials Science and Engineering: A*, *355*(1–2), 114–125. https://doi.org/10.1016/S0921-5093(03)00079-0

Reed, R. C. (2006a). Other Phases in the Superalloys. In *The Superalloys Fundamentals and Applications2* (pp. 49–51).

Reed, R. C. (2006b). The Physical Metallurgy of nickel and its alloys. In *The Superalloys Fundamentals and Applications* (pp. 33–40). Cambridge University Press.

Ren, W., Niu, C., Ding, B., Zhong, Y., Yu, J., Ren, Z., Liu, W., Ren, L., & Liaw, P. K. (2018). Improvement in creep life of a nickel-based single-crystal superalloy via composition homogeneity on the multiscales by magnetic-field-assisted directional solidification. *Scientific Reports*, *8*(1), 1452. https://doi.org/10.1038/s41598-018-19800-5

Roberts, I. A., Wang, C. J., Esterlein, R., Stanford, M., & Mynors, D. J. (2009). A three-dimensional finite element analysis of the temperature field during laser melting of metal powders in additive layer manufacturing. *International Journal of Machine Tools and Manufacture*, *49*(12–13), 916–923. https://doi.org/10.1016/J.IJMACHTOOLS.2009.07.004

Rombouts, M., Froyen, L., Gusarov, A. V., Bentefour, E. H., & Glorieux, C. (2005). Light extinction in metallic powder beds: Correlation with powder structure. *Journal of Applied Physics*, *98*(1). https://doi.org/10.1063/1.1948509

Sabelkin, V. P., Cobb, G. R., Shelton, T. E., Hartsfield, M. N., Newell, D. J., O'Hara, R. P., & Kemnitz, R. A. (2019). Mitigation of anisotropic fatigue in nickel alloy 718 manufactured via selective laser melting. *Materials & Design*, *182*, 108095. https://doi.org/10.1016/J.MATDES.2019.108095

Sadowski, M., Ladani, L., Brindley, W., & Romano, J. (2016). Optimizing quality of additively manufactured Inconel 718 using powder bed laser melting process. *Additive Manufacturing*, *11*, 60–70. https://doi.org/https://doi.org/10.1016/j.addma.2016.03.006

Sarkar, S., Kumar, C. S., & Nath, A. K. (2019). Effects of heat treatment and build orientations on the fatigue life of selective laser melted 15-5 PH stainless steel. *Materials Science and Engineering: A*, *755*, 235–245. https://doi.org/10.1016/J.MSEA.2019.04.003

Schirra, J. J., Caless, R. H., & Hatala, R. W. (1991). The effect of laves phase on the mechanical properties of wrought and cast + hip inconel 718. *Superalloys 718, 625 and Various Derivatives (1991)*.

Shankar, V., Bhanu Sankara Rao, K., & Mannan, S. . (2001). Microstructure and mechanical properties of Inconel 625 superalloy. *Journal of Nuclear Materials*, *288*(2–3), 222–232. https://doi.org/10.1016/S0022-3115(00)00723-6

Shi, X., Duan, S.-C., Yang, W.-S., Guo, H.-J., & Guo, J. (2018). Effect of Cooling Rate on Microsegregation During Solidification of Superalloy INCONEL 718 Under Slow-Cooled Conditions. *Metallurgical and Materials Transactions B*, *49*(4), 1883–1897. https://doi.org/10.1007/s11663-018-1169-z

Shuai, L., Wei, Q., Shi, Y., Zhang, J., & Wei, L. (2016). Micro-Crack Formation and Controlling of Inconel625 Parts Fabricated by Selective Laser Melting. *Solid Freeform Fabrication Symposium – An Additive Manufacturing Conference*, 520–529.

Sivaprasad, K., & Ganesh Sundara Raman, S. (2008). Influence of Weld Cooling Rate on Microstructure and Mechanical Properties of Alloy 718 Weldments. *Metallurgical and Materials Transactions A*, *39*(9), 2115–2127. https://doi.org/10.1007/s11661-008-9553-y

Slama, C., Servant, C., & Cizeron, G. (1997). Aging of the Inconel 718 alloy between 500 and 750 °C. *Journal of Materials Research*, *12*(09), 2298–2316. https://doi.org/10.1557/JMR.1997.0306

Slotwinski, J. A., & Garboczi, E. J. (2015). Metrology Needs for Metal Additive Manufacturing Powders. *Jom*, *67*(3), 538–543. https://doi.org/10.1007/s11837-014-1290-7

Sohrabi, M. J., Mirzadeh, H., & Rafiei, M. (2018). Solidification behavior and Laves phase dissolution during homogenization heat treatment of Inconel 718 superalloy. *Vacuum*, *154*, 235–243. https://doi.org/10.1016/J.VACUUM.2018.05.019

Song, J. L., Li, Y. T., Deng, Q. L., & Hu, D. J. (2007). Rapid prototyping manufacturing of silica sand patterns based on selective laser sintering. *Journal of Materials Processing Technology*, *187–188*, 614–618. https://doi.org/10.1016/j.jmatprotec.2006.11.108

Song, K. H., & Nakata, K. (2010). Effect of precipitation on post-heat-treated Inconel 625 alloy after friction stir welding. *Materials & Design*, *31*(6), 2942–2947. https://doi.org/10.1016/J.MATDES.2009.12.020

SpaceX. (n.d.). *SpaceX Launches 3D-Printed Part to Space, Creates Printed Engine Chamber | SpaceX*. Retrieved July 24, 2018, from http://www.spacex.com/news/2014/07/31/spacex-launches-3d-printed-part-space-creates-printed-engine-chamber-crewed

Special Metals Corporation. (2004). *Technical bulletin: Inconel alloy 718 (Publication number SMC-045)*.

Special Metals Corporation. (2007). *Inconel Alloy 718*.

Special Metals Corporation. (2013). *Inconel Alloy 625*.

Spierings, A. B., Voegtlin, M., Bauer, T., & Wegener, K. (2015). Powder flowability characterisation methodology for powder-bed-based metal additive manufacturing. *Progress in Additive Manufacturing*, *1*(1), 9–20. https://doi.org/10.1007/s40964-015-0001-4

Strano, G., Hao, L., Everson, R. M., & Evans, K. E. (2013). Surface roughness analysis, modelling

and prediction in selective laser melting. *Journal of Materials Processing Technology*, *213*(4), 589–597. https://doi.org/10.1016/J.JMATPROTEC.2012.11.011

Stucke, M., Nicholas, T., Khobaib, M., & Majumdar, B. (1984). ENVIRONMENTAL ASPECTS IN CREEP CRACK GROWTH IN A NICKEL BASE SUPERALLOY. *Fracture 84*, 3967–3975. https://doi.org/10.1016/B978-1-4832-8440-8.50418-X

Sui, S., Chen, J., Fan, E., Yang, H., Lin, X., & Huang, W. (2017). The influence of Laves phases on the high-cycle fatigue behavior of laser additive manufactured Inconel 718. *Materials Science and Engineering: A*, *695*, 6–13. https://doi.org/10.1016/J.MSEA.2017.03.098

Sui, S., Chen, J., Ma, L., Fan, W., Tan, H., Liu, F., & Lin, X. (2019). Microstructures and stress rupture properties of pulse laser repaired Inconel 718 superalloy after different heat treatments. *Journal of Alloys and Compounds*, *770*, 125–135. https://doi.org/10.1016/J.JALLCOM.2018.08.063

Sun, W. ., Guo, S. ., Lee, J. ., Park, N. ., Yoo, Y. ., Choe, S. ., & Hu, Z. . (1998). Effects of phosphorus on the δ-Ni3Nb phase precipitation and the stress rupture properties in alloy 718. *Materials Science and Engineering: A*, *247*(1–2), 173–179. https://doi.org/10.1016/S0921-5093(97)00753-3

Sun, W. R., Guo, S. R., Lu, D. Z., & Hu, Z. Q. (1997). Effect of phosphorus on the microstructure and stress rupture properties in an Fe-Ni-Cr base superalloy. *Metallurgical and Materials Transactions A*, *28*(3), 649–654. https://doi.org/10.1007/s11661-997-0050-5

Sundararaman, M., & Mukhopadhyay, P. (1993). Carbide Precipitation in Inconel 718. *High Temperature Materials and Processes*, *11*(1–4). https://doi.org/10.1515/HTMP.1993.11.1-4.351

Sundararaman, M., Mukhopadhyay, P., & Banerjee, S. (1992). Some aspects of the precipitation of metastable intermetallic phases in INCONEL 718. *Metallurgical Transactions A*, *23*(7), 2015–2028. https://doi.org/10.1007/BF02647549

Tabilo-Munizaga, G., & Barbosa-Cánovas, G. V. (2005). Rheology for the food industry. *Journal of Food Engineering*, *67*(1–2), 147–156. https://doi.org/10.1016/J.JFOODENG.2004.05.062

Tanner, D. W. J. (2009). *Life assessment of welded INCONEL 718 at high temperature* [University of Nottingham]. https://eprints.nottingham.ac.uk/10796/1/DWJ_Tanner_PhD_Thesis.pdf

Tao, P., Li, H., Huang, B., Hu, Q., Gong, S., & Xu, Q. (2019). The crystal growth, intercellular spacing and microsegregation of selective laser melted Inconel 718 superalloy. *Vacuum*, *159*, 382–390. https://doi.org/10.1016/J.VACUUM.2018.10.074

Taylor Edward, C. A. (2016). *Daimler Trucks to use 3D printing in spare parts production*. https://www.reuters.com/article/us-daimler-3dprinting/daimler-trucks-to-use-3d-printing-in-spare-parts-production-idUSKCN0ZT201

Teunou, E., & Fitzpatrick, J. . (2000). Effect of storage time and consolidation on food powder flowability. *Journal of Food Engineering*, *43*(2), 97–101. https://doi.org/10.1016/S0260-8774(99)00137-5

Thébaud, L., Villechaise, P., Crozet, C., Devaux, A., Béchet, D., Franchet, J.-M., Rouffié, A.-L., Mills, M., & Cormier, J. (2018). Is there an optimal grain size for creep resistance in Ni-based disk superalloys? *Materials Science and Engineering: A*, *716*, 274–283. https://doi.org/10.1016/J.MSEA.2017.12.104

Thijs, L., Kempen, K., Kruth, J.-P., & Van Humbeeck, J. (2013). Fine-structured aluminium products with controllable texture by selective laser melting of pre-alloyed AlSi10Mg powder. *Acta Materialia*, *61*(5), 1809–1819. https://doi.org/10.1016/J.ACTAMAT.2012.11.052

Thompson, R. G., Radhakrishnan, B., & Mayo, D. E. (1989). Intergranular Liquid Formation, Distribution, and Cracking. *Superalloy 718 - Metallurgy and Applications*, 437–455.

Tillmann, W., Schaak, C., Nellesen, J., Schaper, M., Aydinöz, M. E., & Hoyer, K.-P. (2017). Hot isostatic pressing of IN718 components manufactured by selective laser melting. *Additive Manufacturing*, *13*, 93–102. https://doi.org/10.1016/J.ADDMA.2016.11.006

Trosch, T., Strößner, J., Völkl, R., & Glatzel, U. (2016). Microstructure and mechanical properties of selective laser melted Inconel 718 compared to forging and casting. *Materials Letters*, *164*, 428–431. https://doi.org/10.1016/j.matlet.2015.10.136

Trumpf. (n.d.). *TruPrint Series 1000 | TRUMPF*. Retrieved September 11, 2018, from https://www.trumpf.com/en_INT/products/machines-systems/3d-printing-systems/truprint-series-1000/

Tucho, W. M., Cuvillier, P., Sjolyst-Kverneland, A., & Hansen, V. (2017). Microstructure and hardness studies of Inconel 718 manufactured by selective laser melting before and after solution heat treatment. *Materials Science and Engineering: A*, *689*, 220–232. https://doi.org/10.1016/J.MSEA.2017.02.062

Vilaro, T., Colin, C., & Bartout, J. D. (2011). As-Fabricated and Heat-Treated Microstructures of the Ti-6Al-4V Alloy Processed by Selective Laser Melting. *Metallurgical and Materials Transactions A*, *42*(10), 3190–3199. https://doi.org/10.1007/s11661-011-0731-y

Visser, J. (1989). *An Invited Review Van der Waals and Other Cohesive Forces Affecting Powder Fluidization*. *58*, 1–10.

Vrancken, B. (2016). *Study of Residual Stresses in Selective Laser Melting*. *June*.

Wang, M., Du, J., Deng, Q., Tian, Z., & Zhu, J. (2015). The effect of phosphorus on the microstructure and mechanical properties of ATI 718Plus alloy. *Materials Science and Engineering: A*, *626*, 382–389. https://doi.org/10.1016/J.MSEA.2014.12.094

Wang, Q. ., Apelian, D., & Lados, D. . (2001). Fatigue behavior of A356-T6 aluminum cast alloys. Part I. Effect of casting defects. *Journal of Light Metals*, *1*(1), 73–84. https://doi.org/10.1016/S1471-5317(00)00008-0

Wang, Z., Guan, K., Gao, M., Li, X., Chen, X., & Zeng, X. (2012). The microstructure and mechanical properties of deposited-IN718 by selective laser melting. *Journal of Alloys and Compounds*, *513*, 518–523. https://doi.org/10.1016/J.JALLCOM.2011.10.107

Watanabe{, T., & Tsurekawa, S. (2008). *THE CONTROL OF BRITTLENESS AND DEVELOPMENT OF DESIRABLE MECHANICAL PROPERTIES IN POLYCRYSTALLINE SYSTEMS BY GRAIN BOUNDARY ENGINEERING*. https://ac.els-cdn.com/S135964549900275X/1-s2.0-S135964549900275X-main.pdf?_tid=e220233a-18ac-11e8-817f-00000aacb35f&acdnat=1519399324_beb88d4d280f16a8378bae4e89a73ee2

WD, C., RL, K., & MP, W. (1991). Differential Thermal Analysis (DTA) Study of the Homogenization Process in Alloy 718. *Superalloys*, *718*(625), 147–160.

Wisniewski, A., & Beddoes, J. (2009). Influence of grain-boundary morphology on creep of a wrought Ni-base superalloy. *Materials Science and Engineering: A*, *510–511*, 266–272.

https://doi.org/10.1016/J.MSEA.2008.04.130

Wohlers Associates. (13 C.E.). *Wohlers Report 2013*.

Wong, K. V., & Hernandez, A. (2012). A Review of Additive Manufacturing. *ISRN Mechanical Engineering*, *2012*, 1–10. https://doi.org/10.5402/2012/208760

Wu, M.-W., Chen, J.-K., Lin, B.-H., & Chiang, P.-H. (2017). Improved fatigue endurance ratio of additive manufactured Ti-6Al-4V lattice by hot isostatic pressing. *Materials & Design*, *134*, 163–170. https://doi.org/10.1016/J.MATDES.2017.08.048

Xiao, L., Chen, D. L., & Chaturvedi, M. C. (2005). Shearing of γ" precipitates and formation of planar slip bands in Inconel 718 during cyclic deformation. *Scripta Materialia*, *52*(7), 603–607. https://doi.org/10.1016/J.SCRIPTAMAT.2004.11.023

Xie, X., Dong, J., Wang, G., You, W., Du, J., Zhao, C., Wang, Z., & Carneiro, T. (2005). The effect of nb, ti, al on precipitation and strengthening behavior of 718 type superalloys. *Proceedings of the International Symposium on Superalloys and Various Derivatives*, *3*, 287–298. https://doi.org/10.7449/2005/superalloys_2005_287_298

Xie, X. S., Dong, J. X., & Zhang, M. C. (2007). Research and Development of Inconel 718 Type Superalloy. *Materials Science Forum*, *539–543*, 262–269. https://doi.org/10.4028/www.scientific.net/MSF.539-543.262

Xu, J., Huang, Z., & Jiang, L. (2017). Effect of heat treatment on low cycle fatigue of IN718 superalloy at the elevated temperatures. *Materials Science and Engineering: A*, *690*, 137–145. https://doi.org/10.1016/J.MSEA.2017.02.104

Xu, Xiang, Mi, G., Chen, L., Xiong, L., Jiang, P., Shao, X., & Wang, C. (2017). Research on microstructures and properties of Inconel 625 coatings obtained by laser cladding with wire. *Journal of Alloys and Compounds*, *715*, 362–373. https://doi.org/10.1016/J.JALLCOM.2017.04.252

Xu, Xiangfang, Ganguly, S., Ding, J., Seow, C. E., & Williams, S. (2018). Enhancing mechanical properties of wire + arc additively manufactured INCONEL 718 superalloy through in-process thermomechanical processing. *Materials & Design*, *160*, 1042–1051. https://doi.org/10.1016/J.MATDES.2018.10.038

Yang, W., Hu, S., Huo, M., Sun, D., Zhang, J., & Liu, L. (2019). Orientation controlling of Ni-based single-crystal superalloy by a novel method: grain selection assisted by un-melted reused seed. *Journal of Materials Research and Technology*, *8*(1), 1347–1352. https://doi.org/10.1016/J.JMRT.2018.10.005

Yang, Y., Han, Y., Liang, X., & Zhang, R. (1994). An Investigation and Deformation of the Homogenization of Alloy 718 Ingots. *Superalloys 718, 625, 706 and Various Derivatives (1994)*, 947–956.

Yeh, A.-C., Lu, K.-W., Kuo, C.-M., Bor, H.-Y., & Wei, C.-N. (2011). Effect of serrated grain boundaries on the creep property of Inconel 718 superalloy. *Materials Science and Engineering: A*, *530*, 525–529. https://doi.org/10.1016/J.MSEA.2011.10.014

Zhang, D., Feng, Z., Wang, C., Wang, W., Liu, Z., & Niu, W. (2018). Comparison of microstructures and mechanical properties of Inconel 718 alloy processed by selective laser melting and casting. *Materials Science and Engineering: A*, *724*, 357–367. https://doi.org/10.1016/J.MSEA.2018.03.073

Zhang, D., Niu, W., Cao, X., & Liu, Z. (2015). Effect of standard heat treatment on the

microstructure and mechanical properties of selective laser melting manufactured Inconel 718 superalloy. *Materials Science and Engineering: A*, *644*, 32–40. https://doi.org/10.1016/J.MSEA.2015.06.021

Zhang, H. Y., Zhang, S. H., Cheng, M., & Zhao, Z. (2017). Microstructure evolution of IN718 alloy during the delta process. *Procedia Engineering*, *207*, 1099–1104. https://doi.org/10.1016/J.PROENG.2017.10.1137

Zhang, Y. C., Li, Z. G., Nie, P. L., & Wu, Y. X. (2013). Effect of ultrarapid cooling on microstructure of laser cladding IN718 coating. *Surface Engineering*, *29*(6), 414–418. https://doi.org/10.1179/1743294413Y.0000000142

Zhang, Y., Yang, L., Chen, T., Zhang, W., Huang, X., & Dai, J. (2017). Investigation on the optimized heat treatment procedure for laser fabricated IN718 alloy. *Optics & Laser Technology*, *97*, 172–179. https://doi.org/10.1016/J.OPTLASTEC.2017.06.027

Zhang, Y., Yang, L., Lu, W., Wei, D., Meng, T., & Gao, S. (2020). Microstructure and elevated temperature mechanical properties of IN718 alloy fabricated by laser metal deposition. *Materials Science and Engineering: A*, *771*, 138580. https://doi.org/10.1016/J.MSEA.2019.138580

Zhao, L., Liao, H., Pan, Y., Wang, L., & Wang, Q. (2011). Abnormal macrosegregation induced by formed porosity during solidification of an Al-Sn alloy. *Scripta Materialia*. https://doi.org/10.1016/j.scriptamat.2011.07.034

Zhou, X., Li, K., Zhang, D., Liu, X., Ma, J., Liu, W., & Shen, Z. (2015). Textures formed in a CoCrMo alloy by selective laser melting. *Journal of Alloys and Compounds*, *631*, 153–164. https://doi.org/10.1016/J.JALLCOM.2015.01.096